Search for Nucleon Decay into Charged Antilepton plus Meson in Super-Kamiokande

Haruki Nishino

February, 2009

Abstract

Systematic searches for nucleon decays into a charged anti-lepton (e^+ or μ^+) plus a light meson (π^0, π^-, η, ρ^0, ρ^-, ω) were performed. Twelve nucleon decay modes were analyzed. The total exposure is 140.9 kiloton·year exposure which includes a 91.7 kiloton·year (1489.2 live days) of Super-Kamiokande-I and a 49.2 kiloton·year (798.6 live days) of Super-Kamiokande-II.

The number and the feature of candidate events are consistent with the atmospheric neutrino background expectation. We did not observe statistically significant evidence for the nucleon decay. Thus, the lower limits of nucleon partial lifetime at 90% confidence level were obtained for all the studied modes. The lifetime limit for the $p \to e^+\pi^0$ mode is set to be $\tau/B(p \to e^+\pi^0) > 8.2 \times 10^{33}$ years, which is 5 times longer than the current best limit. For the other modes, their lifetime limits range from 3.6×10^{31} to 6.6×10^{33} years depending on the decay modes. The more stringent limits than the current best limits are set for ten modes in the twelve searched modes.

Acknowledgments

First of all, I would like to express my great gratitude to my supervisor, Prof. Kenji Kaneyuki for introducing me to the Super-Kamiokande experiment. His enormous support and advices were invaluable for my research.

I would like to thank Prof. Yoichiro Suzuki, the spokesperson of the Super-Kamiokande experiment. He gave me insightful comments on many occasions.

My deep appreciation goes to Prof. Masato Shiozawa. Without his valuable guidance and encouragement, this thesis would never have been completed.

I would like to express my appreciation to Prof. Takaaki Kajita and Prof. Ed Kearns for their constructive suggestions on my research.

I would be grateful to all the members of the atmospheric neutrino and proton decay analysis group in ICRR, Prof. S. Moriyama, Prof. Y. Hayato, K. Okumura, M. Miura, Y. Obayashi, J. Kameda, T. Kaji, Y. Shimizu, N. Tanimoto, G. Mitsuka, C. Ishihara, T. Mclachlan and S. Hazama.

I also wish to thank M. Fechner, Y. Itow, M. Litos, S. Mine, J.L. Raaf, C. Regis, K. Scholberg, T. Tanaka and C.W. Walter for their helpful comments and discussions on my work.

I would like to extend my gratitude to ICRR staffs and members, Prof. M. Nakahata, Prof. Y. Takeuchi, Prof. M. Yamashita, K. Abe, Y. Koshio, H. Sekiya, A. Takeda, K. Kobayashi, S. Nakayama, H. Ogawa, S. Yamada, Y. Takenaga, H. Watanabe, T. Iida, M. Ikeda, K. Ueshima, K. Ueno, Y. Nakajima, Y. Kouzuma and T. Yokozawa.

The analysis in this thesis has also relied on the hard work by all the members of Super-Kamiokande. This thesis is gratefully indebted to them.

I also would like to thank those who worked with me for the new electronics development, Y. Arai, K. Awai, S. Hayakawa, K. Ishikawa, E. Kimura, T. Uchida, and especially A. Minegishi.

I gratefully acknowledge the cooperation of Kamioka Mining and Smelting Company. This work was partially supported by the JSPS research fellowships for young scientists.

Finally, I would like to thank my family for their unwavering supports during my studies.

Contents

Chapter 1

Introduction

The motivation for this thesis is to test grand unified theories (GUTs) by searching for baryon number violating nucleon decay signals with the Super-Kamiokande detector.

Chapter 2 briefly describes theoretical motivations for GUTs and how GUT models predict the nucleon decay as a consequence of the model. The minimal SU(5) GUT, its extensions and their predictions are summarized. Some earlier experiments motivated by the nucleon decay search are also described in this chapter.

Chapter 3 is the overview of the Super-Kamiokande experiment, which is the largest water Cherenkov experiment for nucleon decay searches. Basic components and calibrations for the detector are explained in this chapter. In particular, the energy scale calibrations are crucial for the nucleon decay search. Its methods and results are shown.

Nucleon decay signals were simulated by a custom developed simulator. The details of the simulator is described in Chapter 4. Atmospheric neutrinos are irreducible background for nucleon decay search. The simulation for the interactions of the atmospheric neutrinos are also explained in this chapter

The data reduction algorithms to extract fully contained event samples from the enormous amount of the Super-Kamiokande data are explained in Chapter 5. The quick summary of the extracted data samples are shown in Chapter 8.

The event reconstruction algorithms were applied to the observed and simulated events passing the data reduction. Chapter 6 describes how the algorithms reconstruct interaction points, particle types and momenta and so on by detected charges and timings of PMTs.

Finally, the details and the results of the nucleon decay analysis are discussed in Chapter 9. Twelve nucleon decay modes predicted by the exchange of a super heavy gauge boson were studied in this thesis. Systematical searches with simple selection criteria were performed. Chapter 10 concludes this thesis with the new nucleon partial lifetime limits for the studied modes.

Chapter 2

Physics Background

The standard model is based on the gauge group, SU(3)×SU(2)×U(1). The SU(2)×U(1) symmetry describes the electroweak theory, and SU(3) color symmetry describes the strong interactions. The standard model has been successful in accounting for many experimental results. All the fermions and the gauge bosons in the standard model have been discovered. At present, only the Higgs boson is remaining to be discovered.

However, the standard model has a lot of unanswered questions. There are a lot of free empirical parameters, such as masses and generations of fermions, coupling constants, mixing angles and so on. Various attempts have been made to resolve the shortcomings by unifying the electroweak and the strong interactions in the context of Grand Unified Theory (GUT).

2.1 Grand Unified Theories

2.1.1 SU(5) GUT

The basic idea of GUTs is that the SU(2)×U(1) symmetry of the electroweak interactions and the SU(3) color symmetry of the strong interactions might be incorporated into a more global symmetry at some high unification energy scale. The simplest GUT model is the minimal SU(5) model proposed by Georgi and Glashow [1] in 1974. There are 24 independent matrices defining SU(5), which means that there are 24 gauge bosons mediating interactions as follows:

$$V_\mu = \begin{pmatrix} G_1^1 - \frac{2B}{\sqrt{30}} & G_2^1 & G_3^1 & \bar{X}^1 & \bar{Y}^1 \\ G_1^2 & G_2^2 - \frac{2B}{\sqrt{30}} & G_3^2 & \bar{X}^2 & \bar{Y}^2 \\ G_1^3 & G_2^3 & G_2^3 - \frac{2B}{\sqrt{30}} & \bar{X}^3 & \bar{Y}^3 \\ X_1 & X_2 & X_3 & \frac{W^3}{\sqrt{2}} + \frac{3B}{\sqrt{30}} & W^+ \\ Y_1 & Y_2 & Y_3 & W^- & -\frac{W^3}{\sqrt{2}} + \frac{3B}{\sqrt{30}} \end{pmatrix} \tag{2.1}$$

where G_i^j is the field related to the eight gluons, and W^+, W^-, W^3 and B are the gauge bosons in the electroweak interactions. In addition to the electroweak and strong interactions, there appeared two new very heavy gauge bosons X and Y with electric charges $\frac{4}{3}$ and $\frac{1}{3}$, respectively.

The fermions of each family or generation consist of 15 states as follows;

$$\begin{pmatrix} u_i \\ d_i \end{pmatrix}_L,\ u_{iR},\ d_{iR},\ \begin{pmatrix} \nu_e \\ e^- \end{pmatrix}_L,\ e_R^- \tag{2.2}$$

where i denotes color indices ($i = r, g, b$) of SU(3) symmetry.

They are assigned to the $\bar{5} + 10$ dimensional representations as follows;

$$\bar{5} = \begin{pmatrix} d_1^c \\ d_2^c \\ d_3^c \\ e^- \\ -\nu_e \end{pmatrix}_L \tag{2.3}$$

$$10 = \frac{1}{\sqrt{2}} \begin{pmatrix} 0 & u_3^c & -u_2^c & -u^1 & -d^1 \\ -u_3^c & 0 & u_1^c & -u^2 & -d^2 \\ u_2^c & -u_1^c & 0 & -u^3 & -d^3 \\ u^1 & u^2 & u^3 & 0 & -e^+ \\ d^1 & d^2 & d^3 & e^+ & 0 \end{pmatrix}_L \tag{2.4}$$

This model incorporates leptons and quarks into the same multiplets.

Since leptons and quarks are in the same multiplets, the coupling constants for the strong and electroweak interactions (g_s, g and g') must be related to each other by Clebsch-Gordan coefficients at the energy scale of GUT. For example, the weak mixing angle $\theta_{\rm W}$ at the GUT scale can be predicted as;

$$\sin^2 \theta_{\rm W} = \frac{g'^2}{g'^2 + g^2} = \frac{3}{8}. \tag{2.5}$$

The evolution of the three running coupling constants (α_i) can be given as follows;

$$\frac{1}{\alpha_i(\mu)} = \frac{1}{\alpha(M_X)} - \frac{b_i}{2\pi} \ln \frac{M_X}{\mu} \tag{2.6}$$

where μ is the energy scale, and $b_i = \left(-\frac{41}{10}, \frac{19}{6}, 7\right)$. The mixing angle $\theta_{\rm W}$ at the energy scale μ can be extrapolated using Equation (2.6) by requiring the following unification condition;

$$\alpha_1(M_X) = \alpha_2(M_X) = \alpha_3(M_X) = \alpha_{\rm GUT}. \tag{2.7}$$

Then, the weak mixing angle is predicted as;

$$\sin^2 \hat{\theta}_{\rm W}(M_Z) = 0.2102^{+0.0037}_{-0.0031} \text{ [7]} \tag{2.8}$$

where M_Z is the Z boson mass.

As a consequence of the SU(5) GUT model, there will be new interactions in which leptons and quarks can transform one into the other. This interaction can lead to the baryon number violation, such as nucleon decay, which is one of the most dramatic predictions from GUTs. Two quarks in a proton can transform into a lepton and an anti-quark resulting in a lepton plus meson final state. Figure 2.1 shows examples of possible diagrams for proton decay, $p \to e^+ q\bar{q}$ (neutral meson), in SU(5) GUT.

Even at normal energy scale, the X, Y boson exchanges can take place, although the decay rate, which is proportional to M_X^{-4}, is very small. The proton lifetime can be calculated as;

$$\tau_p \sim \frac{1}{\alpha_G^2} \frac{M_X^4}{m_p^5} \tag{2.9}$$

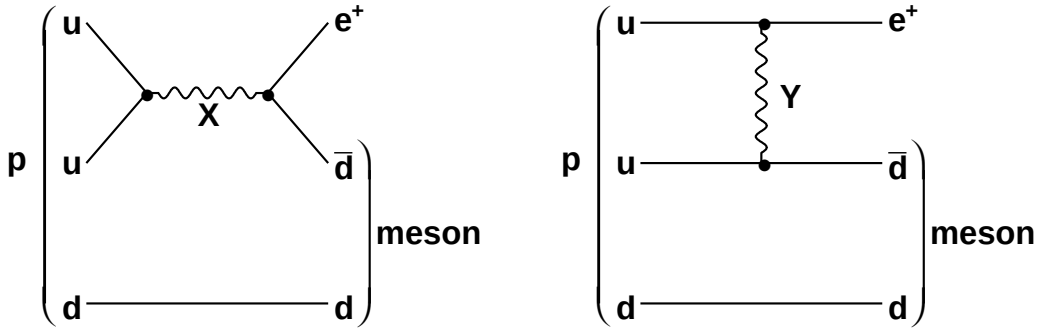

Figure 2.1: Diagrams of proton decay via X and Y bosons exchanges.

where α_G is the coupling constant at the unification scale, M_X is the mass of the gauge boson X, and m_p is the proton mass. In the minimal SU(5) GUT, the GUT unification scale is $M_X \sim (2 - 7) \times 10^{14}$ GeV. The predicted partial lifetime for the proton decaying to $p \to e^+\pi^0$, which is the dominant mode in the SU(5) GUT, is $\tau/B_{p\to e^+\pi^0} \sim 10^{31\pm1}$ years [2, 3]. However, the experimental lifetime lower limits from the IMB and KAMIOKANDE experiments are $\tau/B_{p\to e^+\pi^0} > 5.40 \times 10^{32}$ years [5] and $\tau/B_{p\to e^+\pi^0} > 2.60 \times 10^{32}$ years [6] at 90% C.L., respectively.

Furthermore, there are some inconsistencies in the minimal SU(5) GUT predictions with the results from precise measurements. The predicted mixing angle θ_W (Equation 2.8) is significantly smaller than the experimental results of $\sin^2\hat{\theta}_W(M_Z) = 0.23119 \pm 0.00014$ [8]. If we use the experimental data as input parameters the three couplings do not meet exactly in a point as shown in Figure 2.2.

Therefore, the minimal SU(5) GUT model is excluded by the experimental results. We need to consider a larger group to unify particles and fields.

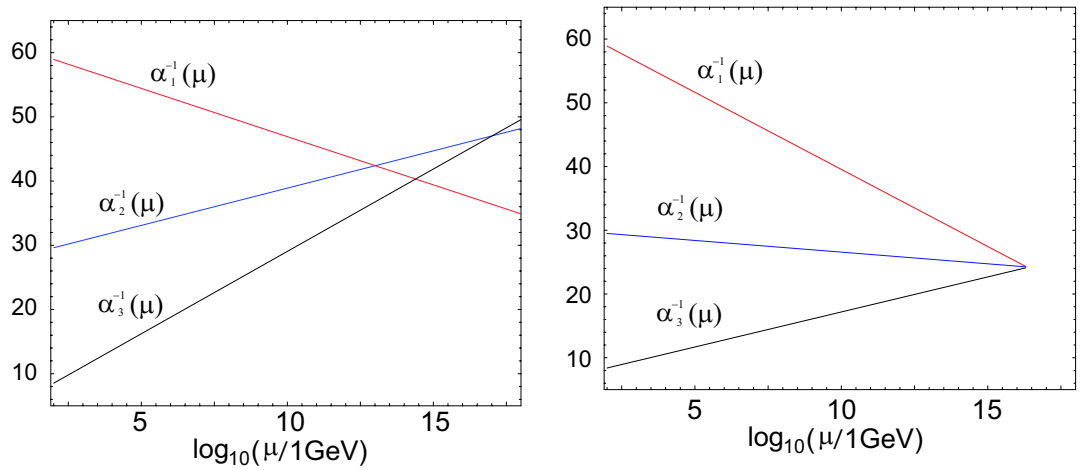

Figure 2.2: Evolution of the couplings α_1^{-1}, α_2^{-1} and α_3^{-1} as a function of energy scale for the minimal SU(5) GUT (left) and the minimal SUSY SU(5) GUT (right) [4].

2.1.2 Beyond SU(5) GUT

One possible extension of SU(5) GUT is supersymmetric (SUSY) GUT. The SUSY hypothesis introduces a new symmetry between fermions and bosons. Every particle has its own SUSY partner. Because of these extra degrees of freedom, the coefficients b_i in Equation (2.6) are modified to be smaller values. That results in the reduction of the slopes of the α^{-1} dependence on $\ln(M_X/\mu)$ and the higher unification energy scale. The three couplings α_1, α_2 and α_3 can meet on a single energy scale, $\sim 3 \times 10^{16}$ GeV, as shown in Figure 2.2. In the minimal SUSY SU(5) GUT model, the predicted weak mixing angle is $\sin^2\hat{\theta}_{\rm W}(M_Z) = 0.2334^{+0.0036}_{-0.0030}$ [7], which agrees well with the experiment [8]. The predicted partial lifetime of a proton decaying to $p \rightarrow e^+\pi^0$ is $\tau/B_{p\rightarrow e^+\pi^0} \sim 2 \times 10^{35\pm1}$ [9], and the theoretical lower limit is calculated as $\tau/B_{p\rightarrow e^+\pi^0} > 4.1 \times 10^{33}$ [9], which can be reached by the Super-Kamiokande data used in this thesis. However, in the SUSY SU(5) GUT, the $p \rightarrow \bar{\nu}K^+$ mode induced by the exchange of supersymmetric particles is the favored proton decay mode compared to the $p \rightarrow e^+\pi^0$ mode. The partial lifetime of a proton for the $p \rightarrow \bar{\nu}K^+$ mode is estimated to be $\tau/B_{p\rightarrow\bar{\nu}K^+} \leq 2.9\times10^{30}$ [9], while the experimental lower limit of this mode is 2.3×10^{33} years [12] by the Super-Kamiokande experiment. As a result, the minimal SUSY SU(5) GUT is strongly constrained by the experimental limit.

Another extension of GUT is to use a larger symmetry containing the standard group, SU(3)×SU(2)×U(1). One of the most popular example is the GUT model based on the SO(10) symmetry. One of the interesting features of the SO(10) GUT is that it can include left-right symmetry and has the power to predict the neutrino mass. There are some intermediate symmetries to break the symmetry to SU(3)×SU(2)×U(1) from SO(10). The SO(10) model breaking the symmetry via G_{422} =SU(4)×SU(2)$_L$×SU(2)$_R$ [13] is one of the viable models. The dominant proton decay mode for the model is $p \rightarrow e^+\pi^0$, and it predicts the partial lifetime of a proton to be in the accessible range of the Super-Kamiokande experiment as;

$$\tau/B_{p\rightarrow e^+\pi^0} \sim 1.44 \times 10^{32.1\pm0.7\pm1.0\pm1.9}[14]. \tag{2.10}$$

However, predicted partial lifetimes of a proton by the other models with various intermediated symmetries have large uncertainties ranging from 10^{32} to 10^{39} [14, 15].

In addition, various GUT models are proposed, such as flipped SU(5) model [19] and SO(10) models in extra dimensions [17, 18]. The recent predictions including those models are summarized in Table 2.1.

2.1.3 Predictions for the Branching Ratios

Although the $p \rightarrow e^+\pi^0$ mode is considered to be the dominant decay mode in many GUT models, branching ratios for the other modes are not negligible. Table 2.2 shows some of the results of the detailed estimations of proton decay branching ratios. Those calculations are based on the non-supersymmetric SU(5) or SO(10) GUT models. Though the uncertainty of the branching ratio is large depending on the models, there are considerable fractions from the sub dominant decay modes.

Various predictions for τ_n/τ_p, the ratio of neutron to proton lifetime, are also shown in Table 2.2. The neutron and proton lifetimes are estimated to be comparable in the SU(5) GUT model. In most of the models, the $n \rightarrow e^+\pi^-$ mode is the dominant neutron decay mode.

As for the $N \rightarrow \mu^+(meson)$ mode, μ^+ can be produced by mixing effects between families. The ratio of the decay width of muons to positrons in the SU(5) GUT model are predicted to

Model	Prediction (years)	Reference
Minimal SU(5)	$\sim 10^{31\pm1}$	[3]
SO(10) G_{422}	$1.44 \times 10^{32.1\pm0.7\pm1.0\pm1.9}$	[14]
Minimal SUSY SU(5)	$\sim 2 \times 10^{35\pm1}$	[9]
SUSY SU(5) or SO(10)/G_{422}	$\sim 10^{35\pm1}$	[16]
Flipped SU(5)	$\sim 5 \times 10^{35\pm1}$	[19]
5-dimensions SO(10)	$\sim 7 \times 10^{33\pm2}$	[17]
6-dimensions SO(10)	$\sim 1 \times 10^{35}$	[18]

Table 2.1: Predictions from various models for the proton partial lifetime for $p \to e^+\pi^0$.

be as follows [24];

$$\frac{\Gamma\left(N \to \mu^+(meson)\right)}{\Gamma\left(N \to e^+(meson)\right)} = \frac{\sin\theta_c^2 \cos\theta_c^2}{\left(1+\cos\theta_c^2\right)^2 + 1} = 0.010 \tag{2.11}$$

where θ_c is the Cabbibo angle. The $N \to \mu^+(meson)$ rate is estimated to be very small compared to the $N \to e^+(meson)$ rate. On the other hand, the flipped SU(5) GUT [19] predicts the ratio as;

$$\frac{\Gamma\left(p \to \mu^+\pi^0\right)}{\Gamma\left(p \to e^+\pi^0\right)} = \frac{|U_{l_{12}}|^2}{|U_{l_{11}}|^2} \tag{2.12}$$

where U_l is the charged-lepton mixing matrix. Due to the uncertainty in the mixing matrix, the $p \to \mu^+\pi^0$ mode can have a comparable branching ratio with the $p \to e^+\pi^0$ mode in the flipped SU(5) GUT.

In summary, a lot of possibilities for nucleon decays are theoretically proposed. Therefore, we should search for all the possible nucleon decay modes in order to test them. This is the motivation for this thesis.

	Br. (%)				
	SU(5)				(SO10)
References	[20]	[21]	[22]	[23]	[23]
$p \to e^+\pi^0$	33	37	9	35	30
$p \to e^+\eta$	12	7	3	15	13
$p \to e^+\rho^0$	17	2	21	2	2
$p \to e^+\omega$	22	18	56	17	14
others	17	35	11	31	31
τ_p/τ_n	0.8	1.0	1.3		

Table 2.2: Predictions for the branching ratios for proton decay in the SU(5) and SO(10) GUT models. The ratio of of neutron to proton lifetime is also shown in the last line.

2.2 Nucleon Decay Experiments

In the late 1970s, several nucleon decay experiments were proposed motivated by the prediction of the minimal SU(5) GUT. The lifetime of proton was estimated to be $10^{27} \sim 10^{31}$ years at that time. One kiloton of material detector, which contains $\sim 3 \times 10^{32}$ protons, was expected to yield $10^{-1} \sim 10^{3}$ proton decays per day. Therefore, first of all, detectors are required to be very massive. The detectors are also required to have a high particle tracking performance and to be placed deep underground to reduce cosmic ray muon background. For nucleon decay experiments, there have been two types of detectors, i.e., fine grained iron calorimeters and water Cherenkov detectors.

Fine grained iron calorimeters consist of alternating layers of iron plates and tracking detectors. This type of detector has good performances in energy determination and particle identification. However, the detectors are more expensive than water Cherenkov detectors, and their total mass is limited to a few kilotons. The KGF [25], Soudan [27, 33], NUSEX [29] and Frejus [31] experiments used this type of detectors. Basic characteristics for these experiments are summarized in Table 2.3.

Water Cherenkov detectors have high resolutions of momentum and direction by detecting the intensity and the pattern of Cherenkov ring images. The particle identification also can be achieved by the Cherenkov ring pattern. Water Cherenkov detectors are less expensive and can be scaled up to tens of kilotons. The IMB [34], KAMIOKANDE [35, 36] and Super-Kamiokande [37] experiments used water Cherenkov technique and have much larger fiducial mass than the other type of experiments. The IMB experiment had a fiducial mass of 3.3 kilotons and had been the largest water Cherenkov detector until the Super-Kamiokande experiment started. KAMIOKANDE used 984 of 20-inch photomultiplier tubes and had a much higher photon collection efficiency than the IMB detector. KAMIOKANDE had better performances in momentum and vertex determination and particle identification. These two experiments had found no evidences for nucleon decays, and IMB had set the best lifetime limits for $p \to e^+\pi^0$ and many other nucleon decay modes [5].

The Super-Kamiokande experiment is a successor to the KAMIOKANDE experiment and have been the largest nucleon decay experiment as ever. In Super-Kamiokande-I and II, the accumulated exposure reached 141 kiloton·year exposure, which is about 20 times larger than the exposure of the IMB-3 experiment. The details of the Super-Kamiokande detector are described in the next chapter. The $p \to e^+\pi^0$ mode was searched for with the data of 414 days of Super-Kamiokande. No candidate events were found in the Super-Kamiokande data, and the more stringent lower lifetime limit than the IMB limit was obtained [38]. Super-Kamiokande also searched for $p \to \bar{\nu}K^+$, $n \to \bar{\nu}K^0$, $p \to e^+K^0$ and $p \to \mu^+K^0$ [11, 12], which are favored by SUSY GUT models. No candidate events were found for these modes as well.

Experiment	Operation (year)	Fiducial Mass (ton)	Source of Nucleons	Depth (m.w.e.)	Limits ($p \to e^+\pi^0$) (10^{30}yrs at 90%CL)
KGF	1980∼1992	60∼150	Fe	6050∼7000	1 candidate*[25]
Soudan-I	1981∼1990	16∼24	Fe	1800	1.31 [28]
NUSEX	1982∼1998	110∼130	Fe	5000	15 [30]
Frejus	1984∼1988	550	Fe	4850	70 [32]
Soudan-II	1992∼2001	809	Fe	2070	
IMB	1982∼1992	3300	H_2O	1580	540 [5]
KAMIOKANDE	1983∼1997	1040	H_2O	2700	260 [6]
Super-Kamiokande	1996∼	22500	H_2O	2700	1600 [38]

Table 2.3: Earlier nucleon decay experiments. *KGF found one candidate for $p \to e^+\pi^0$. They estimated the proton lifetime to be $\tau_p \sim 6 \times 10^{30}$ years [26].

2.3 Nucleon Decay Searches in This Thesis

The nucleon decay modes mediated by the exchange of the super heavy gauge bosons, X and Y are commonly important for most of the GUT models. In spite of its importance, only the $p \to e^+\pi^0$ mode search result was published by the early data of the Super-Kamiokande experiment. As described in Section 2.1.3, the other modes decaying into a charged antilepton (e^+, μ^+) plus a meson (π, η, ρ, ω) can have considerable branching ratios depending on the models. Thus, first systematical studies for these decay modes are performed in this thesis.

This thesis searches 12 nucleon decay modes; 8 modes for a decay of a proton and 4 modes for a decay of a neutron. Table 2.4 summarizes the searched modes. As for the decay into the η meson and the ω meson, two different meson decays are searched for each mode. Therefore, 16 types of decay modes are studied in this thesis.

$N \to$	lepton	meson	meson decay mode	(Br.)
$p \to$	e^+ (μ^+)	π^0	$\pi^0 \to 2\gamma$	(98.8%)
$p \to$	e^+ (μ^+)	η	$\eta \to 2\gamma$	(39.3%)
			$\eta \to 3\pi^0$	(32.6%)
$p \to$	e^+ (μ^+)	ρ^0	$\rho^0 \to \pi^+\pi^-$	(∼100%)
$p \to$	e^+ (μ^+)	ω	$\omega \to \pi^0\gamma$	(8.9%)
			$\omega \to \pi^+\pi^-\pi^0$	(89.2%)
$n \to$	e^+ (μ^+)	π^-		
$n \to$	e^+ (μ^+)	ρ^-	$\rho^- \to \pi^-\pi^0$	(∼100%)

Table 2.4: Searched nucleon decay modes in this thesis.

Currently, we have 6 times greater exposure than the previous publication for the $p \to e^+\pi^0$

mode. Moreover, two different detector phases, Super-Kamiokande I and II, are used for this search. The number of photo detectors in the Super-Kamiokande-II period is only a half of those in the Super-Kamiokande-I period. This thesis shows the first nucleon decay search results using the Super-Kamiokande-II data. The results can be an implication for the study of a next generation nucleon decay search detector.

All the searched nucleon decay modes are two body decays. Thus, more than two Cherenkov rings are emitted in a detector. The dominant backgrounds for the nucleon decay are events induced by atmospheric neutrinos. The most significant difference between the nucleon decay signal and the atmospheric neutrino background is in the total momentum of an event. Since the total momentum of the nucleon decay event should be equivalent to the momentum of a source nucleon, it tend to be relatively smaller than that of the atmospheric neutrino event with the same total amount of Cherenkov light.

Therefore, the ring counting and the momentum reconstruction are essential event reconstruction tools for the nucleon decay search. The details of those event reconstruction algorithms are described in Chapter 6. Especially for the momentum reconstruction, its algorithm is improved for this analysis for Super-Kamiokande-II. Reliability for the energy and momentum scale is also crucial for this analysis. That is discussed in Chapter 7.

Chapter 3

Experimental Apparatus

3.1 Overview of the Super-Kamiokande Detector

The Super-Kamiokande detector [37] is a large water Cherenkov detector located in the Mozumi zinc mine below the peak of Mt.Ikenoyama, under $\sim$ 1000m rock overburden as shown in Figure 3.1. This rock overburden is equivalent to 2700m of water and acts as a shield from the cosmic ray muon background. It reduces the cosmic ray flux to 6×10^{-8} cm^{-2}s^{-1}sr^{-1}, a reduction of 5 orders of magnitude compared to that on the surface of the earth.

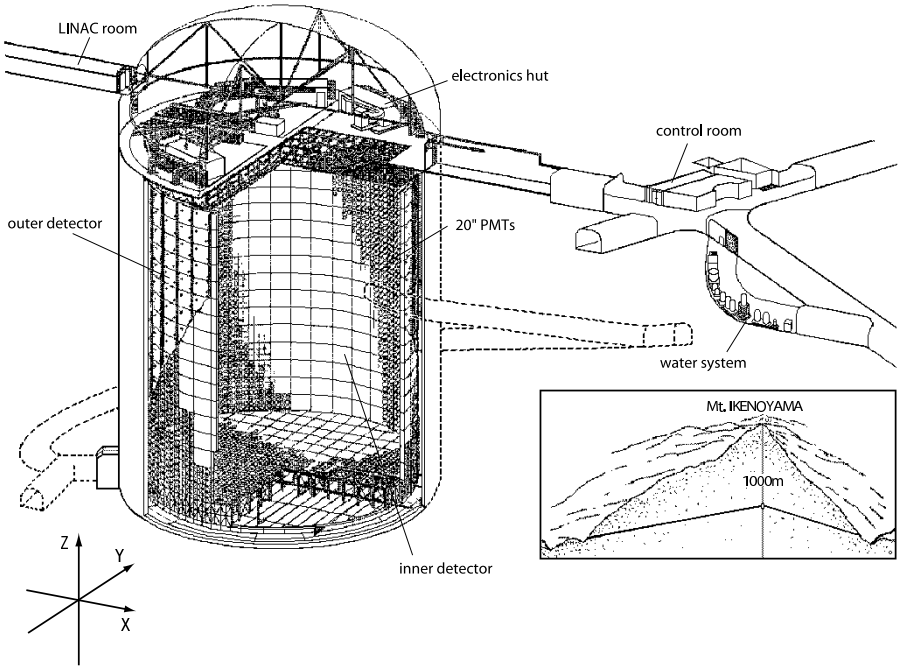

Figure 3.1: The Super-Kamiokande detector

The Super-Kamiokande experiment started data taking in April, 1996 and had continued observation for five years until the detector maintenance in July 2001. This period is referred to Super-Kamiokande I (SK-I). On November 2001, while filling the tank with water after

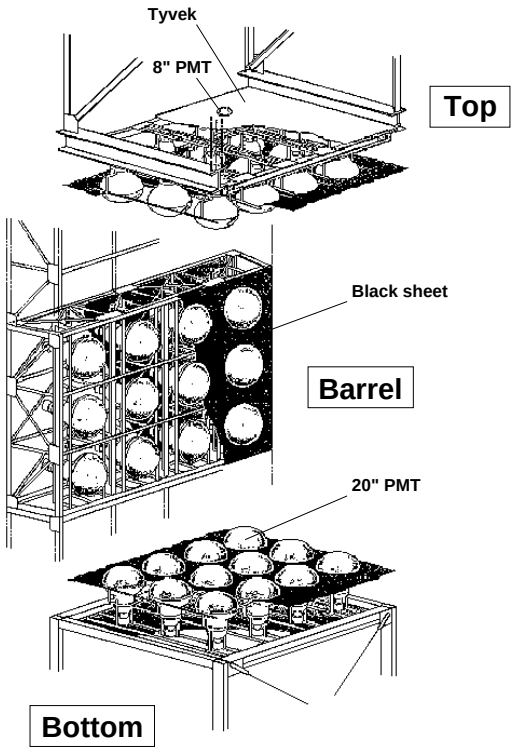

Figure 3.2: Supporting frame of PMTs.

the upgrade, an accident which destroyed more than half of the PMTs occurred. The Super-Kamiokande detector was partially rebuilt with half the density of photo-sensor coverage in the inner detector. Observation began again in October 2002 and stopped in October 2005 for a full detector reconstruction. This latter period is referred to as Super-Kamiokande II (SK-II). This thesis shows the nucleon decay search results in these two periods of SK-I and SK-II.

The Super-Kamiokande detector is made of a cylindrical stainless steel tank, of which the size is 39.3m in diameter and 41.4m in height. The detector is optically separated into two regions, which are called the inner detector (ID) and the outer detector (OD), by a photomultiplier tube (PMT) support structure and a pair of opaque sheets as shown in Figure 3.2. The ID contains 32 kiloton of water with the size of 36.2m in height and 33.8m in diameter. On the surface of the ID, 11,146 inward-facing 20-inch PMTs were uniformly attached and covered 40% of the ID surface with their photocathodes for SK-I. For SK-II, 5182 20-inch PMTs were attached and their photocathode coverage on the ID is 19%. The OD, which surrounds the ID with a 2m thickness of water, is used to reject cosmic ray muon events and to tag outgoing charged particles with 1,885 outward-facing 8-inch PMTs. The OD region also serves as a shield from radioactivity from materials around the detector wall.

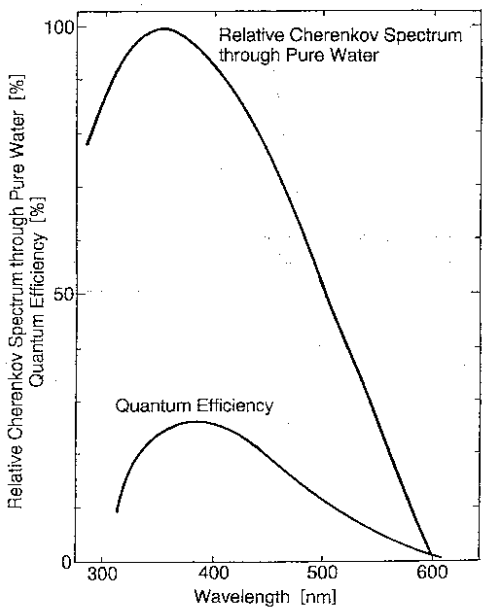

Figure 3.3: The spectrum of Cherenkov light through pure water. The quantum efficiency of the 20-inch PMT is also illustrated for comparison.

3.2 Water Cherenkov Technique

The Super-Kamiokande detector detects relativistic charged particles by emitted Cherenkov light in water. When the speed of particles exceeds the speed of light in the medium, Cherenkov light is emitted on a cone along the track of the charged particle with a characteristic half opening angle θ_{C}:

$$\cos\theta_{\mathrm{C}} = \frac{1}{n\beta} \tag{3.1}$$

where n is the refractive index of the medium, and β is the speed of charged particles v over the speed of light in vacuum c. The Cherenkov radiation threshold of electrons, muons and charged pions are 0.57, 118 and 156 MeV/c, respectively, because the refractive index of water is about 1.34. For particles with $\beta \simeq 1$, θ_{C} is 42°.

The spectrum of Cherenkov light per unit path length dx is given by the following formula.

$$\frac{d^2N}{dxd\lambda} = \frac{2\pi\alpha}{\lambda^2}\left(1 - \frac{1}{n^2\beta^2}\right) \tag{3.2}$$

where α is the fine structure constant, and λ is the wavelength of Cherenkov light. About 340 photons/cm are emitted between the wavelength of 300 nm to 600 nm, which is the most sensitive region of the PMTs used in Super-Kamiokande as shown in Figure 3.3.

Cherenkov light emitted by charged particles project ring images on the detector wall. Figure 3.4 shows a typical event display observed with Super-Kamiokande detector. A clear and sharp Cherenkov ring can be seen. By detecting and analyzing the Cherenkov ring images, we can reconstruct the events. For example, the number of Cherenkov ring corresponds to the number of charged particle. The Cherenkov ring edge sharpness tells us the particle type,

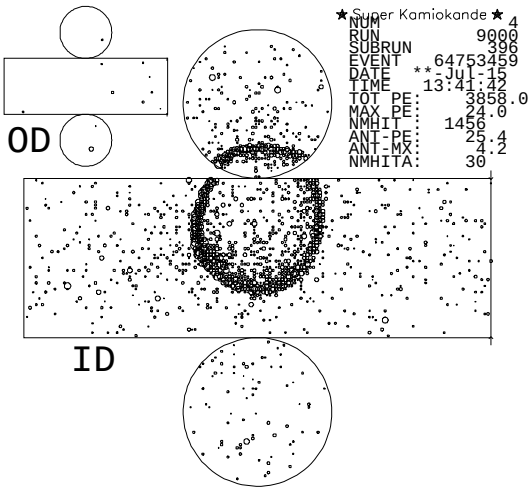

Figure 3.4: A typical event in Super-Kamiokande. The size of small circles in the unrolled cylinder represents the amount of Cherenkov photons detected in each photomultiplier tube. The Cherenkov ring image is clearly visible.

shower type ($e^{\pm}$, γ) or non-shower type ($\mu^{\pm}$, $\pi^{\pm}$). Moreover, the momentum of the particle can be obtained mainly by the total amount of the Cherenkov light. The details of the event reconstruction algorithms are described in Chapter 6.

3.3 Photomultiplier Tube

3.3.1 Inner Detector Photomultiplier Tube

The large size PMT used in the inner detector, which has a photocathode of 20-inch (50 cm) in diameter, was originally developed by Hamamatsu Photonics K.K. in cooperation with the Kamiokande collaborators [39]. For the Super-Kamiokande experiment, the PMT was improved in order to achieve better timing resolution and photon collection efficiency [40]. The specifications of the 20-inch PMT are summarized in Table 3.1.

The photocathode of the PMT is coated by Bialkali (Sb-K-Cs) for its high sensitivity to Cherenkov light and low thermionic emission. As shown in Figure 3.5, the quantum efficiency of the PMT covers the wavelength of Cherenkov light emitted in pure water. The dynode structure and the bleeder circuit were optimized to achieve high collection efficiency, which results in a good energy resolution and a fast timing response. Figure 3.6 shows the charge distribution for the single photo-electron (p.e.) signal. The transit time is about 90 nsec at 10^7 gain, and its spread is about 2.2 nsec as shown in Figure 3.7. The average dark noise rate is about 3 kHz at the threshold of 1/4 p.e.s used in the normal observation in Super-Kamiokande.

The performance of large size PMTs can easily be affected by magnetic fields. The geomagnetic field at the detector site is about 450 mG, which is enough to make the timing resolution worse since the PMT tolerates up to 100 mG. In order to compensate for the magnetic field, 26 sets of Helmholtz coils are installed around the tank, and the magnetic field inside the detector is kept around 50 mG.

Product Name	R3600
Shape	Hemispherical
Photocathode area	50 cm diameter
Window material	Pyrex glass ($4 \sim 5$ mm)
Photocathode material	Bialkali (Sb-K-Cs)
Quantum efficiency	22 % at $\lambda = 390$ nm
Dynodes	11 stage Venetian blind type
Gain	10^7 at ~ 2000 V
Dark current	200 nA at 10^7 gain
Dark pulse rate	3 kHz at 10^7 gain (1/4 p.e threshold)
Cathode non-uniformity	< 10 %
Anode non-uniformity	< 40 %
Transit time	90 nsec at 10^7 gain
Transit time spread	2.2 nsec ($1\,\sigma$) for 1 p.e. equivalent signals
Weight	13 kg
Pressure tolerance	6 kg/cm^2 water proof

Table 3.1: The specifications of the 20-inch PMT.

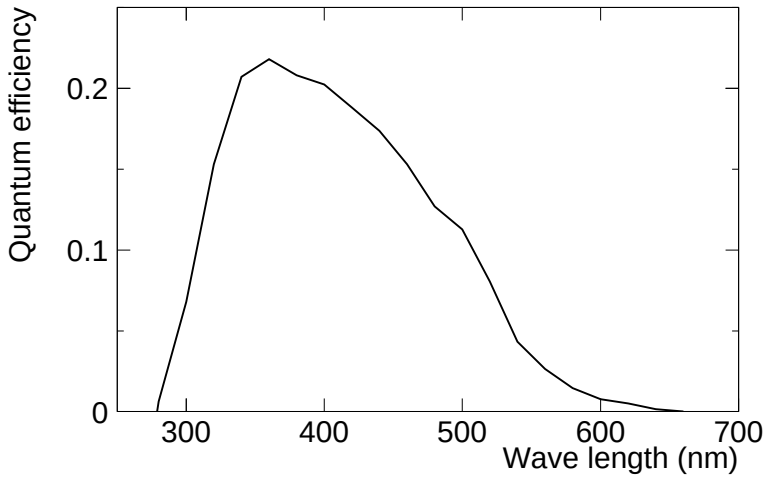

Figure 3.5: The quantum efficiency of the 20-inch PMT.

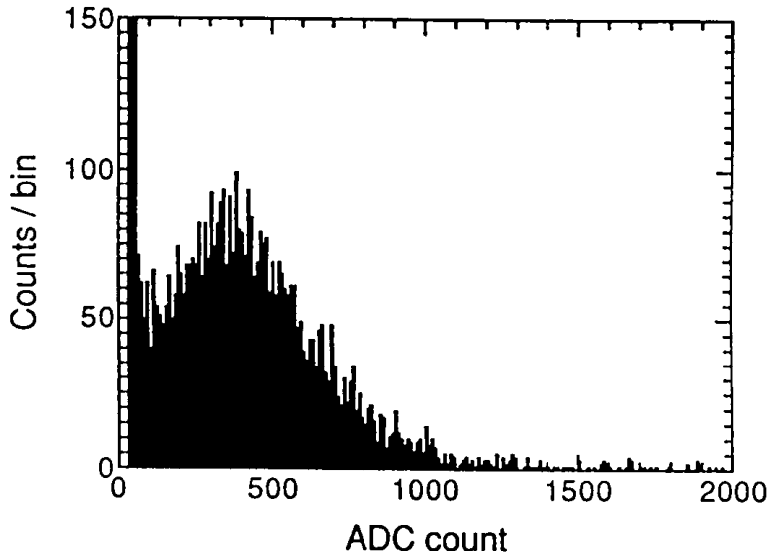

Figure 3.6: The single photo-electron distribution of the 20-inch PMT [40]. A single p.e. is equivalent to approximately 2 pC at 10^7 gain. A peak around 0 ADC count corresponds to dark current.

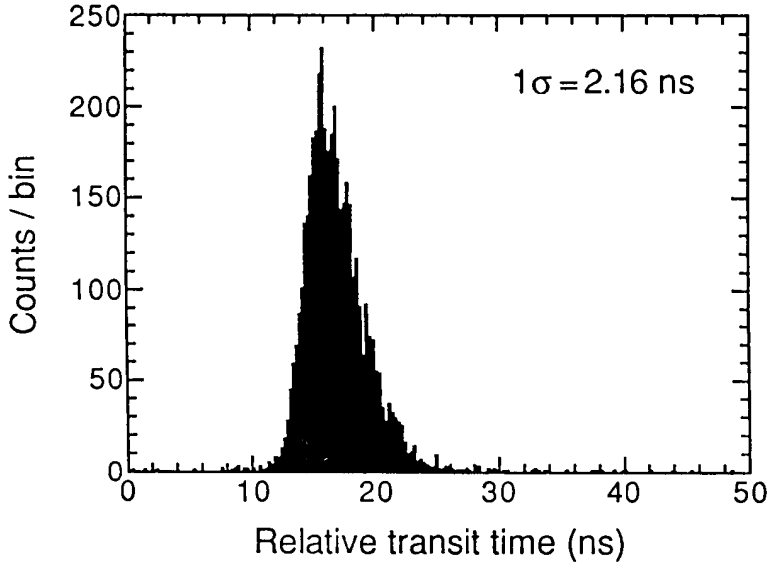

Figure 3.7: The transit time spread of the 20-inch PMT for single p.e. equivalent signals [40]. This spread corresponds to the timing resolution of the PMT.

As described in the overview of this chapter, about 55% of the PMTs were destroyed by the accident in 2001. In order to avoid such a cascade of implosions of PMTs, all of the inner detector PMTs have been covered by acrylic covers and fiber reinforced plastic cases since the start of the SK-II period. Figure 3.8 shows the transparency of the acrylic cover for photons with normal incidence in water, which is more than 96% at 350 nm of wavelength. The effect of the acrylic cover is confirmed to be small.

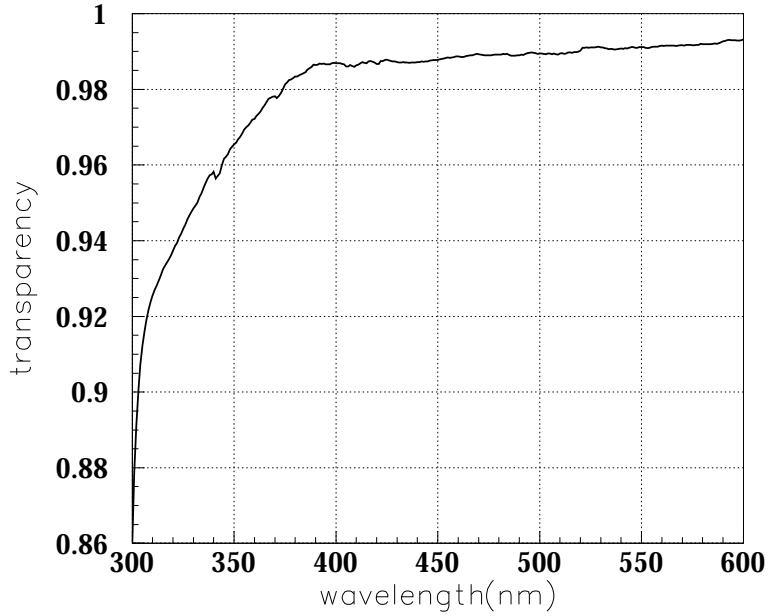

Figure 3.8: The transparency of the acrylic case as a function of wavelength.

3.3.2 Outer Detector Photomultiplier Tube

8-inch PMTs, Hamamatsu R1408, are used in the outer detector. At the beginning of SK-I, these PMTs were recycled from the IMB experiment [41], but 57% of the PMTs were newly manufactured for SK-II because of the accident.

The photocathode of the PMT is fitted with 60 cm $\times$ 60 cm $\times$ 1.3 cm wavelength shifter plates, which increases the light collection efficiency by 60%. Although the wavelength shifter degrades the timing resolution from 11 nsec to 15 nsec, it is still accurate enough for the function of the OD as a veto counter.

3.4 Data Acquisition System

3.4.1 Inner Detector

The schematic view of the inner detector data acquisition system is shown in Figure 3.10. Signals from the ID PMTs are fed into the front-end electronics, called ATM (Analog Timing Module) [42, 43], which was developed based on the TKO (Tristan KEK Online) standard [44] for the Super-Kamiokande experiment. The ATM module records and digitizes the integrated

charge and the arrival time information for each PMT signal with a 12-bit ADC (Analog to Digital Converter).

Figure 3.9 shows the block diagram of the analog input part of the ATM. Input signals to the ATM is first divided in the hybrid IC (integrated circuit) [42]. One of the split signals is amplified 100 times and fed into the discriminator with the threshold of 1/4 p.e.s. When the pulse height of the input signal exceeds the threshold, a HIT signal is generated, QAC (Charge to Analog Converter) starts to integrate the charge of another split signal with a gate of 400 nsec, and TAC (Time to Analog Converter) also starts to integrate charge with a constant current. The HITSUM signal, which is the sum of the HIT signals on the ATM module, is sent to a global trigger system to generate a global trigger which is the definition of an 'event' in Super-Kamiokande. If the global trigger signal is issued, the TAC stops the charge integration and the integrated charge in the QAC and the TAC are digitized by a ADC. If a global trigger is not issued within 1.3 μsec, the information in QAC and TAC for the channel are cleared. It takes 5.5 μsec for the ADC to process one channel. Therefore, each channel of the ATM has two switching pairs of QAC and TAC so that two successive events, such as a muon and the subsequent decay, can be processed. However, input signals which comes arrive 400 nsec to 900 nsec after the HIT signal generation are neglected to remove the noise from signal reflections. The performances of the ATM module are summarized in Table 3.2.

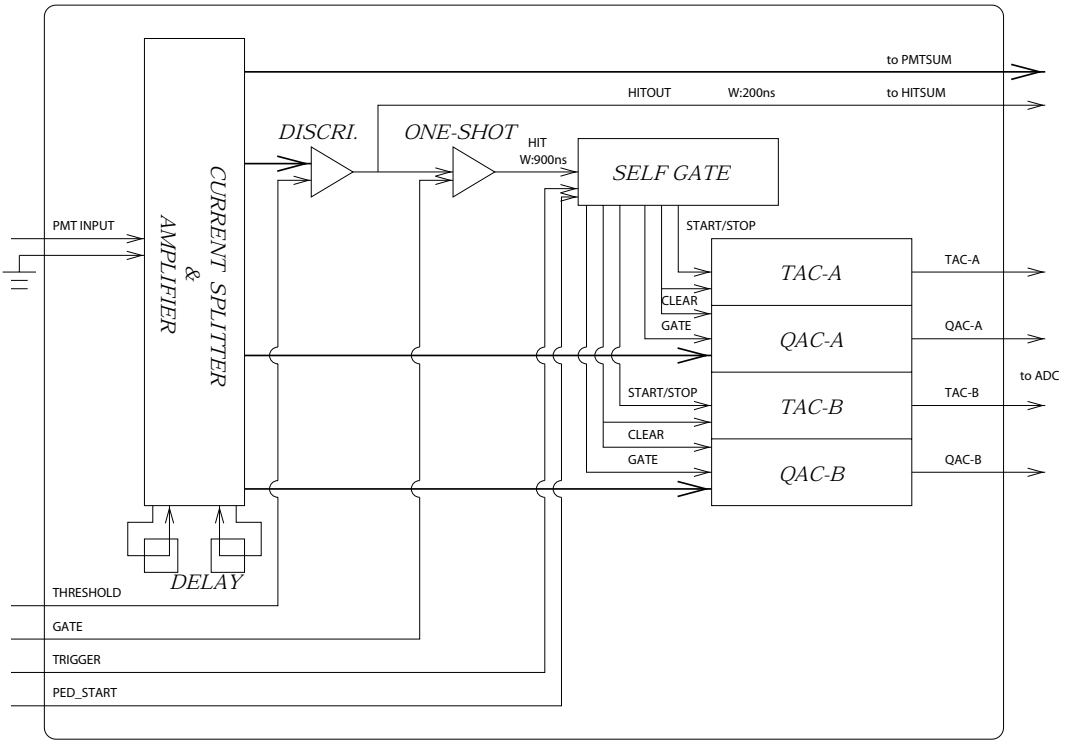

Figure 3.9: The analog input of the ATM.

Signals from 12 PMTs are fed to an ATM module to be processed. Every 16 events, the digitized data in the ATMs are sent to VME memory modules called SMP (Super Memory Partner) [45], with a typical data transfer speed of $\sim$ 2 MB/sec. 48 SMPs are installed in 8

Table 3.2: The specifications of the ATM module.

Number of channels	12 ch/board
One hit processing time	$\sim$ 5.5 μsec
Charge dynamic range	$\sim$ 400 $\sim$ 600 pC (12-bit)
Timing dynamic range	$\sim$ 1300 nsec (12-bit)
Charge resolution (LSB)	0.2 pC/LSB
Charge resolution (RMS)	0.2 pC (RMS)
Timing resolution (LSB)	0.3 $\sim$ 0.4 nsec/LSB
Timing resolution (RMS)	0.4 nsec (RMS)
Temperature dependence (QAC)	3 Count/deg. $\leftrightarrow$ 0.6 pC/deg.
Temperature dependence (TAC)	2 Count/deg. $\leftrightarrow$ 0.8 nsec/deg.
Event number	8 bit
Data size of one hit	6 Byte
FIFO	2 kByte ($\sim$ 340 hits)

VME crates, and one SMP module handles the data of 20 ATMs. The data in the SMP memories are read out by 8 slave computers and sent to the online host computer.

3.4.2 Outer Detector

Figure 3.11 shows the schematic view of the OD data acquisition system [46]. The paddle cards distribute high voltage from the main frame to the OD PMTs. The high voltage to an OD PMT is supplied through a coaxial cable. Signals from the PMT are also sent to the OD electronics through this cable and picked off by a high voltage capacitor on the paddle card.

Signals from the OD PMTs are sent to QTC (Charge to Time Converter) modules. The QTC module, which consists of LeCroy MQT200 chips and comparators, converts the PMT signal to a rectangular pulse whose width is proportional to the input charge. At the same time, a rectangular HITSUM signal is generated by the QTC module and sent to the global trigger system. The threshold of the QTC module is set to be 1/4 p.e.s. If the OD electronics receives a global trigger signal, the leading edge and the width of the rectangular pulse are converted to the timing and charge information by a LeCroy 1877 multi-hit TDC module. The TDC module can record up to 8 QTC output pulses with a resolution of 0.5 nsec. The dynamic range of the TDC module is set to be 16 μsec which starts from 10 μsec before the global trigger timing. The digitized data stored in the TDC module are read by a slave computer through a VME memory module called DPM (Dual Port Memory) and then sent to the online host computer.

3.4.3 Trigger System

The overview of the global trigger generation scheme for the ID is shown in Figure 3.12. The global trigger signal is generated by the total number of the hit PMTs within 200 nsec. In order to count the number of hit PMTs, HITSUM signals sent from each ATM with 200 nsec in width and with 15 mV in pulse height for each hit are analog-summed over all PMTs. The

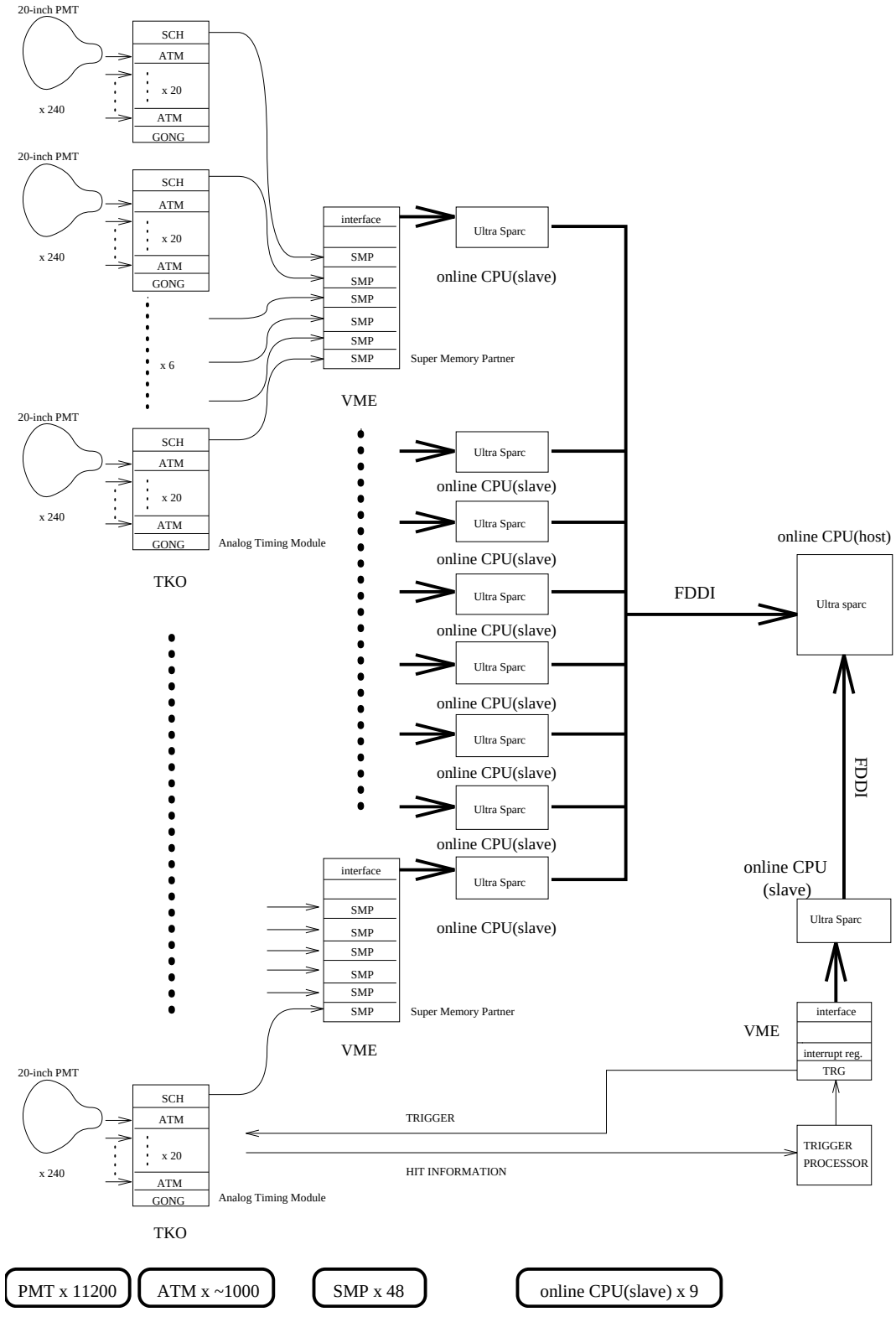

Figure 3.10: The schematic view of the inner detector data acquisition system.

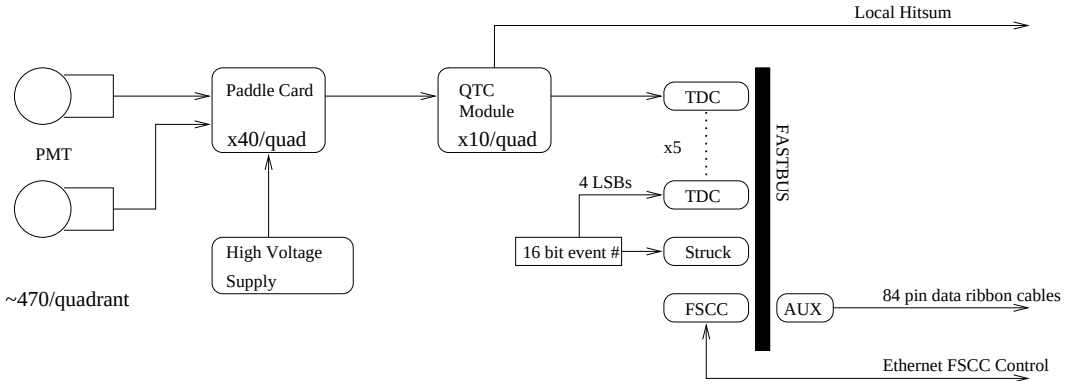

Figure 3.11: The schematic view of the outer detector data acquisition system.

pulse height of the summed signal is proportional to the number of hit PMTs within 200 nsec time window. There are three types of global triggers depending on energy regions: the high energy trigger (HE), the low energy trigger (LE), and the super low energy trigger (SLE). In the SK-I period, the trigger thresholds of the HE and LE triggers correspond to 31 hits and 29 hits, and the trigger rates for the HE and LE triggers are $\sim$ 5 Hz and $\sim$ 11 Hz, respectively. The LE trigger threshold is equivalent to a 5.7 MeV electron assuming 50% efficiency. The SLE trigger was implemented in May 1997 in order to lower the energy threshold for solar neutrino analysis, and achieved the energy threshold of 4.6 MeV equivalent. In the SK-II period, the threshold of the number of hit PMTs were changed due to a half density of PMTs. The threshold energy for the LE trigger in SK-II is 8 MeV.

The OD trigger generation scheme is similar to that of the ID. HITSUM signals from all the QTC modules are summed up to count the number of hits in the OD within a 200 nsec time window. The threshold for the OD trigger is set to 19 hits.

These four types of trigger signals (HE, LE, SLE and OE) are fed to a hardware trigger module called TRG. The TRG module records the trigger types and trigger generation timings with a 50 MHz clock, counts an event number with a 16-bit counter, and generates a global trigger signal when any one of the trigger signals is issued.

3.5 Water Purification System

For a large water Cherenkov detector, it is essential to keep the water clean, not only for long light attenuation length, but also for the reduction of the radioactive materials, especially radon, which can be a background source for the neutrino observation of the MeV range.

The water in the tank is constantly circulated through the water purification system with the flow rate of about 35 ton/hour. The schematics of the system is shown in Figure 3.13.

The typical number of particles larger than 0.2 μm is reduced to 6 particles/cc, and the light attenuation length is achieved to be $\sim$100m after the purification. The typical resistivity of the water entering the water purification system from the tank is about 11 MΩ·cm. After the water purification, the water has an average resistivity of 18.20 MΩ·cm, approaching the chemical limit.

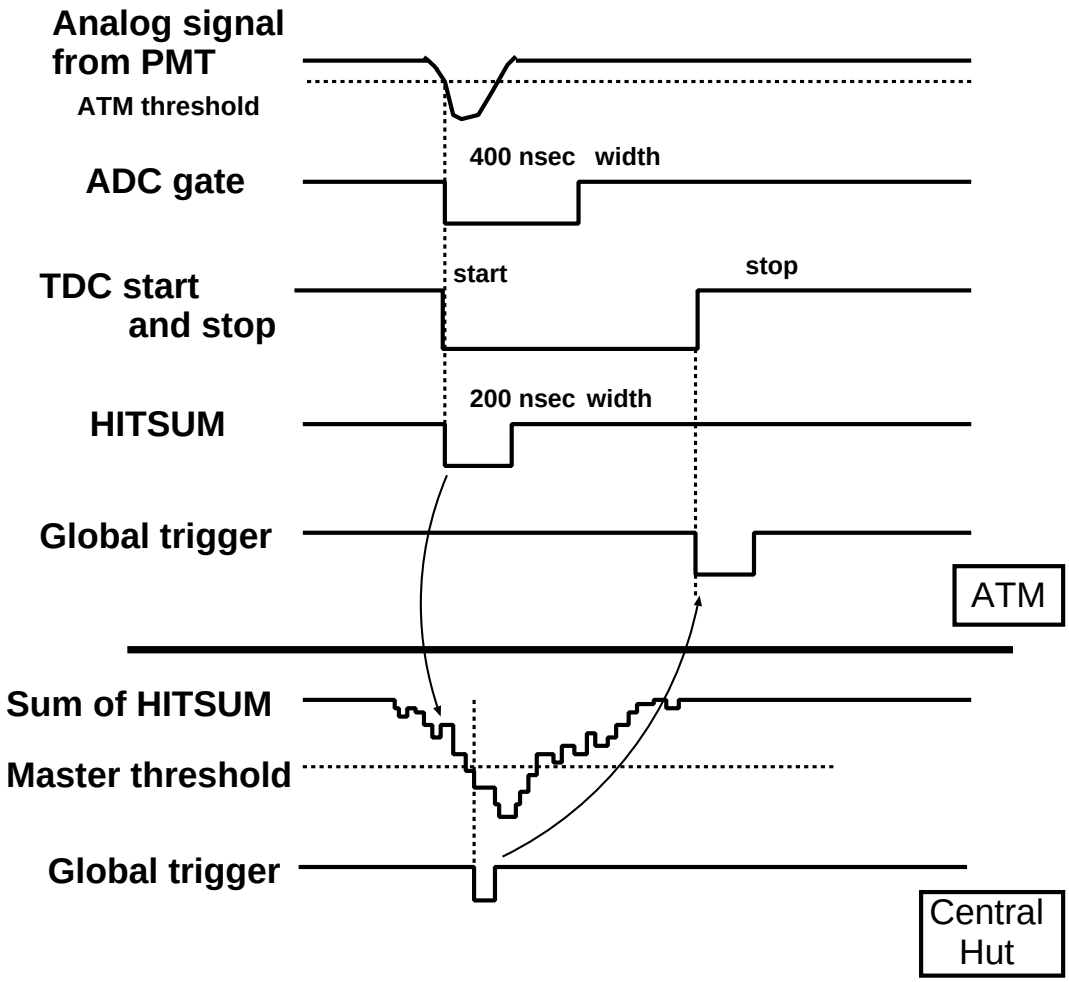

Figure 3.12: The overview of the global trigger generation.

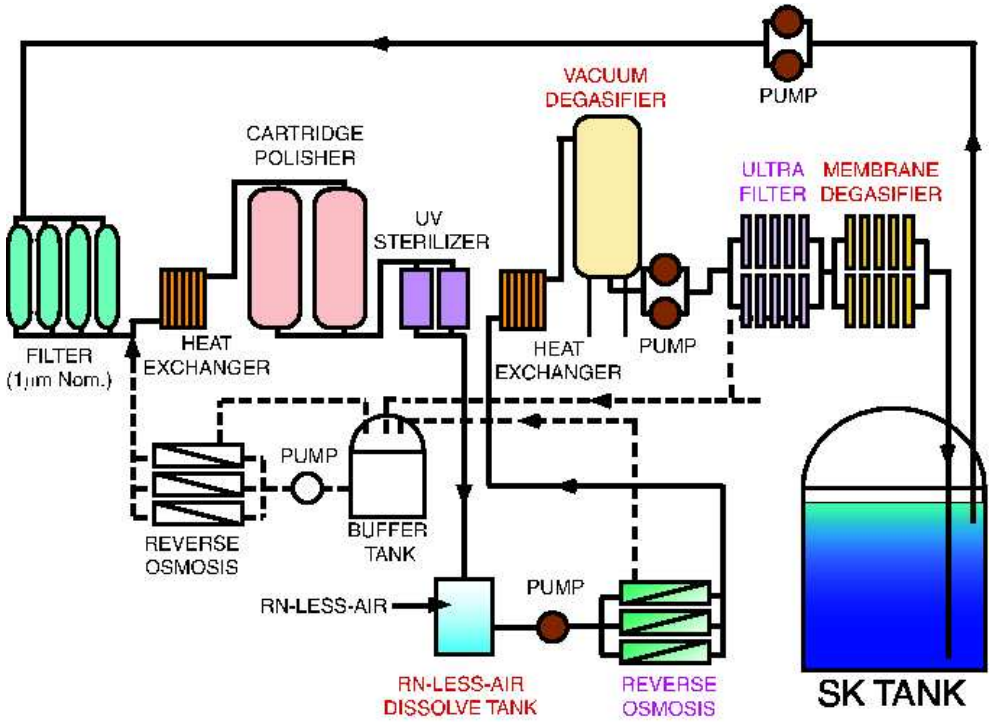

Figure 3.13: The water purification system.

3.6 Calibration

3.6.1 Relative Gain Calibration

The uniformity of the PMT gain is necessary to determine the momentum without systematic difference depending on its vertex position or direction, which results in the systematic error of the total momentum of an event for nucleon decay searches. Therefore, the high voltage supplied to each PMT is individually adjusted to provide a uniform gain.

The relative gain calibration system is illustrated in Figure 3.14. Light generated by a Xe lamp is passed through an ultraviolet (UV) filter and a neutral density (ND) filter, and then split into four. One is injected into a scintillator ball in the tank via an optical fiber. The other split lights are monitored to measure the intensity of the Xe light and to generate a calibration trigger.

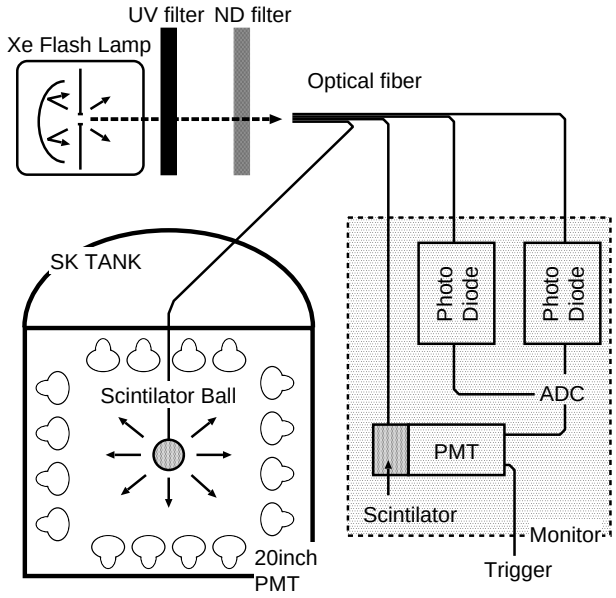

Figure 3.14: A schematic view of the relative gain calibration system.

The relative gain G_i of the i-th PMT is obtained by :

$$G_i = \frac{Q_i}{Q_0 f(\theta)} \cdot l_i^2 \cdot \exp\left(\frac{l_i}{L}\right) \tag{3.3}$$

where Q_i is the charge detected by the i-th PMT, l_i is the distance from the light source to the PMT, $f(\theta)$ is the PMT acceptance as a function of the photon incidence angle θ, L is the attenuation length, and Q_0 is the normalization factor. This measurement is performed for several positions of the scintillator ball, changing the high voltage. As a result of this calibration, the relative PMT gain spread is about 7%.

3.6.2 Absolute Gain Calibration

In order to convert the charge detected by each PMT in pC into the number of photoelectrons, the absolute gain of PMTs are calibrated by the charge distribution of single photoelectron

signals.

The low energy gamma ray generated from neutron capture on a Nickel nucleus is used as a calibration source. The calibration source is shown in Figure 3.15. Neutrons produced by spontaneous fissions of ^{252}Cf are captured on surrounding Ni wires in a polyethylene vessel, and low energy ($6 \sim 9$ MeV) gamma rays are simultaneously generated. The number of hit PMTs is about $50 \sim 80$ in total, and the number of p.e.s detected by each PMT is at most one, The clear single photoelectron charge are observed and the mean value of the peaks, 2.055 pC, is used as a constant to convert the PMT charge from pC to the number of photoelectrons.

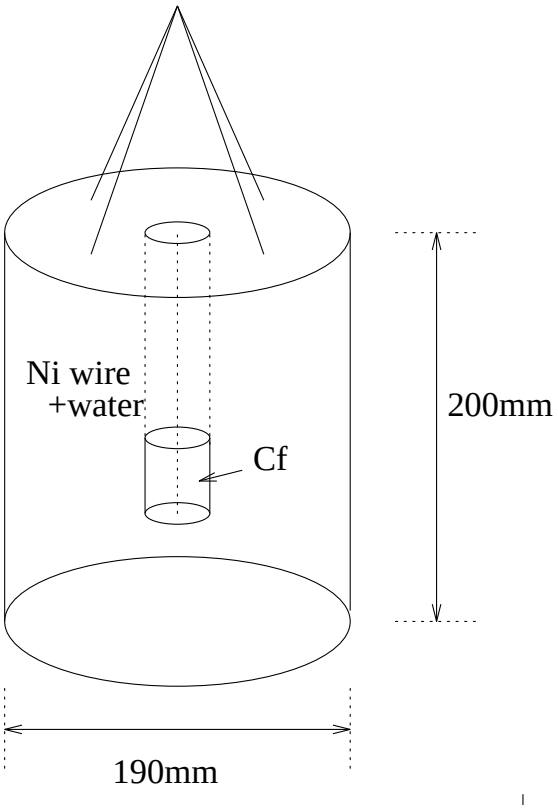

Figure 3.15: A schematic view of the absolute gain calibration source.

3.6.3 Relative Timing Calibration

The relative timing calibration is important for the reconstruction of a vertex position. The timing responses of PMT signals depend not only on the length of signal cables also on the amplitude of detected charge because of the time-walk effect of discriminators as shown in Figure 3.16. This scatter plot of the timing and the charge is called TQ-map.

For the timing calibration, N_2 laser generator, which can emit intense light with 337 nm wavelength within a time width of 3 nsec, is used. The wavelength of the laser light is converted to 384 nm by a dye laser module. The light intensity can be changed by using a variable attenuation filter. After passing through the filter, the laser light is injected into a diffuser ball

in the tank via an optical fiber. To emit the light uniformly in the detector, the injected light is first diffused by a TiO_2 and then further diffused by the surrounding LUDOX silica gel made of 20nm glass fragments. In the SK-II period, the acrylic ball containing MgO powder is used as a diffuser ball to improve the uniformity of the light.

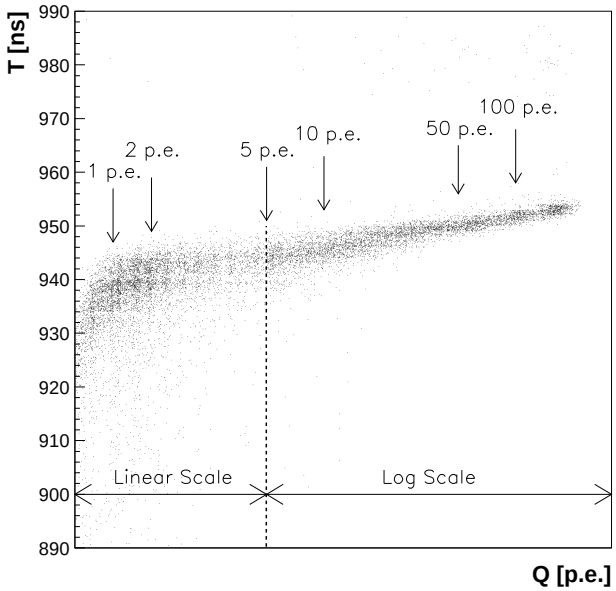

Figure 3.16: A typical TQ-map, a measured two-dimensional plot of timing vs. charge distribution. Larger values in the vertical axis correspond to earlier hits.

3.6.4 Water Transparency Measurement

Water transparency is the optical attenuation length in water, which represents the combined effect of absorption and scattering of the light. The transparency is measured using N_2 laser light injected into the detector. The wavelength dependence of the attenuation length can be measured by changing the dye of the laser. The absorption and scattering coefficients are separately measured by this method. Furthermore, the transparency is independently measured by Cherenkov light from cosmic ray muons. The time variation of the water transparency can be monitored by this method without disturbing the normal data taking.

Light scattering measurement by a laser

The light attenuation length in water can be described as $L = (\alpha_{\rm abs} + \alpha_{\rm scat})^{-1}$, where $\alpha_{\rm abs}$ and $\alpha_{\rm scat}$ are the absorption and scattering coefficients, respectively. Each coefficient is separately measured using a N_2 laser. The setup of the measurement is shown in Figure 3.17. Each laser, wavelength of 337, 371, 400 and 420 nm, fires every 6 seconds during normal data taking. The laser light is injected into the detector via an optical fiber toward the bottom of the tank.

The barrel part of the detector is separated into 5 regions as shown in Figure 3.17. Figure 3.18 shows the PMT hit timing distributions in each region for the calibration data and a Monte

Carlo detector simulation (see Section 4.4). The PMT hits on the top and barrel wall are due to the photons scattered in water, or the photons reflected by the surfaces of the bottom PMTs or black sheets. For the Monte Carlo simulation, the absorption and scattering coefficients are tuned so that the PMT hit time distributions agree with the calibration data.

The attenuation coefficients obtained by this method are shown in Figure 3.19. The lines show the models used in the Monte Carlo simulation, which are determined by fitting to the data.

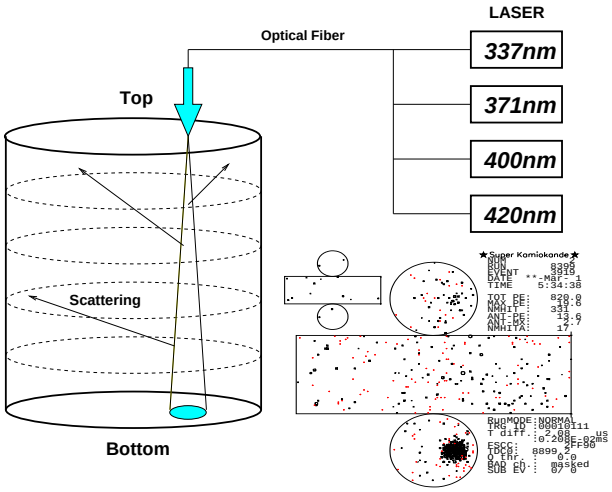

Figure 3.17: A schematic view of the scattering and absorption parameter measurement.

Measurement with cosmic ray muons

The water transparency is also measured by Cherenkov light from cosmic ray muons, of which energy deposit is almost constant in water. Only vertical downward muons are selected for this measurement. The muon track is reconstructed by connecting the entrance and the exit points in the detector. The detected charge by each PMT is expressed as :

$$Q = Q_0 \cdot \frac{f(\theta)}{l} \cdot \exp\left(-\frac{l}{L}\right) \tag{3.4}$$

where Q_0 is a constant, $f(\theta)$ is the PMT acceptance, l is the photon path length, and L is the attenuation length.

Figure 3.20 shows the time variation of the attenuation length measured by the cosmic ray muons. The attenuation length in event reconstruction processes are corrected by this calibration data.

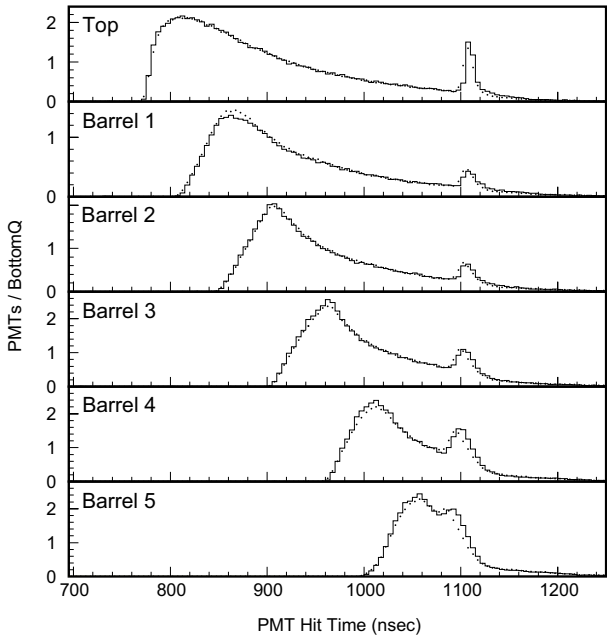

Figure 3.18: PMT hit time distributions of 337 nm laser events in each detector region (as shown in Figure 3.17) for the data (dots) and the Monte Carlo simulated events which is tuned by the scattering and absorption parameters (solid line). The first peak and second peak correspond to the light from the scattering in water and the reflection on the bottom surface, respectively.

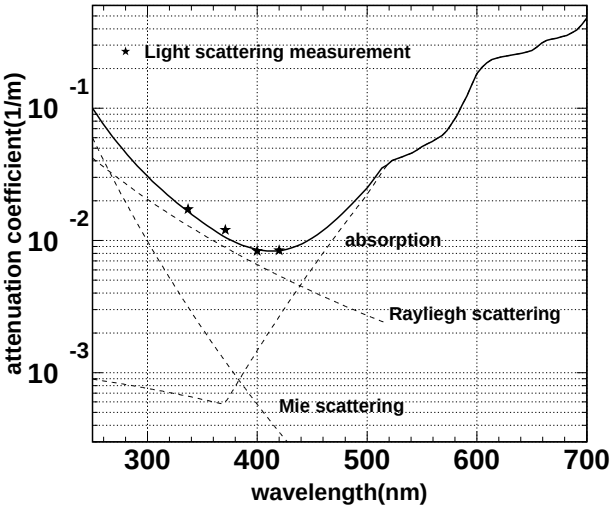

Figure 3.19: Attenuation coefficients as a function of wavelength obtained by the water scattering measurement (star) with the model in the detector simulation (solid and dashed lines).

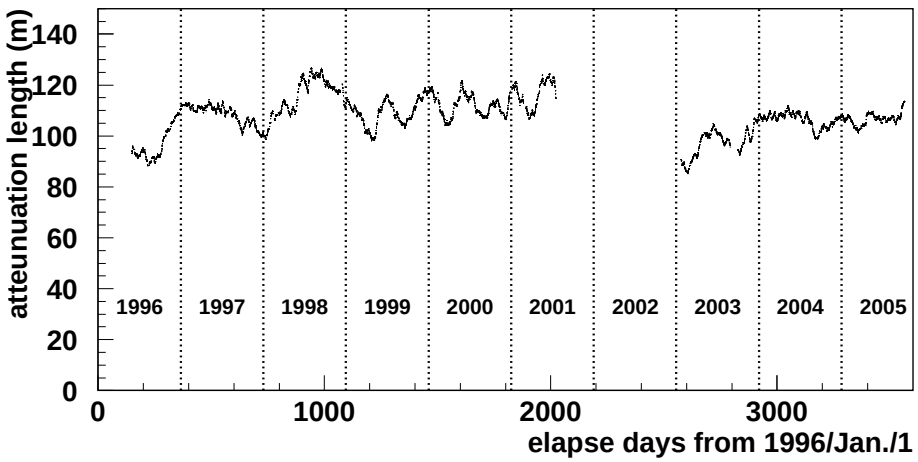

Figure 3.20: The time variation of the attenuation length measured by cosmic ray muons.

Chapter 4

Event Simulation

In order to estimate the detection efficiencies of nucleon decays, a custom nucleon decay event simulator has been developed. The number of background events was also estimated by the simulations of atmospheric neutrino flux and neutrino interaction in the detector.

Mesons produced in a nucleus by a nucleon decay or a neutrino interaction strongly interact with nucleons (nuclear effect) until it escapes from the nucleus. This effect is important especially for estimating detection efficiencies of nucleon decay searches. This was treated in the common simulation code both in nucleon decay events and atmospheric neutrino events.

As for the backgrounds from the atmospheric neutrino interaction, a charged current single (multi) pion production can be the dominant background source for the studied modes. A charged current quasi-elastic scattering can also contribute the background because a nucleon produced by the neutrino interaction can produce pions by hadronic interactions in water. They were taken into account in the simulation.

4.1 Nucleon Decay Simulation

In a H_2O molecule, there are two free protons from hydrogen nuclei, and eight bound protons and eight bound neutrons in an oxygen nucleus. The decay probabilities of free protons and bound nucleons were assumed to be equal in the simulator. All the decay modes studied in this thesis are two body decays. A charged lepton and a meson are back-to-back with a monochromatic momentum in the nucleon rest frame.

For the decay of bound nucleons in oxygen, the simulation should consider the effect of Fermi motion of the nucleons, correlation with another nucleon, and meson-nucleon interactions in the nucleus (nuclear effect). Nucleon momentum and nuclear binding energy in the nucleus was measured by an electron scattering experiment on ^{12}C [47]. Figure 4.1 shows the experimental momentum distributions with the theoretical calculations [47]. The theoretical calculations were used in our simulation since it agrees well with the experimental data. The measured nuclear binding energies were 39.0 MeV for the 1s state and 15.5 MeV for the 1p state. They were also taken into account in the simulation by modifying the proton mass.

Generated mesons in an oxygen nucleus strongly interact with nucleons until they escape from the nucleus. The nuclear effect should be carefully simulated since the detection efficiencies for nucleon decays are largely affected by the effect. Nucleon decay position in a nucleus was

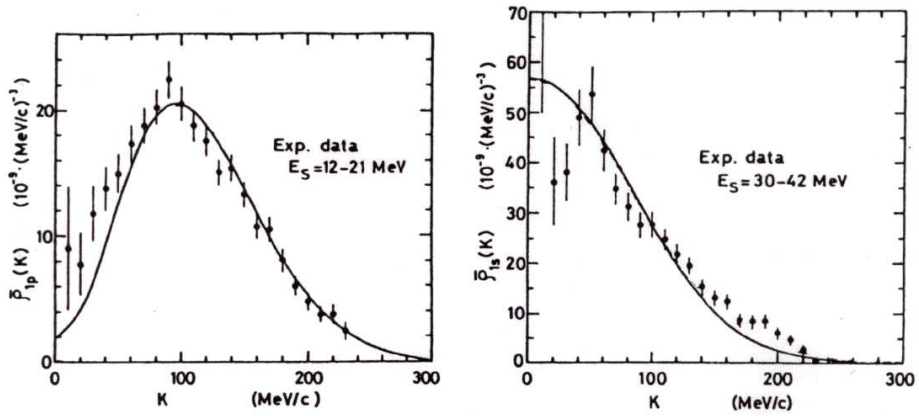

Figure 4.1: Nucleon momentum distributions [47]. The left and right figures show momenta of 1s state and 1p state in ^{12}C nucleus, respectively. Solid lines show theoretical calculations [47].

determined by the Woods-Saxon nuclear density distribution in the simulation,

$$\rho(r) = \frac{\rho(0)}{1 + \exp\left(\frac{r-a}{b}\right)} \tag{4.1}$$

where $\rho(0)$ is the average density of nuclei, and a and c are the density parameters for nuclei.

From this position, π, η and ω mesons were tracked in oxygen nuclei. For ρ meson, the lifetime is so short ($\beta\gamma\tau \simeq 0.3$ fm) that it decays in a nucleus immediately into 2 π mesons and the nuclear effect of ρ meson itself was not considered in the simulation. Details of the nuclear effects are described in Sections 4.1.1, 4.1.2 and 4.1.3. The mass of the ρ meson was assumed to have a Breit-Wigner type distribution with a width of $\Gamma = 149$ MeV as shown in Figure 4.2. Therefore, generated particles via the modes including ρ meson does not have monochromatic momentum even in the case of free proton decay.

Ten percent of nucleons in oxygen were assumed to decay correlating with another nucleon [48]. Figure 4.3 shows the invariant mass distribution of $e^+\pi^0$ in the $p \to e^+\pi^0$ MC. In such correlated decay events, the invariant mass of e^+ and π^0 is smaller than the mass of a nucleon because of the invisible momentum of another nucleon.

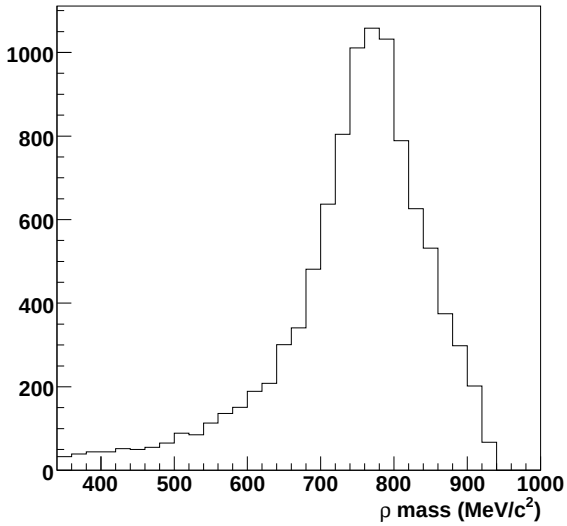

Figure 4.2: The ρ meson mass distribution in the nucleon decay simulation. The upper limit of the mass corresponds to the mass of a nucleon.

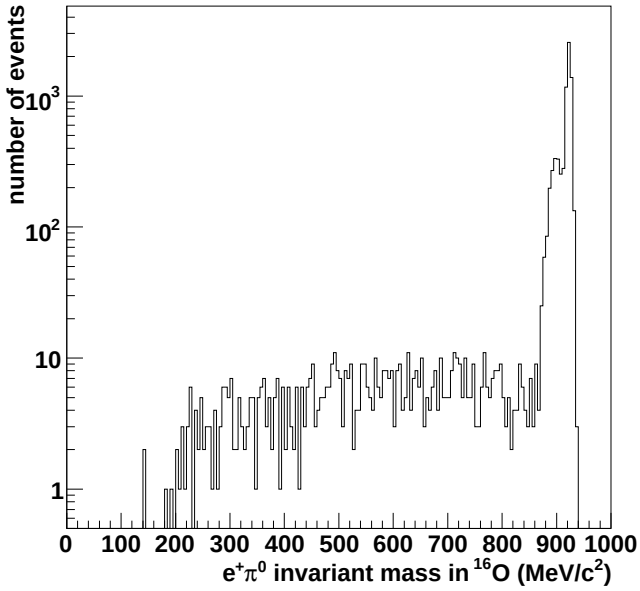

Figure 4.3: Invariant mass distribution of $e^+\pi^0$ in the $p \to e^+\pi^0$ MC in H_2O. The effect of nucleon correlated decay can be seen in the lower invariant mass tail in this distribution. Two peaks around the proton mass are corresponding to 1s state and 1p state, which are separated by the difference of the nuclear binding energy.

4.1.1 π Meson Nuclear Effect

As for the pion nuclear effect, inelastic scattering, absorption, charge exchange and pion production were considered in the simulation. The pion production is caused by relatively high momentum pions ($p_\pi > 500$ MeV/c). Thus, its effect is not significant for nucleon decay events. Cross-sections for those processes were calculated based on the model of Oset *et al.*[49]. Figure 4.4 shows the cross sections of pion nuclear effect compared with the experimental data [51]. The angular and momentum distributions of pions were determined from the results of the phase shift analysis of the π-N scattering experiments [50]. On account of the Pauli exclusion principle, the momentum of the scattered nucleon is required to be more than the Fermi surface momentum given by

$$p_F(r) = \left(\frac{3}{2}\pi^2\rho(r)\right)^{\frac{1}{3}}, \tag{4.2}$$

where $\rho(r)$ is the nuclear density distribution (Equation 4.1).

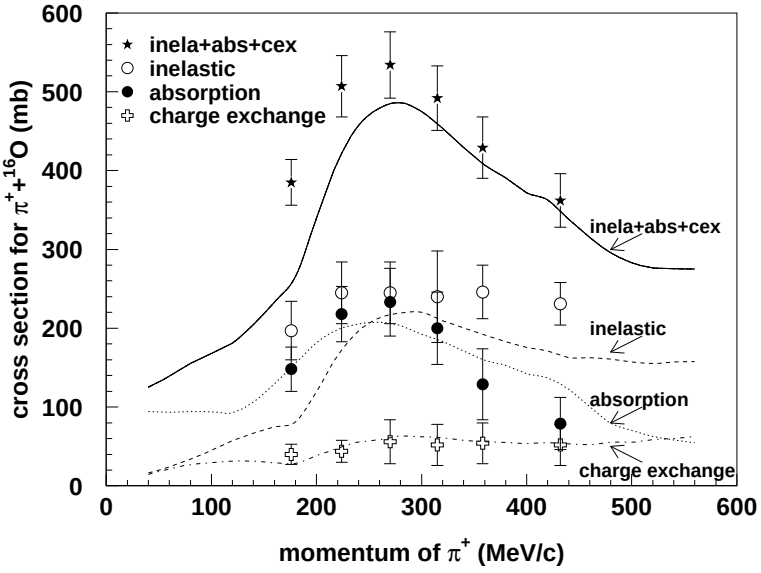

Figure 4.4: The cross-sections of π^+-^{16}O scattering as a function as π^+ momentum. Lines show the calculation in our simulation, and data points are taken from the experimental data [51].

The π^0 momentum from the decay mode of $p \to e^+\pi^0$ is 459 MeV/c at the rest frame of the nucleon. As shown in Figure 4.5, 37% of π^0s were simulated to be absorbed or charged-exchanged in the nuclei. This was a major reason for the inefficiency of the $p \to e^+\pi^0$ and $p \to \mu^+\pi^0$ modes. The probability of escape without any scattering was estimated to be 44%, and 19% of π^0s were scattered.

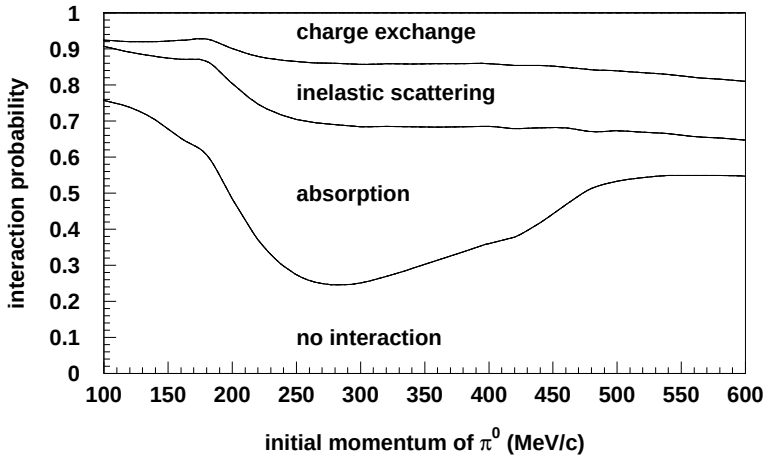

Figure 4.5: Fraction of pion nuclear effect as a function of initial pion momentum

4.1.2 η Meson Nuclear Effect

The interaction of η-nucleon in nuclei was considered through a baryon resonance of $S_{11}(1535)$.

$$\begin{aligned} \eta + N &\rightarrow S_{11}(1535) \\ S_{11}(1535) &\rightarrow N + meson\ (\pi, \eta, \pi\pi) \end{aligned} \tag{4.3}$$

The cross-section of the η meson nuclear effect shown in Figure 4.6 was calculated by the Breit-Wigner formula as follows.

$$\sigma = \frac{\pi}{k^2} \frac{\Gamma_{\eta N} \left(\Gamma_{\rm Total} - \Gamma_{\eta N}\right)}{\left(E_{\rm CMS} - M_{\rm res}\right)^2 + \Gamma^2_{\rm Total}/4}, \tag{4.4}$$

where $E_{\rm CMS}$ is the center of mass energy of η-N, $M_{\rm res}$ is the mass of the resonance, $\Gamma_{\rm Total}$ is the total width of $S(1535)$ resonance, $\Gamma_{\eta N}$ is the partial width of $S(1535) \rightarrow \eta N$, and k is the wave number ($p/\hbar$). Pions can be generated by the decay of the resonance. The nuclear effect for the π meson was also considered according to Section 4.1.1. Approximately 56% of η mesons generated by $p \rightarrow e^+\eta$ escaped from the nucleus without any scattering, while 38% of η mesons were absorbed or decayed into other particles from the resonance.

The η meson nuclear effect simulation was checked by a comparison with the experimental cross-section of η photoproduction measured at MAINZ [52]. The differential cross sections of the η photoproduction were measured for $E_\gamma = 735 \sim 765$ MeV. The peak momentum of the η meson is about 300 MeV/c. This is equivalent to the η momentum generated by $p \rightarrow e^+$(or μ^+) η. Since photons are insensitive to strong interactions and able to probe the inside of nuclei, meson photoproduction data were used for the study of the nuclear effects. In the η photoproduction on a ^{12}C target simulation, η mesons were generated following the cross-section data of a proton target from the SAID calculation [53], and tracked in nuclei suffering the $\eta - N$ interaction described above. For the cross-section of the η photoproduction on a neutron target in the simulation, the cross-section was assumed to be 2/3 of that of a proton

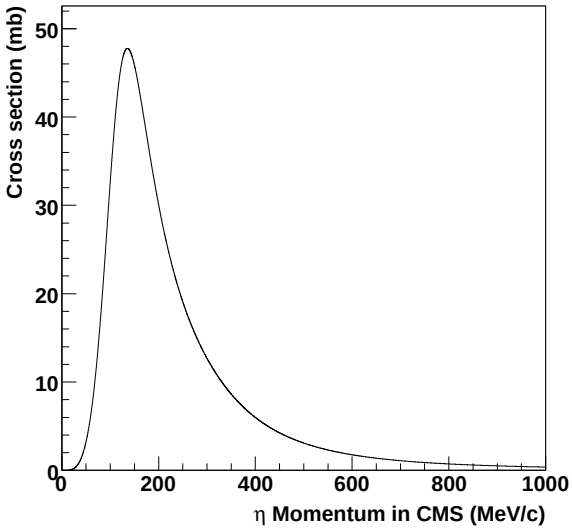

Figure 4.6: Calculated cross section of η nuclear effect considering $S_{11}(1535)$ resonance in the custom simulation code.

target, since this assumption reproduces the experimental cross-sections of a deuteron target [54].

Figure 4.7 is the comparison of an experimental η photoproduction cross-section, with a ^{12}C target, and the cross-section simulated by our nuclear effect simulation. The dashed line in Figure 4.7 is the simulated cross section without the nuclear effect, which corresponds to the elementary cross section of a nucleon times the number of nucleons in the nucleus. The simulated photoproduction cross-section predicted well the experimental data. The difference between the experiment and the simulation was considered as the uncertainty of the cross section of the η nuclear effect. The uncertainty of the cross section was estimated to be a factor of two.

4.1.3 ω Meson Nuclear Effect

The width of ω meson resonance is $\Gamma = 8.49$ MeV and its lifetime is $\tau = \hbar/\Gamma = 0.77 \times 10^{-22}$ sec. In the proton decay of $p \to e^+\omega$, the ω meson momentum is ~ 140 MeV/c so that the mean free path ($\beta\gamma\tau$) of the ω meson is ~ 4 fm. The decay of ω was taken into account in the ω meson tracking in nuclei because the mean free path is comparable to the size of the radius of a nucleus.

The ω meson interaction with a nucleon in an oxygen nucleus was calculated by Lykasov *et al.*[55] with a boson exchange model. The coupling constants and the form factor of this model were fixed by the experimental data of $\pi N \to \omega N$. Inelastic reactions such as $\omega N \to \omega N$, $\omega N \to \pi N$, $\omega N \to \rho N$, $\omega N \to \rho\pi N$, $\omega N \to \pi\pi N$, $\omega N \to \sigma N$ were considered in the simulation. Approximately 53% of ω mesons generated in $p \to e^+\omega$ decayed in the nucleus. Therefore, the nuclear effect of secondary pions should also be considered.

The calculated cross section described above were compared with experimental data. The CBELSA/TAPS collaboration measured the ω photoproduction cross section on the various

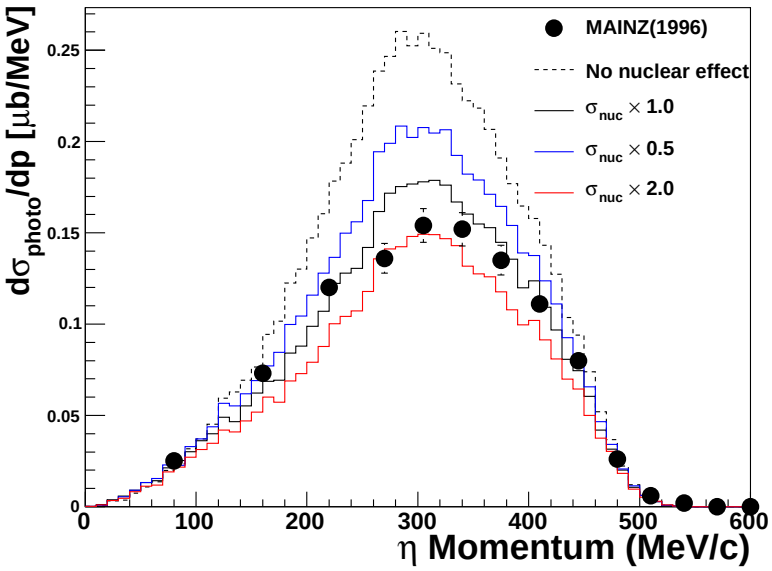

Figure 4.7: The differential cross sections of photoproduction of the η meson on a ^{12}C target with the γ energy of 735 $\sim$ 765 MeV. The experimental data at MAINZ [52] are shown as circles. The black solid line shows the simulated production cross-section. The dashed line shows the cross-section without nuclear effect, and the blue and red solid lines show simulated cross-sections with doubled and half the cross-sections of the η nuclear effect, respectively.

nuclei targets of C, Ca, Nb and Pb [56]. They extracted the ωN cross section from the photoproduction cross sections and compared it with the calculated cross section by Lykasov *et al.* as shown in Figure 4.8. This cross-section obtained by the experiment is approximately 3 times larger than the calculated cross section. We took this difference as an uncertainty of the cross-section of the ω meson nuclear effect.

If a ω meson escapes from a nucleus, the ω meson immediately decays to $\pi^+\pi^-\pi^0$, $\pi^0\gamma$ and $\pi^+\pi^-$ with branching ratios of 89%, 9% and 2%, respectivelly.

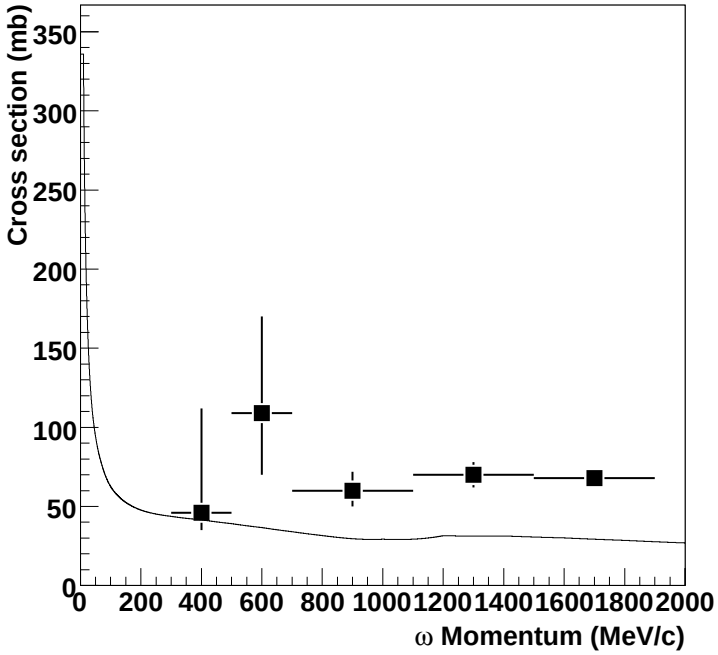

Figure 4.8: The comparison of the total ωN cross-section between the extracted cross-section from the experiment (square) [56], and the calculated cross section (solid line) by Lykasov *et al.*[55]

4.2 Atmospheric Neutrino Flux

The most important and irreducible background for nucleon decay searches in Super-Kamiokande is the events caused by the interactions of atmospheric neutrinos because these events may mimic the nucleon decay signals. In order to estimate the amount of background, the atmospheric neutrino flux and neutrino interactions were simulated precisely. The atmospheric neutrino flux at Kamioka used in our simulation was calculated by M. Honda *et al.*[57] (Honda flux).

The primary cosmic ray flux has been precisely measured by the BESS [58] and AMS [59] experiments up to 100 GeV/c. The model of the primary flux used in the calculation of the Honda flux is parameterized and fitted to the experimental primary flux data as shown in Figure 4.9 with some experimental results. The primary cosmic ray flux is affected by the solar wind and the geomagnetic field of the Earth. These effects were considered in the calculation. The difference of the flux at solar maximum and solar minimum is more than a factor of two for 1 GeV cosmic rays, while it decreases to $\sim 10\%$ for 10 GeV.

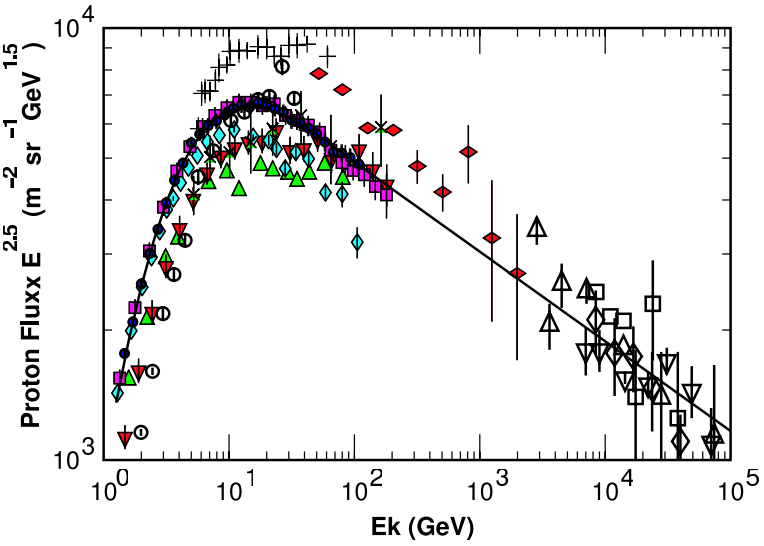

Figure 4.9: Primary cosmic ray flux measurements compared with the model used in the Honda flux calculation. The data are taken from Webber [60] (crosses), LEAP [61] (upward triangles), MASS1 [62] (open circles), CAPRICE [63] (vertical diamonds), IMAX [64] (downward triangles), BESS98 [58] (circles), AMS [59] (squares), Ryan [65] (horizontal diamonds), JACEE [66] (downward open triangles), Ivanenko [67] (upward open triangles), Kawamura [68] (open squares) and Runjob [69] (open diamonds).

Interactions of primary cosmic ray with air nuclei were simulated based on the two theoretical models, NUCRIN [70] for the primary cosmic ray energies below 5 GeV, and DPMJET-III [71] for above 5 GeV. The atmospheric neutrino flux can be obtained from the decays of secondary particles, mostly pions and partially kaons, generated by the interactions.

The calculated energy spectrum of atmospheric neutrinos at the Super-Kamiokande site is shown in Figure 4.10 with the predictions of G. Battistoni *et al.*[72] (Fluka flux) and G. Barr *et al.*[73] (Bartol flux). Neutrinos with the energy of the order of 1 GeV contribute to the background for nucleon decay searches. The systematic uncertainty of the absolute flux was

estimated to be approximately 25% due to the uncertainty of the absolute primary cosmic ray flux and the uncertainties of the cosmic ray interactions.

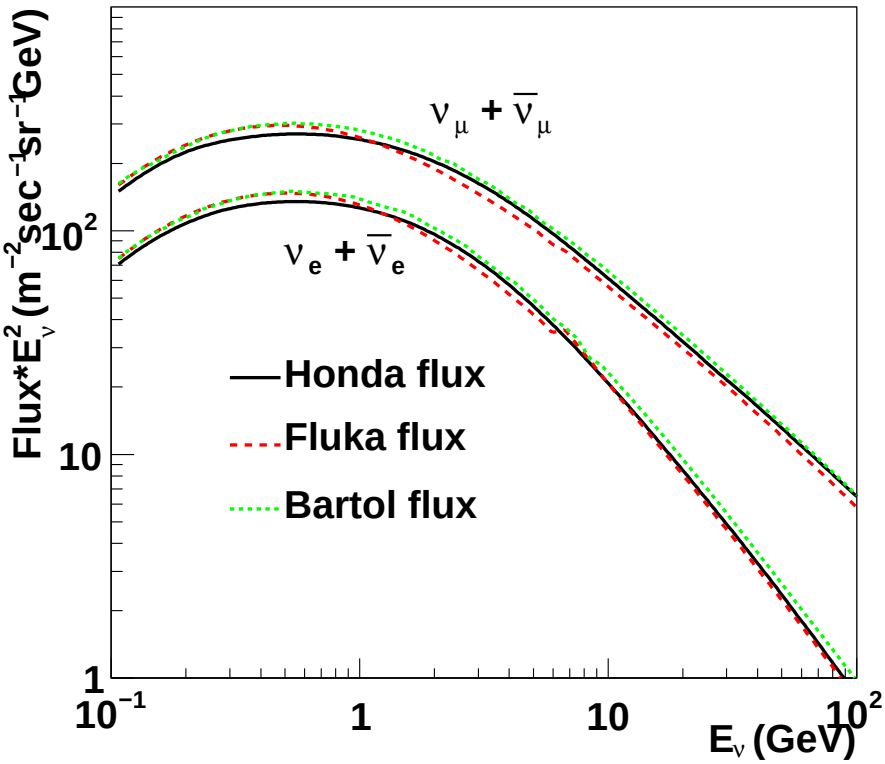

Figure 4.10: The Predicted atmospheric neutrino fluxes at the Super-Kamiokande site. Solid lines show the Honda flux, dashed lines show the Fluka flux [72], and dotted lines show the Bartol flux [73].

4.3 Neutrino Interaction

Atmospheric neutrinos interact with nucleons and electrons in water in the Super-Kamiokande detector. Neutrino interactions were treated by NEUT [74, 75] in our simulation. In NEUT, the following charged current (CC) and neutral current (NC) interactions were considered:

CC/NC (quasi-)elastic scattering	$\nu + N \rightarrow\ l + N'$
CC/NC single meson production	$\nu + N \rightarrow\ l + N' + meson$
CC/NC deep inelastic interaction	$\nu + N \rightarrow\ l + N' + hadrons$
CC/NC coherent pion production	$\nu +\ ^{16}\mathrm{O} \rightarrow\ l +\ ^{16}\mathrm{O} + \pi$

where ν is a neutrino (either a neutrino or an anti-neutrino), N and N' are nucleons (proton or neutron), and l is a lepton (either a neutrino or a charged lepton).

4.3.1 Elastic Scattering and Quasi-Elastic Scattering

The differential cross-section of the charged current quasi-elastic scattering for free protons is given by [76, 77] :

$$\frac{d\sigma^{\nu(\bar{\nu})}}{dq^2} = \frac{M^2 G_F^2 \cos^2\theta_c}{8\pi E_\nu^2}\left[A(q^2) \mp B(q^2)\frac{s-u}{M^2} + C(q^2)\frac{(s-u)^2}{M^4}\right], \tag{4.5}$$

where E_ν is the neutrino energy, M is the mass of the target nucleon, G_F is the Fermi coupling constant, θ_c is the Cabbibo angle, q is the four-momentum transfer, and s and u are Mandelstam variables [76]. The factors A, B and C are :

$$\begin{aligned} A(q^2) &= \frac{m^2-q^2}{4M^2}\left[\left(4-\frac{q^2}{M^2}\right)|F_A|^2 - \left(4+\frac{q^2}{M^2}\right)|F_V^1|^2 \right. \\ &\quad - \frac{q^2}{M^2}|\xi F_V^2|^2\left(1+\frac{q^2}{4M^2}\right) - \frac{4q^2 F_V^1 \xi F_V^2}{M^2} \\ &\quad \left. - \frac{m^2}{M^2}\left((F_V^1+\xi F_V^2)^2 + |F_A|^2\right)\right] \qquad (4.6) \\ B(q^2) &= \frac{q^2}{M^2}\left(F_A(F_V^1+\xi F_V^2)\right) \qquad (4.7) \\ C(q^2) &= \frac{1}{4}\left(|F_A|^2 + |F_V^1|^2 - \frac{q^2}{4M^2}|\xi F_V^2|^2\right) \qquad (4.8) \end{aligned}$$

where m is the charged lepton mass, and $\xi \equiv \mu_p - \mu_n = 3.71$. The vector form factors, $F_V^1(q^2)$ and $F_V^2(q^2)$, and the axial vector form factor, $F_A(q^2)$ are determined experimentally and given by :

$$\begin{aligned} F_V^1(q^2) &= \left(1-\frac{q^2}{4M^2}\right)^{-1}\left[G_E(q^2) - \frac{q^2}{4M^2}G_M(q^2)\right] \qquad (4.9) \\ \xi F_V^2(q^2) &= \left(1-\frac{q^2}{4M^2}\right)^{-1}\left[G_E(q^2) - G_M(q^2)\right] \qquad (4.10) \\ F_A(q^2) &= -1.23\left(1-\frac{q^2}{M_A^2}\right)^{-2} \qquad (4.11) \\ G_E(q^2) &= (1+\xi)^{-1}G_M(q^2) = \left(1-\frac{q^2}{M_V^2}\right)^{-2} \qquad (4.12) \end{aligned}$$

where G_E and G_M are the electric and magnetic form factor, the vector mass M_V is set to be 0.84 GeV and the axial vector mass M_A is set to be 1.21 GeV, which is a common parameter for the single meson production model.

For scattering off nucleons in ^{16}O, the Fermi motion of the nucleons and Pauli exclusion principle must be considered [78]. Since nucleons are fermions, the outgoing momentum of the nucleons in the interactions is required to be greater than the Fermi surface momentum to allow quasi-elastic scattering to occur. In NEUT, the Fermi surface momentum is set to be 225 MeV/c.

The cross-section for neutral current elastic scattering are estimated from the following relations [79, 80] :

$$\sigma(\nu p \to \nu p) = 0.153 \times \sigma(\nu n \to e^- p) \quad (4.13)$$
$$\sigma(\bar{\nu} p \to \bar{\nu} p) = 0.218 \times \sigma(\bar{\nu} p \to e^+ n) \quad (4.14)$$
$$\sigma(\nu n \to \nu n) = 1.5 \times \sigma(\nu p \to \nu p) \quad (4.15)$$
$$\sigma(\bar{\nu} n \to \bar{\nu} n) = 1.0 \times \sigma(\bar{\nu} p \to \bar{\nu} p) \quad (4.16)$$

Figure 4.11 shows the cross-section of the quasi-elastic scattering for the experimental data and the calculation by NEUT.

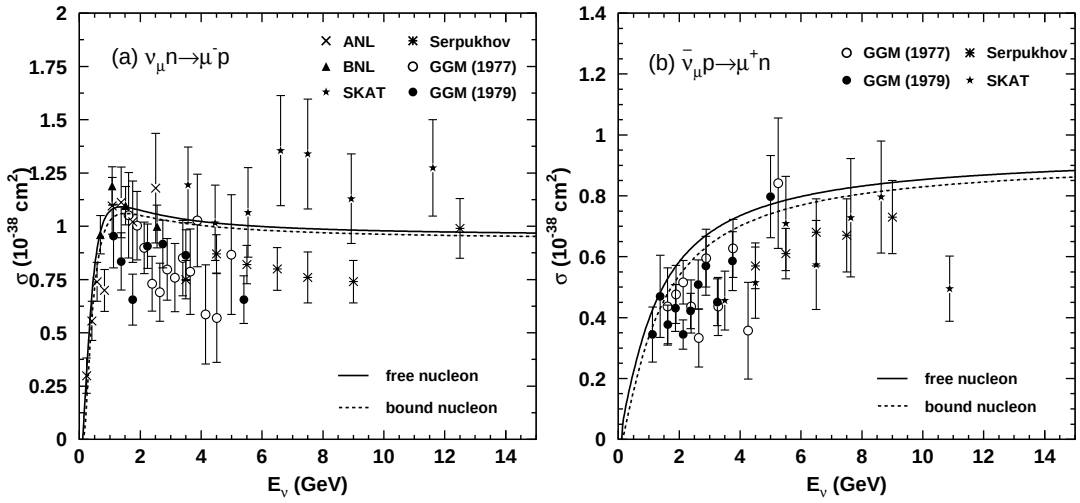

Figure 4.11: cross-sections of (a) ν_μ and (b) $\overline{\nu}_\mu$ with the experimental data from ANL [81], Gargamelle [82, 83], BNL [84], Serpukhov [85] and SKAT [86].

4.3.2 Single Meson Production

The resonant single meson production of π, K, and η was simulated based on the model of Rein & Sehgal [87]. This method assumes an intermediate baryon resonance :

$$\begin{aligned} \nu + N &\to l + N^* \\ N^* &\to N' + \text{meson} \end{aligned} \quad (4.17)$$

where N and N' are nucleons, N^* is a baryon resonance, and l is a lepton (either a charged lepton or a neutrino). The differential cross-section of single-meson production is a product of the amplitude of each resonance production and the probability of their baryon resonance decay to the meson. For a baryon resonance with a negligible decay width, the differential cross-section is :

$$\frac{d^2\sigma}{dq^2 dE_\nu} = \frac{1}{32\pi M E_\nu^2} \cdot \frac{1}{2} \sum_{j,spin} \left| T(\nu N \to l N_j^*) \right|^2 \delta(W^2 - M_j^2) \quad (4.18)$$

where M is the mass of the target nucleon, E_ν is neutrino energy, W is the invariant mass of the hadronic system (or the mass of the intermediate baryon resonance), M_j is the mass of the baryon resonance, and $T(\nu N \to lN^*)$ is the amplitude of resonance production, which is calculated using the FKR (Feynman-Kislinger-Ravndal) model [88]. The invariant mass, W, is restricted to be less than $2\,\mathrm{GeV/c^2}$. For W larger than $2\,\mathrm{GeV/c^2}$, the interactions were simulated as deep-inelastic scattering as described in the next section. For a baryon resonance with a finite decay width, the differential cross-section can be derived by replacing the δ-function with a Breit-Wigner factor :

$$\delta(W^2 - M_j^2) \quad \to \quad \frac{1}{2\pi} \cdot \frac{\Gamma}{(W - M_j)^2 + \Gamma^2/4}. \tag{4.19}$$

For a single-meson production, the axial vector mass M_A is also set to be $1.21\,\mathrm{GeV}$. A total of 28 resonances were simulated in our simulation. The effect of the Pauli exclusion principle in the decay of the baryon resonance was considered by requiring the momentum of the scattered nucleon to be greater than the Fermi surface momentum. The pion-less decay of Δ resonance in ^{16}O nuclei, where about 20 % of the events do not have a pion in the decay, was also simulated [89]. Figure 4.12 show the cross-sections of charged currentresonant single-meson productions for our calculations and the experimental data.

Most of the baryon resonances decay to the final states including π. The production cross section for the η meson and K meson are much less than that for π. The fractions for the single η meson and the K meson production in the total single meson production events in the atmospheric neutrino MC were approximately 4% and 0.6%, respectively.

4.3.3 Deep Inelastic Scattering

The cross-section of charged current deep inelastic scattering is calculated by integrating the following equation in the range of the invariant mass $W > 1.3\,\mathrm{GeV}/c^2$ [90] :

$$\begin{aligned}
\frac{d^2\sigma^{\nu,\bar{\nu}}}{dxdy} &= \frac{G_F^2 M_N E_\nu}{\pi}\left((1 - y + \frac{y^2}{2} + C_1)F_2(x,q^2) \pm y(1 - \frac{y}{2} + C_2)xF_3(x,q^2)\right) \\
C_1 &= \frac{yM_l^2}{4M_N E_\nu x} - \frac{xyM_N}{2E_\nu} - \frac{m_l^2}{4E_\nu^2} - \frac{m_l^2}{2M_N E_\nu x} \\
C_2 &= -\frac{m_l^2}{4M_N E_\nu x}
\end{aligned} \tag{4.20}$$

where $x(= -q^2/(2M(E_\nu - E_l)))$ and $y(= (E_\nu - E_l)/E_\nu)$ are Bjorken scaling parameters, M_N is the nucleon mass, m_l is the outgoing lepton mass, E_ν and E_l are the energy of incoming neutrino and outgoing lepton in the laboratory frame, respectively. The nucleon structure functions F_2 and xF_3 are taken from GRV98 [91].

In our simulation, the cross-section of deep inelastic scattering induced by neutral current were assumed to have the following relations which were estimated from experimental results [92,

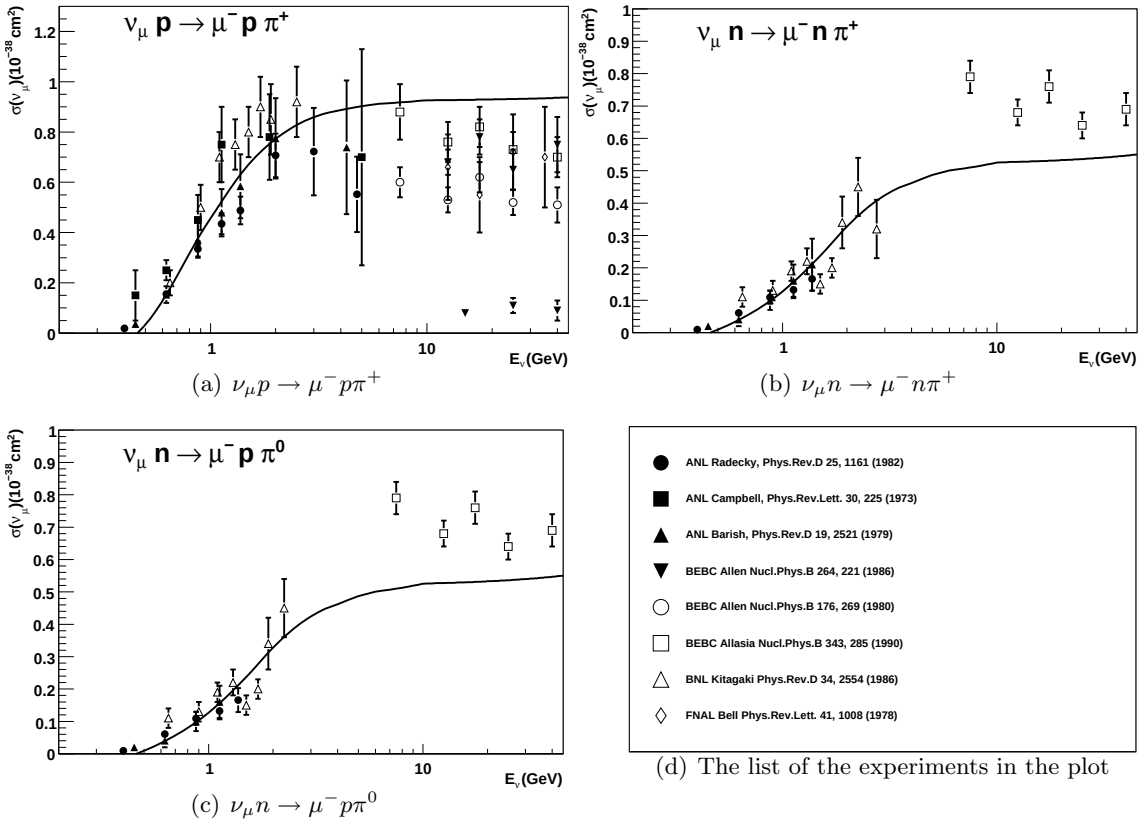

(a) $\nu_\mu p \rightarrow \mu^- p \pi^+$

(b) $\nu_\mu n \rightarrow \mu^- n \pi^+$

(c) $\nu_\mu n \rightarrow \mu^- p \pi^0$

(d) The list of the experiments in the plot

Figure 4.12: Cross sections for charged current single pion productions of ν_μ. Solid lines indicate our calculations. Experimental data are summarized in the panel (d).

93] :

$$\frac{\sigma(\nu N \to \nu X)}{\sigma(\nu N \to \mu^- X)} = \begin{cases} 0.26 & (E_\nu < 3\,\mathrm{GeV}) \\ 0.26 + 0.04\,(E_\nu/3 - 1) & (3\,\mathrm{GeV} \le E_\nu < 6\,\mathrm{GeV}) \\ 0.30 & (E_\nu \ge 6\,\mathrm{GeV}) \end{cases} \tag{4.21}$$

$$\frac{\sigma(\bar{\nu} N \to \bar{\nu} X)}{\sigma(\bar{\nu} N \to \mu^+ X)} = \begin{cases} 0.39 & (E_\nu < 3\,\mathrm{GeV}) \\ 0.39 - 0.02\,(E_\nu/3 - 1) & (3\,\mathrm{GeV} \le E_\nu < 6\,\mathrm{GeV}) \\ 0.37 & (E_\nu \ge 6\,\mathrm{GeV}) \end{cases} \tag{4.22}$$

The kinematics of the hadronic system was simulated by two different methods according to the range of invariant mass. In the region of $1.3\,\mathrm{GeV}/c^2 < W < 2.0\,\mathrm{GeV}/c^2$, only pions were considered as outgoing mesons. The mean multiplicity of pions was estimated from the result of the Fermilab 15-foot hydrogen bubble chamber experiment [94] :

$$\langle n_\pi \rangle = 0.09 + 1.83 \ln(W^2) \tag{4.23}$$

The number of pions in each event was determined by using KNO (Koba-Nielsen-Olsen) scaling. Since the range of W overlaps with that in single pion production, $n_\pi \ge 2$ is required in this W region. The forward-backward asymmetry of pion multiplicity in the hadronic center of mass system is included using the results from the BEBC experiment [95] :

$$\frac{n_\pi^F}{n_\pi^B} = \frac{0.35 + 0.41 \ln(W^2)}{0.5 + 0.09 \ln(W^2)} \tag{4.24}$$

In the region of $W > 2.0\,\mathrm{GeV}/c^2$, the kinematics of the hadronic system were calculated by using the PHYTIA/JETSET package [96]. This package treats not only π but also K, η, ρ and so on.

The cross section of the CC ν_μ and $\bar{\nu_\mu}$ interactions are shown in Figure 4.13.

4.3.4 Coherent Pion Production

Coherent pion production is a neutrino interaction with an oxygen nucleus, which remains intact, and one pion with the same charge as the incoming weak current is produced. Since very little momentum is transferred to the oxygen nucleus, the angular distributions of the outgoing leptons and pions are peaked in the forward direction. The formalism developed by Rein and Sehgal [97] was used to simulate the interactions, and the differential cross-section is given by :

$$\begin{aligned} \frac{d^3\sigma}{dQ^2 dy dt} &= \beta \times \frac{G_F^2 M}{2\pi^2} f_\pi^2 A^2 E_\nu (1-y) \frac{1}{16\pi} (\sigma_{total}^{\pi N})^2 \\ &\quad \times (1 + r^2) \left(\frac{M_A^2}{M_A^2 + Q^2} \right)^2 e^{-b|t|} F_{abs} \qquad (4.25) \\ r &= Re(f_{\pi N}(0))/Im(f_{\pi N}(0)) \qquad (4.26) \end{aligned}$$

where β is the axial vector couping constant and is 1 (2) for neutral current (charged current) interactions, G_F is the weak coupling constant, M is the nucleon mass, f_π is pion decay constant

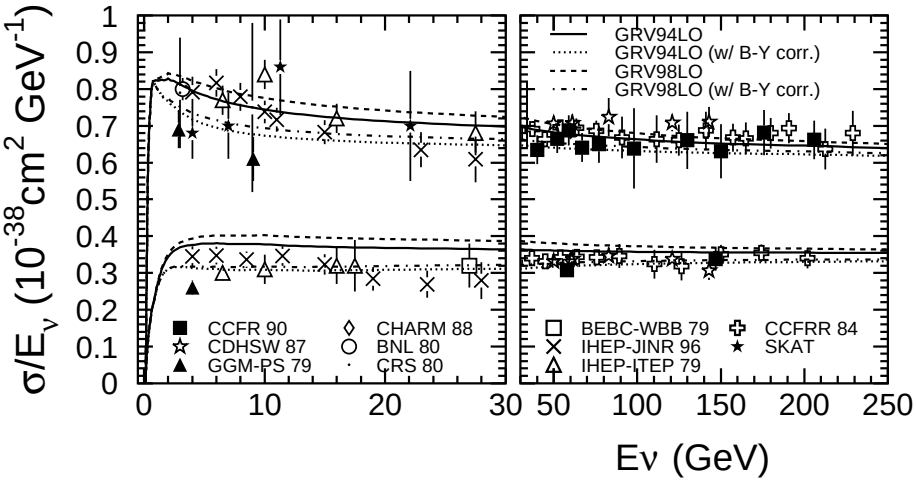

Figure 4.13: Cross sections for charged current ν_μ and $\overline{\nu}_\mu$ interactions. Upper(lower) lines are $\nu_\mu(\overline{\nu}_\mu)$.

and is $0.93\,m_\pi$, A is the atomic number ($=16$ for oxygen), E_ν is the neutrino energy, y is the lepton fractional energy loss, $\sigma^{\pi N}_{total}$ is the averaged pion-nucleon cross-section, b is in the order of the nucleus transverse dimensions and is $80\,\mathrm{GeV}^{-2}$, M_A is the axial-vector mass, Q^2 is the square of the four–momentum transfer of the lepton, and t is the square of the four-momentum transfer to the nucleus, and F_{abs} is a factor to account for the absorption of pions in the nucleus. $f_{\pi N}(0)$ in r is the πN scattering amplitude. However, the K2K experiment set an upper limit on the cross-section of coherent CC pion production [98]. The upper limit is significantly lower than the predicted cross-section by Rein and Sehgal. Therefore some modification is necessary to the Monte Carlo coherent pion production cross-sections. The calculated cross-sections of the coherent pion production for the CC and NC interactions by Kartavtsev and Paschos [99] agree better with the several experimental data than that of Rein and Sehgal as shown in Figure 4.14. The difference between the experimental data and the model proposed by Kartavtsev and Paschos was taken into account as a systematic uncertainty of 100 %.

4.3.5 Nucleon Nuclear Effect

Nucleons produced in a nucleus by neutrino interactions can cause secondary interactions with other nucleons. The nucleon-nucleon elastic scattering cross section is based on the measurements by Betrini *et al.* [104], which is used in GCALOR. The pion production caused by the decay of produced deltas was also taken into account, according to the isobar production model by Lindenbaum *et al.* [105].

4.4 Detector Simulation

Particles produced in the nucleon decay simulation and atmospheric neutrino interactions were passed through a GEANT-3 [106] based custom detector simulator. Cherenkov light emis-

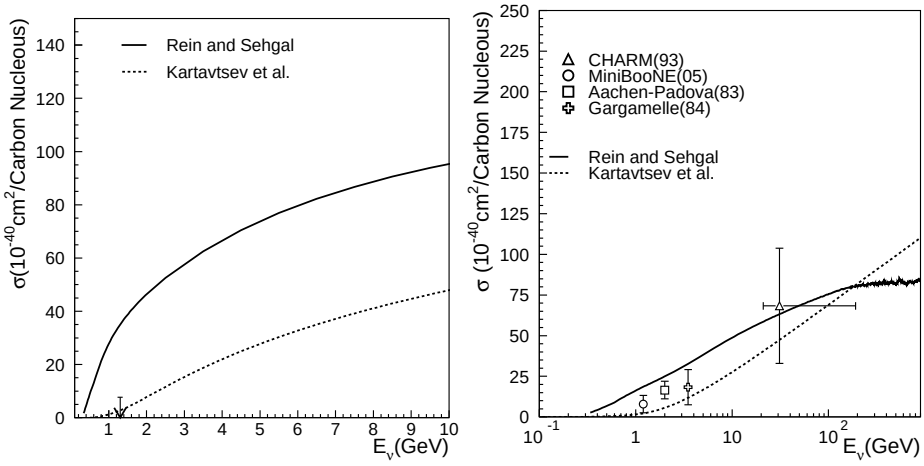

Figure 4.14: The cross-sections of coherent pion productions off the carbon nucleus for CC interaction(left) and NC interaction(right) by two models with the experimental data. The solid lines are calculation by Rein and Sehgal, while the dashed lines are by Kartavtsev and Paschos. On the left figure, the arrow shows the experimental upper limit by K2K [98], and on the right figure. The experimental data are from CHARM [100], MiniBooNE [101], Aachen-Padove [102] and Gargamelle [103].

sion, light propagation through matter, particle propagation and hadronic interaction in water, and the response of PMTs, data acquisition electronics and trigger systems are simulated in this simulator.

In many of the nucleon decay modes searched in this thesis, charged pions are produced and propagate in water radiating Cherenkov photons. Therefore, hadronic interactions in water should be simulated precisely. In order to reproduce low energy pion interactions, hadronic interactions were treated by a custom simulation program [108] based on experimental data of π-^{16}O scattering [109] and π-p scattering [110] for charged pions of $p_\pi \leq 500$ MeV/c, while CALOR [107] was employed for nucleons and charged pions of $p_\pi > 500$ MeV/c.

In the photon tracking in the detector simulator, absorption and Mie and Rayleigh scattering processes were taken into account. Rayleigh scattering is a dominant process for short wavelength because of the λ^{-4} dependence, and photons are scattered symmetrically in forward and backward directions in this process. Absorption is a dominant process for longer wavelength (450 nm) photons. Coefficients for these processes were tuned to reproduced the calibration data as described in Section 3.6.4.

Chapter 5

Data Reduction

The nominal trigger rate in Super-Kamiokande except for the Super Low Energy trigger is ∼11 Hz. About 10^6 events are accumulated every day. Most of those events are cosmic ray muon events or low energy background events from radioactivities from materials around the detector wall. A flasher event, which is caused by a flashing PMT due to a discharge around the dynode structure, can also be a non-negligible background. Some relatively intelligent reduction techniques were applied to reduce the background.

We have to reject these background events before proceeding further detailed event reconstruction processes. For nucleon decay searches, fully contained (FC) events were selected by the reduction algorithms described in this chapter. The fully contained event is defined to have some activities only in the inner detector.

There are five steps for the FC reduction scheme. All the data reduction schemes for the FC events are automated. The reduction algorithms are basically common for SK-I and SK-II except for some criteria because of the difference in the number of the ID PMTs.

5.1 First Reduction

The 1st reduction were applied in order to reduce low energy backgrounds from radio isotopes (by criterion (1)), cosmic ray muon events (by criterion (2)) and electron events from the decay of the cosmic ray muons (by criterion (3)).

These cuts reduced the data size from 10^6 events/day to 3000 (2200) events/day for SK-I (SK-II).

The selection criteria of the 1st reduction are defined as;

(1) $PE_{300} \geq 200$ p.e.s (100 for SK-II),
(PE_{300} is the maximum number of total p.e.s observed by the ID PMTs in a sliding 300 nsec time window.
The threshold for PE_{300} cut corresponds to 22 MeV/c for electrons. The PE_{300} distributions for the raw data and the proton decay MC are shown in Figure 5.1.)

(2) $NHITA_{800} \leq 50$ or OD trigger is off,
($NHITA_{800}$ is the number of hit OD PMTs in a fixed 800 nsec time window from -400 nsec to +400 nsec before and after the trigger timing.
The $NHITA_{800}$ distributions for the raw data and the proton decay MC are shown in Figure 5.2.)

(3) TDIFF > 100 μsec.
(TDIFF is a time interval to the previous event.)

The criterion (3) removes the electron events from the decay of the cosmic ray muons which stopped in the ID. The events within 30 μsec after another selected events by the above criteria are selected to keep the decay electrons. These events are attached to the fully contained event candidates as sub-events and not counted as a primary events.

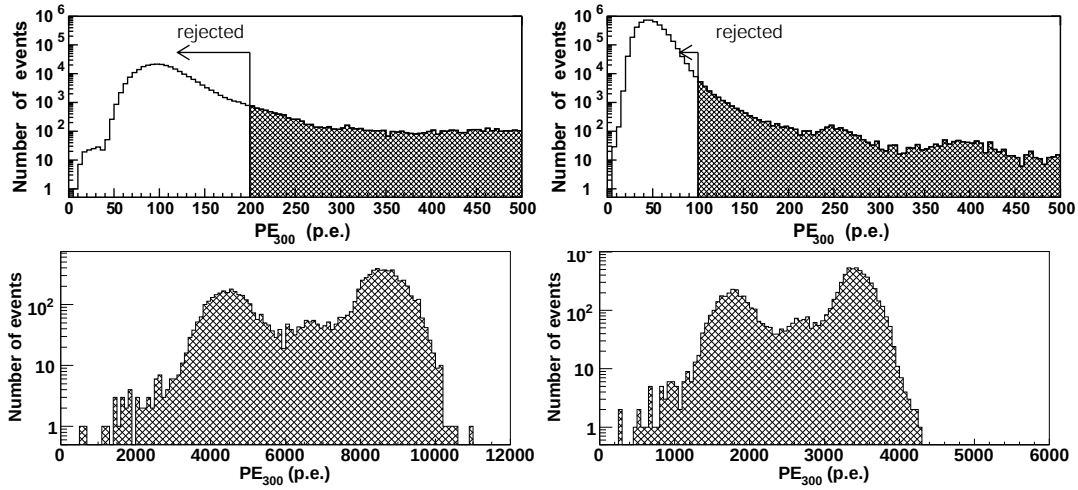

Figure 5.1: PE_{300} distribution for the raw data (top) and the $p \to e^+\pi^0$ MC (bottom) in SK-I (left) and SK-II (right). The selection criterion is indicated by the arrows.

5.2 Second Reduction

The 2nd reduction were applied in order to further eliminate the cosmic ray muon events (by criterion (1)), low energy events and electrical noise events, which have one larger hit signal from a single PMT (by criterion (2)).

The event rate after the 2nd reduction decreased to 200 (280) events/day for SK-I (SK-II).

The selection criteria of the 2nd reduction are defined as;

(1) $NHITA_{800} \leq 25$ if $PE_{tot} < 100{,}000$ p.e.s (50,000 for SK-II) or OD trigger is off,
(PE_{tot} is the total p.e.s observed in the ID.
This criterion is shown in Figure 5.2 by the solid line.)

(2) $PE_{max}/PE_{300} < 0.5$.
(PE_{max} is the maximum number of p.e.s observed in the ID PMTs. The PE_{max}/PE_{300} distributions are shown in Figure 5.3.)

5.3 Third Reduction

In order to reduce the background events after the 2nd reduction, tighter cuts were applied to eliminate noise events, such as flasher events, and cosmic ray muon events which have a small

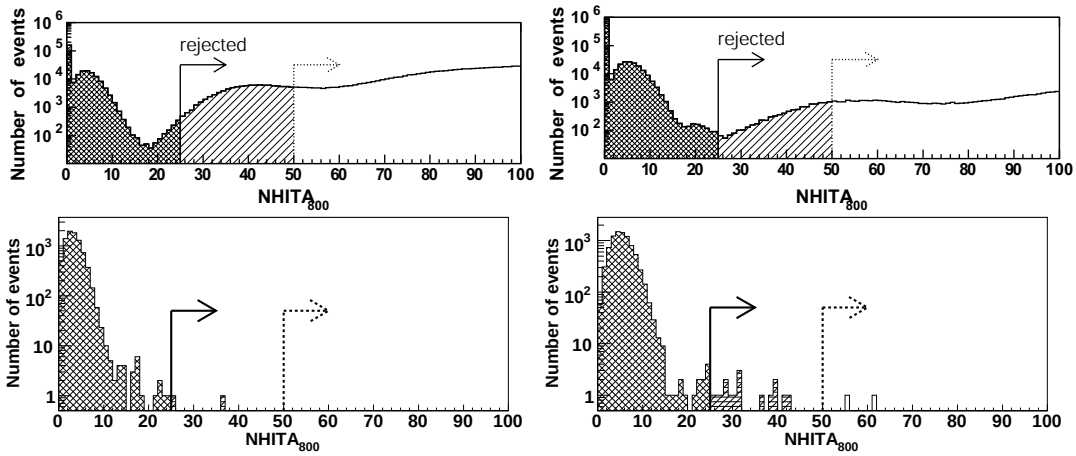

Figure 5.2: NHITA_{800} distributions for the raw data (top) and the $p \to e^+\pi^0$ MC (bottom) in SK-I (left) and SK-II (right). The dotted (solid) arrows indicated the selection criteria in the 1st (2nd) reduction.

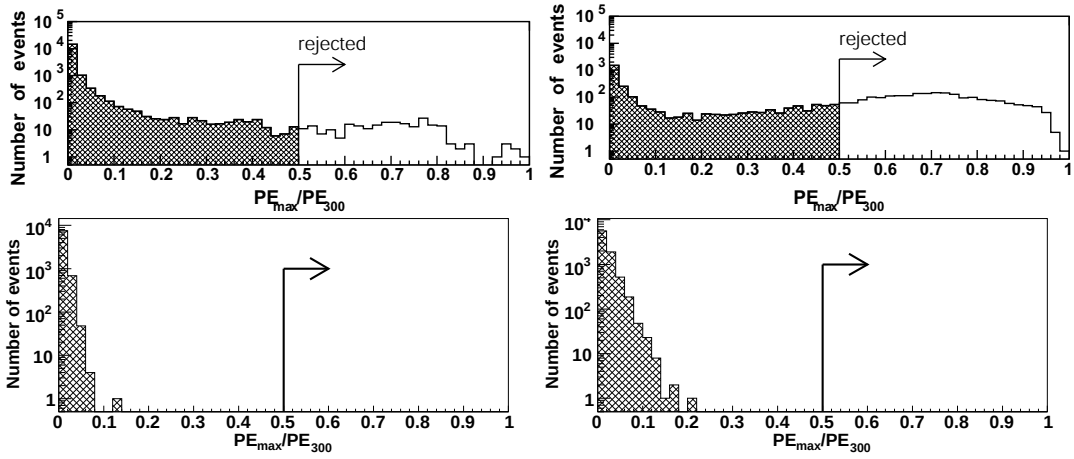

Figure 5.3: $\mathrm{PE}_{\mathrm{max}}/\mathrm{PE}_{300}$ distributions for the data (top) and the $p \to e^+\pi^0$ MC (bottom) in SK-I (left) and SK-II (right) after the 1st reduction. The selection criteria are indicated by the arrows.

number of the OD hits.

The 3rd reduction is separated into six parts as follows;

- through-going muon cut,
- stopping muon cut,
- cable hole muon cut,
- flasher event cut,
- accidental coincidence events cut,
- low energy events cut.

After applying these cuts, the event rate decreased to 45 (21) events/day for SK-I (SK-II). The details of these reduction criteria are described below.

Through-going Muon Cut

The remaining through going muon events have fewer number of hit PMTs in the OD and cannot be easily rejected. Therefore, we applied a special through-going muon fitter and counted the number of hit PMTs in the OD around the entrance and exit points. Events which satisfy all the conditions below are rejected;

(1) $\mathrm{PE_{max}} > 230$ (and the number of hit PMTs exceeds 1000 for SK-II),

(2) $\mathrm{NHITA_{in}} \geq 10$ or $\mathrm{NHITA_{out}} \geq 10$,
($\mathrm{NHITA_{in}}$ ($\mathrm{NHITA_{out}}$) is the number of hit OD PMTs in a fixed 800 nsec time window located within 8m from the entrance (exit) point.) These distributions are shown in Figure 5.4.

(3) the goodness of the through-going muon fit > 0.75.

The goodness of the fitter is defined as;

$$goodness = \frac{1}{\sum_i \frac{1}{\sigma_i^2}} \times \sum_i \frac{1}{\sigma_i^2} \exp\left(-\frac{(t_i - T_i)^2}{2\,(1.5 \times \sigma_i)^2}\right) \tag{5.1}$$

where t_i and σ_i are the observed hit time of the i-th PMT and its resolution, and T_i is the hit time expected from the entering time of muon and its track.

Stopping Muon Cut

There are also remaining events by cosmic ray muons which stopped in the detector. This type of events can also be rejected by fitting the muon track and counting the number of hit PMTs of the OD around the entrance. The stopping muon fitter assumes the location of the PMT having the earliest signal to be the entrance point. The direction of the muon is determined by maximizing the total charge in the Cherenkov cone. The goodness of this fitter is same as that for through-going muons.

The events satisfying the following criteria are classified as stopping muon events and removed;

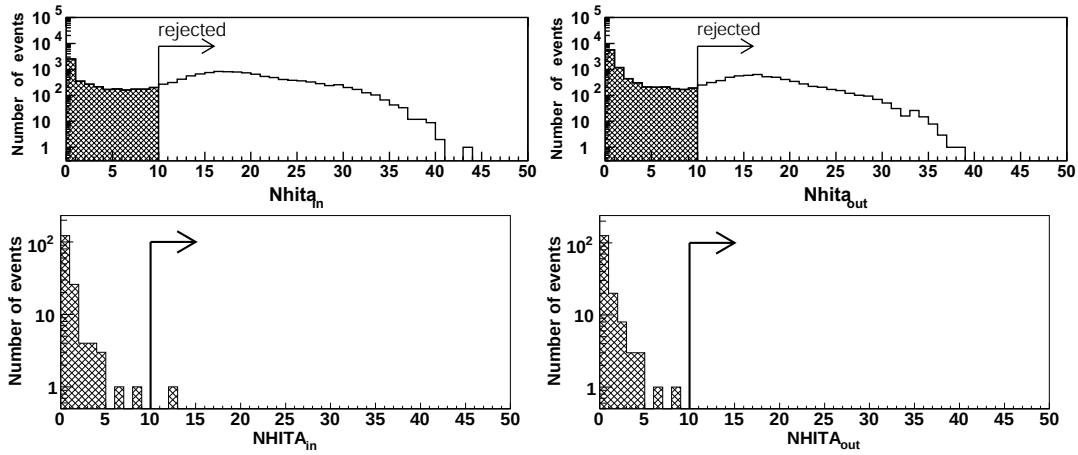

Figure 5.4: $\mathrm{NHITA_{in}}$ (left) and $\mathrm{NHITA_{out}}$ (right) distributions after the 2nd reduction for the data (top) and the $p \to e^+\pi^0$ MC (bottom) in SK-I. The rejection criteria are indicated by the arrows.

(1) $\mathrm{NHITA_{in}} \geq 10$
or
$\mathrm{NHITA_{in}} \geq 5$ if goodness of the stopping muon fit ≥ 0.5.

Cable Hole Muon Cut

On the top of the detector tank, there are twelve cable holes where all the signal and high voltage supply cables go through. Four holes out of twelve are directly above the ID and block the OD. Cosmic ray muons going through these holes would not leave any OD activities and could be identified as contained events. In order to eliminate this mis-identification possibility, a set of veto counters (2.0m $\times$ 2.5m plastic scintillation counters) were installed as shown in Figure 5.5.

The rejection criteria are defined as;

(1) one veto counter hit,

(2) $\mathrm{L_{veto}} < 4$ m.
($\mathrm{L_{veto}}$ is the distance from the cable hole to the reconstructed vertex.)

Figure 5.6 shows the reconstructed vertex distributions for the 1-ring non-shower type events before and after the installation of veto counters. The muons going through the cable holes are well eliminated by the veto counters.

Flasher Event Cut

The flasher events usually show a broad timing distribution as shown in Figure 5.7. In order to remove these events, the number of hit PMTs is counted within a 100 μsec sliding time window, and the minimizing point ($\mathrm{NMIN_{100}}$) is searched.

The rejection criterion for SK-I is defined as;

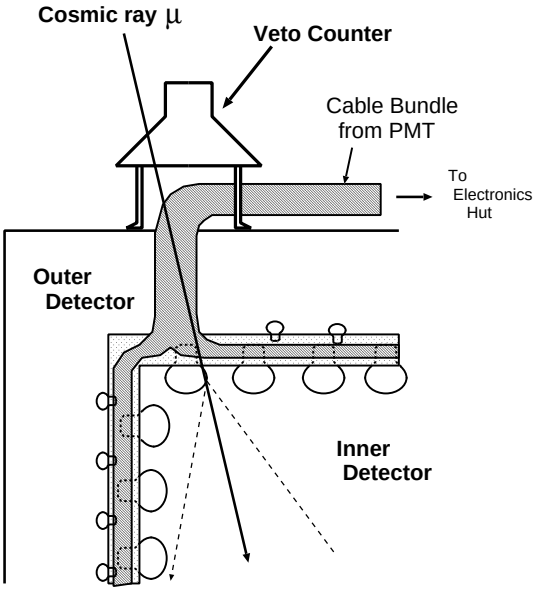

Figure 5.5: A schematic view of a cable hole muon and a veto counter.

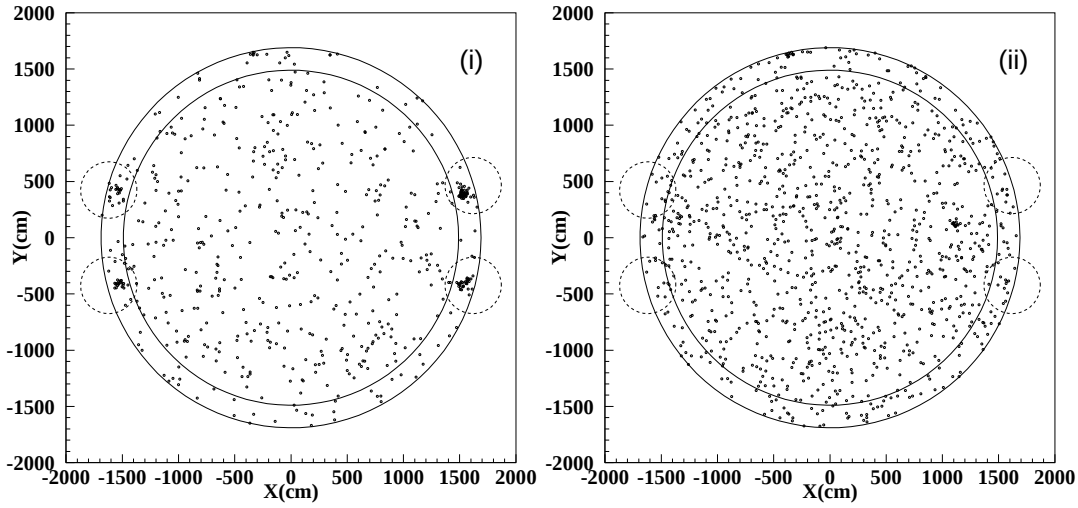

Figure 5.6: Reconstructed vertex distributions for the fully contained 1-ring non-shower type events; (i) before the installation of the veto counters and (ii) after the installation. The outer and inner solid circle shows the ID wall and the fiducial volume (2m from the wall), respectively. The small dashed circles indicated the positions of the veto counters.

(1) $\mathrm{NMIN}_{100} \geq 14$
or
$\mathrm{NMIN}_{100} \geq 10$ if the number of hit ID PMTs < 800.
(NMIN_{100} is the minimum number of hit ID PMTs in a sliding 100 nsec time window from +300 nsec to +800 nsec after the trigger. NMIN_{100} distributions are shown in Figures 5.8, 5.9.)

The rejection criterion for SK-II is defined as;

(1) $\mathrm{NMIN}_{100} \geq 10$.

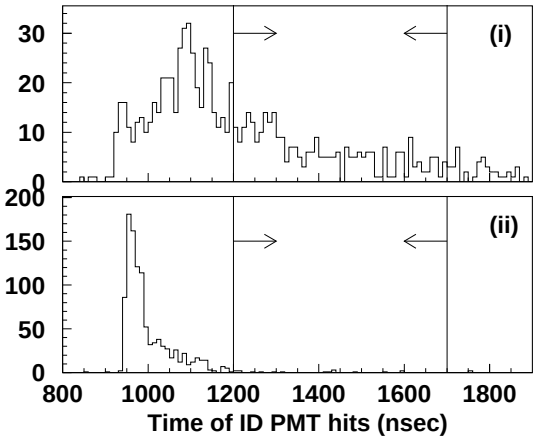

Figure 5.7: The timing distribution of a typical flashing PMT (top) event and a typical fully contained event (bottom). The arrows indicate the time window for counting NMIN_{100}.

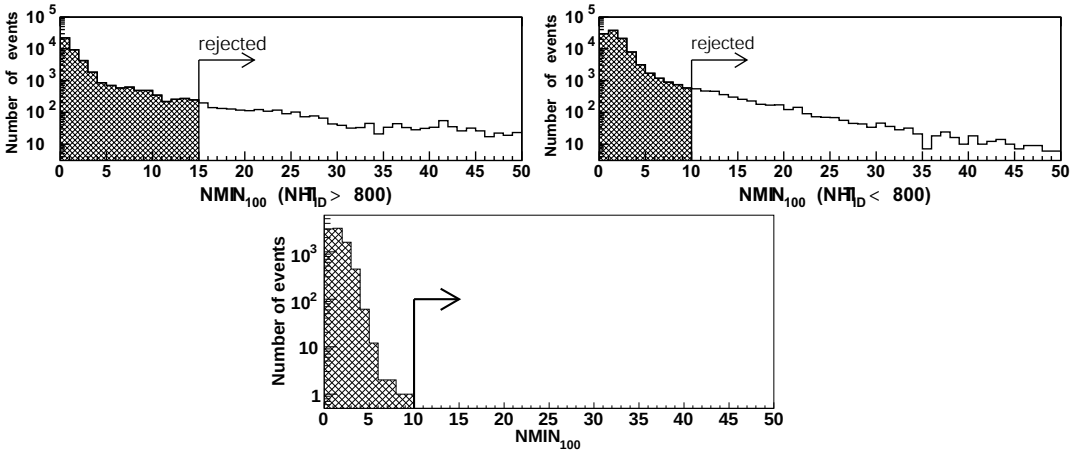

Figure 5.8: NMIN_{100} distributions for the data (top) and the $p \rightarrow e^{+}\pi^{0}$ MC (bottom) in SK-I after the 2nd reduction. For the observed data, events with more (less) than 800 hit PMTs in the ID are filled in the left (right) figure. The rejection criteria are indicated by the arrows.

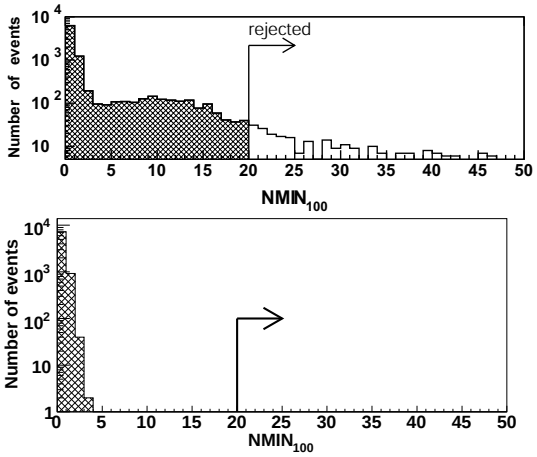

Figure 5.9: NMIN_{100} distributions for the data (top) and the $p \to e^+\pi^0$ MC (bottom) in SK-II after the 2nd reduction. The rejection criteria are indicated by the arrows.

Accidental Coincidence Events Cut

The accidental coincidence occurs when a low energy event generates the trigger and a cosmic ray muon event follows in a single trigger gate. Such events were rejected by the following rejection criteria:

(1) $\mathrm{NHITA}_{\mathrm{off}} \geq 20$.
($\mathrm{NHITA}_{\mathrm{off}}$ is the number of hit OD PMTs in a fixed 500 nsec off-timing window from +400 nsec to +900 nsec after the trigger timing.)

(2) $\mathrm{PE}_{\mathrm{off}} > 5000$ p.e.s (2500 for SK-II).
($\mathrm{PE}_{\mathrm{off}}$ is the number of p.e.s observed by ID PMTs in a fixed 500 nsec off-timing window from +400 nsec to +900 nsec.)

Low Energy Events Cut

The remaining low energy events are from the decay of radio isotopes and the electrical noise. Such events were rejected by the following rejection criteria:

(1) $\mathrm{NHIT}_{50} < 50$ (25 for SK-II).
(NHIT_{50} is the number of hit ID PMTs in a sliding 50 nsec time window. The threshold for this cut corresponds to 9 MeV for electron.)

5.4 Fourth Reduction

Most of remaining backgrounds after the 3rd reduction are flasher events. The typical event display of a flasher event is shown in Figure 5.10. In order to eliminate the flasher events, an intelligent pattern matching algorithm is used. Flasher events usually repeat similar PMT hit patterns in the detector in the course of hours and days. Such repeated events are not likely to be caused by nucleon decays or neutrinos.

The 4th reduction algorithm compares event patterns between every two events and estimated the correlation factors for those events in order to find "matched" events.

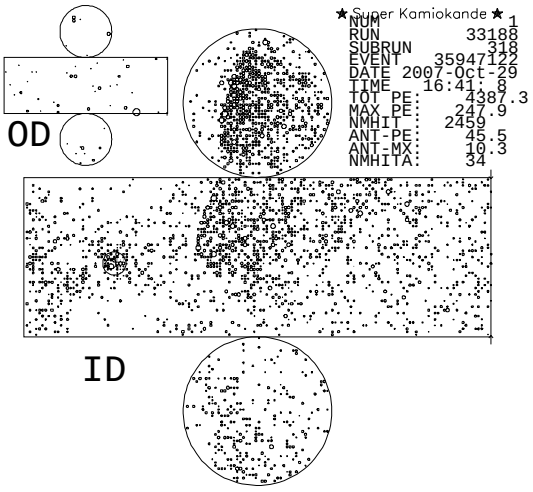

Figure 5.10: Event display of a typical flasher event. The circle in the left side of the display indicates the flashing PMT. The light from the flashing PMT reaches to the other side of the detector.

The event rate after the 4th reduction decreased to 18 events/day for both SK-I and SK-II. The detailed procedure of the 4th reduction algorithm is summarized as follows:

(1) The ID wall is divided into 1450 patches of 2m × 2m square.

(2) The correlation factor r is calculated by comparing the total charge in each patch of two events, A and B, as follows,

$$r = \frac{1}{N} \sum_i \frac{\left(Q_i^A - \langle Q^A \rangle\right) \times \left(Q_i^B - \langle Q^B \rangle\right)}{\sigma_A \times \sigma_B} \tag{5.2}$$

where N is the number of patches, and $\langle Q^{A(B)} \rangle$ and $\sigma_{A(B)}$ are the averaged charge and its standard deviation for the event A (B).

  (a) The distance ($\mathrm{DIST_{max}}$) between the PMTs with the maximum charge in the two compared events is calculated.

  (b) IF $\mathrm{DIST_{max}} < 75$ cm, an offset value is added as; $r \rightarrow r + 0.15$.

(3) If r exceeds the threshold (r_{th}), events A and B are recognized as matched events. The threshold is defined as;

$$r_{th} = 0.168 \times \log_{10}\left(\left(PE_{\mathrm{tot}}^A + PE_{\mathrm{tot}}^A\right)/2\right) + 0.130 \tag{5.3}$$

where PE_{tot} is the total number of p.e.s observed in the ID.

(4) The above calculation is repeated over 10,000 events around the target event. Then, the number of matched events are counted.

(5) The events with large correlation factor r or large number of matched events are removed.

5.5 Fifth Reduction

The remaining background events were removed by the following criteria specialized for each kind of background events.

- stopping muon cut
- invisible muon cut
- coincidence muon cut
- long-tail flasher cut

After applying these reduction criteria, the event rate was 16 events/day for both SK-I and SK-II.

The details of these reduction criteria are described below.

Stopping Muon Cut

The remaining stopping muons were rejected by tighter criteria than those in the 3rd reduction. The entrance position in the OD is estimated by a backward extrapolation from the reconstructed vertex determined by TDC fit (see Section 6.1).

Events satisfying the following criterion were rejected;

(1) $\mathrm{NHITA_{in}} \geq 5$
($\mathrm{NHITA_{in}}$ is the number of hit OD PMTs located within 8m from the entrance point in a sliding 200 nsec time window from -400 nsec to +400 nsec.)

Invisible Muon Cut

Invisible muon events are caused by cosmic ray muons with momenta less than the Cherenkov threshold and the subsequent decay electrons being observed. These events are characterized by a low energy signal from decay electron and a signal in the OD before the trigger timing. Events which satisfied the following cut criteria were rejected as invisible muons:

(1) $\mathrm{PE_{tot}} < 1000$ p.e.s (500 for SK-II).
($\mathrm{PE_{tot}}$ is the total number of p.e.s observed in the ID.)

(2) $\mathrm{NHITAC_{early}} > 4$.
($\mathrm{NHITAC_{early}}$ is the maximum number of hit PMTs in the OD hit cluster in a sliding 200 nsec time window from -800 nsec to -100 nsec.)

(3) $\mathrm{NHITAC_{early}} + \mathrm{NHITAC_{500}} > 9$ (if $\mathrm{DIST_{clust}} < 500\,\mathrm{cm}$)
$\mathrm{NHITAC_{early}} > 9$ (otherwise).
($\mathrm{NHITAC_{500}}$ is the number of hit PMTs in the OD hit cluster in a fixed 500 nsec time window from -100 nsec to $+400$ nsec.
$\mathrm{DIST_{clust}}$ is a distance between two OD hit clusters, which are used for the $\mathrm{NHITAC_{early}}$ and the $\mathrm{NHITAC_{500}}$.)

Coincidence Muon Cut

The remaining accidental coincidence muon events are removed by the following rejection criteria;

(1) $PE_{500} < 300$ p.e.s (150 for SK-II).
(PE_{500} is the total number of p.e.s observed in the ID in a fixed 500 nsec time window from -100 nsec to +400 nsec.)

(2) $PE_{late} \geq 20$ p.e.s.
(PE_{late} is the maximum number of hit OD PMTs in a 200 nsec sliding time window from 400 nsec to 1600 nsec. PE_{late} distributions are shown in Figure 5.11.)

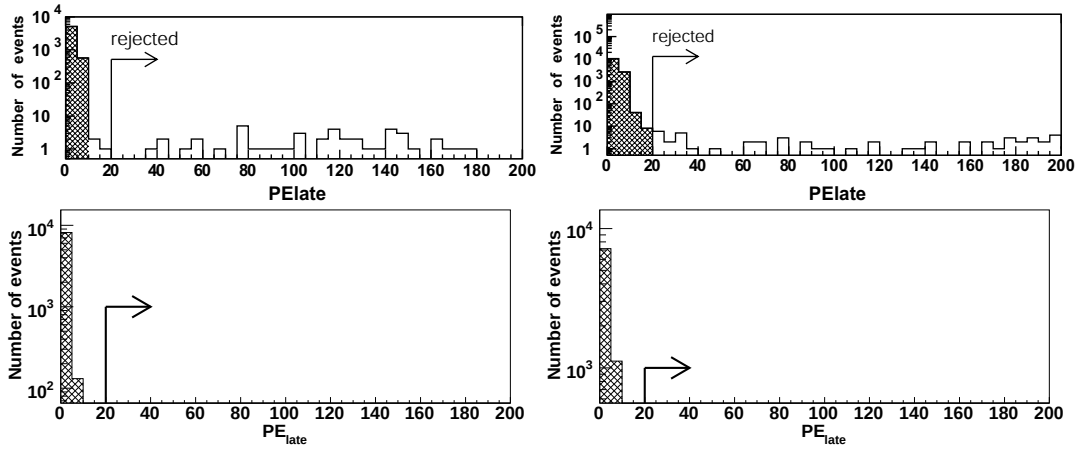

Figure 5.11: PE_{late} distributions after the 4th reduction for the data (top) and the $p \rightarrow e^+\pi^0$ MC (bottom) in SK-I (left) and SK-II (right). The rejection criteria are indicated by the arrows.

Long-tail Flasher Cut

This is a stricter version of the flasher cut in the 3rd reduction. Events satisfying the following criteria are removed as flasher events:

(1) $NMIN_{100} > 5$ if the goodness of point fit < 0.4.
($NMIN_{100}$ is the minimum number of the hit ID PMTs in a sliding 100 nsec time window from 300 nsec to 800 nsec.)
(See Section 6.1 for the explanation of point fit.)

(2) The goodness of point fit < 0.3 (only for SK-II).

(3) $NHITMIN_{100} < 6$ (only for SK-II).

5.6 Summary

Finally, the fully contained samples are selected by applying the following cut:

- The vertex (interaction point) should be inside the fiducial volume (2m away from the ID detector wall).
- The number of hit PMTs in the highest charge OD cluster (NHITAC) should be less than10 (16 for SK-II).
- The visible energy should be greater than 30 MeV. (The visible energy is defined as the sum of the energy of each ring assuming all rings are produced by electrons.)

The event rate of the fully contained events for the real data was 8.18 ± 0.07 (8.26 ± 0.10) events/day for SK-I (SK-II). The background events from cosmic ray muons, flasher events and neutrons from the rock around the detector were largely rejected by requiring the fiducial volume cut. The contaminations of the backgrounds were estimated to be negligible as shown in Table 5.1. After applying reduction criteria to the observed data, we obtained 12232 and 6584 fully contained event samples in the SK-I and SK-II data, respectively. The characteristics of those event samples are described in Chapter 8.

SK-I	Sub-GeV (E_{vis} < 1330 MeV/c)		Multi-GeV ($E_{vis} \geq$ 1330 MeV/c)	
	e-like (%)	μ-like (%)	e-like (%)	μ-like (%)
Cosmic ray μ	—	0.07	—	0.09
Flashing PMT	0.42	—	0.16	—
Neutron event	0.1	—	0.1	—
SK-II	Sub-GeV		Multi-GeV	
	e-like(%)	μ-like(%)	e-like(%)	μ-like(%)
Cosmic ray μ	—	0.01	—	0.07
Flashing PMT	0.27	—	0.65	—
Neutron event	0.1	—	0.1	—

Table 5.1: Summary of the estimated upper limit of the contamination of each background. [111, 112]

The same reduction criteria were also applied to the nucleon decay MC (see Chapter 4). For the nucleon decay via the $N \to e^+meson$ modes, the detection efficiencies surviving the reduction criteria were estimated to be greater than 97%. On the other hand, for the $N \to \mu^+(\rho$ or $\omega)$ modes, the muon can be invisible due to the large meson mass. Moreover, the meson sometimes cannot escape from a nucleus or can be immediately absorbed by nucleons in water. Such events were rejected at the 1st reduction because of the very small visible energy. That resulted in relatively lower efficiencies for these modes.

Mode	SK-I	SK-II	Mode	SK-I	SK-II
$p \to e^+\pi^0$	99.4%	99.5%	$p \to e^+\omega$	99.6%	99.8%
$p \to \mu^+\pi^0$	99.6%	99.8%	$p \to \mu^+\omega$	92.5%	93.8%
$p \to e^+\eta$	99.4%	99.7%	$n \to e^+\pi^-$	99.7%	99.7%
$p \to \mu^+\eta$	99.6%	99.6%	$n \to \mu^+\pi^-$	99.8%	99.9%
$p \to e^+\rho^0$	97.9%	97.9%	$n \to e^+\rho^-$	97.1%	97.1%
$p \to \mu^+\rho^0$	81.2%	81.5%	$n \to \mu^+\rho^-$	83.1%	84.0%

Table 5.2: The detection efficiency by the data reduction criteria for the nucleon decay MC for SK-I and SK-II. The fiducial volume cut is not included.

Chapter 6

Event Reconstruction

Event reconstruction processes were applied to the fully contained events which passed the data reduction described in the previous chapter. The common reconstruction algorithms were used for the observed data and the Monte Carlo (MC) simulation events. This chapter describes the outline of the event reconstruction algorithms and their performances. The details of the reconstruction algorithms are well described in another document [113].

The reconstruction algorithms were applied through the following procedure:

(1) Vertex Fitting:
The vertex position is determined as the point at which the timing residual distribution of hit PMTs has the sharpest peak. The direction and the outer edge of the dominant ring is estimated.

(2) Ring Counting:
Additional possible rings are searched using the vertex position and the direction of the dominant ring. The ring candidates are tested whether the ring really exists or not by a likelihood method. The total number of ring is also determined in this step.

(3) Particle Identification:
Each ring is classified into two types, a showering type ($e^{\pm}, \gamma$) or a non-showering type ($\mu^{\pm}, \pi^{\pm}$), by the ring pattern and the opening angle. The showering type and non-showering type are commonly called e-like and μ-like, respectively.

(4) Momentum Determination:
The momentum of each ring is determined from the charge detected inside a 70° cone. The conversion from the charge to the momentum is done based on the MC simulation and the detector calibration. The observed charge at each PMT is divided into each ring in this step. The separation is one of the most important part for this nucleon decay analysis because it determines momenta for multi-ring events.

(5) Ring Number Correction:
Rings which have low momentum and overlapped with the other energetic rings are discarded as fitting mistakes.

(6) Decay Electron Finding:
Decay electrons following the primary events are searched.

6.1 Vertex Fitter

The event reconstruction process starts from the vertex fitting. The vertex fitting consists of three steps: point-fit, ring edge search and TDC-fit.

Point-Fit

The vertex position is roughly estimated by assuming all of the photons are emitted at the same time from a point source. The time of flight (TOF) of photon is subtracted from the hit timing of each PMT. The vertex is estimated as the point where the TOF-subtracted timing distribution is peaked. This algorithm is called point-fit. The goodness of the fit is defined as follows;

$$goodness = \frac{1}{N}\sum_i \exp\left(-\frac{(t_i - t_0)^2}{2\,(1.5\times\sigma)^2}\right) \tag{6.1}$$

where N is the number of hit PMTs, t_i is the TOF-subtracted timing of the i-th PMT, t_0 is a free parameter chosen to maximize the goodness, and σ is the PMT timing resolution taken to be 2.5 nsec. The numerical factor 1.5 was chosen to optimize the fitter performance. The fitter searches for the vertex point maximizing the goodness.

Ring Edge Search

In the second step, the direction and the edge of the dominant Cherenkov ring (the most energetic ring) are determined. To determine the ring direction, the estimator $Q(\theta_{\rm edge})$ is defined as follows;

$$Q(\theta_{\rm edge}) = \frac{\int_0^{\theta_{\rm edge}} {\rm PE}(\theta)d\theta}{\sin\theta_{\rm edge}} \times \left(\left.\frac{d{\rm PE}(\theta)}{d\theta}\right|_{\theta=\theta_{\rm edge}}\right)^2 \times \exp\left(-\frac{(\theta_{\rm edge}-\theta_{\rm exp})^2}{2\sigma_\theta^2}\right). \tag{6.2}$$

where $\theta_{\rm exp}$ and σ_θ are the Cherenkov opening angle expected from the charge within the cone and its resolution, respectively. ${\rm PE}(\theta)$ is the angular distribution of the observed charge as a function of the opening angle θ from the particle direction as shown in Figure 6.1. The ring edge $\theta_{\rm edge}$ is determined to satisfy the following two conditions :

$$\theta_{\rm edge} > \theta_{\rm peak} \tag{6.3}$$

$$\left.\frac{d^2{\rm PE}(\theta)}{d^2\theta}\right|_{\theta_{\rm edge}} = 0 \tag{6.4}$$

where $\theta_{\rm peak}$ is the opening angle where ${\rm PE}(\theta)$ takes maximum.

The estimator $Q(\theta_{\rm edge})$ is calculated changing the particle direction around the initial direction estimated by the point fit. The direction of the ring and the ring edge are determined to maximize the estimator $Q(\theta_{\rm edge})$.

TDC-Fit

In the last step of the vertex fitting, the vertex position is more precisely determined by the TDC-fit. The track of a charged particle and the scattered Cherenkov photons are taken into account using the fitted direction by the ring edge search.

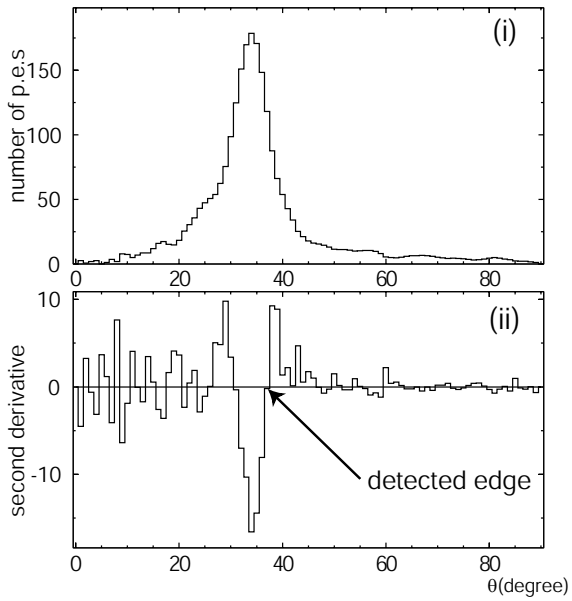

Figure 6.1: The typical PE(θ) distribution (top) and its second derivative (bottom) for a single ring event as a function of Cherenkov opening angle.

The track of the charged particle is considered for the TOF-subtracted timing calculation for PMTs inside the Cherenkov ring cone as follows;

$$t_i = t_i^0 - \frac{1}{c}\left|\vec{X}_i - \vec{O}\right| - \frac{n}{c}\left|\vec{P}_i - \vec{X}_i\right| \tag{6.5}$$

where $\vec{O}$ is the vertex position, $\vec{X}_i$ is the position at which Cherenkov photons are emitted toward the i-th PMT, n is the refractive index of water, $\vec{P}_i$ is the position and t_i^0 is the hit timing of the i-th PMT.

The TDC-fit consists of two different estimators, G_I and G_O. G_I is the estimator for the hit PMTs inside the Cherenkov ring cone. The definition of G_I is almost same as Equation (6.1), but the charge dependent timing resolution is considered. The other estimator, G_O , is for the hit PMTs outside the Cherenkov ring cone. If the TOF-subtracted timing is later than t_0 , the contribution from the scattered photons is considered in G_O. The total estimator of TDC-fit is obtained by;

$$G_T = \frac{G_I + G_O}{\sum_i \frac{1}{\sigma_i^2}} \tag{6.6}$$

The vertex position and the ring direction are determined to maximize the G_T.

Figure 6.2 shows the distance between the true vertex and the reconstructed vertex for the free proton decay MC ($p \to e^+\pi^0$). The resolutions of the TDC-fit for the free proton decay MC samples were estimated to be 18.1 (20.1) cm in SK-I and SK-II, respectively. For the atmospheric neutrino MC samples, the resolutions were estimated to be 62 cm (85 cm) for the fully contained multi-ring μ-like samples in SK-I (SK-II). For only single ring events, the vertex will be re-fitted more precisely using the Cherenkov ring pattern after the particle identification. However, that can not be applied for multi-ring events and not used for this analysis.

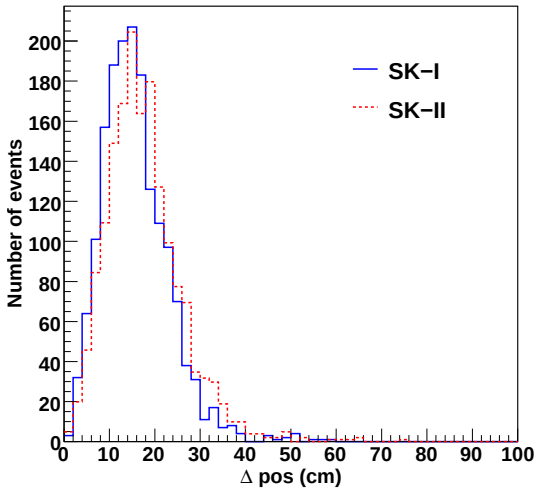

Figure 6.2: Distance between the true vertex and the reconstructed vertex for the free proton decay $p \to e^+\pi^0$ MC for SK-I (solid) and SK-II (dashed).

6.2 Ring Counting

Once the event vertex and the dominant Cherenkov ring are found, a ring counting algorithm is applied to search for any additional Cherenkov rings in the event.

Ring Candidate Search

Cherenkov ring candidates are searched by an algorithm using a Hough transformation [114]. The basic concept to find additional possible rings are illustrated in Figure 6.3. The shaded circle in this figure represents the Cherenkov ring image projected to a plane perpendicular to the particle direction. Hit PMTs are picked up, and virtual circles (dashed line) centered on the position of the hit PMT are drawn with 42° half angle. As a result of this procedure, the direction of a Cherenkov ring is identified as the intersection point of these virtual circles. In practice, instead of drawing virtual circles, an expected charge distribution function $f(\theta)$ is mapped on a polar coordinate plane (Θ, Φ) for each hit PMT. It is weighted by the observed charge distribution. As a result of this Hough transformation method, ring center candidates are visible as the peaks of charge on the map as shown in Figure 6.4.

Ring Candidate Test

The ring candidates found by the Hough transformation method are tested by a log likelihood method. When N rings are already found in the event, whether the $(N+1)$-th ring candidate really exists or not is tested.

The likelihood for the ring counting is calculated as;

$$F = \sum_{i}^{5} \left\{ \log \left[(P_i)_{N+1} \right] - \log \left[(P_i)_N \right] \right\} \tag{6.7}$$

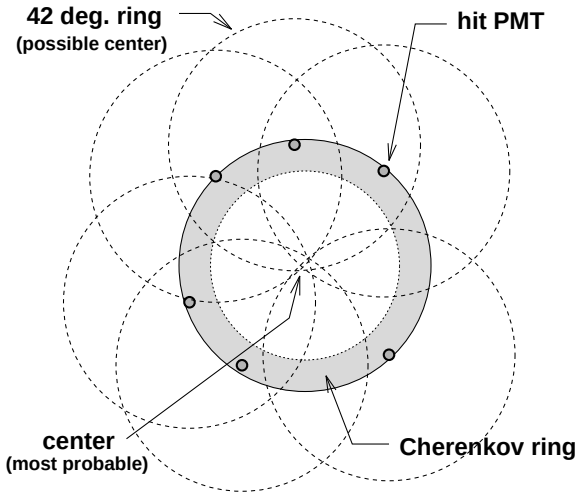

Figure 6.3: A basic idea of finding ring candidates. By drawing rings around the hit PMT with Cherenkov opening angle of 42 ° from the vertex, the center of the actual Cherenkov ring can be identified.

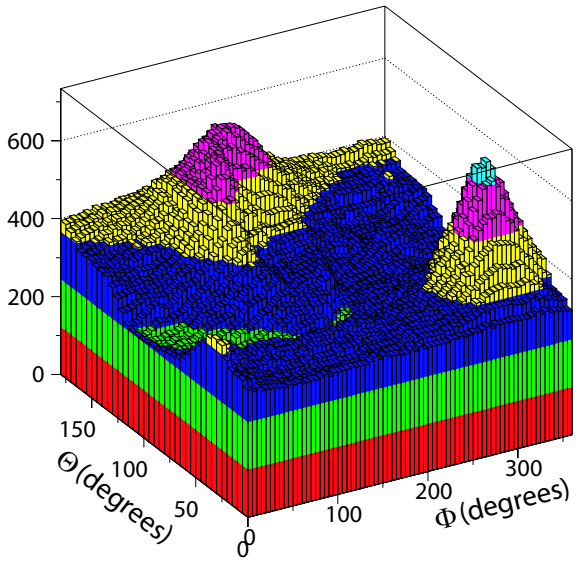

Figure 6.4: A typical charge map by the Hough transformation on the polar coordinate for a two ring event. The two peaks in the figure are the directions for the candidate Cherenkov rings.

where P_i is the probability density function for i-th evaluation function, and P_{N+1} and P_N are the probability for $(N+1)$-ring and N-ring events. The evaluation functions are defined by the following quantities;

- the difference $L(N+1) - L(N)$,
- the average of the expected charge from the $(N+1)$ ring near the edges of the Cherenkov rings,
- the average of the expected charge outside the $(N+1)$ ring,
- the residual charge from the expectation from N rings,
- the difference of charge between the peak of a candidate ring and the average of inside and outside the ring,

where $L(N) = \sum_i \log\left(prob\left(q_i^{\rm obs}, \sum_{n=1}^{N} \alpha_n \cdot q_{i,n}^{\rm exp}\right)\right)$ and $prob(q_i^{\rm obs}, q_i^{\rm exp})$ is the probability to detect $q_i^{\rm obs}$ when $q_i^{\rm exp}$ is expected.

The probability density functions for the evaluation functions were determined using the atmospheric neutrino MC samples.

Figure 6.5 shows the ring counting likelihood distributions for the data and the atmospheric neutrino MC. The efficiency for identifying ν_μ charged current quasi-elastic scattering events with the visible energy below 1.33 GeV as a single-ring event was 96% (97%) for SK-I (SK-II).

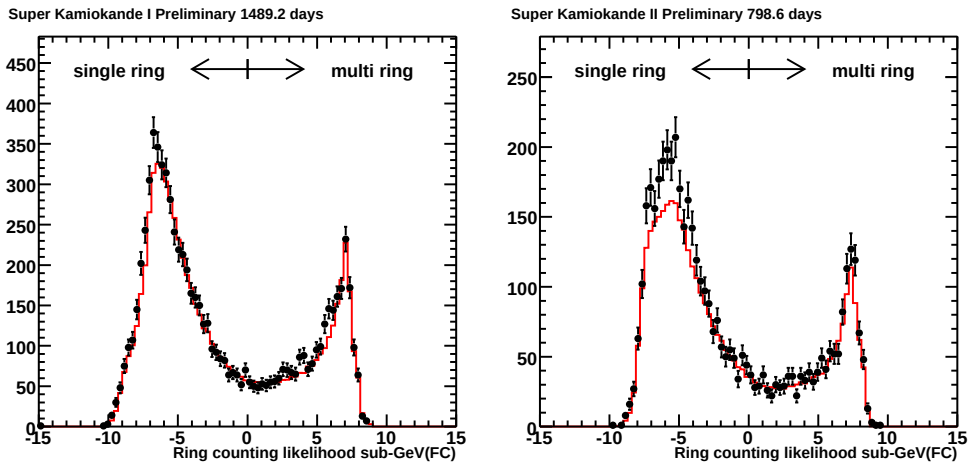

Figure 6.5: The ring counting likelihood distributions for fully contained events of the data (points) and the atmospheric neutrino MC (solid line) assuming 2-flavor $\nu_\mu \leftrightarrow \nu_\tau$ oscillation assumed with $(\sin^2 2\theta, \Delta m^2) = (1.00, 2.5 \times 10^{-3}\mathrm{eV}^2)$ for SK-I (left) and SK-II (right). Events with the visible energy below 1.33 GeV are filled in the figures.

6.3 Particle Identification

A particle identification (PID) program is applied to classify the Cherenkov rings into two types: a showering type (e-like) or a non-showering type (μ-like). Due to the electromagnetic

shower and multiple scattering, electrons or gamma-rays produce e-like rings, which give diffused ring patterns. Non-showering (μ-like) rings are produced by muons or charged pions and have sharper ring edges. Figure 6.6 shows the typical event displays of electron and muon neutrino MC events with a momentum of 1 GeV/c. In addition, the Cherenkov rings from electrons and gamma-rays have the Cherenkov opening angle of 42 °, but the Cherenkov rings from muons or charged pions can have smaller angles if they are not highly relativistic ($\beta = v/c < 1$) and when they lose energy. The PID algorithm exploits these differences in the patterns and the opening angles of the Cherenkov rings. The details of PID are described below.

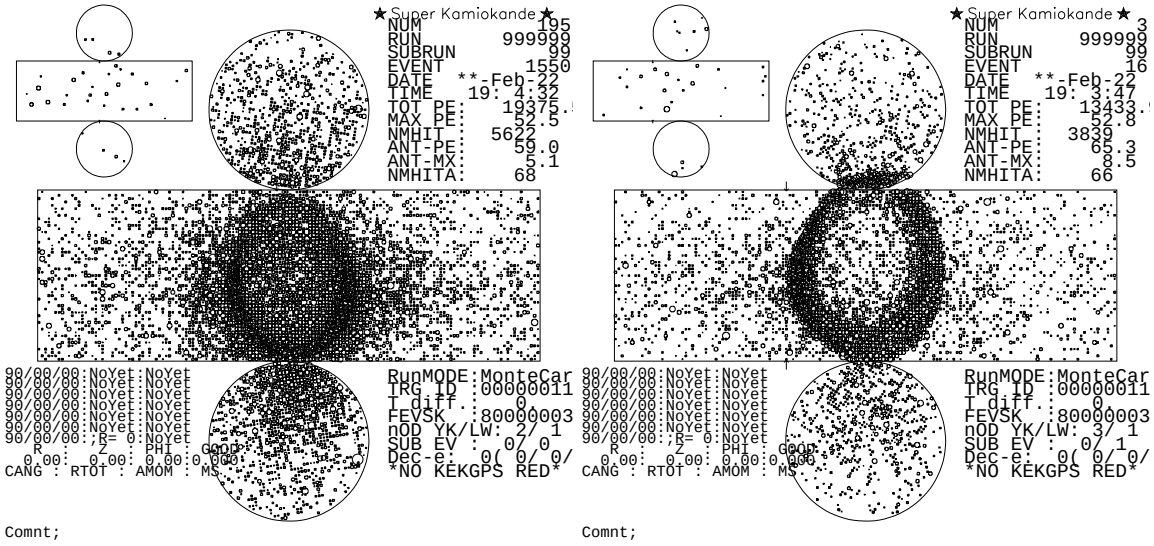

Figure 6.6: Event display of single-ring electron (left) and single-ring muon (right) neutrino MC event. Each small circle on the figure represents a hit ID PMT, and the size of a circle corresponds to the number of photoelectrons detected. An electron event gives diffused ring pattern, and a muon event has a sharp ring edge.

Expected Charge Distributions

The first step of the PID is to calculate the expected p.e.s in each PMT from an electron or a muon. The expected p.e. distributions in the i-th PMT from an electron and a muon are calculated as follows;

$$q_i^{\rm exp}(e) = \alpha_e \times Q^{\rm exp}(p_e, \theta_i) \times \left(\frac{R}{r_i}\right)^{1.5} \times \frac{1}{\exp(r_i/L)} \times f(\Theta_i) + q_i^{\rm scatt}, \tag{6.8}$$

$$q_i^{\rm exp}(\mu) = \left(\alpha_\mu \times \frac{\sin^2\theta_{x_i}}{r_i\left(\sin\theta_{x_i} + r_i \cdot \frac{d\theta}{dx}\big|_{x=x_i}\right)} + q_i^{\rm knock}\right) \times \frac{1}{\exp(r_i/L)} \times f(\Theta_i) + q_i^{\rm scatt} \tag{6.9}$$

where

α_e, α_μ : normalization factor

r_i : distance from the vertex to the i-th PMT

θ_i : opening angle between the i-th PMT direction and the ring direction

L : light attenuation length in water

$f(\Theta_i)$: correction for the PMT acceptance as a function of the photon incidence angle Θ_i

R : radius of the virtual sphere (16.9 m)

$Q^{\rm exp}(p_e, \theta_i)$: expected p.e. distribution from an electron as a function of the opening angle and the electron momentum

x : track length of the muon

x_i : track length of the muon at which Cherenkov photons are emitted toward the i-th PMT

$q_i^{\rm scatt}$ ($q_i^{\rm knock}$) : expected p.e.s for the i-th PMT from scattered photons (knock-on electrons)

θ (θ_{x_i}) : Cherenkov opening angle of the muon traveling at x (x_i)

The expected p.e. $Q^{\rm exp}(p_e, \theta_i)$ distribution for electron was obtained by the MC simulation. In addition to the direct photons, the expectation from scattered photons are also considered by $q_i^{\rm scatt}$.

In the case of a muon, the expected p.e. distributions are analytically calculated. The term $\sin^2\theta$ comes from the Cherenkov angle dependence of the Cherenkov light intensity. The term $r(\sin\theta + r(d\theta/dx))$ comes from the area where Cherenkov photons are emitted to.

Estimation of Particle Types

The definition of likelihood for the n-th ring is expressed by:

$$L_n(e \text{ or } \mu) = \prod_{\theta_i < (1.5\times\theta_c)} prob\left(q_i^{\rm obs} \ , \ q_{i,n}^{\rm exp}(e \text{ or } \mu) + \sum_{n' \neq n} q_{i,n'}^{\rm exp} \right) \tag{6.10}$$

where the product is made over the PMTs inside the n-th ring. $q_i^{\rm obs}$ is the observed p.e.s in the i-th PMT, $q_{i,n}^{\rm exp}(e \text{ or } \mu)$ is the expected p.e.s from the n-th ring assuming an electron or a muon (Equation (6.8), (6.9)) and $q_{i,n'}^{\rm exp}$ are the expected p.e.s from the n'-th ring. The function $prob(q_i^{\rm obs}, q_i^{\rm exp})$ gives the probability to detect $q_i^{\rm obs}$ in the i-th PMT when $q_i^{\rm exp}$ is expected. The $q_{i,n}^{\rm exp}(e)$ and $q_{i,n}^{\rm exp}(\mu)$ are optimized by changing the direction and the opening angle of the n-th ring to give the maximum likelihood value.

In order to combine with another estimator which uses the Cherenkov opening angle, the likelihood for the ring pattern is translated into a χ^2 parameter :

$$\chi_n^2(e \text{ or } \mu) = -2 \log L_n(e \text{ or } \mu) + \text{constant} \tag{6.11}$$

The probability from the ring pattern is given by:

$$P_n^{\rm pattern}(e \text{ or } \mu) = \exp\left(- \frac{\left(\chi_n^2(e \text{ or } \mu) - \min\left[\chi_n^2(e)\,,\, \chi_n^2(\mu)\right] \right)^2}{2\,\sigma^2_{\chi_n^2}} \right) \tag{6.12}$$

The resolution of the χ^2 distribution is approximated by $\sigma_{\chi_n^2} = \sqrt{2N}$, where N is the number of PMTs used in the calculation.

The probability from the Cherenkov opening angle is given by :

$$P_n^{\rm angle}(e \text{ or } \mu) = \exp\left(- \frac{\left(\theta_n^{\rm obs} - \theta_n^{\rm exp}(e \text{ or } \mu) \right)^2}{2\,(\delta\theta_n)^2} \right) \tag{6.13}$$

where $\theta_n^{\rm obs}$ and $\delta\theta_n$ are the reconstructed opening angle of the n-th ring and the fitting error, respectively. $\theta_n^{\rm exp}(e \text{ or } \mu)$ is the expected opening angle of the n-th ring, which is estimated from the reconstructed momentum assuming an electron or a muon.

This PID algorithm with $P_n^{\rm pattern}(e \text{ or } \mu)$ and $P_n^{\rm angle}(e \text{ or } \mu)$ was checked by a beam test experiment at KEK [115]. Two types of PID probability functions were used for the nucleon decay searches. One is the probability using only the ring pattern, and the other is defined as the product of the probabilities from the ring pattern and the opening angle.

$$P_1(e,\mu) = P^{\,\rm pattern}(e,\mu) \tag{6.14}$$

$$P_2(e,\mu) = P^{\,\rm pattern}(e,\mu) \times P^{\,\rm angle}(e,\mu) \tag{6.15}$$

For the nucleon decay modes generating low momentum μ and/or $\pi^{\pm}$, the PID probability with the opening angle was used in order to improve the PID efficiency.

Figure 6.7 shows the distributions of the PID likelihood, $P_{\rm PID} \equiv \sqrt{-\log P_2(\mu)} - \sqrt{-\log P_2(e)}$, for single-ring events. The mis-identification probabilities were estimated to be 0.8% (0.7%) and 0.7% (1.0%) for the fully contained single-ring ν_e and ν_μ using charged current quasi-elastic scattering events with the visible energy below 1.33 GeV for SK-I (SK-II). For the free proton decay MC samples, the mis-identification probabilities were estimated to be 3.3% (3.4%) and 4.8% (5.4%) for the $p \to e^+\pi^0$ and $p \to \mu^+\pi^0$ in SK-I (SK-II).

6.4 Momentum Determination

The momentum of each particle is estimated by the observed p.e.s inside the Cherenkov cone with a half angle of 70°. The number of observed p.e.s in each PMT is corrected for the light attenuation in water and the acceptance of the PMT. The integrated charge for each ring, called RTOT, is corrected as follows;

$$\mathrm{RTOT}_n = \frac{G_{\rm MC}}{G_{\rm data}} \left[\alpha \times \sum_{\substack{\theta_{i,n}<70^\circ \\ -50{\rm nsec}<t_i<250{\rm nsec}}} \left(q_{i,n}^{\rm obs} \times \exp\left(\frac{r_i}{L}\right) \times \frac{\cos\Theta_i}{f(\Theta_i)} \right) - \sum_{\theta_{i,n}<70^\circ} S_i \right]. \tag{6.16}$$

where

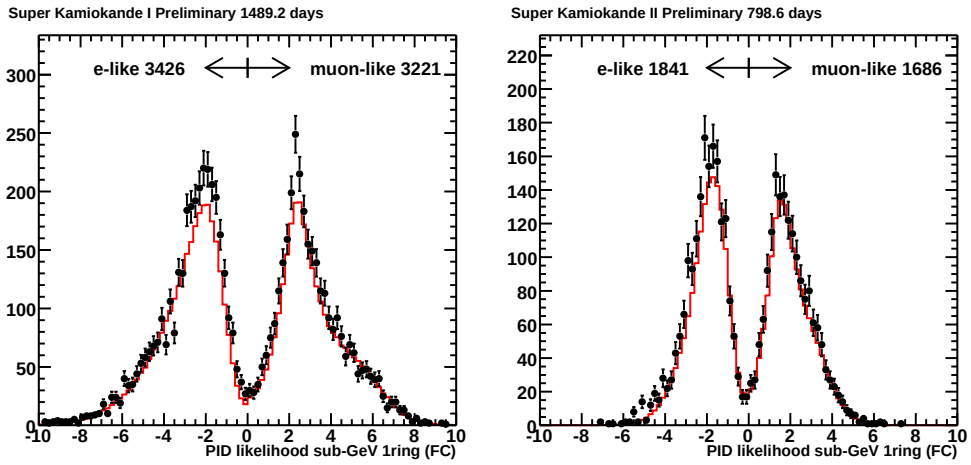

Figure 6.7: The PID likelihood distributions for fully contained events of the data (points) and the atmospheric neutrino MC (solid line) assuming 2-flavor $\nu_\mu \leftrightarrow \nu_\tau$ oscillation assumed with $(\sin^2 2\theta, \Delta m^2) = (1.00, 2.5 \times 10^{-3}\mathrm{eV}^2)$ for SK-I (left) and SK-II (right). Single ring events with the visible energy below 1.33 GeV are filled in figures.

α	:	normalization factor,
$G_{\mathrm{data}}\,, G_{\mathrm{MC}}$	:	the relative PMT gain parameter for the data and the MC,
$\theta_{i,n}$	:	the opening angle between the n-th ring direction and the i-th PMT direction,
t_i	:	the TOF subtracted hit timing of the i-th PMT position,
L	:	the light attenuation length in water,
r_i	:	the distance from the vertex position to the i-th PMT,
$f(\Theta_i)$	:	the correction function for the PMT acceptance as a function of the photon incidence angle Θ_i,
S_i	:	expected p.e.s for the i-th PMT from scattered photons.

The summation is restricted inside the time window from -50 nsec to +250 nsec around the peak of the TOF subtracted hit timing distribution to reject the effect from muon decay electrons.

As described in Chapter 7, the energy scale stability of the detector was tested by the mean reconstructed energy of stopping cosmic ray muons and their decay electrons. It varied within $\pm 0.88\%$ (± 0.55 %) over the SK-I (SK-II) period. The absolute energy scales for SK-I and SK-II were separately adjusted by observed p.e.s of penetrating cosmic ray muons. The scale was checked by many calibration data such as stopping cosmic ray muons, their Michel electrons, and the invariant mass of π^0s produced in atmospheric neutrino interactions. From comparisons of these sources and MC simulation, the absolute calibration error was estimated to be less than $\pm 0.74\%$ ($\pm 1.60\%$) for SK-I (SK-II) period.

Ring Separation

In order to determine the momentum for individual rings for multi-ring events, the observed p.e.s in hit PMTs are separated into the contribution from each ring. The separation of the observed p.e.s is carried out based on the expected p.e. distribution from each ring.

In the nucleon decay signals studied in this thesis, a charged lepton and a meson are generally back-to-back. The expected charge in the backward region can directly affect the charge separation for the other ring in that case. Therefore, the expected charge distribution, especially in the backward region, should be relatively more precise for the charge separation than the other algorithms.

However, the expected charge distribution used in the old ring separation did not reproduce well the simulated charge distribution in SK-II as shown in Figure 6.8. That resulted in the error of the total invariant mass for nucleon decay events. Figure 6.9 shows the total invariant mass distribution by the old ring separation for the $p \to e^+\pi^0$ MC for free proton decay events in SK-I and SK-II. The total invariant mass in SK-II was about 20 MeV/c^2 lower than that in SK-I. Therefore, the expected charge distribution for the ring separation was improved by introducing new corrections for the nucleon decay searches in this thesis. It is corrected by the amount of scattered Cherenkov light in water, reflected light on PMT surface, and the vertex position shift due to the γ's conversion length. The expected charge distribution for the charge separation is calculated as;

$$q_i^{\rm exp}(e,\mu) = Q_{e,\mu}^{\rm exp}(p,\theta_i) \times \exp\left(\frac{R}{L^{\rm MC}}\right) \times \frac{1}{\exp(r_i/L)} \times f(\Theta_i) + q_i^{\rm scatt} \tag{6.17}$$

where

- r_i : distance from the vertex to the i-th PMT,
- θ_i : opening angle between the i-th PMT direction and the ring direction,
- L : light attenuation length in water,
- $L^{\rm MC}$: light attenuation length in water in MC,
- $f(\Theta_i)$: correction for the PMT acceptance as a function of the photon incidence angle Θ_i,
- R : radius of the virtual sphere (16.9 m),
- $Q_{e,\mu}^{\rm exp}(p,\theta_i)$: expected p.e. distribution for e and μ on the virtual sphere as a function of the momentum and the opening angle,
- $q_i^{\rm scatt}$: expected p.e.s for the i-th PMT from scattered photons.

The expected p.e. $Q^{\rm exp}(p,\theta_i)$ distribution for muon was also obtained by the MC simulation. For e-like rings except for the most energetic ring, the γ's conversion length are taken into account for the distance calculation. The effect of the reflection on the PMT surface is considered as;

$$q_i^{\rm exp}(e,\mu) \to \alpha \times \left(q_i^{\rm exp}(e,\mu) + \sum_{j\neq i} \beta_{ij} \cdot q_j^{\rm exp}(e,\mu) \right) \tag{6.18}$$

where α is a normalization factor, and β_{ij} is the PMT reflection factor from the j-th PMT to the i-th PMT calculated as;

$$\beta_{ij} = \beta \times f(\Theta_{ij}) \times \exp\left(-\frac{r_{ij}}{L}\right) \tag{6.19}$$

where r_{ij} is the distance from the i-th PMT to j-th PMT, Θ_{ij} is the photon incidence angle to the i-th PMT from the j-th PMT, and β is the PMT reflection factor. The constant β was determined by the MC simulation and common in the SK-I and SK-II event reconstructions. After applying these corrections, the expected charge distribution agrees well with the simulated charge distribution also in SK-II as shown in Figure 6.8.

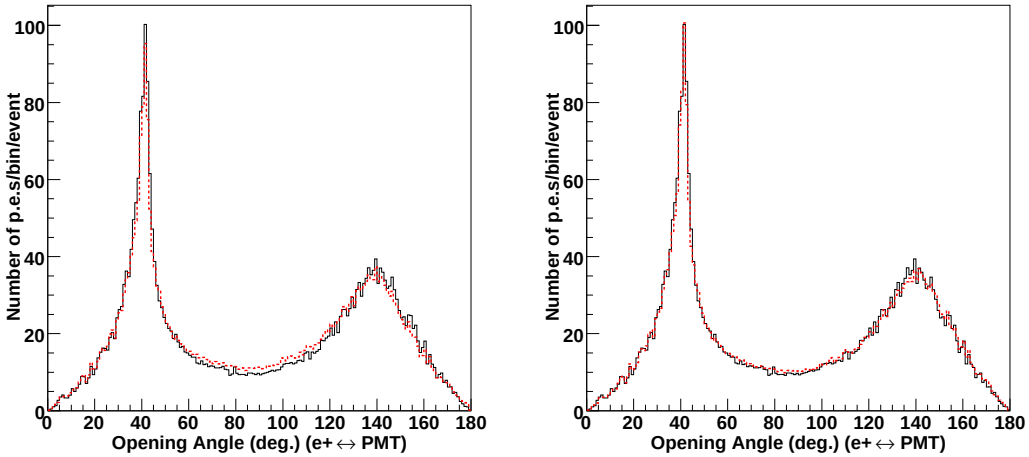

Figure 6.8: The angular distribution of detected charge as a function of opening angle between a positron direction and each PMT for the $p \to e^+\pi^0$ MC in SK-II. The solid and dashed lines show the observed charge in the MC and the expected charge used in the ring separation, respectively. The old and new expected charge are shown in the left and right figures, respectively. The forward and backward peak consist of Cherenkov rings from a positron and two γ-rays, respectively.

The observed p.e.s for each PMT are estimated by maximizing the following likelihood function L;

$$L = \sum_{\theta_{i',n}<70^\circ} \log\left(prob\left(q_{i'}, \sum_{n'} \alpha_{n'} \cdot q^{\rm exp}_{i'.n'}\right)\right) \tag{6.20}$$

where $q_{i'}$ is the observed p.e.s in the i'-th PMT and $q^{\rm exp}_{i',n'}$ is the expected p.e.s in the i'-th PMT from the n'-th ring, $prob(q^{\rm obs}_i, q^{\rm exp}_i)$ is the function giving the probability to detect $q^{\rm obs}_i$ in the i-th PMT when $q^{\rm exp}_i$ is expected, and $\alpha_{n'}$ is the scaling and optimization parameter for each ring. The optimization parameter α_n is selected to reproduce the observed charge distribution by scaling the expected charge pattern $q^{\rm exp}_{i',n'}$ of each ring.

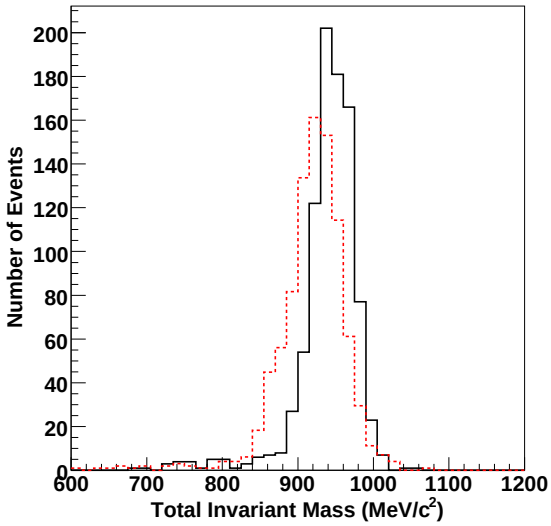

Figure 6.9: The total invariant mass distribution using the reconstructed momenta by the old ring separation for the $p \to e^+\pi^0$ MC. Only the free proton decay events with three rings are filled in the figure for SK-I(solid line) and SK-II(dashed line).

The observed p.e.s in the i-th PMT from the n-th ring are obtained as;

$$q_{i,n}^{\rm obs} = q_i^{\rm obs} \times \frac{\alpha_n \cdot q_{i,n}^{\rm exp}}{\sum_{n'} \alpha_{n'} \cdot q_{i,n'}^{\rm exp}} \tag{6.21}$$

using the best optimized parameter α_n maximizing L. Figure 6.11 shows the example of the charge separation for the $p \to e^+\pi^0$ MC event with three rings.

Figure 6.10 shows the reconstructed momentum distributions for positrons in $p \to e^+\pi^0$ and for muons in $p \to \mu^+\pi^0$. The resolutions (1σ) for the positron and the muon were estimated to be 4.9% (6.0%) and 2.8% (4.1%) in SK-I (SK-II), respectively. The mean reconstructed momenta in SK-I and SK-II agreed within 1%. The total invariant mass distributions in SK-I and SK-II also agreed with each other as shown in Figure 9.9. The common separation algorithm works well with the different PMT densities.

Charged Pion Momentum

Charged pions suffer from interactions with nucleons in water. The charged pion momentum is hard to be reconstructed only by the observed p.e.s. Therefore, the charged pion momentum is reconstructed using both the observed p.e.s and the Cherenkov opening angle to maximize the likelihood defined as follows;

$$L_\pi = \log\left(\frac{1}{\sigma_q}\exp\left(-\frac{\left(Q_n(p_\pi) - Q_n^{\rm obs}\right)^2}{2\sigma_q^2}\right) \times \frac{1}{\sigma_\theta}\exp\left(-\frac{\left(\theta_n(p_\pi) - \theta_n^{\rm obs}\right)^2}{2\sigma_\theta^2}\right)\right) \tag{6.22}$$

where

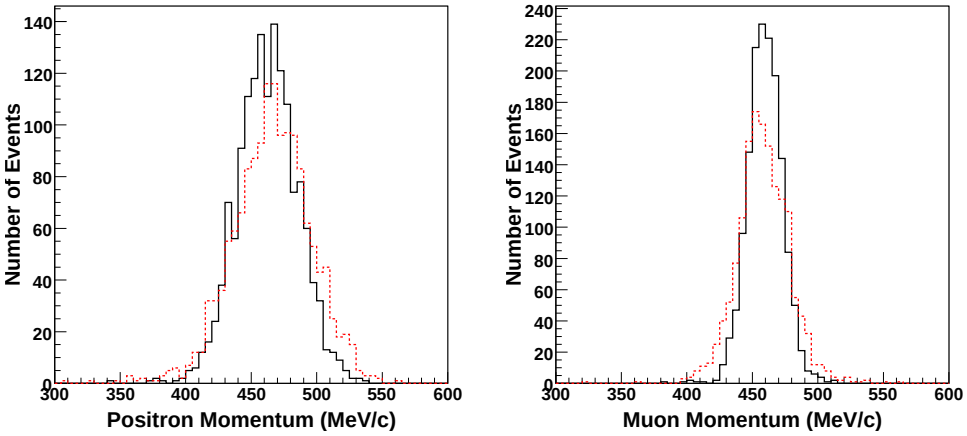

Figure 6.10: The reconstructed momentum distributions for positrons in $p \to e^+\pi^0$ (left) and for muons in $p \to \mu^+\pi^0$ (right) in SK-I (solid) and SK-II (dashed). Only the free proton decay events are filled in the figures

p_π	:	the charged pion momentum,
$Q_n(p_\pi)$	:	the expected p.e.s for n-th ring as a function of the pion momentum,
$\theta_n(p_\pi)$	:	the expected opening angle for n-th ring as a function of the pion momentum,
$Q_n^{\rm obs}$	:	the observed p.e.s,
$\theta_n^{\rm obs}$	:	the observed opening angle,
σ_q	:	the error for the expected p.e.s,
σ_θ	:	the error for the expected opening angle.

The functions of the expected p.e.s $Q_n(p_\pi)$ were determined by the MC simulation.

Figure 6.12 shows the charged pion momentum distributions for the $n \to e^+\pi^-$ MC and the atmospheric neutrino MC and the data. In order to extract charged pion rings, only not most energetic and non-shower type rings in multi-ring events are filled in the right figure. The resolution for the charged pion momentum in the $n \to e^+\pi^-$ MC was estimated to be 9.2% (9.7%) for SK-I (SK-II).

6.5 Ring Number Correction

If the number of rings are larger than 2, the ring number correction is applied.

If one of the reconstructed rings has very small momentum or is overlapped with another much energetic ring, such a ring is rejected by the ring number correction as a mis-fit ring.

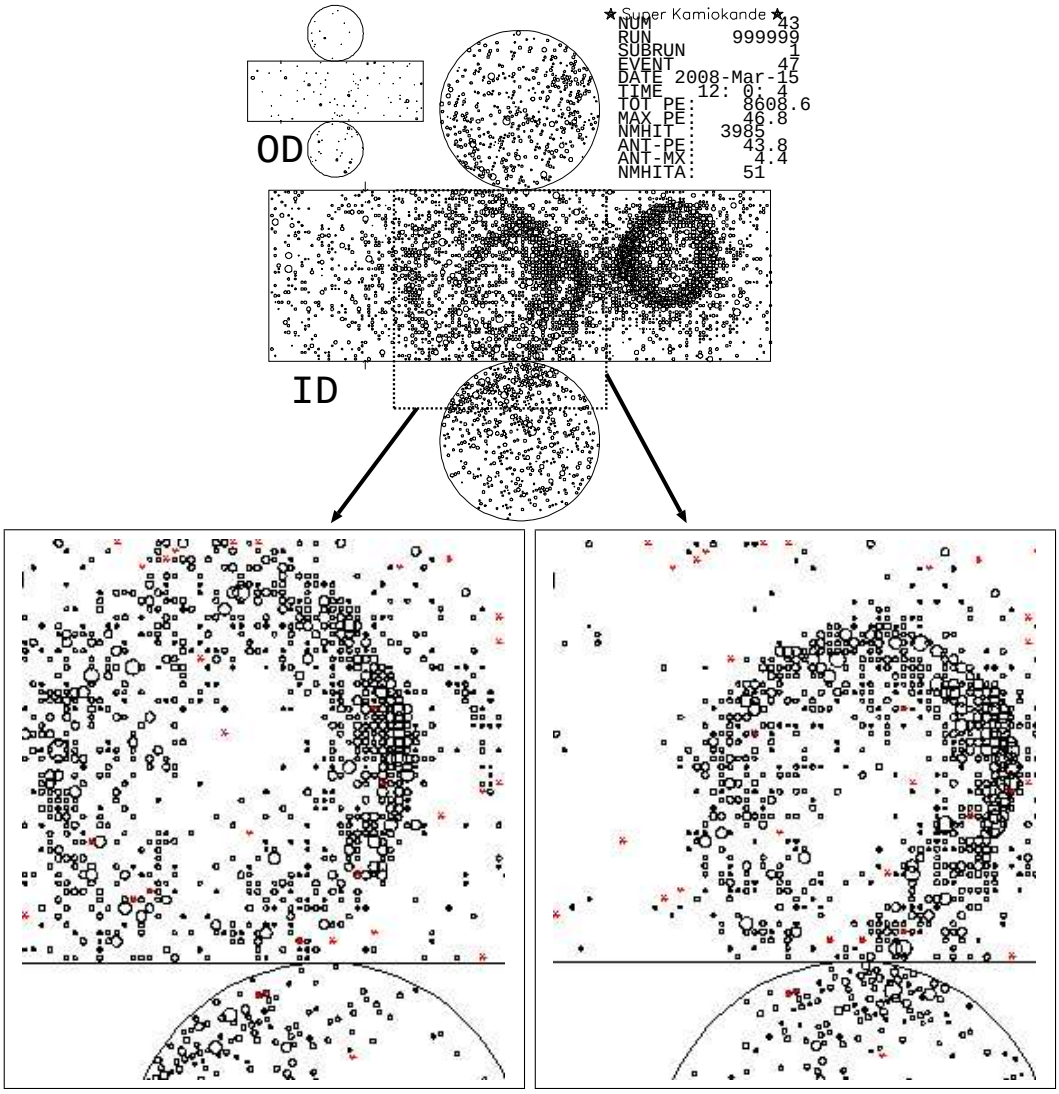

Figure 6.11: Example of the charge separation for the $p \to e^+\pi^0$ MC event with three rings in SK-I. The top figure shows the charge distribution before the separation. The bottom two figures show the divided charge distributions for the overlapped two rings. The overlapped charge from the two ring for each PMT is correctly divided by the ring separation algorithm.

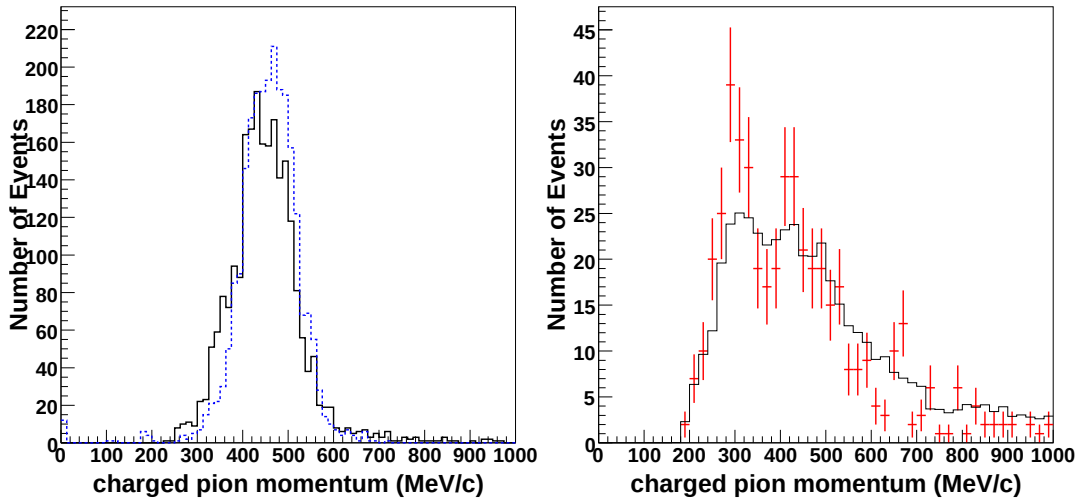

Figure 6.12: The charged pion momentum distributions for the $n \rightarrow e^{+}\pi^{-}$ MC (left) and the atmospheric neutrino MC (solid line in the right) and the data (points with errors in the right). In the left figure, the solid line and the dashed line show the reconstructed and true pion momentum distributions, respectively. In the right figure, the reconstructed momenta only for not most energetic, non-shower type rings in multi-ring events are filled in order to extract charged pion rings.

6.6 Decay Electron Finding

In this section, the detection method of electrons from muon decays following the primary events is described. There are three types of observed decay electrons :

- sub-event type
  Decay electrons observed as a separate event (sub-event).
- primary-event type
  Decay electrons observed in the same event as primary event.
- split type
  Decay electrons occurred around the end of event timing window. The event is recorded separately in the primary event and the sub-event.

For sub-event type events, the following criteria are required :

(1) The time interval from a primary event(Δt) is $< 20\,\mu$sec.

(2) The total number of hit PMTs is greater than 50 (25 for SK-II).

(3) The goodness of vertex fit is greater than 0.5.

(4) The number of hit PMTs in a 50 nsec time window is greater than 30 (15 for SK-II).

(5) The total number of photoelectrons is less than 2000 (1000 for SK-II).

(6) The number of hit PMTs in a 50 nsec time window (N_{50}) is greater than 60 (30 for SK-II).

For primary-event type decays, another peak after the primary event is searched with requirement more than 20 hits in 30 nsec window above the background level. Additional conditions for decay electrons are as follows :

(7) The number of hit PMT in a 30 nsec time window is greater than 40 (20 for SK-II). (for primary-event type and split type)

(8) $0.1\,\mu\text{sec} < \Delta t < 0.8\,\mu\text{sec}$ or $1.2\,\mu\text{sec} < \Delta t < 20\,\mu\text{sec}$ (for all types)

N_{50}=60 (30 for SK-II) corresponds to about 11 MeV of electron energy. Criterion (1) rejects the gamma emission from μ^- captured on ^{16}O nuclei. Criterion (8) rejects the decays in the inefficient time interval around 1 μsec. The efficiency of detecting these electrons are 80 % and 63 % for μ^+ and μ^-, respectively.

Chapter 7

Energy Scale

The most distinguished characteristics of nucleon decay signals are that the total invariant mass and the total momentum are consistent with source nucleons. Thus, a precise momentum determination is crucial for nucleon decay searches.

The absolute energy scale were checked by four kinds of methods ranging from a few ten MeV/c to about 10 GeV/c using independent calibration sources; decay electrons from stopping muons, π^0 events and low and high energy stopping muons. The long term stability monitoring and the detector uniformity checking for the energy scale were also performed.

7.1 Decay Electron Energy Spectrum

Many electron events produced by the decay of cosmic ray muons are observed in Super-Kamiokande. The energy spectrum of these electrons are well known and used to determine the absolute energy scale by comparing the the spectrum between the observed data and the Monte Carlo (MC) simulation.

The event selection criteria for decay electron events are as follows;

(1) the time interval from a stopping muon event is 2.0 μsec to 8.0 μsec,

(2) the number of hit PMT in a 50 nsec time window is larger than 60 (30) for SK-I (SK-II),

(3) the goodness of the vertex fit is greater than 0.5,

(4) the vertex position is reconstructed more than 2m away from the ID wall.

The criterion (2) rejects $\sim$ 6 MeV γ-rays from μ^- captures on nucleons. Figure 7.1 shows the momentum spectra of decay electrons compared with the prediction from the MC simulation. In the MC simulation, the measured cosmic ray muon charge ratio μ^+/μ^- of 1.37 [116] was used and the effect of μ^- capture by nuclei was also considered. The mean values of the observed data agreed with the MC prediction within 0.6% (1.6%) for SK-I (SK-II).

7.2 π^0 Invariant Mass

The π^0 events produced in the interactions of the atmospheric neutrino were used for the energy scale calibration in the several hundred MeV energy range. Since the π^0 decays immediately into two γ-rays, the invariant mass of π^0 is obtained by the reconstructed momentum of

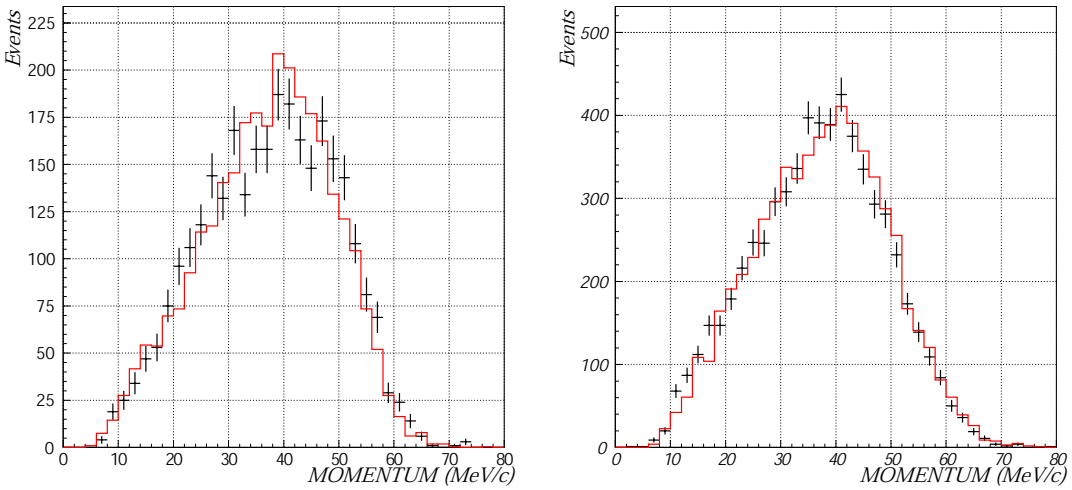

Figure 7.1: The momentum distributions of decay electrons of the observed data(bar) and the MC(line) for SK-I(left) and SK-II(right).

the two γ-rays ($P_{\gamma 1}$ and $P_{\gamma 2}$) and the opening angle θ as follows;

$$M_{\pi^0} = \sqrt{2P_{\gamma 1}P_{\gamma 2}\,(1-\cos\theta)}. \tag{7.1}$$

The π^0 events are selected from the fully contained data sample (see Chapter 5) by the following criteria:

(1) Two Cherenkov rings are recognized and both of them are identified as shower-type ring.

(2) Electrons from muon decay are not detected.

(3) The vertex position is reconstructed more than 2m away from the ID wall.

The criterion (2) rejects the contamination of $\pi^+\pi^0$ or $\mu^\pm\pi^0$ events. Figure 7.2 shows the invariant mass distribution of the π^0 events compared with the MC prediction. A peak from the π^0 is clearly observed around 135 MeV/c^2. The peak position of the data was 0.7% (1.3%) higher than that of the MC for SK-I (SK-II).

7.3 Low Energy Stopping Muons (Cherenkov Opening Angle)

The Cherenkov opening angle θ_C of charged particles is expressed as a function of their momentum as follows;

$$\cos\theta_C = \frac{1}{n\beta} = \frac{1}{n}\sqrt{1+\frac{m^2}{p^2}} \tag{7.2}$$

where n is the refractive index of water, $\beta = v/c$, and m and p are the mass and momentum of a charged particle, respectively. Since the Cherenkov opening angle has a large dependence

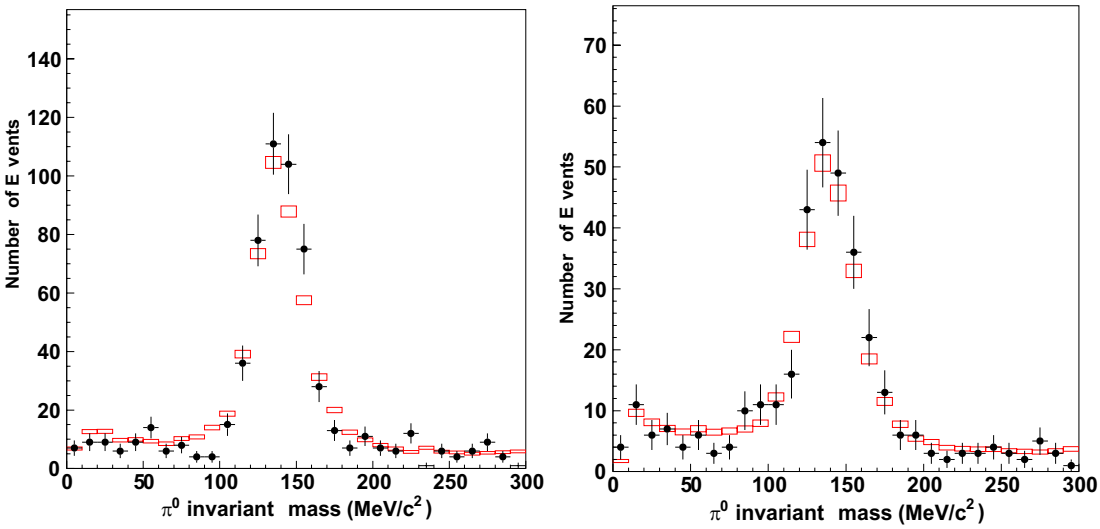

Figure 7.2: The invariant mass distributions of neutrino induced π^0 events of the observed data(dot) and the atmospheric neutrino MC (box) for SK-I (left) and SK-II (right).

on momentum especially for low energy stopping muons (< 400 MeV/c), their momenta can be estimated by measuring the Cherenkov opening angle. The systematic uncertainty of the momentum determination was checked by comparing the momentum estimated from the observed photoelectrons ($P_{p.e.}$) with the momentum derived from the Cherenkov opening angle (P_θ). Low momentum stopping muon events are selected by the following criteria:

(1) The total number of p.e.s in the ID is less than 1500 p.e.s for SK-I (750 p.e.s for SK-II).

(2) There is one cluster of hit PMTs in the OD.

(3) The entrance point is on the top wall.

(4) The direction is downward ($\cos\theta_{\rm zenith} > 0.9$).

(5) One decay electron is detected.

The criterion (1) approximately corresponds to the muon momentum of < 380 MeV/c. The criterion (2) requires an entrance point of a muon in the OD. The criteria (3) and (4) select the muon events which are straight down-going.

Figure 7.3 shows the scatter plots of the reconstructed Cherenkov opening angle and the momentum from the observed photoelectrons for the observed data and the MC simulation. The momentum dependence of the Cherenkov opening angle is seen in both figures. The energy scale of the data was compared with that of the MC simulation by the ratio $P_{p.e.}/P_\theta$. The averaged momentum ratio $P_{p.e.}/P_\theta$ for the data and the MC simulation are shown in Figure 7.4. The energy scales of the observed data and the MC agreed within 1.1% for SK-I and 1.3% for SK-II.

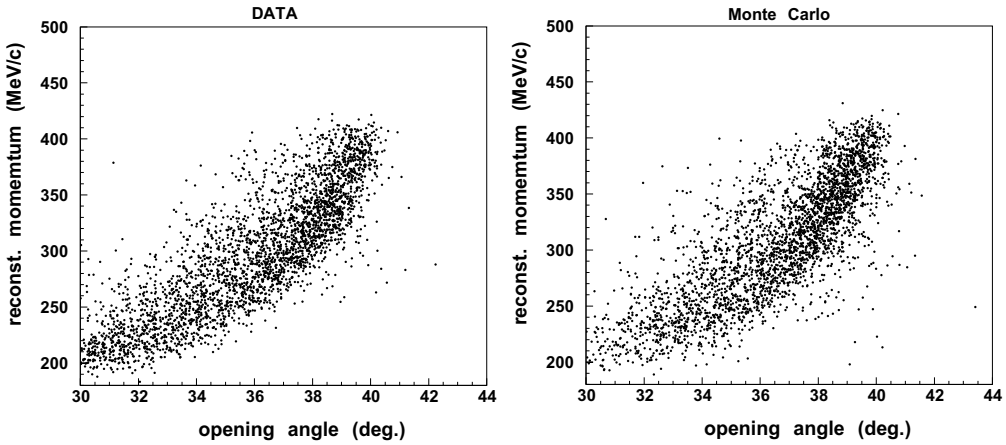

Figure 7.3: The scatter plots of the reconstructed Cherenkov opening angle and the reconstructed momentum from the observed photoelectrons for the data (left) and the MC simulation (right).

7.4 High Energy Stopping Muons (Track Length)

The momentum of high energy stopping muons can be estimated from its track length because the range of the muon track is well understood and approximately proportional to the momentum. Since the measurement of the muon range can be independent on the momentum measurement based on the observed photoelectrons, the estimated momentum from its range is used for checking the energy scale from 1 GeV/c to 10 GeV/c. Stopping muon events are selected by the following criteria:

(1) The entrance point is on the top wall.

(2) The direction is downward ($\cos_{\mathrm{zenith}>0.94}$).

(3) One decay electron is detected.

(4) The reconstructed range of muon track is greater than 7m.

The range of the muon is determined by the entrance position and the vertex position of the subsequent decay electron. Figure 7.5 shows the averaged value of the ratio momentum/range as a function of the range for the observed data and the MC simulation. The momentum loss per cm is about 2.3 MeV/c. The energy scale of the data and the MC simulation agreed within 0.7% (1.1%) for SK-I (SK-II).

7.5 Time Variation of Energy Scale

The stability of the energy scale was monitored by the stopping muon and the decay electron events. The time variation of the ratio (momentum/range) of stopping muons and the decay electron momentum are shown in Figures 7.6 and 7.7. The RMS of the energy scale variation was 0.83% (0.53%) for SK-I (SK-II).

7.6 Uniformity of Energy Scale

The detector non-uniformity of the energy scale can cause the error for the total momentum reconstruction, which is important information for nucleon decay searches. The uniformity of the detector was measured by the decay electron momentum from cosmic ray muons. They are good calibration sources to check the detector uniformity, because the vertex and the momentum distributions are almost uniform in the fiducial volume and in all directions, respectively. In order to avoid energy bias by muon polarization, only electrons whose direction is perpendicular to the parent muon direction are used. This condition is $-0.25 < \cos\Theta_{e\mu} < 0.25$, where $-0.25 < \cos\Theta_{e\mu} < 0.25$ is the opening angle between the electron and muon directions. Figure 7.8 shows the momentum of decay electrons for the MC normalized by the observed data as a function of the zenith angle of the electrons. The detector gain was uniform within $\pm 0.6\%$ for SK-I (SK-II).

7.7 Summary of the Energy Scale Calibration

Figure 7.9 shows the summary of the absolute energy calibration. The uncertainty of the energy scale was estimated to be less than 0.74% and 1.60% for the momentum range from a few ten MeV/c to about 10 GeV/c for SK-I and SK-II, respectively. Combined with the RMS of the time variation, the systematic error of the energy scale was estimated to be 1.1% (1.7%) for SK-I (SK-II).

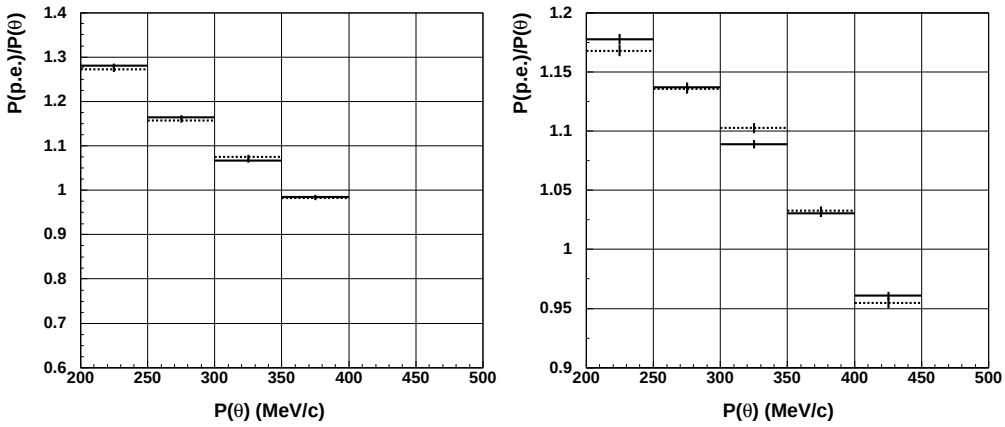

Figure 7.4: The ratio of the momentum by the observed photoelectrons to the momentum by the opening angle ($P_{p.e.}/P_\theta$) as a function of the momentum P_θ for the data (solid lines) and the MC simulation (dotted lines). The left and right figures show the ratio for SK-I and SK-II, respectively.

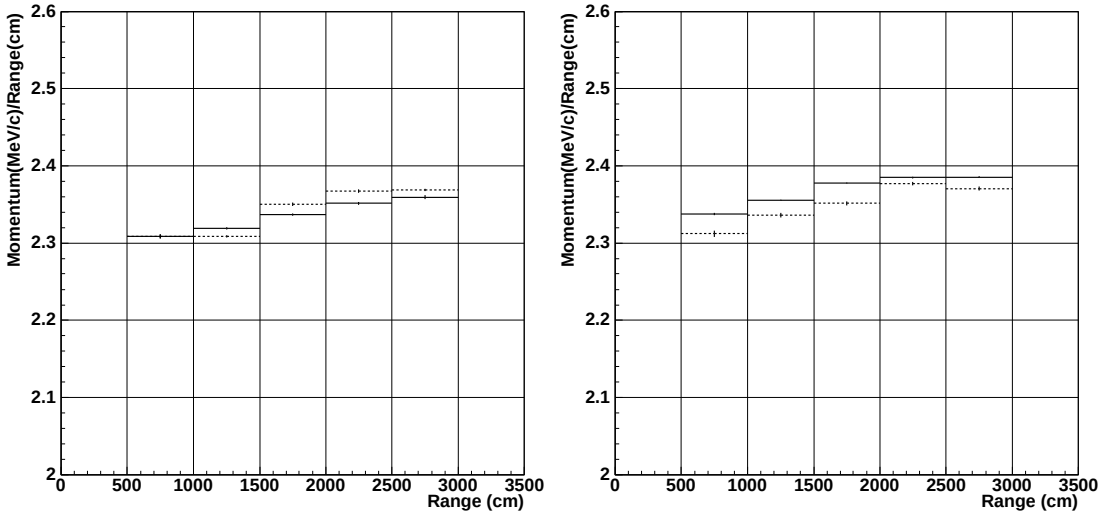

Figure 7.5: The ratio of the momentum to the range as a function of the range of stopping muon events for the data (solid lines) and the MC simulation (dotted lines). The left and right figures show the ratios for SK-I and SK-II, respectively.

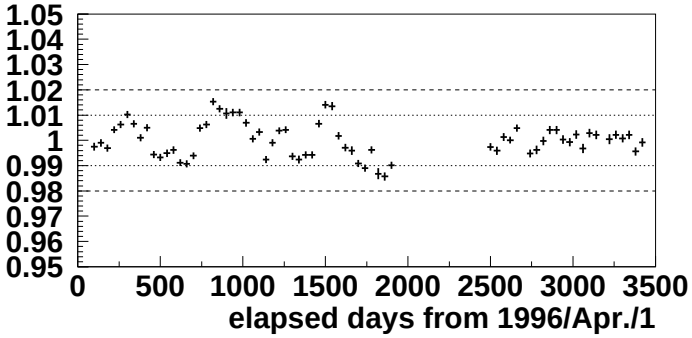

Figure 7.6: The time variation of the decay electron momentum.

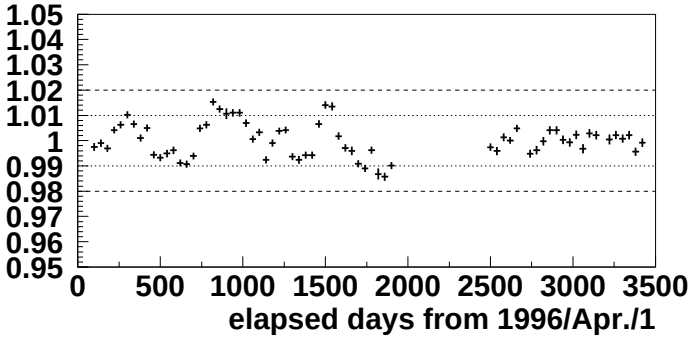

Figure 7.7: The time variation of the ratio (momentum/range) of stopping muons

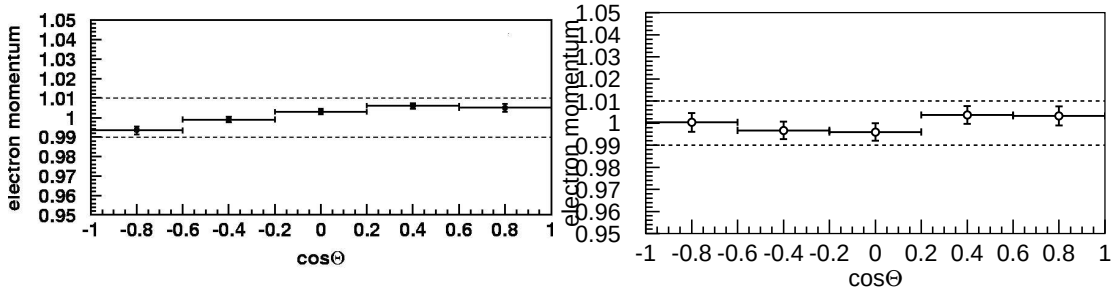

Figure 7.8: The non-uniformity of the detector gain as a function of zenith angle for SK-I (left) and SK-II (right). The vertical axes in the two figures are the momentum of decay electron events for the MC simulation normalized by the observed data.

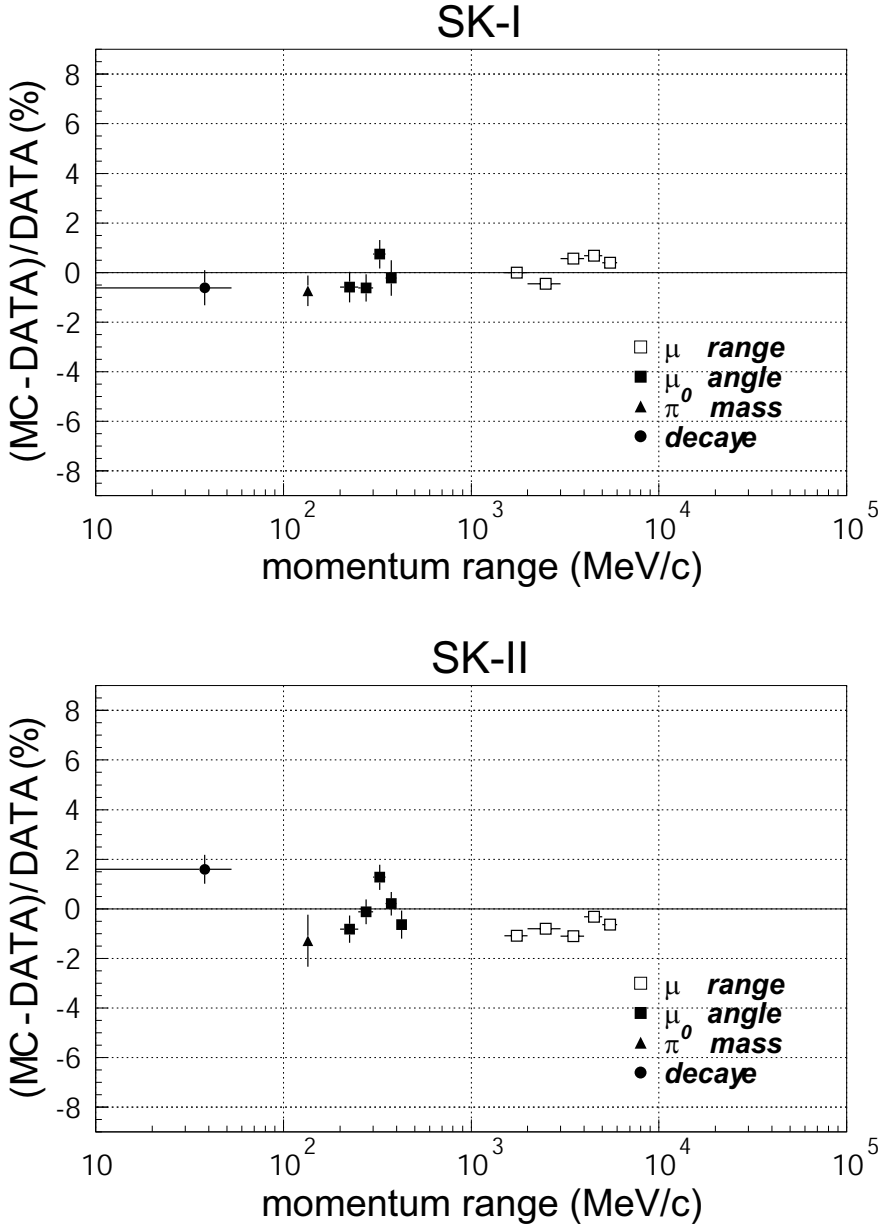

Figure 7.9: The summary of the absolute energy scale calibration for SK-I (top) and SK-II (bottom). The vertical axes show the deviations of the MC from the data.

Chapter 8

Characteristics of the Data Sample

Total livetime for the SK-I and SK-II period were 1489.2 and 798.6 days, respectively. These correspond to 91.7 kiloton·year and 49.2 kiloton·year exposure. Table 8.1 shows the event summary for the fully data samples of the observed data and the atmospheric neutrino MC. In SK-I and SK-II, 12232 and 6584 fully contained events were obtained, respectively. The event reconstruction processes described in Chapter 6 were applied for those samples. The characteristics for those events are described in this chapter. All the neutrino MC in this chapter are normalized with the data by livetime.

	SK-I				SK-II			
	FC all		Sub-GeV		FC all		Sub-GeV	
	Data	MC	Data	MC	Data	MC	Data	MC
1-ring	8536	9461	6647	7327	4520	5078	3527	3879
e-like			3426	3018			1841	1601
μ-like			3221	4309			1686	2278
2-ring	2134	2295	1560	1635	1160	1192	883	871
$\geq$3-ring	1562	1706	777	857	904	953	419	467
Total	12232	13461	8984	9819	6584	7223	4829	5216

Table 8.1: Event summary of the fully contained samples for the data and the atmospheric neutrino MC for SK-I and SK-II. 'Sub-GeV' is the event category for the visible energy below 1.33 GeV.

Figures 8.1 and 8.2 show the vertex distributions for the data and the atmospheric neutrino MC projected on Z axis and $R^2(= X^2 + Y^2)$ axis, respectively. The shapes of the distributions for the data and the MC are consistent. The discrepancy in the absolute normalization are within the systematic uncertainties of the atmospheric neutrino flux (25%) and the cross sections ($\sim$ 20%).

Figure 8.3 shows the number of ring distributions for the data and the atmospheric neutrino MC. Their shapes for the data and the MC are also consistent with each other. the number of single-ring event and multi-ring event were 8536 (4520) and 3696 (2064) for SK-I (SK-II), respectively. Only the multi-ring events were used in the nucleon decay search in this thesis.

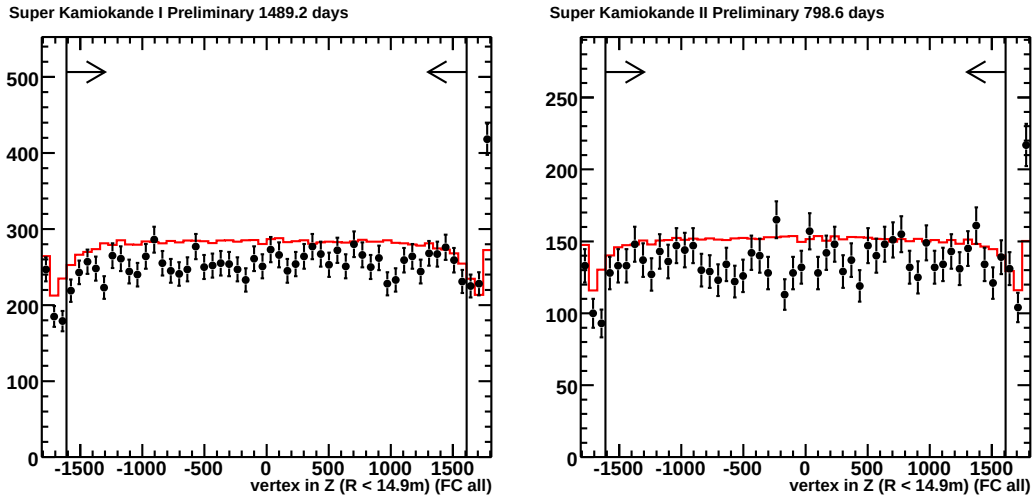

Figure 8.1: The vertex distributions projected on Z axis for the fully contained events of the data (points) and the atmospheric neutrino MC (histogram). The arrows indicate the fiducial volume.

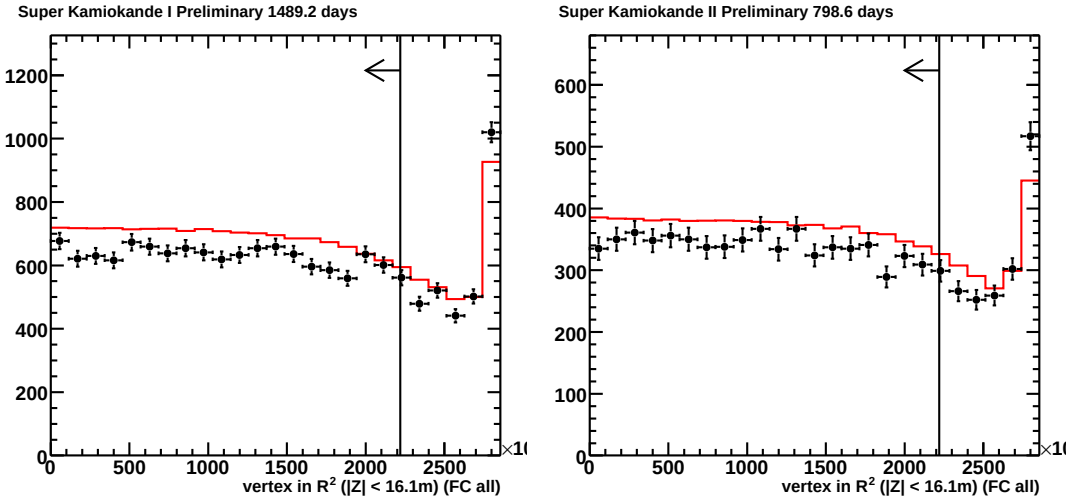

Figure 8.2: The vertex distributions projected on $R^2(= X^2 + Y^2)$ axis for the fully contained events of the data (points) and the atmospheric neutrino MC (histogram). The arrows indicate the fiducial volume.

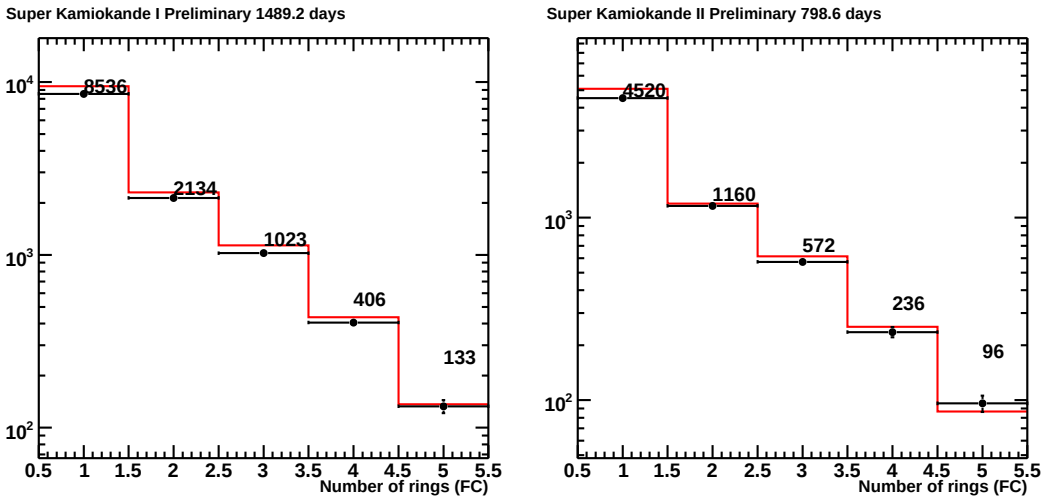

Figure 8.3: The number of ring distributions for the fully contained events of data (points) and the atmospheric neutrino MC (histogram)

The momentum distributions for single ring e-like and μ-like events are shown in Figure 8.4. As indicated by this figure, the observed flavor ratio $R(\mu/e)$ is not consistent with the MC prediction without neutrino oscillation. The measured double ratio for the events with the visible energy below 1.33 GeV are as follows;

$$R(\mu/e) \equiv \frac{(N_\mu/N_e)_{\rm Data}}{(N_\mu/N_e)_{\rm MC}} = \begin{cases} 0.659\ ^{+0.016}_{-0.016}\ (stat.)\ \text{(SK-I)} \\ 0.643\ ^{+0.022}_{-0.021}\ (stat.)\ \text{(SK-II)} \end{cases} \tag{8.1}$$

where N_e and N_μ are the number of e-like and μ-like events, respectively.

This discrepancy is well explained by the 2-flavor $\nu_\mu \leftrightarrow \nu_\tau$ oscillation established by the neutrino oscillation experiments [117, 118, 119]. Therefore, the neutrino oscillation was taken into account for the nucleon decay search described in Chapter 9.

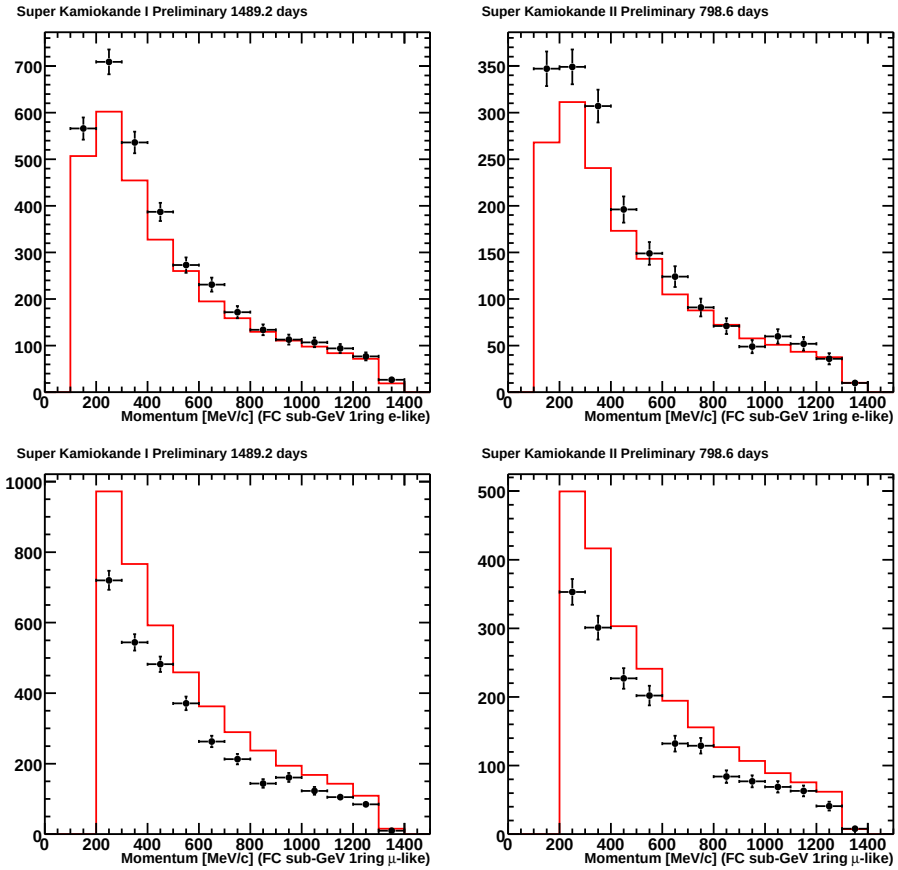

Figure 8.4: The momentum distributions for the data (points) and the atmospheric neutrino MC (histogram). The top two figures are for single-ring e-like events, ant the bottom two figures are for single-ring μ-like events. Events with the visible energy below 1.33 GeV are plotted.

Chapter 9

Nucleon Decay Analysis

In this thesis, nucleon decays into a charged anti-lepton (e^+ and μ^+) plus an un-flavored light meson (π, η, ρ and ω) were searched using the Super-Kamiokande I and II data. The number of studied modes were 8 for decays of a proton and 4 for decays of a neutron. The η meson has three dominant decay modes (2γ: 39%, $3\pi^0$: 33% and $\pi^+\pi^-\pi^0$: 23%), and each decay mode has a clearly different event signature from the other modes. The first two of the three η decay modes were studied in this thesis. The ω meson also has two dominant decay modes, $\omega \to \pi^+\pi^-\pi^0$ with a branching ratio of 89% and $\omega \to \pi^0\gamma$ with a branching ratio of 9%. Both of the ω decay modes were studied. Therefore, 16 types of decay modes were studied in this thesis as shown in Table 9.1.

Event selection criteria to extract nucleon decay signals from the fully contained data and to eliminate atmospheric neutrino backgrounds are first described for each nucleon decay mode. Nucleon decay detection efficiencies were estimated by the nucleon decay Monte Carlo simulation (MC). The comparison of performances between SK-I and SK-II are described especially for the $p \to e^+\pi^0$ mode. Since the event selection criteria are common for many modes, only the difference and the characteristics are shown for the nucleon decay modes except for the $p \to e^+\pi^0$ mode. Details of the selection criteria are described also in the Appendix A. Background rates from the atmospheric neutrino were also estimated by the atmospheric neutrino MC with the large statistics of 500 year observation equivalent. Pure ν_μ to ν_τ oscillation with $\Delta m^2 = 2.5 \times 10^{-3}$ eV^2 and $\sin^2 2\theta = 1.0$, were assumed in the atmospheric neutrino MC. The atmospheric neutrino MC events was normalized with the observed data using the number of single-ring e-like events, which are assumed to have a negligible neutrino oscillation effect. The details of the background are described especially for the $p \to e^+\pi^0$ and $p \to \mu^+\pi^0$ modes. Finally, the selection criteria were applied to the observed data of SK-I and SK-II for each mode. Then, systematic errors for detection efficiencies and background rates were estimated. In the last section, nucleon partial lifetime limits are obtained if no significant nucleon decay signals are observed in the data.

9.1 Nucleon Decay Search

9.1.1 Common Event Selection Criteria

First of all, the data used in the nucleon decay search was the fully contained (FC) data in the SK-I and SK-II period. The definition of the FC events are given in Chapter 5.

In order to study many nucleon decay modes systematically, event selection criteria were chosen to be as simple and common as possible. The primary policy for determining the criteria was not to optimize it for the best sensitivity of lifetime limits, but to obtain a low enough background level. Basically, the following reconstructed informations were used in the event selection criteria,

(A) the number of Cherenkov rings,

(B) particle type of each ring,

(C) the meson invariant mass (if it is possible to be reconstructed),

(D) the number of Michel electrons,

(E) the total invariant mass and the total momentum (if it is possible to be reconstructed).

The total momentum $P_{\rm tot}$, the total energy $E_{\rm tot}$ and the total invariant mass $M_{\rm tot}$ are defined as ;

$$P_{\rm tot} = \left| \sum_{i}^{\rm all} \vec{p_i} \right|, \tag{9.1}$$

$$E_{\rm tot} = \sum_{i}^{\rm all} \sqrt{|\vec{p_i}|^2 + m_i^2}, \tag{9.2}$$

$$M_{\rm tot} = \sqrt{E_{\rm tot}^2 - P_{\rm tot}^2}, \tag{9.3}$$

where $\vec{p_i}$ is the momentum of each ring, m_i is the mass of a particle (γ, $e^{\pm}$, $\mu^{\pm}$, $\pi^{\pm}$). The meson mass is reconstructed in a similar way by summing up the momenta and energies of secondary particles from the meson decay. Although our particle identification algorithm can only classify a Cherenkov ring into a shower type ring ($e^{\pm}$ or γ) or a non-shower type ring ($\mu^{\pm}$ or $\pi^{\pm}$), the invariant mass reconstruction sometimes required to distinguish $e^{\pm}$ from γ or $\mu^{\pm}$ from $\pi^{\pm}$. For example, for the π^0 invariant mass reconstruction in the $p \to e^+\pi^0$ mode search, we should identify a positron and a ring from a γ-ray. However, that cannot be done in a large water Cherenkov detector. In those cases, the invariant mass was calculated for all the possible combinations of particle type assignment. Then, the best combination in which the reconstructed mass is the closest to the true nucleon (or meson) mass is selected. This method can make the mass distribution narrower than the detector intrinsic resolution, and can make a fake peak in the meson mass distribution for the atmospheric neutrino MC even if the meson is not produced in the simulation.

All the studied nucleon decay modes are two body decays with back-to-back kinematics, and have isotropic event signatures, which is the most significant difference from the typical atmospheric neutrino events. Therefore, the event selection by the total mass and the total invariant mass is a powerful tool to eliminate the atmospheric neutrino background. The threshold of the total momentum cut is normally set to be 250 MeV/c considering the Fermi motion of bound nucleons. To keep the background rates low enough (below 0.5 events in the total exposure), the tighter total momentum cut with the threshold of 150 (or 200) MeV/c is applied in some relatively high background mode searches.

We required that the number of identified rings and their particle ID are consistent with a proton decay signal. For the particle identification, two types of algorithm were used in this analysis as described in Section 6.3. One is the PID with only a Cherenkov ring pattern, and the other is the PID with both a Cherenkov ring pattern and an opening angle. Since Cherenkov opening angles become small for low momentum non-shower type particles ($p_\mu <\sim 300$ MeV/c for muons), the PID with both a ring pattern and an opening angle is used for the modes in which low momentum muons or charged pions are searched.

The number of Michel electron was required to be consistent with a proton decay signal. The background events can be effectively eliminated, while the loss of the detection efficiency is zero or small due to the high detection efficiency of Michel electron detections.

The event selection criteria for all the searches are summarized in Table 9.1. Details of each mode search are described in the next section and Appendix A.

	A	B	C	D	E		
Modes	Ring	PID	$M_{\rm meson}$	decay-e	$M_{\rm tot}$	$P_{\rm tot}$	Note
$p \to e^+\pi^0$	2, 3	SS(S)	85∼185 (π)	0	800∼1050	<250	
$p \to \mu^+\pi^0$	2, 3	NS(S)	85∼185 (π)	1	800∼1050	<250	
$p \to e^+\eta$ (2γ)	3	SSS	480∼620 (η)	0	800∼1050	<250	
$p \to \mu^+\eta$ (2γ)	3	NSS*	480∼620 (η)	1	800∼1050	<250	
$p \to e^+\eta$ ($3\pi^0$)	4, 5	SSSS(S)	400∼700 (η)	0	800∼1050	<150	
$p \to \mu^+\eta$ ($3\pi^0$)	4, 5	NSSS(S)*	400∼700 (η)	1	800∼1050	<250	
$p \to e^+\rho^0$	3	SNN*	600∼900 (ρ)	0, 1	800∼1050	<150	
$p \to \mu^+\rho^0$	3	NNN*	600∼900 (ρ)	1, 2	800∼1050	<250	
$p \to e^+\omega$ ($\pi^0\gamma$)	3, 4	SSS(S)	650∼900 (ω)	0	800∼1050	<150	
$p \to \mu^+\omega$ ($\pi^0\gamma$)	2, 3	SS(S)	650∼900 (ω)	1	-	<200	
$p \to e^+\omega$ ($\pi^+\pi^-\pi^0$)	4	SSSN*	85∼185 (π)	0, 1	600∼800	<200	P_{e^+}
$p \to \mu^+\omega$ ($\pi^+\pi^-\pi^0$)	3	SSN*	85∼185 (π)	2	450∼700	<200	
$n \to e^+\pi^-$	2	SN	-	0	800∼1050	<250	
$n \to \mu^+\pi^-$	2	NN	-	1	800∼1050	<250	
$n \to e^+\rho^-$	4	SSSN*	600∼900 (ρ)	0	800∼1050	<250	M_π
$n \to \mu^+\rho^-$	3	SSN*	600∼900 (ρ)	1	-	<150	M_π

Table 9.1: Summary of the selection criteria. 'S' and 'N' in PID stand for shower type rings and non-shower type rings, respectively. '*' in PID means that the PID with a Cherenkov ring pattern and an opening angle was used for that mode search. All the invariant mass and momentum are written in MeV/c^2 or MeV/c units. For the $p \to e^+\omega$ ($3\pi^0$) mode, the positron momentum cut is applied ($100 < P_{e^+} < 200$). For the $n \to l^+\rho^-$ mode, the π^0 invariant mass cut is also applied.

9.1.2 $p \to l^+\pi^0$ Mode Search

The selection criteria for the $p \to l^+\pi^0$ mode are defined as ;

(A) the number of Cherenkov rings is two or three,

(B) one of the rings is a shower (non-shower) type ring for $p \to e^+\pi^0$ ($p \to \mu^+\pi^0$), and all the other rings are shower type rings,

(C) for three ring events, π^0 invariant mass is reconstructed in between 85 to 185 MeV/c^2,

(D) the number of Michel electrons is 0 (1) for $p \to e^+\pi^0$ ($p \to \mu^+\pi^0$),

(E) the total momentum is less than 250 MeV/c, and the total invariant mass is in between 800 to 1050 MeV/c^2.

$\mathbf{p \to e^+\pi^0}$ search in SK-I In the proton decay of $p \to e^+\pi^0$, a positron and a neutral pion are back-to-back and have the same momentum of 459 MeV/c in the proton rest frame. Then, the π^0 immediately decays into two γ-rays. Figure 9.1 shows the event signature of a typical proton decay MC event. One shower type ring from the positron and two shower type rings from the π^0 are clearly seen in this figure.

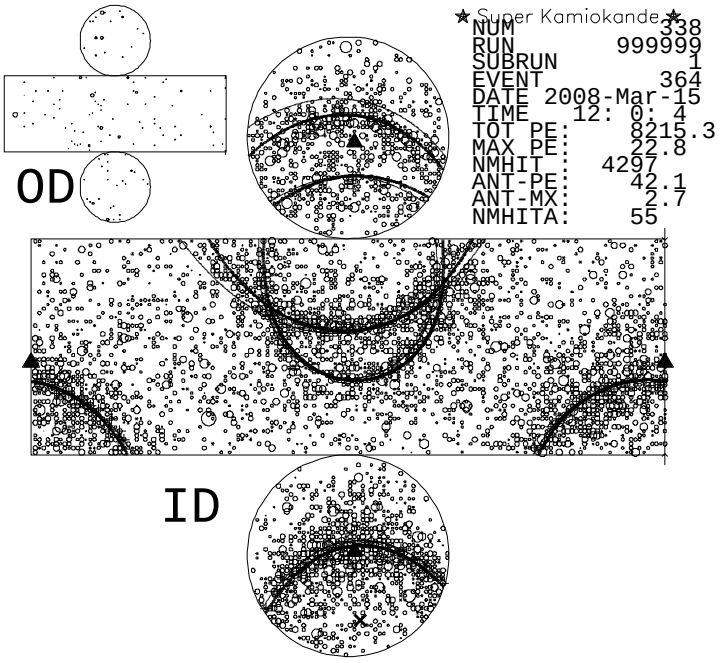

Figure 9.1: A typical proton decay MC event of $p \to e^+\pi^0$ in SK-I. One Cherenkov ring from a positron and two Cherenkov rings from two γ-rays from π^0 decay can be observed around the bottom and the top of the detector, respectively. This event is the same event as that in Figure 6.11, but this is with some reconstructed informations. Solid lines show the reconstructed rings. The reconstruction algorithms correctly find all the rings and identify their particle ID for this event.

The two γ-rays from the π^0 decay are back-to-back in the π^0 rest frame. They are Lorentz-boosted by the momentum of ~ 450 MeV/c. One of the two γ-rays momenta in the laboratory frame can be very low depending on the direction of the Lorentz boost. In such a case, it sometimes happens that only one ring from π^0 decay is identified. Therefore, one Cherenkov ring from the positron and one or two shower type rings from the π^0 decay were required in the criterion (A) and (B). Figure 9.2 shows the number of ring distributions for the proton decay MC as well as the atmospheric neutrino MC. For free proton decays, the fraction of 2 rings and 3 rings was 39% and 60%, respectively.

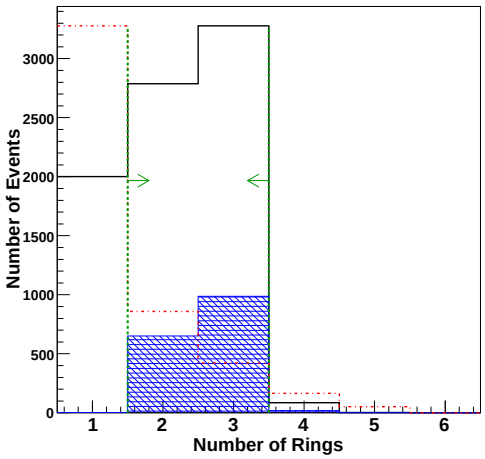

Figure 9.2: The number of ring distribution of $p \to e^+\pi^0$ MC in SK-I. The shaded histogram is the distribution for free proton decay events. The distribution for the atmospheric neutrino MC, which is normalized with the proton decay MC using the maximum bin value, is also shown in the dashed histogram. Dashed lines and arrows indicate the selection criterion.

If all three rings were found, the π^0 invariant mass, which is reconstructed by two of the three rings, was required to be in between 85 to 185 MeV/c (the criterion (C)). The reconstructed π^0 invariant mass distribution for the proton decay MC is shown in Figure 9.3. For free proton decay events, the mean of the π^0 invariant mass is 137 MeV/c^2, and its resolution is 20 MeV/c^2.

The criterion (D) requires no Michel electron to reduce the background. This selection criterion does not reduce the signal efficiency at all.

The criterion (E) selects the events of which total momentum and invariant mass are consistent with the momentum and mass of a source proton, respectively. This criterion can reduce the atmospheric neutrino background by more than three orders of magnitude. Figures 9.4, 9.5 and 9.6 show the distributions of the total momentum, the total invariant mass and their 2-dimensional plots, respectively. For free proton decay events, the total invariant mass was well reconstructed. The mean of the total invariant mass distribution is 933.8 MeV/c^2, and its resolution is 28.2 MeV/c^2. The resolution of the total momentum is 29.8 MeV/c. The total momentum and invariant mass cut was wide enough for free proton decay events.

The detection efficiency for the proton decay MC at each selection criteria is summarized in Table 9.2. The detection efficiency for $p \to e^+\pi^0$ were estimated to be 44.6%. For free proton

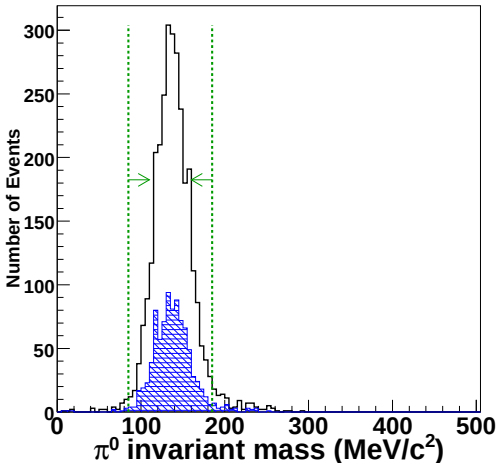

Figure 9.3: The invariant mass of π^0 distribution for SK-I proton decay MC. The Shaded histogram are the distribution for free proton decay events. Dashed lines and arrows indicate the selection criterion.

decay events, the high efficiencies of 87% were achieved for $p \to e^+\pi^0$. The inefficiency is mainly due to nuclear interaction effects of pions in ^{16}O. About 37% of π^0s from proton decay in ^{16}O were absorbed or charge-exchanged by interactions with nucleons in the proton decay MC. Those events hardly survive the selection criteria.

Performance Comparison between SK-I and SK-II In the SK-II period, there were only about a half of the PMT density of SK-I. The performances of SK-I and SK-II were compared using the $p \to e^+\pi^0$ free proton samples.

The number of ring distributions for the free proton decay MC in SK-I and SK-II are shown in Figure 9.7. The efficiencies for the criterion (A), which requires 2 or 3 rings, were 99% and 98% for free proton decay events in SK-I and SK-II, respectively. There was no significant difference in the ring counting performance. The PID performance in SK-II was also comparable to that in SK-I. The mis-PID probabilities for SK-I and SK-II free proton decay of $p \to e^+\pi^0$ were estimated to be 3.3% and 3.4%, respectively.

Figures 9.8 and 9.9 show the distributions of the total momentum and the total invariant mass. The resolutions of the total momentum and the total invariant mass for the free proton decay events in SK-I (SK-II) were 29.8 (32.5) MeV/c and 28.2 (36.2) MeV/c^2, respectively. Though the resolutions in SK-II were slightly worse than those in SK-I, the effect on the total detection efficiency was so small. The detection efficiencies for $p \to e^+\pi^0$ were estimated to be 44.6% and 43.5% in SK-I and SK-II, respectively. Moreover, for the free proton decay events, the efficiencies were 87% and 86% in SK-I and SK-II, respectively.

Consequently, SK-II had comparable performances to SK-I for the $p \to e^+\pi^0$ mode. The efficiency difference for the other modes will be mentioned in Section 9.1.8.

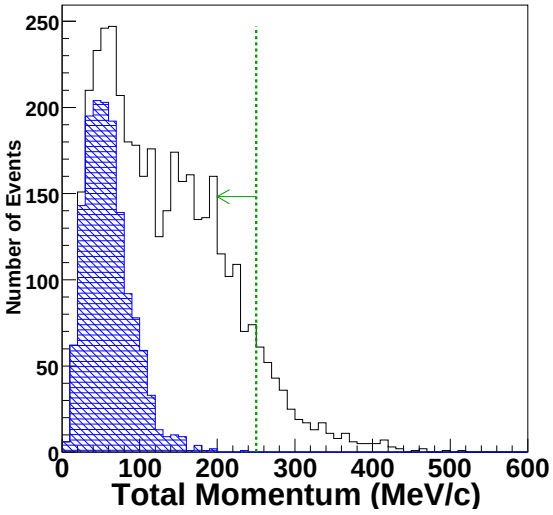

Figure 9.4: The total momentum distributions for proton decay MC in SK-I. Only the events which satisfy the selection criteria (A $\sim$ D) and $800 < M_{\rm tot} < 1050$ MeV/c^2 are plotted.

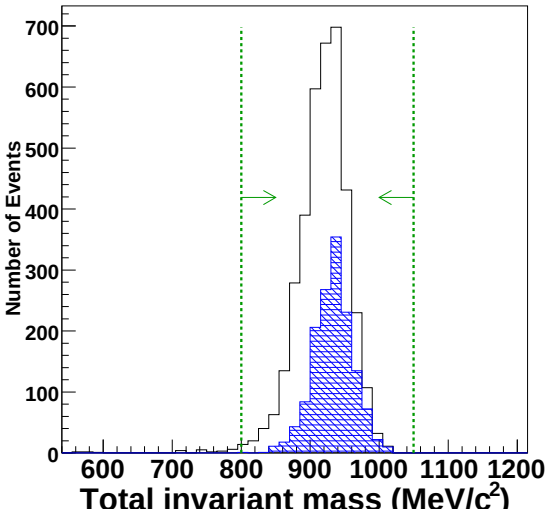

Figure 9.5: The total invariant mass distributions for proton decay MC in SK-I. Only the events which satisfy the selection criteria (A $\sim$ D) and $P_{\rm tot} < 250$ MeV/c are plotted.

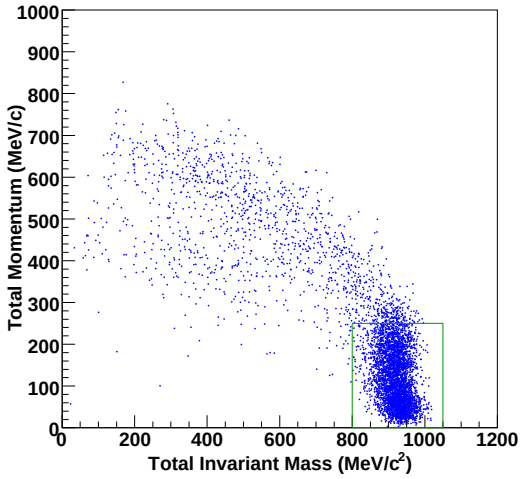

Figure 9.6: The total momentum and the total invariant mass distributions for proton decay MC in SK-I. Only the events which satisfy the selection criteria (A $\sim$ D).

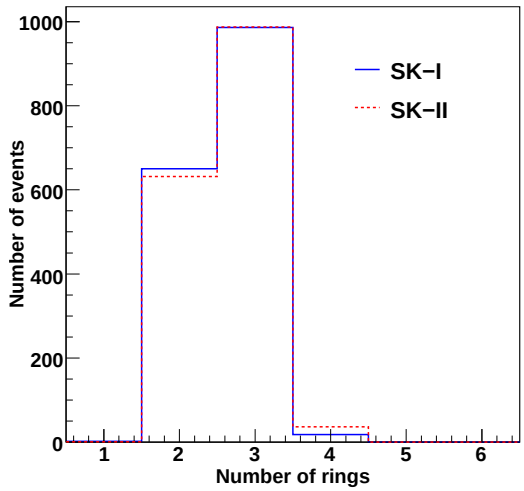

Figure 9.7: The number of ring distribution for the $p \to e^+\pi^0$ MC (free proton).

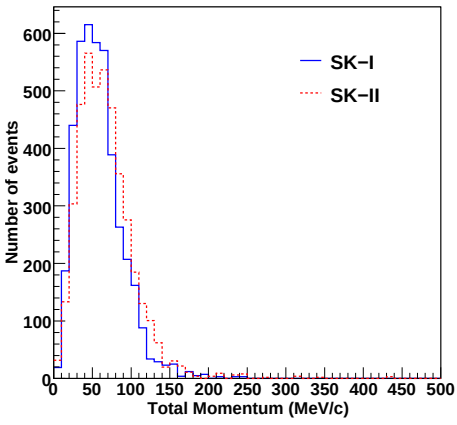

Figure 9.8: The total momentum distribution for the $p \to e^+\pi^0$ MC (free proton).

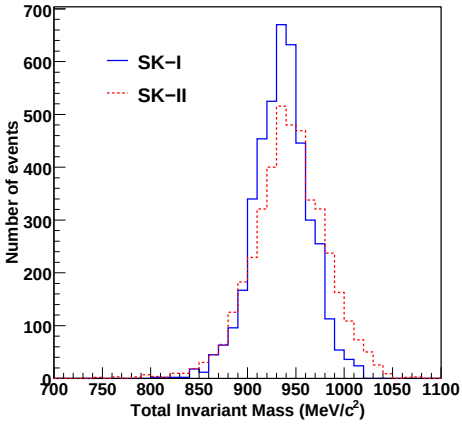

Figure 9.9: The total invariant mass distribution for the $p \to e^+\pi^0$ MC (free proton).

$\mathbf{p \to \mu^+\pi^0}$ search Differences in the selection criteria from the $p \to e^+\pi^0$ mode are to require one non-shower type ring and one Michel electron. The detection efficiency for a Michel electron from the decay of μ was approximately 80%. This is the reason of the detection efficiency difference between $p \to e^+\pi^0$ and $p \to \mu^+\pi^0$. The detection efficiency for the $p \to \mu^+\pi^0$ mode was estimated to be 35.5% (34.7%) in SK-I (SK-II).

	$p \to e^+\pi^0$						$p \to \mu^+\pi^0$					
	eff.(%)		atm. ν MC		FC Data		eff.(%)		atm. ν MC		FC Data	
	SK-I	SK-II	SK-I	SK-II	SK-I	SK-II	SK-I	SK-II	SK-I	SK-II	SK-I	SK-II
F.V.	98.0	99.8	12586	6684	12232	6584	98.6	99.4	12586	6684	12232	6584
A	72.9	73.5	3365	1759	3157	1732	73.6	93.7	3365	1759	3157	1732
B	64.4	65.3	2045	1096	1957	1079	61.2	61.7	1063	541	983	553
C	62.7	62.4	1706	907	1659	882	59.6	59.8	853	431	817	464
D	61.9	61.7	1265	676	1203	656	46.6	45.8	387	193	398	244
E	44.6	43.5	0.20	0.11	0	0	35.5	34.7	0.23	0.11	0	0

Table 9.2: The detection efficiencies for the proton decay MC and the number of surviving event in the atmospheric neutrino MC and in the observed data at each event selection criterion for $p \to e^+\pi^0$ and $p \to \mu^+\pi^0$. The atmospheric neutrino MC is normalized with the observed data using single-ring e-like events. The criteria (A$\sim$E) are described in the text.

Background First, the atmospheric neutrino MC was compared with the data in a sideband region. The sideband region is defined as a region outside of the signal window for the cut by the total momentum and the total invariant mass with a 100 MeV margin. It is illustrated in Figure 9.10. Figures 9.11, 9.12, 9.13 and 9.14 show the sideband distributions of the invariant mass of π^0, the number of Michel electron, the total momentum and the total invariant mass, respectively. The atmospheric neutrino MC reproduces the observed data well. No significant differences between the MC and the data are not observed.

The number of the normalized atmospheric neutrino MC events at each selection criterion are summarized in Table 9.2. The estimated background rates in SK-I and SK-II are consistent with each other. The background events for $p \to e^+\pi^0$ and $p \to \mu^+\pi^0$ were estimated to be 0.31 and 0.34 events in total (SK-I+SK-II), respectively. Therefore, the low background observation with the high efficiency were achieved for these modes with the Super-Kamiokande detector, both in the SK-I and SK-II period. The estimated background for $p \to e^+\pi^0$ were compared with another estimation by the experimental data of K2K ν beam and 1-kiloton water Cherenkov detector [120]. The number of expected background events from the K2K data is $0.23^{+0.06}_{-0.05}(\text{stat.})^{+0.06}_{-0.07}(\text{sys.})$, which is consistent with the estimation by our MC. The background estimation was also compared with a different neutrino interaction MC, NUANCE [121]. The number of background estimated by NUANCE was 0.27 ± 0.10. It is also consistent with our estimation.

The breakdown of the background events is shown in Table 9.3. The dominant background for both modes were charged current single(multi)-π production interactions. A charged lepton and a π^0 produced by this interaction makes a similar event signature to $p \to e^+\pi^0$ or $p \to \mu^+\pi^0$.

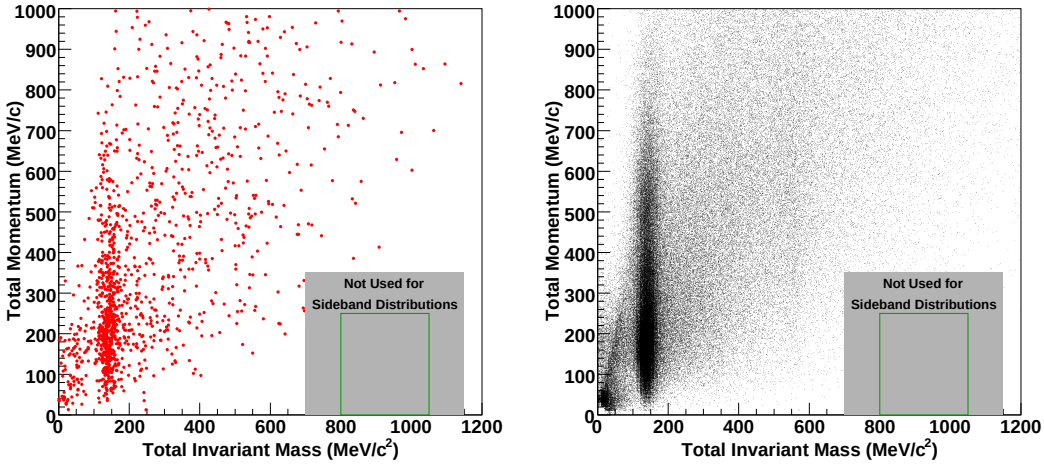

Figure 9.10: The sideband samples in the total momentum and the total invariant mass distributions in SK-I. The observed data and the atmospheric neutrino MC are shown in the left and right figures, respectively. Only the cuts for the number of ring (A) and the particle identification (B) were applied.

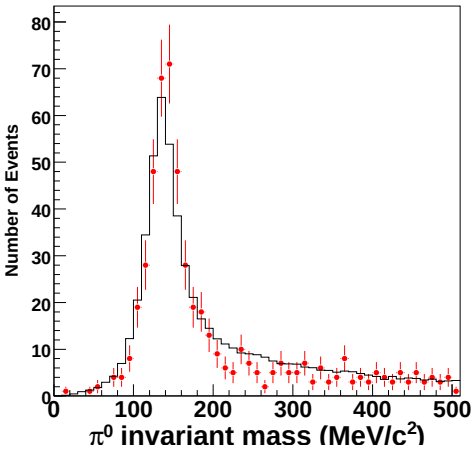

Figure 9.11: The invariant mass of π^0 distributions of the sideband samples in SK-I. The atmospheric neutrino MC and the data are shown in the solid line and the points, respectively.

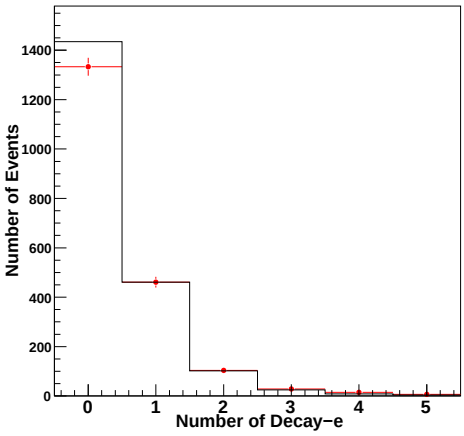

Figure 9.12: The number of Michel electron distributions of the sideband samples in SK-I. The atmospheric neutrino MC and the data are shown in the solid line and the points, respectively.

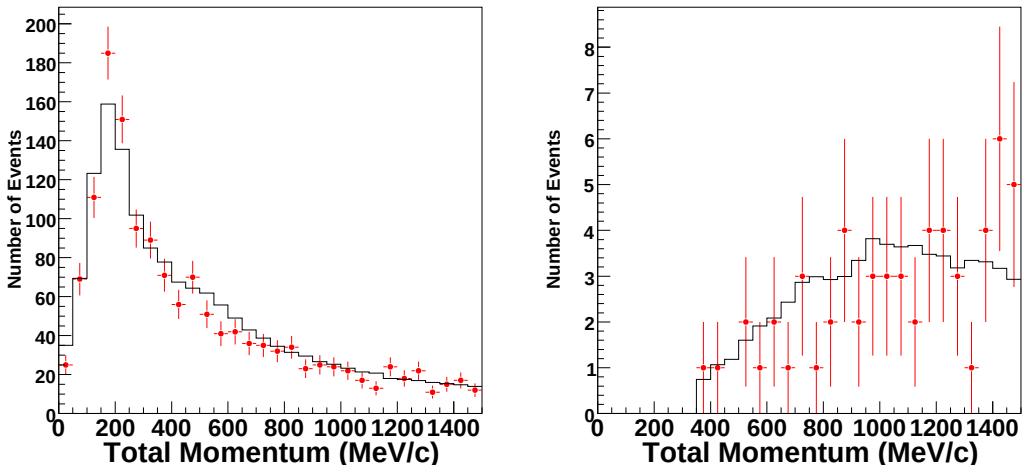

Figure 9.13: The total momentum distributions of the sideband samples in SK-I. The atmospheric neutrino MC and the data are shown in the solid line and the points, respectively. The left figure shows the distribution only after the criteria (A) and (B). The total invariant mass cut of $800 < M_{\rm tot} < 1050$ MeV/c^2 is also applied for the right figure.

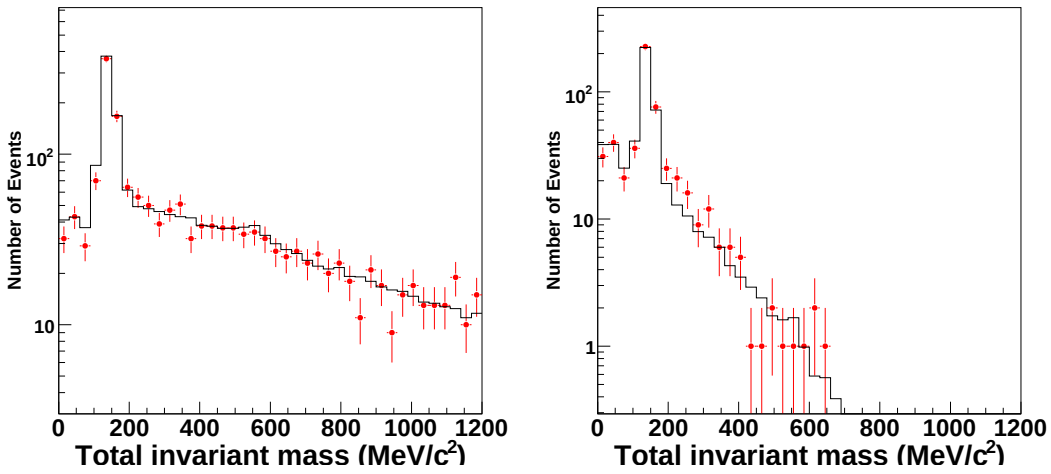

Figure 9.14: The total invariant mass distributions of the sideband samples in SK-I. The atmospheric neutrino MC and the data are shown in the solid line and the points, respectively. The left figure shows the distribution only after the criteria (A) and (B). The total momentum cut of $P_{\rm tot} < 250$ MeV/c is also applied for the right figure.

A typical background event from the single-π production is shown in Figure 9.15. In most background events from charged current quasi-elastic scattering (CCQE), a highly energetic proton ($>$1GeV/c) produced by a neutrino interaction scattered in water and produced a secondary π^0.

Approximately 16% of charged current π production came from ν_e for the background of $p \to \mu^+\pi^0$, while there was no background events from ν_μ charged current π production for the $p \to e^+\pi^0$ mode. This is because one shower type ring from an electron and the other non-shower type ring from a charged pion from the neutrino interaction could mimic a $p \to \mu^+\pi^0$ signal.

Interaction Mode	$p \to e^+\pi^0$	$p \to \mu^+\pi^0$
CCQE	28%	15%
CC single-π production	32%	47%
CC multi-π production	19%	21%
CC others	2%	13%
NC	19%	4%

Table 9.3: The breakdown of the neutrino interaction modes of the background events.

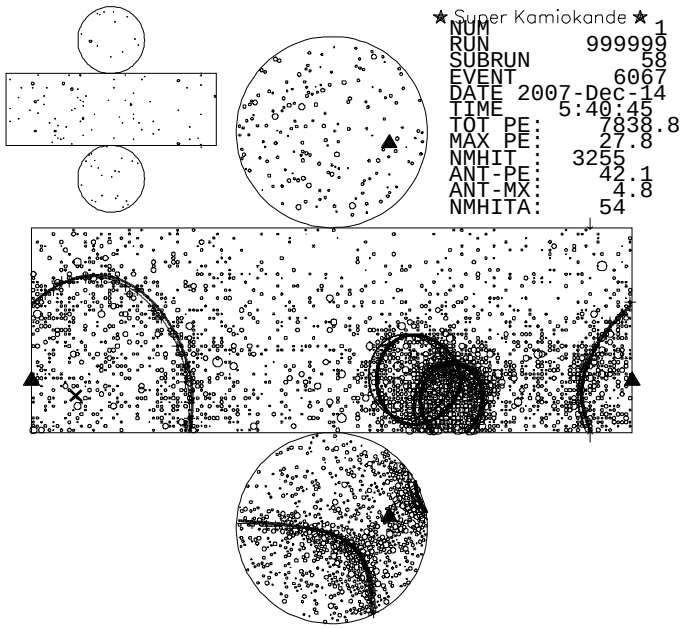

Figure 9.15: A typical background event for the $p \to e^+\pi^0$ mode in the atmospheric neutrino MC. One ring from a charged lepton and the other two rings from the decay of a π^0, which is produced by a neutrino interaction, mimic a proton decay signal from $p \to e^+\pi^0$.

Nucleon Decay Signal Search in the Data The selection criteria described above were applied to the SK-I and SK-II data. The momentum and the total invariant mass distributions for the observed data are shown in Figure 9.19. No candidate event was observed in the data

for both modes. Table 9.2 shows the number of surviving events in the data at each selection criterion with the normalized atmospheric neutrino MC. The atmospheric neutrino MC reproduces the number of events in the observed data well. The data and the atmospheric neutrino MC were compared by the π^0 invariant mass distributions in Figure 9.16, the total momentum distributions in Figure 9.17 and the total invariant mass distributions in Figure 9.18. The data and the atmospheric neutrino MC in these distributions are consistent with each other.

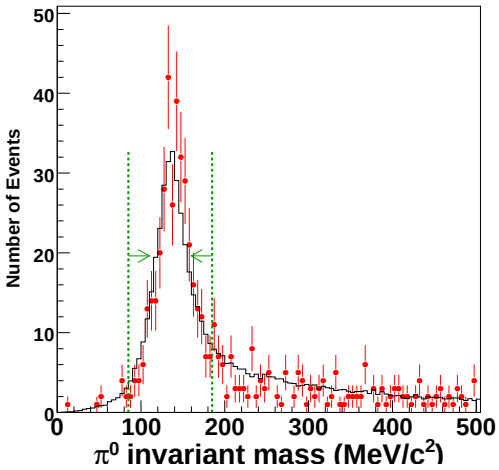

Figure 9.16: The invariant mass of π^0 distribution for SK-I data (points) and the atmospheric neutrino MC (solid line). Dashed lines and arrows indicate the selection criterion.

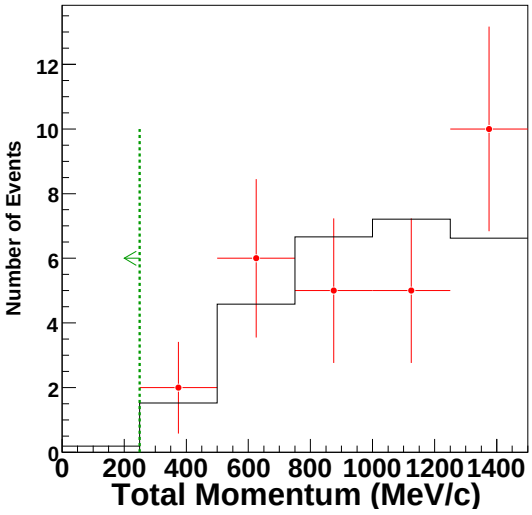

Figure 9.17: The total momentum distributions for the atmospheric neutrino MC (solid line) and the data (points) for $p \rightarrow e^+\pi^0$ in SK-I. Only the events which satisfy the selection criteria (A $\sim$ D) and $800 < M_{\rm tot} < 1050$ MeV/c^2 are plotted.

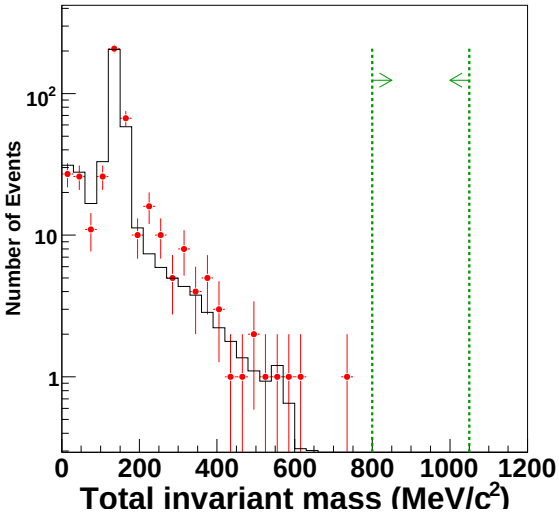

Figure 9.18: The total invariant mass distributions for the atmospheric neutrino MC (solid line) and the data (points) for $p \rightarrow e^+\pi^0$ in SK-I. Only the events which satisfy the selection criteria (A $\sim$ D) and $P_{\rm tot} < 250$ MeV/c are plotted.

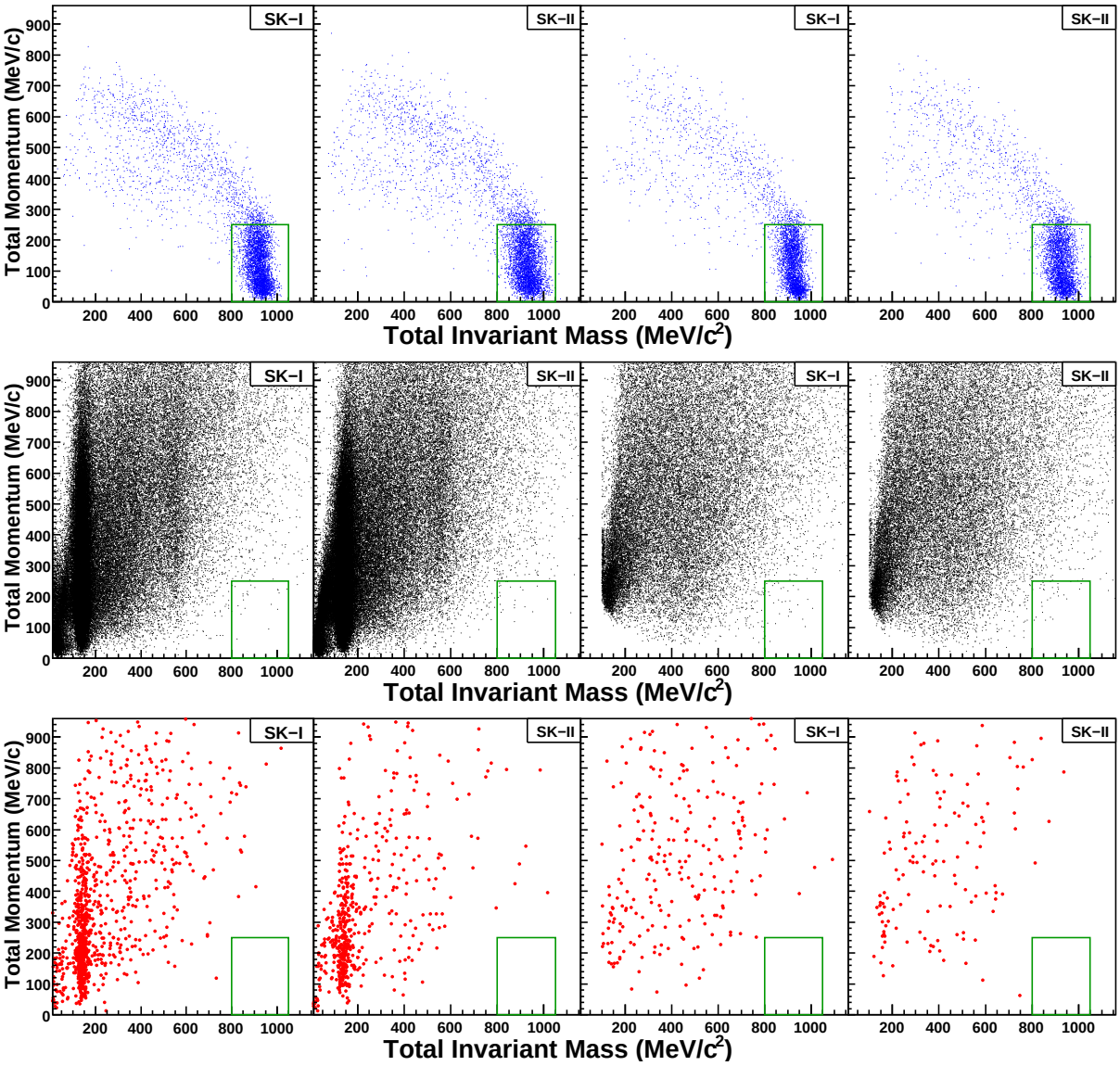

Figure 9.19: Total momentum versus total invariant mass distributions, from left to right: SK-I $p \to e^+\pi^0$; SK-II $p \to e^+\pi^0$; SK-I $p \to \mu^+\pi^0$; and SK-II $p \to \mu^+\pi^0$, from top to bottom: the proton decay MC; the atmospheric neutrino MC; and the observed data. These events satisfy the event selection criteria except for the selection by the total momentum and total mass. The boxes in figures indicate the criteria. No candidates were found for both $p \to e^+\pi^0$ and $p \to \mu^+\pi^0$ in the data.

9.1.3 $p \to l^+\eta$ Mode Search

As described at the beginning of this chapter, η meson has three dominant decay modes, and the two of the three modes were studied in this thesis; $\eta \to 2\gamma$ (Br=39%) and $\eta \to 3\pi^0$ (Br=33%). The decay branch of $\eta \to \pi^+\pi^-\pi^0$ was not studied because it has the smallest branching ratio of the three modes, and its efficiency was expected to be very low.

The mass of η meson is 548 MeV/c^2. Because of the larger mass than π^0 mass, a generated charged lepton and a η meson has a smaller momentum, 309 (296) MeV/c in the proton rest frame. For the $p \to \mu^+\eta$ mode, the PID with a Cherenkov ring pattern and an opening angle was used to improve the PID for a low low momentum μ ring. This is common for both meson decay modes of $p \to \mu^+\eta$.

The search of $p \to l^+\eta$ mode via $\eta \to 2\gamma$ mode is first explained, and then $p \to l^+\eta$ search via $\eta \to 3\pi^0$ mode is explained.

$p \to l^+\eta$ ($\eta \to 2\gamma$) Mode Search

	A	B	C	D	E	
Modes	Ring	PID	$M_{\rm meson}$	decay-e	$M_{\rm tot}$	$P_{\rm tot}$
$p \to e^+\eta$ (2γ)	3	SSS	480∼620 (η)	0	800∼1050	<250
$p \to \mu^+\eta$ (2γ)	3	NSS*	480∼620 (η)	1	800∼1050	<250

Table 9.4: The event selection criteria for $p \to e^+\eta$ and $p \to \mu^+\eta$ (2γ).

Event Characteristics These modes have very similar event signatures with $p \to e^+\pi^0$ and $p \to \mu^+\pi^0$. However, the momentum of the two γ-rays in the η meson rest frame is 274 MeV/c, which is much larger than that in $p \to e^+\pi^0$ and $p \to \mu^+\pi^0$. The opening angle between two γ-rays from the η meson decay is about 132 degree in the laboratory frame. Therefore, three Cherenkov rings are clearly visible and easily be separated as shown in Figure 9.20, so that the number of Cherenkov rings is required to be three. Figure 9.21 shows the number of ring distributions for the proton decay MC. The fraction of 3 rings was 93% for SK-I free proton decay of $\eta \to 2\gamma$ mode of $p \to e^+\eta$.

Because only the three ring events survive the number of ring cut, η invariant mass cut was applied to all the surviving events. Figure 9.22 shows the reconstructed invariant mass of η meson for the proton decay MC of the $p \to e^+\eta$ mode. The η invariant mass was well reconstructed.

The Search Results The detection efficiencies for the proton decay MC and the number of events for the normalized atmospheric neutrino MC and the observed data at each selection criteria are summarized in Table 9.5. The momentum and the total invariant mass distributions in the final selection criterion are shown in Figure 9.23.

The detection efficiencies for $p \to e^+\eta$ and $p \to \mu^+\eta$ (2γ) were estimated to be 18.8% (18.2%) and 12.4% (11.7%) in SK-I (SK-II), respectively. The branching ratio of the meson decay was taken into account in the detection efficiencies. The reason for the inefficiency was due to the nuclear effect of the η meson. Approximately 38% of generated η meson could not escape from

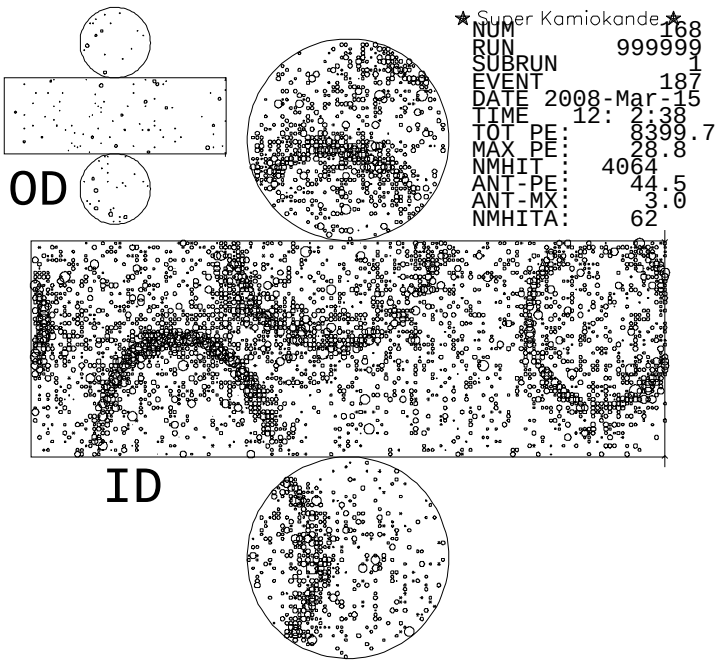

Figure 9.20: A typical proton decay MC event of $p \to e^+\eta$ (2γ). Three Cherenkov rings are clearly visible.

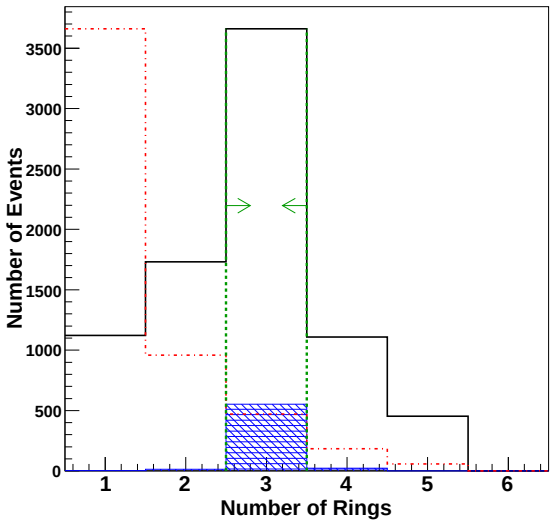

Figure 9.21: The number of ring distributions of the $p \to e^+\eta$ MC in SK-I. All the decay branches of the η meson are filled in the figure. The Shaded histogram is the distribution for the free proton decay events of the $\eta \to 2\gamma$ mode only. The distribution for the atmospheric neutrino MC, which is normalized with the proton decay MC using the maximum bin value, is also shown in the dashed histogram. Dashed lines and arrows indicate the selection criterion.

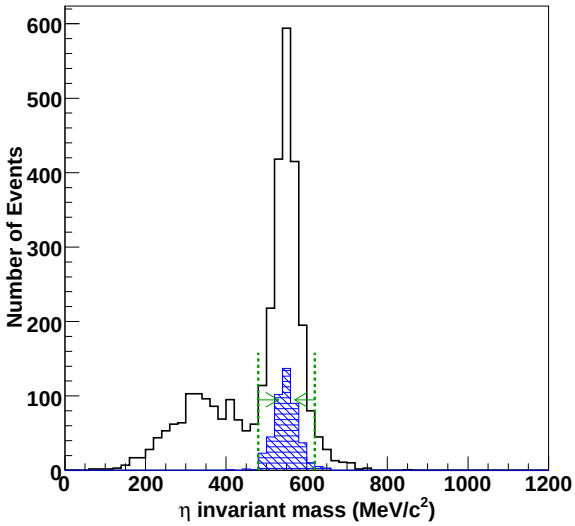

Figure 9.22: The η invariant mass distributions of the $p \to e^+\eta$ MC in SK-I. All the decay branches of the η meson are filled in the figure. The shaded histogram is the distribution for the free proton decay events of the $\eta \to 2\gamma$ mode only Dashed lines and arrows indicate the selection criterion. The lower momentum peak consisted of the other η meson decay events, such as $\eta \to 3\pi^0$ and $\eta \to \pi^+\pi^-\pi^0$.

nuclei. For the free proton decay events of $\eta \to 2\gamma$ mode in SK-I, the high efficiencies of 74% and 58% were achieved for $p \to e^+\eta$ and $p \to \mu^+\eta$, respectively.

The low background rate was also achieved. The background events for $p \to e^+\eta$ and $p \to \mu^+\eta$ were estimated to be 0.28 and 0.04 events in total (SK-I+SK-II), respectively.

Finally, Nucleon decay signals were searched in the SK-I and SK-II data. No candidate event was observed in the data for both modes as shown in Figure 9.23.

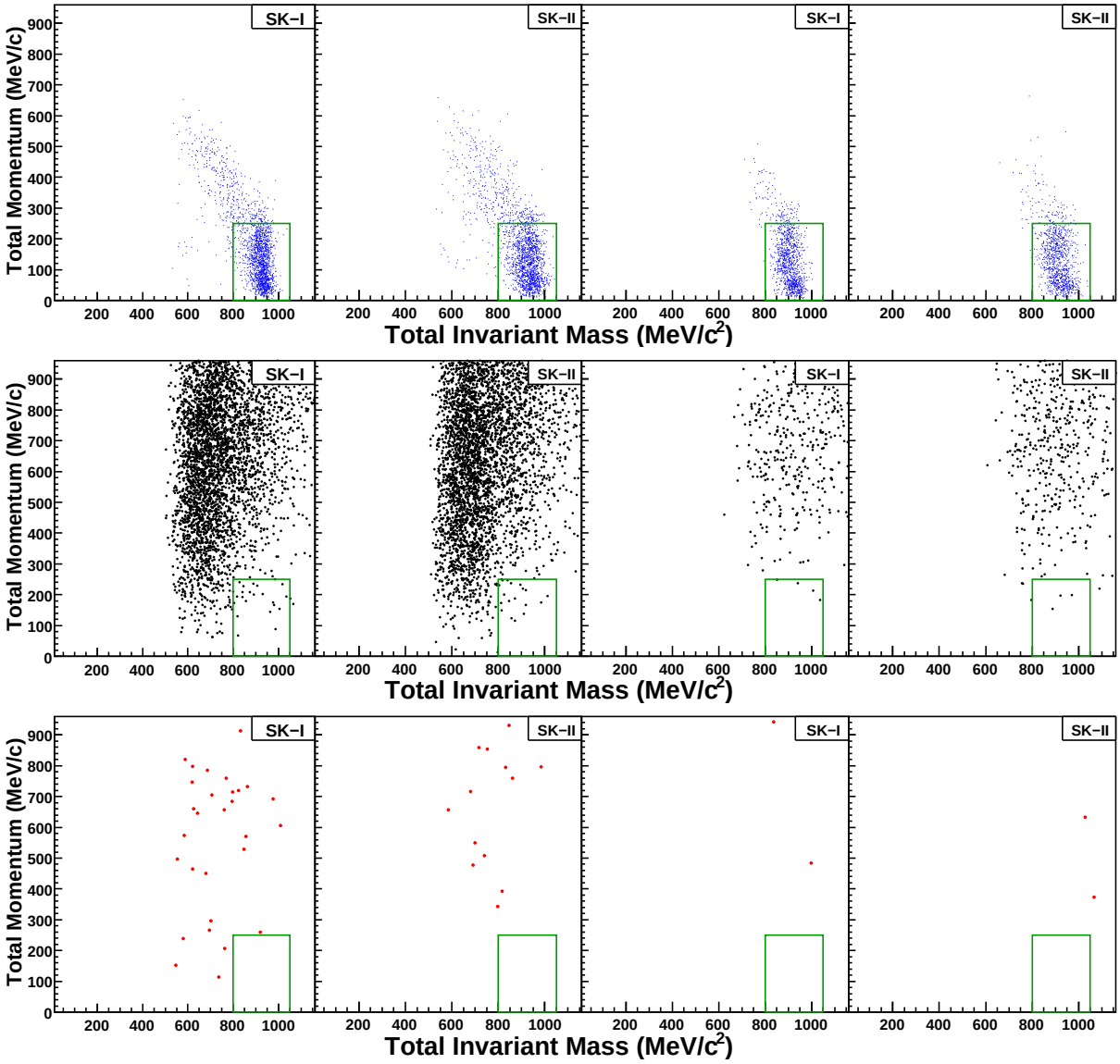

Figure 9.23: Total momentum versus total invariant mass distributions, from left to right: SK-I $p \to e^+\eta$; SK-II $p \to e^+\eta$; SK-I $p \to \mu^+\eta$; and SK-II $p \to \mu^+\eta$, from top to bottom: the proton decay MC; the atmospheric neutrino MC; and the observed data. These events satisfy the event selection criteria for $p \to e^+\eta$ (2γ) or $p \to \mu^+\eta$ (2γ) except for the selection by the total momentum and total mass. The boxes in figures indicate the criteria. No candidates were found for both $p \to e^+\eta$ (2γ) and $p \to \mu^+\eta$ (2γ) in the data.

	$p \to e^+\eta$ ($\eta \to 2\gamma$)						$p \to \mu^+\eta$ ($\eta \to 2\gamma$)					
	eff.(%)		atm. ν MC		FC Data		eff.(%)		atm. ν MC		FC Data	
	SK-I	SK-II	SK-I	SK-II	SK-I	SK-II	SK-I	SK-II	SK-I	SK-II	SK-I	SK-II
F.V.	97.9	100.4	12586	6684	12232	6584	98.1	99.4	12586	6684	12232	6584
A	44.4	44.8	1109	597	1023	572	43.9	43.6	1109	597	1023	572
B	38.6	39.1	677	373	647	373	33.8	32.5	417	232	370	208
C	24.7	24.2	154	85	163	81	18.2	17.0	35	20	30	18
D	24.4	23.9	91	51	89	46	14.0	13.1	15	8	11	14
E	18.8	18.2	0.19	0.09	0	0	12.4	11.7	0.03	0.01	0	0

Table 9.5: The detection efficiencies for the proton decay MC and the number of surviving event in the atmospheric neutrino MC and in the observed data at each event selection criterion for $p \to e^+\eta$ and $p \to \mu^+\eta$ ($\eta \to 2\gamma$). All the decay modes of η meson are included in the proton decay MC. The atmospheric neutrino MC is normalized with the observed data using single-ring e-like events. The criteria (A$\sim$E) are described in Section 9.1.1 and Table 9.4.

$p \to l^+\eta$ ($\eta \to 3\pi^0$) Mode Search

Modes	A Ring	B PID	C $M_{\rm meson}$	D decay-e	E $M_{\rm tot}$	$P_{\rm tot}$
$p \to e^+\eta$ ($3\pi^0$)	4, 5	SSSS(S)	400$\sim$700 (η)	0	800$\sim$1050	$<$150
$p \to \mu^+\eta$ ($3\pi^0$)	4, 5	NSSS(S)*	400$\sim$700 (η)	1	800$\sim$1050	$<$250

Table 9.6: The event selection criteria for $p \to e^+\eta$ and $p \to \mu^+\eta$ ($3\pi^0$).

Event Characteristics In these proton decay modes, η meson decays into 3 π^0s, and 3 π^0s immediately decay into 6 γ-rays. Therefore, one ring from a charged lepton and 6 rings from the γ-rays can be observed in principle. However, the ring counting algorithm was only possible to find up to 5 rings. Consequently, the criterion of the number of ring was applied to select events with 4 or 5 rings. The number of ring distribution for the proton decay MC is shown in Figure 9.24. The fraction of 4 or 5 rings was 77% (84%) for SK-I free proton decay of the $\eta \to 3\pi^0$ mode of $p \to e^+\eta$ ($p \to \mu^+\eta$).

The invariant mass of the η meson was reconstructed only by three or four shower type rings, though there should be 6 rings from $3\pi^0$s. That resulted in the worse invariant mass resolution for the η meson. Therefore, the event selection window of the η invariant mass was larger than that in the search via the $\eta \to 2\gamma$ mode. The reconstructed η invariant mass distributions for the proton decay MC are shown in Figure 9.25.

The background rates for $p \to e^+\eta$ was not low enough with the standard event selection criteria of $P_{\rm tot} < 250$ MeV/c. In order to further reduce the background, the tighter total momentum cut of $P_{\rm tot} < 150$ MeV/c was applied for the $p \to e^+\eta$ mode.

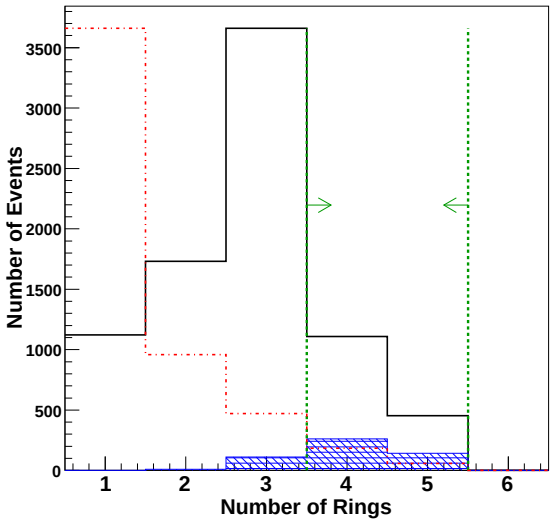

Figure 9.24: The number of ring distributions of $p \rightarrow e^{+}\eta$ in SK-I. The black line shows the distribution for all the decay branch of the η meson (same as Figure 9.21). The shaded histogram is the distribution for the free proton decay events of the $\eta \rightarrow 3\pi^{0}$ mode only. The dashed line histogram shows the atmospheric neutrino backgrounds.

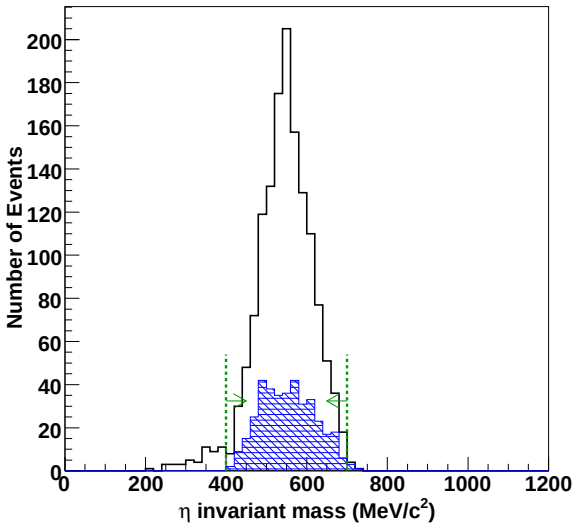

Figure 9.25: The η invariant mass distributions of $p \rightarrow e^{+}\eta$ in SK-I. The black solid line shows the distribution for all the decay branch of the η meson. The Shaded histogram is the distribution for the free proton decay events of the $\eta \rightarrow 3\pi^{0}$ mode only.

The Search Results The detection efficiencies for the proton decay MC and the number of events for the normalized atmospheric neutrino MC and the observed data at each selection criteria are summarized in Table 9.7. The momentum and the total invariant mass distributions in the final selection criterion are shown in Figure 9.26.

The detection efficiencies for $p \to e^+\eta$ and $p \to \mu^+\eta$ ($3\pi^0$) were estimated to be 8.1% (7.6%) and 6.1% (5.4%) in SK-I (SK-II), respectively. For free proton decay events of the $\eta \to 3\pi^0$ mode in SK-I, the detection efficiencies were 67% and 34% for $p \to e^+\eta$ and $p \to \mu^+\eta$, respectively.

The background events for $p \to e^+\eta$ and $p \to \mu^+\eta$ were estimated to be 0.16 and 0.45 events in total (SK-I+SK-II), respectively.

Nucleon decay signals were searched in the SK-I and SK-II data. Two candidates were found in the SK-II data for $p \to \mu^+\eta$ mode, while the number of the expected background was 0.45. The details of the candidates are described in Appendix B.1.

	$p \to e^+\eta$ ($\eta \to 3\pi^0$)						$p \to \mu^+\eta$ ($\eta \to 3\pi^0$)					
	eff.(%)		atm. ν MC		FC Data		eff.(%)		atm. ν MC		FC Data	
	SK-I	SK-II	SK-I	SK-II	SK-I	SK-II	SK-I	SK-II	SK-I	SK-II	SK-I	SK-II
F.V.	97.9	100.4	12586	6684	12232	6584	98.1	99.4	12586	6684	12232	6584
A	18.9	20.8	571	334	539	332	21.5	21.3	571	334	539	332
B	17.2	18.8	395	234	370	253	13.4	12.7	178	112	158	103
C	16.6	17.8	165	94	156	101	10.5	9.2	52	29	39	28
D	16.3	17.5	89	51	66	43	7.9	7.1	21	11	15	14
E	8.1	7.6	0.08	0.08	0	0	6.1	5.4	0.30	0.15	0	2

Table 9.7: The detection efficiencies for the proton decay MC and the number of surviving event in the atmospheric neutrino MC and in the observed data at each event selection criterion for the $p \to e^+\eta$ and $p \to \mu^+\eta$ ($\eta \to 3\pi^0$). All the decay modes of η meson are included in the proton decay MC. The atmospheric neutrino MC is normalized with the observed data using single-ring e-like events. The criteria (A$\sim$E) are described in Section 9.1.1 and Table 9.6.

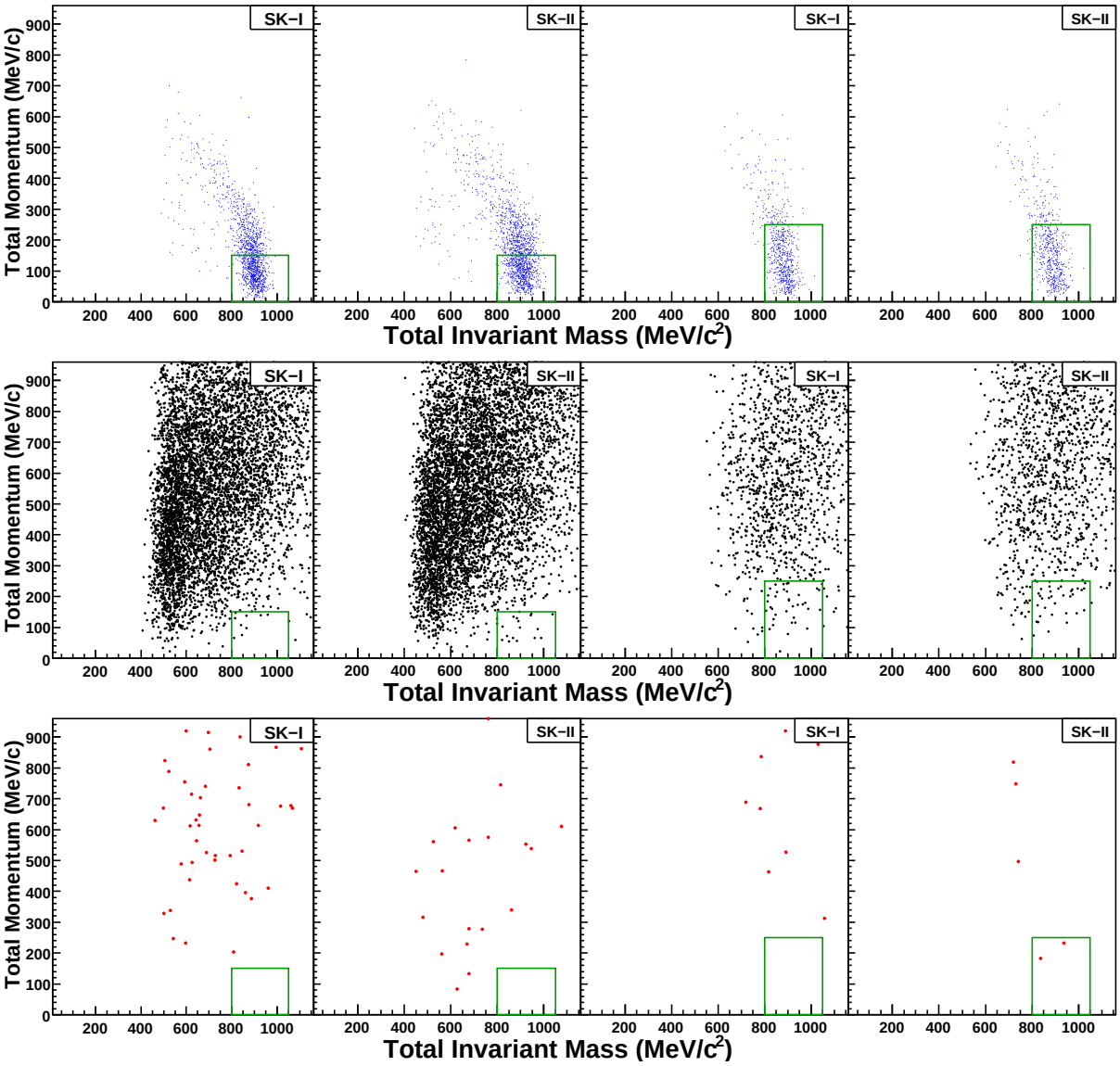

Figure 9.26: Total momentum versus total invariant mass distributions, from left to right: SK-I $p \to e^+\eta$; SK-II $p \to e^+\eta$; SK-I $p \to \mu^+\eta$; and SK-II $p \to \mu^+\eta$, from top to bottom: the proton decay MC; the atmospheric neutrino MC; and the observed data. These events satisfy the event selection criteria for $p \to e^+\eta$ $(3\pi^0)$ or $p \to \mu^+\eta$ $(3\pi^0)$ except for the selection by the total momentum and total mass. The boxes in figures indicate the criteria. Two candidates were found in the SK-II data for $p \to \mu^+\eta$.

9.1.4 $p \to l^+\rho^0$ Mode Search

	A	B	C	D	E	
Modes	Ring	PID	$M_{\rm meson}$	decay-e	$M_{\rm tot}$	$P_{\rm tot}$
$p \to e^+\rho^0$	3	SNN*	600∼900 (ρ)	0, 1	800∼1050	<150
$p \to \mu^+\rho^0$	3	NNN*	600∼900 (ρ)	1, 2	800∼1050	<250

Table 9.8: The event selection criteria for $p \to e^+\rho^0$ and $p \to \mu^+\rho^0$.

Event Characteristics In the proton decay of $p \to e^+\rho^0$ and $p \to \mu^+\rho^0$, the momentum of a charged lepton and a ρ meson, which depends on the ρ meson mass with the width of Γ =149 MeV, is about 170 MeV/c. For $p \to \mu^+\rho^0$, the muon momentum can be lower than the Cherenkov threshold for muons. The ρ meson decays into $\pi^+\pi^-$ with the branching ratio of $\sim$ 100%. The two pions suffer from strong interactions with nucleons in water, also in a nucleus in the case of a proton decay in a ^{16}O nucleus. Accordingly, finding all the three Cherenkov rings from the charged lepton and the two charged pions is intrinsically difficult. However, in order to reduce the background with the selection by the total invariant mass and the total momentum, finding all three rings were required to reconstruct the mass and the momentum of a proton. Figure 9.27 shows the number of ring distributions for the proton decay MC. The fraction of 3 rings was 50% and 27% for the free proton decay of $p \to e^+\rho^0$ and $p \to \mu^+\rho^0$, respectively. The lower efficiency for $p \to \mu^+\rho^0$ was due to proton decay events with an invisible muon.

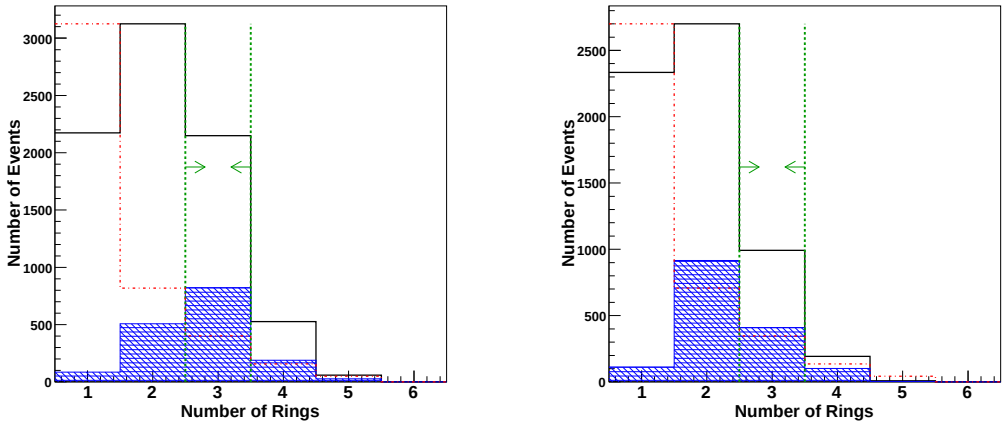

Figure 9.27: The number of ring distributions for the $p \to e^+\rho^0$ MC (left) and the $p \to \mu^+\rho^0$ MC (right) in SK-I. The shaded histograms are the distributions for the free proton decay events. The dashed histograms show the atmospheric neutrino backgrounds.

The charged pions from the decay of the ρ meson has a low momentum of about 300 MeV/c. Therefore, the PID with a Cherenkov ring pattern and an opening angle was used for both $p \to e^+\rho^0$ and $p \to \mu^+\rho^0$.

The invariant mass of the ρ meson was reconstructed by two non-shower type rings and

required to be in between 600 to 900 MeV/c^2 as shown in Figure 9.28. Most of the events shown in ρ meson distributions were from free proton decay events. This means that the events from proton decays in a ^{16}O nucleus were difficult to survive the selection by the number of ring and the PID.

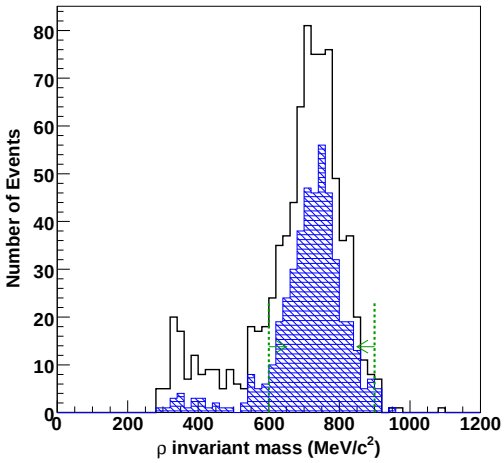

Figure 9.28: The ρ invariant mass distributions for $p \to e^+\rho^0$ in SK-I. The Shaded histogram is the distribution for the free proton decay events.

For these mode searches, one more Michel electron is expected from the π^+ decay in addition to one Michel electron from the μ decay. The number of Michel electrons were required to be consistent with this expectation.

The total momentum versus total invariant mass distributions for the atmospheric neutrino MC is shown in Figure 9.29. The $p \to e^+\rho^0$ mode had a relatively higher background rate than that of $p \to \mu^+\rho^0$ mode. In order to reduce the background, the tighter total momentum cut of $P_{\rm tot} < 150$ MeV/c was applied for the $p \to e^+\rho^0$ mode.

The Search Results The detection efficiencies for the proton decay MC and the number of events for the normalized atmospheric neutrino MC and the observed data at each selection criteria are summarized in Table 9.9. The momentum and the total invariant mass distributions in the final selection criterion are shown in Figure 9.29.

The detection efficiencies for $p \to e^+\rho^0$ and $p \to \mu^+\rho^0$ were estimated to be 4.9% (4.2%) and 1.8% (1.5%) in SK-I (SK-II), respectively. For the free proton decay events in SK-I, the detection efficiencies were 20% and 7% for $p \to e^+\rho^0$ and $p \to \mu^+\rho^0$, respectively. Most of the surviving events in the proton decay MC were from free proton decay events. Their fraction in total surviving events was about 80% for both modes.

The background events for $p \to e^+\eta$ and $p \to \mu^+\eta$ were estimated to be 0.35 and 0.42 events in total (SK-I+SK-II), respectively.

Nucleon decay signals were searched in the SK-I and SK-II data. One candidate was found in the SK-I data for the $p \to \mu^+\rho^0$ mode, while the number of the expected background is 0.42. The details of the candidate is described in Appendix B.2.

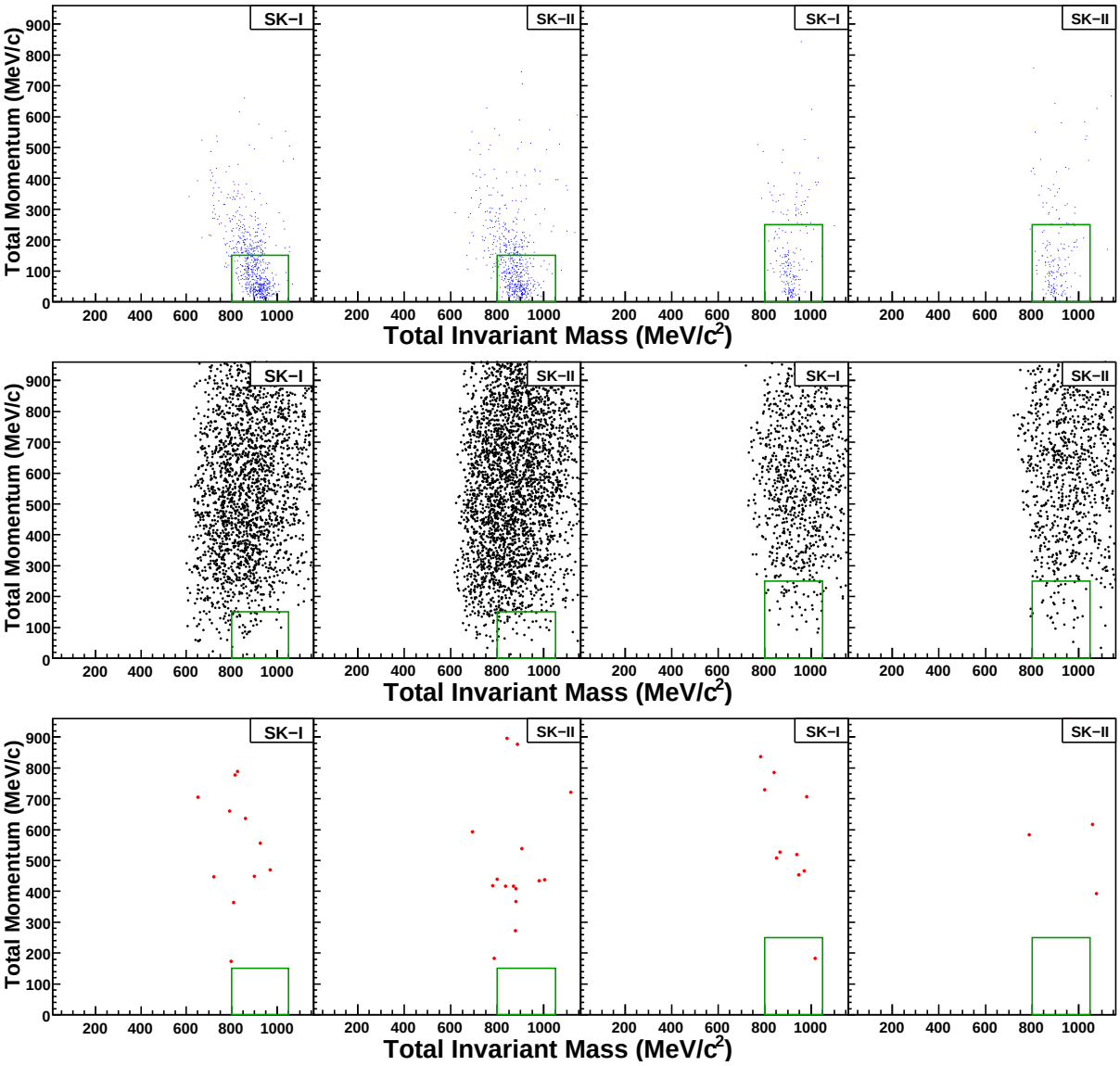

Figure 9.29: Total momentum versus total invariant mass distributions, from left to right: SK-I $p \to e^+\rho^0$; SK-II $p \to e^+\rho^0$; SK-I $p \to \mu^+\rho^0$; and SK-II $p \to \mu^+\rho^0$, from top to bottom: the proton decay MC; the atmospheric neutrino MC; and the observed data. These events satisfy the event selection criteria for $p \to e^+\rho^0$ or $p \to \mu^+\rho^0$ except for the selection by the total momentum and total mass. The boxes in figures indicate the criteria. One candidate was found in the SK-I data for $p \to \mu^+\rho^0$ mode.

	$p \to e^+\rho^0$						$p \to \mu^+\rho^0$					
	eff.(%)		atm. ν MC		FC Data		eff.(%)		atm. ν MC		FC Data	
	SK-I	SK-II	SK-I	SK-II	SK-I	SK-II	SK-I	SK-II	SK-I	SK-II	SK-I	SK-II
F.V.	96.6	99.4	12586	6684	12232	6584	74.3	76.7	12586	6684	12232	6584
A	25.8	25.6	1109	597	1023	572	11.8	11.4	1109	597	1023	572
B	10.3	9.2	127	86	129	87	3.0	2.9	32	19	33	20
C	8.1	7.2	37	27	33	33	2.6	2.3	21	13	20	14
D	8.1	7.2	31	22	22	27	2.4	2.1	14	9	15	11
E	4.9	4.2	0.23	0.12	0	0	1.8	1.5	0.30	0.12	1	0

Table 9.9: The detection efficiencies for the proton decay MC and the number of surviving event in the atmospheric neutrino MC and in the observed data at each event selection criterion for $p \to e^+\rho^0$ and $p \to \mu^+\rho^0$. The atmospheric neutrino MC is normalized with the observed data using single-ring e-like events. The criteria (A∼E) are described in Section 9.1.1 and Table 9.8.

9.1.5 $p \to l^+\omega$ Mode Search

Two of the ω meson decay modes were studied in this thesis: One is the $\omega \to \pi^+\pi^-\pi^0$ mode (Br=89%), and the other is the $\omega \to \pi^0\gamma$ mode (Br=9%). The momentum of a generated charged lepton and a ω meson is 143 (105) MeV/c^2 in $p \to e^+\omega$ ($p \to \mu^+\omega$). For the $p \to \mu^+\omega$ mode, the muon momentum is lower than the Cherenkov threshold, and the muon ring cannot be observed. Therefore, the existence of the muon is indicated only by a Michel electron detection from the muon decay. The ω meson suffers from the nuclear effect in the case of a decay in a ^{16}O nucleus. Only $\sim$ 20% of the ω meson could escape from the nucleus. This cause the inefficiency for these two mode searches. In this section, the selection criteria of the $p \to l^+\omega$ search via $\omega \to \pi^0\gamma$ is first explained, and then the criteria of $p \to l^+\omega$ search via $\omega \to \pi^+\pi^-\pi^0$ is explained.

$p \to l^+\omega$ ($\omega \to \pi^0\gamma$) Mode Search

	A	B	C	D	E	
Modes	Ring	PID	$M_{\rm meson}$	decay-e	$M_{\rm tot}$	$P_{\rm tot}$
$p \to e^+\omega$ ($\pi^0\gamma$)	3, 4	SSS(S)	650∼900 (ω)	0	800∼1050	<150
$p \to \mu^+\omega$ ($\pi^0\gamma$)	2, 3	SS(S)	650∼900 (ω)	1	-	<200

Table 9.10: The event selection criteria for $p \to e^+\omega$ and $p \to \mu^+\omega$ ($\pi^0\gamma$).

Event Characteristics In the $\omega \to \pi^0\gamma$ decay mode, the π^0 decays into two γ-rays, and three shower type rings can be observed from the decays of the ω meson. The π^0 momentum from the ω decay is about 380 MeV/c in the ω meson rest frame. Due to the same reason as $p \to e^+\pi^0$ or $p \to \mu^+\pi^0$, one of the two rings from the π^0 decay cannot be observed in a certain probability. Therefore, two or three shower type rings were required from the ω meson decay,

and one more shower type ring from e^+ was required only in the case of the $p \to e^+\omega$ mode. Figure 9.30 shows the number of ring distributions for the proton decay MC. The fraction of 3-rings or 4-rings (2-rings or 3-rings) was 95% (97%) for SK-I free proton decay of the $\omega \to \pi^0\gamma$ mode for $p \to e^+\omega$ ($p \to \mu^+\omega$).

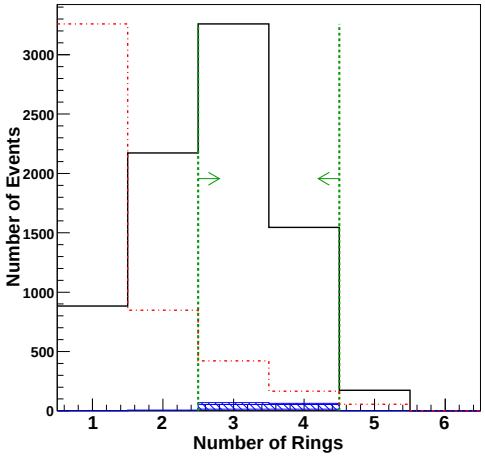

Figure 9.30: The number of ring distributions of $p \to e^+\omega$ in SK-I. The black solid line histogram shows the distribution for all the ω meson decay modes. The shaded histograms is the distribution for the free proton decay events of the $\omega \to \pi^0\gamma$ mode only. Dashed lines and arrows indicate the selection criterion. The dashed histogram is the atmospheric neutrino backgrounds.

The ω invariant mass was reconstructed by all the detected rings for the $p \to \mu^+\omega$ mode. For the $p \to e^+\omega$ mode, it was reconstructed by the detected rings except for one ring, which was assumed to be e^+ ring. The ω invariant mass distribution for the proton decay MC are shown in Figure 9.31. The invariant mass was well reconstructed, The lower invariant mass peak in the proton decay MC was due to the another ω meson decay mode of $\omega \to \pi^+\pi^-\pi^0$.

Since the muon is invisible for the $p \to \mu^+\omega$ mode, the total momentum corresponds not to the source proton momentum, but to the ω meson momentum. Thus, the reconstructed momentum for the free proton decay in SK-I was peaked at 123 MeV/c as shown in Figure 9.32. In order to eliminate the background sufficiently, the tighter total momentum cuts were applied for both modes; $P_{\rm tot} < 150$ MeV/c for $p \to e^+\omega$ and $P_{\rm tot} < 200$ MeV/c for $p \to \mu^+\omega$.

The Search Results The detection efficiencies for the proton decay MC and the number of events for the normalized atmospheric neutrino MC and the observed data at each selection criteria are summarized in Table 9.11. The momentum and the total invariant mass distributions in the final selection criterion are shown in Figure 9.33.

The detection efficiencies for $p \to e^+\omega$ and $p \to \mu^+\omega$ ($\pi^0\gamma$) were estimated to be 2.4% (2.2%) and 2.8% (2.8%) in SK-I (SK-II), respectively. The branching ratio was taken into account in the estimation. For the free proton decay of the $\omega \to \pi^0\gamma$ mode in SK-I, the detection efficiencies were 82.5% and 66.9%, and their fraction in total surviving events were 59% and 41%, respectively. In the proton decays of the $p \to \mu^+\omega$ mode, the efficiency of the fiducial

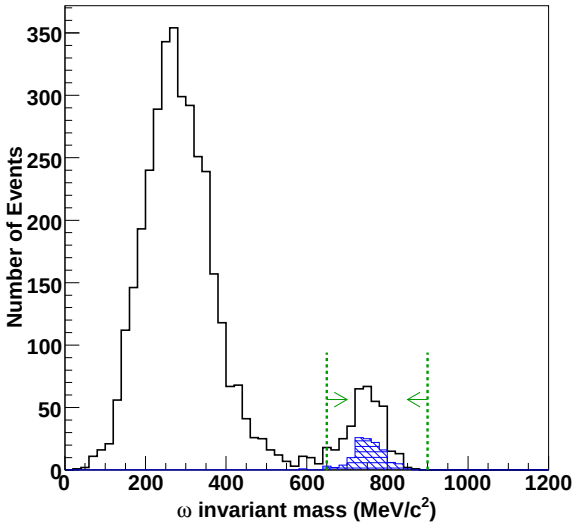

Figure 9.31: The ω invariant mass distributions of $p \rightarrow e^{+}\omega$ in SK-I. The black solid line histogram shows the distribution for all the ω meson decay modes. The shaded histograms are the distribution for the free proton decay events of the $\omega \rightarrow \pi^{0}\gamma$ mode only. The lower invariant mass peak consists of the another decay mode of $\omega \rightarrow \pi^{+}\pi^{-}\pi^{0}$.

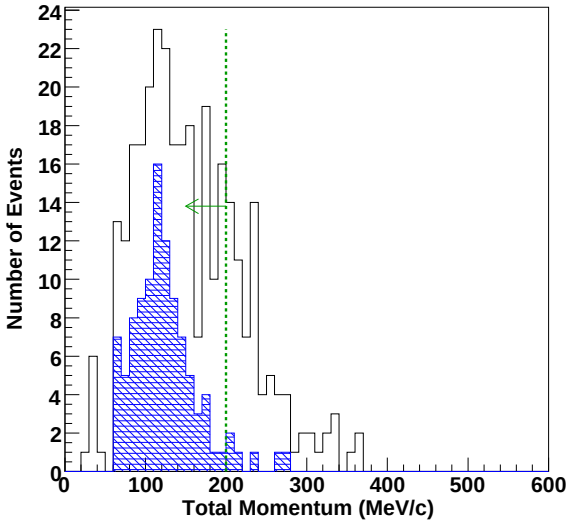

Figure 9.32: The total momentum distributions of the $p \rightarrow \mu^{+}\omega$ MC in SK-I. The black solid line histogram shows the distribution for all the ω meson decay modes. The shaded histograms is the distribution for the free proton decay events of the $\omega \rightarrow \pi^{0}\gamma$ mode only. Only the events which satisfy the selection criteria (A $\sim$ D) are plotted.

volume cut was not about 100%. This is because a ω meson and other secondary particles could not escape from a nucleus in some proton decay events, which could not pass the FC reduction process as described in Section 5.6.

The background events for $p \to e^+\omega$ and $p \to \mu^+\omega$ were estimated to be 0.14 and 0.31 events in total (SK-I+SK-II), respectively. The low background rate was achieved with the tighter total momentum cut.

Nucleon decay signals were searched in the SK-I and SK-II data No candidate event was observed in the data for both modes.

	$p \to e^+\omega$ ($\omega \to \pi^0\gamma$)						$p \to \mu^+\omega$ ($\omega \to \pi^0\gamma$)					
	eff.(%)		atm. ν MC		FC Data		eff.(%)		atm. ν MC		FC Data	
	SK-I	SK-II	SK-I	SK-II	SK-I	SK-II	SK-I	SK-II	SK-I	SK-II	SK-I	SK-II
F.V.	97.6	99.3	12586	6684	12232	6584	86.8	90.6	12586	6684	12232	6584
A	58.4	58.6	1542	845	1429	808	60.6	61.3	3365	1759	3157	1732
B	46.1	47.3	966	542	917	544	46.7	47.4	2045	1096	1957	1037
C	4.3	4.3	248	139	233	156	5.0	4.9	182	97	184	90
D	4.3	4.3	131	75	108	62	3.8	3.7	51	27	56	23
E	2.4	2.2	0.10	0.04	0	0	2.8	2.8	0.24	0.07	0	0

Table 9.11: The detection efficiencies for the proton decay MC and the number of surviving event in the atmospheric neutrino MC and in the observed data at each event selection criterion for $p \to e^+\omega$ and $p \to \mu^+\omega$ ($\omega \to \pi^0\gamma$). All the ω meson decay modes are included in the proton decay MC. The atmospheric neutrino MC is normalized with the observed data using single-ring e-like events The criteria (A$\sim$E) are described in Section 9.1.1 and Table 9.10.

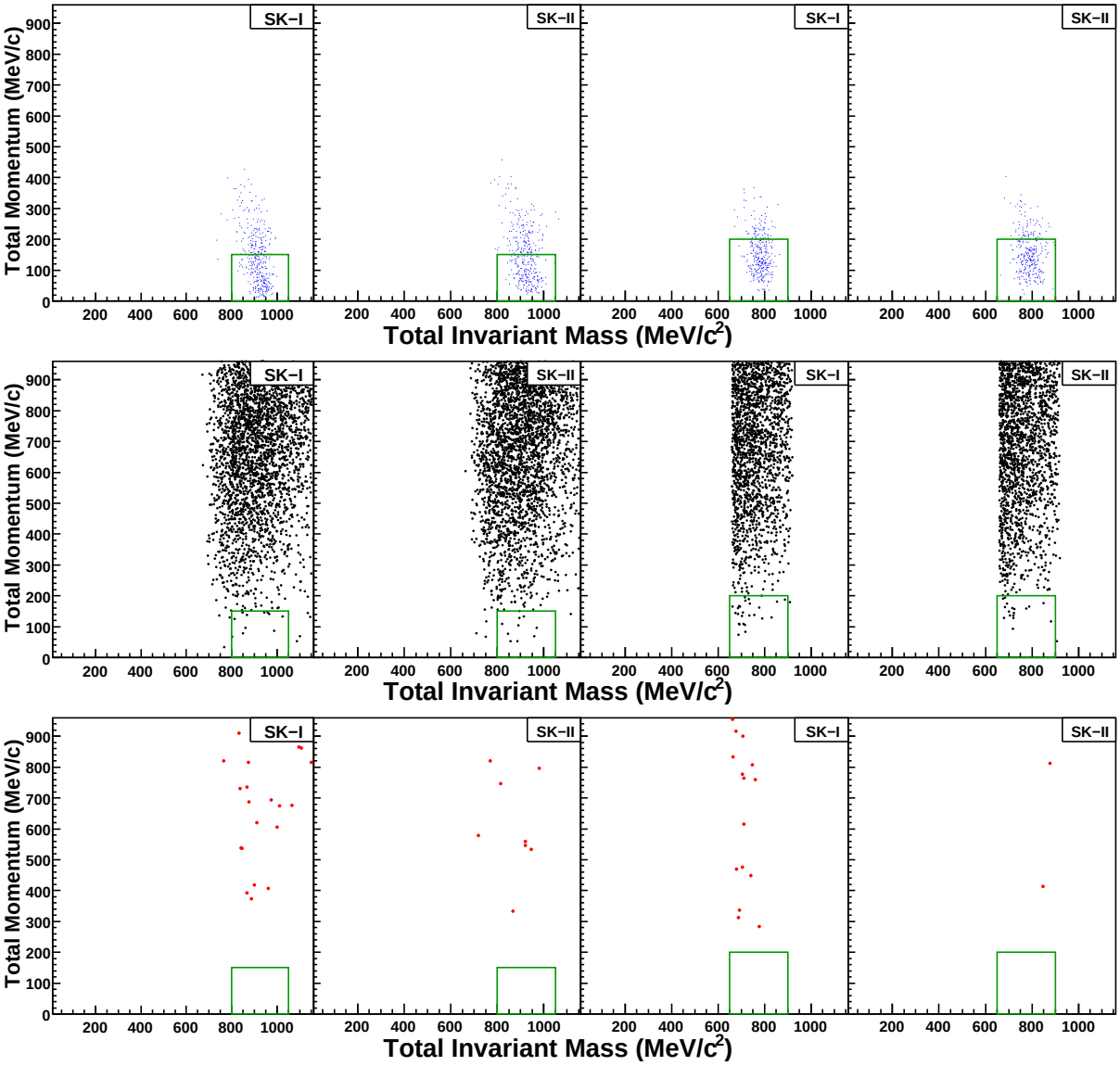

Figure 9.33: Total momentum versus total invariant mass distributions, from left to right: SK-I $p \to e^+\omega$; SK-II $p \to e^+\omega$; SK-I $p \to \mu^+\omega$; and SK-II $p \to \mu^+\omega$, from top to bottom: the proton decay MC; the atmospheric neutrino MC; and the observed data. These events satisfy the event selection criteria for $p \to e^+\omega$ ($\pi^0\gamma$) or $p \to \mu^+\omega$ ($\pi^0\gamma$) except for the selection by the total momentum and total mass. The boxes in figures indicate the criteria. No candidates were found for both $p \to e^+\omega$ ($\pi^0\gamma$) and $p \to \mu^+\omega$ ($\pi^0\gamma$) in the data.

$p \to l^+\omega$ $(\omega \to \pi^+\pi^-\pi^0)$ **Mode Search**

	A	B	C	D	E		F
Modes	Ring	PID	$M_{\rm meson}$	decay-e	$M_{\rm tot}$	$P_{\rm tot}$	
$p \to e^+\omega$ $(\pi^+\pi^-\pi^0)$	4	SSSN*	85∼185 (π)	0, 1	600∼800	<200	P_{e^+}
$p \to \mu^+\omega$ $(\pi^+\pi^-\pi^0)$	3	SSN*	85∼185 (π)	2	450∼700	<200	

Table 9.12: The event selection criteria for $p \to e^+\omega$ and $p \to \mu^+\omega$ $(\pi^+\pi^-\pi^0)$. The selection criterion F is the positron momentum cut ($100 < P_{e^+} < 200$ MeV/c).

Event Characteristics In this ω decay mode, the ω decays into two low momentum charged pions and a neutral pion. Their momenta are about 220 MeV/c. In order to find the low momentum non-shower type ring, the PID with both a Cherenkov ring pattern and an opening angle was used for these modes. Due to the strong interaction of the charged pions in water, finding both of the two charged pion rings is difficult. Therefore, finding only one of the two charged pion rings were required for these mode searches. The number of ring distribution is shown in Figure 9.34. For the $p \to e^+\omega$ $(p \to \mu^+\omega)$ mode, 4 (3) rings were required to be found in total. The efficiency of the number of ring cut was 27% (42%) for SK-I free proton decay MC of the $p \to e^+\omega$ $(p \to \mu^+\omega)$, $\omega \to \pi^+\pi^-\pi^0$ mode.

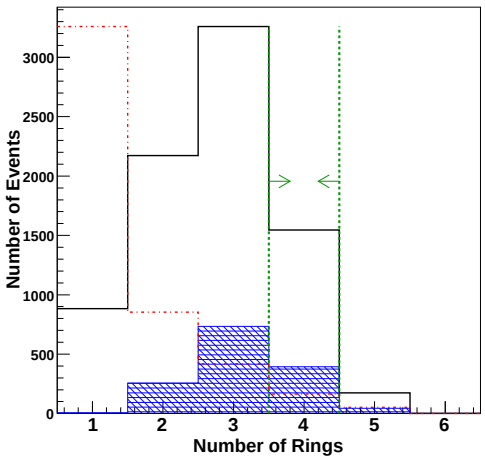

Figure 9.34: The number of ring distributions of $p \to e^+\omega$ MC in SK-I. The black solid line histogram shows the distribution for all the ω meson decay modes (same as Figure 9.34). The shaded histogram is the distribution for the free proton decay events of the $\omega \to \pi^+\pi^-\pi^0$ mode only. Dashed lines and arrows indicate the selection criterion. The dashed histogram is the atmospheric neutrino backgrounds.

Since one of the two charged pions were assumed to be invisible in the selection criteria, the invariant mass of the ω and the proton cannot be reconstructed for these modes. Instead of the ω mass reconstruction, the reconstructed π^0 invariant mass was required to be consistent with

π^0 mass. As for the total invariant mass, the event selection criteria for the total mass were set to be lower than the normal event selection criteria as shown in Figure 9.36. The selection windows were determined to reduce the atmospheric neutrino MC though they were not wide enough even for the free proton decay events.

For the $p \to \mu^+\omega$ mode, both of two Michel electrons from the decay of μ^+ and π^+ were required to be found. Although the detection efficiency is decreased by a factor of 2, this cut could greatly reduce the background by a order of magnitude.

In order to reduce the background further, the positron momentum was also required to be consistent with the source positron momentum for the $p \to e^+\omega$ mode. Figure 9.35 shows the positron momentum distributions for the proton decay MC, the atmospheric neutrino MC and the observed data. This criteria could reduce the background by a factor of 2, while the detection efficiency is decreased by about 20%.

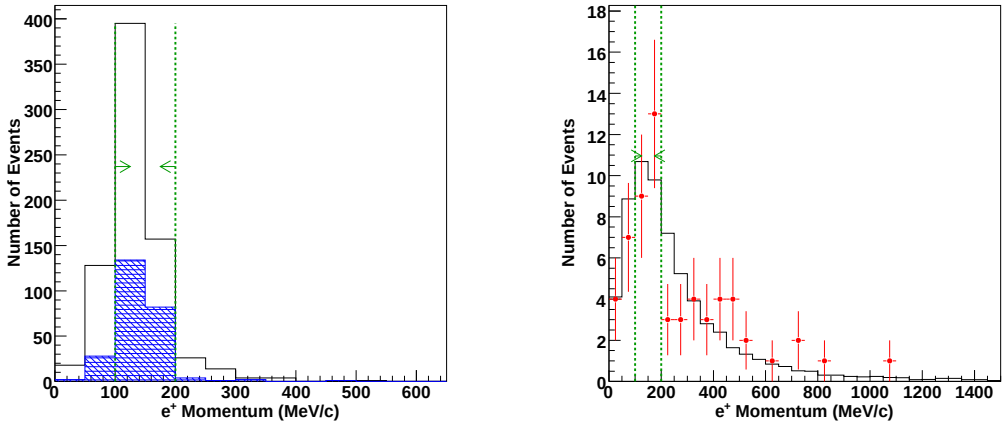

Figure 9.35: Positron momentum distribution for $p \to e^+\omega$ MC (left) and the atmospheric neutrino MC (solid lines in the right) and the observed data (points in the right) in SK-I. The solid line histogram in the left figure shows the distribution for all the ω meson decay modes. A shaded histogram is the distribution for the free proton decay events of the $\omega \to \pi^+\pi^-\pi^0$ mode only. Dashed lines and arrows indicates the selection criterion. Only the events which satisfy the selection criteria (A$\sim$D) are plotted.

The Search Results The detection efficiencies for the proton decay MC and the number of events for the normalized atmospheric neutrino MC and the observed data at each selection criteria are summarized in Table 9.13. The momentum and the total invariant mass distributions in the final selection criterion are shown in Figure 9.36.

The detection efficiencies for $p \to e^+\omega$ and $p \to \mu^+\omega$ ($\pi^+\pi^-\pi^0$) were estimated to be 2.5% (2.3%) and 2.7% (2.4%) in SK-I (SK-II), respectively. The branching ratio was included in the estimation. For free proton decay of the $\omega \to \pi^+\pi^-\pi^0$ mode in SK-I, the detection efficiencies were 8.5% and 7.7%, and their fraction in total surviving events were 61% and 51%, respectively.

The background events for $p \to e^+\omega$ and $p \to \mu^+\omega$ were estimated to be 0.39 and 0.17 events in total (SK-I+SK-II), respectively.

Nucleon decay signals were searched in the SK-I and SK-II data. Each one event survived the criteria A $\sim$ E in SK-I and SK-II for $p \to e^+\omega$. However, one event in SK-II was rejected by the selection by the positron momentum. One event in SK-I passed the selection by the positron momentum and remained as a candidate for $p \to e^+\omega$ (3π) mode, while the expected background was 0.39. The details of the candidate is described in Appendix B.3.

	$p \to e^+\omega$ ($\omega \to 3\pi$)						$p \to \mu^+\omega$ ($\omega \to 3\pi$)					
	eff.(%)		atm. ν MC		FC Data		eff.(%)		atm. ν MC		FC Data	
	SK-I	SK-II	SK-I	SK-II	SK-I	SK-II	SK-I	SK-II	SK-I	SK-II	SK-I	SK-II
F.V.	97.6	99.3	12586	6684	12232	6584	86.8	90.6	12586	6684	12232	6584
A	18.8	18.9	432	248	406	236	27.0	26.1	1109	597	1023	572
B	9.6	9.5	139	86	117	77	15.0	14.4	417	232	370	208
C	9.1	8.9	75	41	70	34	13.1	12.4	175	90	164	79
D	9.1	8.9	65	36	61	30	6.4	5.2	15	7	15	5
E	3.2	2.9	0.57	0.25	1	1	2.7	2.4	0.10	0.07	0	0
F	2.5	2.3	0.26	0.13	1	0	-	-	-	-	-	-

Table 9.13: The detection efficiencies for the proton decay MC and the number of surviving event in the atmospheric neutrino MC and in the observed data at each event selection criterion for $p \to e^+\omega$ and $p \to \mu^+\omega$ ($\omega \to \pi^+\pi^-\pi^0$). All the ω meson decay modes are included in the proton decay MC. The atmospheric neutrino MC is normalized with the observed data using single-ring e-like events. The criteria (A$\sim$F) are described in Section 9.1.1 and Table 9.12. The criterion F is the positron momentum cut, which is the special cut for $p \to e^+\omega$.

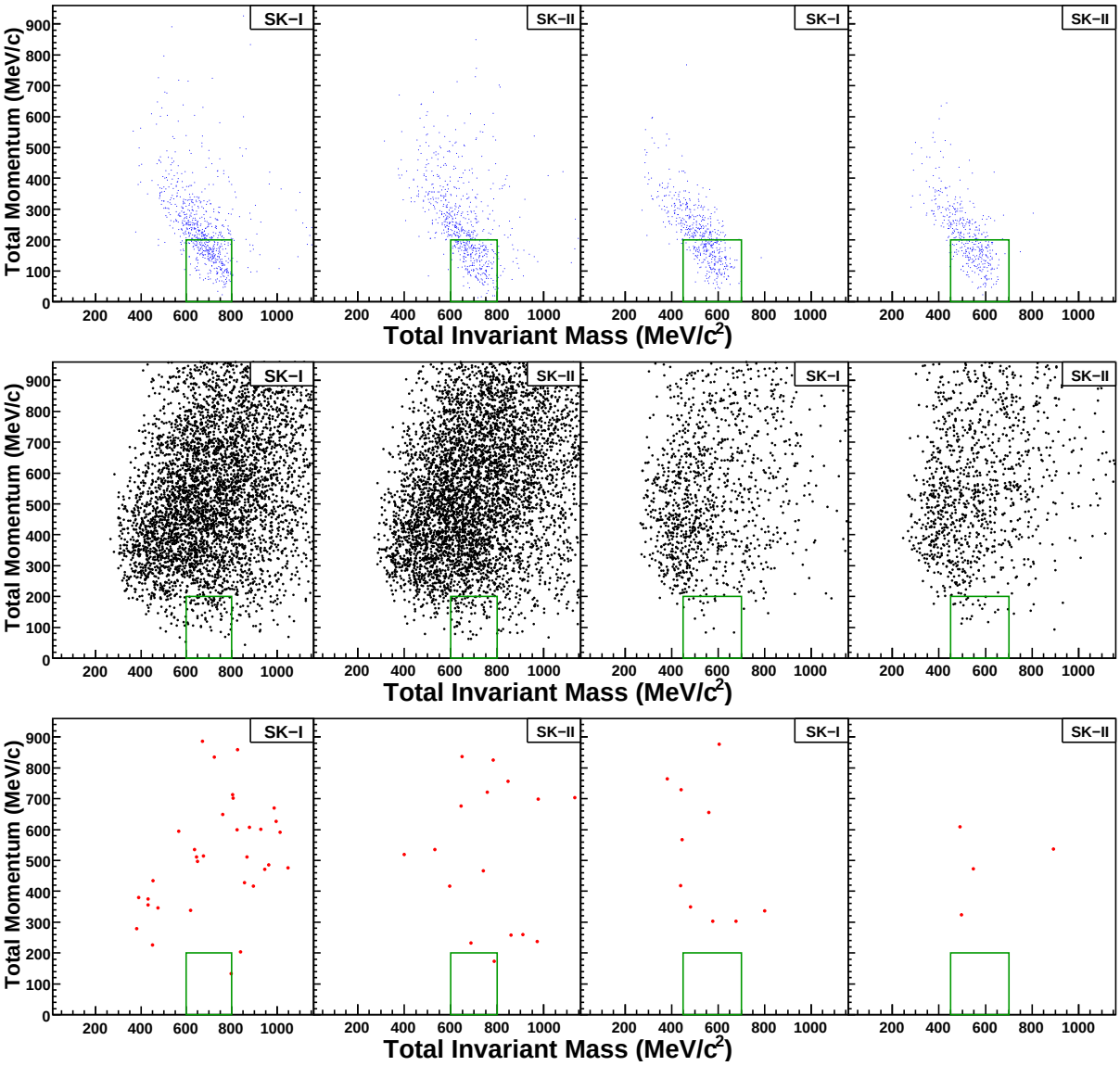

Figure 9.36: Total momentum versus total invariant mass distributions, from left to right: SK-I $p \to e^+\omega$; SK-II $p \to e^+\omega$; SK-I $p \to \mu^+\omega$; and SK-II $p \to \mu^+\omega$, from top to bottom: the proton decay MC; the atmospheric neutrino MC; and the observed data. These events satisfy the event selection criteria for $p \to e^+\omega$ (3π) or $p \to \mu^+\omega$ (3π) except for the selection by the total momentum and total mass. The boxes in figures indicate the criteria. One candidate was found in the SK-I data for $p \to e^+\omega$. The other remaining event in the SK-II data for $p \to e^+\omega$ is rejected by the positron momentum cut.

9.1.6 $n \to l^+\pi^-$ Mode Search

	A	B	C	D	E	
Modes	Ring	PID	$M_{\rm meson}$	decay-e	$M_{\rm tot}$	$P_{\rm tot}$
$n \to e^+\pi^-$	2	SN	-	0	800∼1050	<250
$n \to \mu^+\pi^-$	2	NN	-	1	800∼1050	<250

Table 9.14: The event selection criteria for $n \to e^+\pi^-$ and $n \to \mu^+\pi^-$

Event Characteristics All the neutrons in a H_2O molecule are bounded in a nucleus. Then, all the generated charged pions suffer from the nuclear effect, and detection efficiencies for neutron decay searches tend to be lower compared to proton decay searches.

The momentum of a charged lepton and a charged pion is about 460 MeV/c, almost same as that of $p \to l^+\pi^0$. In these modes, a Cherenkov ring from the charged pion generated from the nucleon decay can be directly observed. Figure 9.37 shows the number of ring distributions of the neutron decay MC. Approximately 50% of the neutron decay events in SK-I were 2-rings event from the charged lepton and the charged pion. Therefore, there was no event selection by a meson invariant mass for these modes.

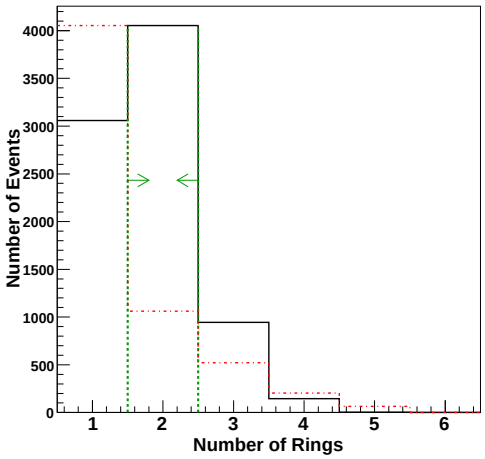

Figure 9.37: The number of ring distributions for the $n \to e^+\pi^-$ MC in SK-I. Dashed lines and arrows indicate the selection criterion. The dashed line histogram is the atmospheric neutrino backgrounds.

For the total invariant mass reconstruction in the $n \to \mu^+\pi^-$ mode, we should determine which ring the muon or the charged pion is. As described before, a better combination for the neutron mass was selected. This resulted in the narrower invariant mass distribution of $n \to \mu^+\pi^-$ than that of the $n \to e^+\pi^-$ MC as shown in Figure 9.38.

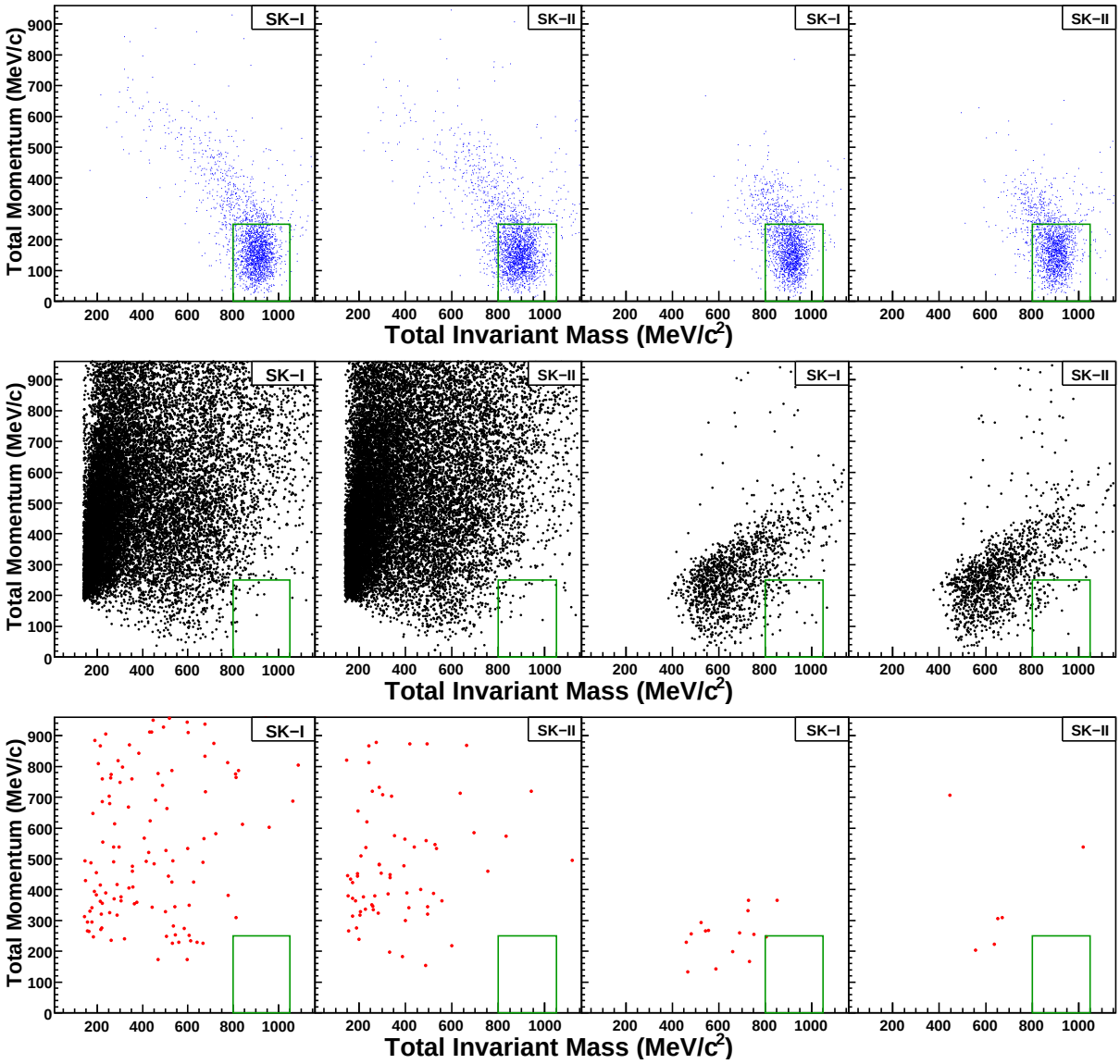

Figure 9.38: Total momentum versus total invariant mass distributions, from left to right: SK-I $n \to e^+\pi^-$; SK-II $n \to e^+\pi^-$; SK-I $n \to \mu^+\pi^-$; and SK-II $n \to \mu^+\pi^-$, from top to bottom: the proton decay MC; the atmospheric neutrino MC; and the observed data. These events satisfied the event selection criteria for $n \to e^+\pi^-$ or $n \to \mu^+\pi^-$ except for the selection by the total momentum and total mass. The boxes in figures indicate the criteria. One candidate was found in the SK-I for $n \to \mu^+\pi^-$.

The Search Results The detection efficiencies for the proton decay MC and the number of events for the normalized atmospheric neutrino MC and the observed data at each selection criteria are summarized in Table 9.15. The momentum and the total invariant mass distributions in the final selection criterion are shown in Figure 9.38.

The detection efficiencies for $n \to e^+\pi^-$ and $n \to \mu^+\pi^-$ were estimated to be 19.4% (19.3%) and 16.7% (15.6%) in SK-I (SK-II), respectively. The background events for $n \to e^+\pi^-$ and $n \to \mu^+\pi^-$ were estimated to be 0.27 and 0.43 events in total (SK-I+SK-II), respectively.

Nucleon decay signals were searched in the SK-I and SK-II data. One candidate was observed in SK-I for the $n \to \mu^+\pi^-$ mode, while the number of the expected background was 0.43. The details of the candidates are described in Appendix B.4.

	$n \to e^+\pi^-$						$n \to \mu^+\pi^-$					
	eff.(%)		atm. ν MC		FC Data		eff.(%)		atm. ν MC		FC Data	
	SK-I	SK-II	SK-I	SK-II	SK-I	SK-II	SK-I	SK-II	SK-I	SK-II	SK-I	SK-II
F.V.	99.0	99.9	12586	6684	12232	6584	99.5	100.2	12586	6684	12232	6584
A	48.9	49.4	2255	1162	2134	1160	49.4	49.3	2255	1162	2134	1160
B	28.7	29.1	700	352	662	383	31.6	30.3	187	88	162	71
D	28.6	29.0	291	150	256	128	25.5	23.9	96	44	89	34
E	19.4	19.3	0.16	0.11	0	0	16.7	15.6	0.30	0.13	1	0

Table 9.15: The detection efficiencies for the proton decay MC and the number of surviving event in the atmospheric neutrino MC and in the observed data at each event selection criterion for $n \to e^+\pi^-$ and $n \to \mu^+\pi^-$. The atmospheric neutrino MC is normalized with the observed data using single-ring e-like events. The criteria (A$\sim$E) are described in Section 9.1.1 and Table 9.14.

9.1.7 $n \to l^+\rho^-$ Mode Search

Modes	A Ring	B PID	C(M_ρ) M_ρ	C(M_π) M_π	D decay-e	E $M_{\rm tot}$	$P_{\rm tot}$
$n \to e^+\rho^-$	4	SSSN*	600∼900	85∼185	0	800∼1050	<250
$n \to \mu^+\rho^-$	3	SSN*	600∼900	85∼185	1	-	<150

Table 9.16: The event selection criteria for $n \to e^+\rho^-$ and $n \to \mu^+\rho^-$.

Event Characteristics In the neutron decay of $n \to l^+\rho^-$, the ρ^- meson decays into $\pi^-\pi^0$. Then, the π^0 decays into two γ-rays. Accordingly, two shower type rings and one non-shower type ring were required from the ρ^- meson decay. One more shower type ring from the positron was required for the $n \to e^+\rho^-$ mode search, while one more non-shower type ring from the muon was not required for the $n \to \mu^+\rho^-$ mode search. In order to find the low momentum non-shower type ring, the PID with both a Cherenkov ring pattern and an opening angle was used for these modes. Figure 9.39 shows the number of ring distributions of the neutron decay MC. The fraction of 4-rings (3-rings) was 9% (23%) for $n \to e^+\rho^-$ ($n \to \mu^+\rho^-$).

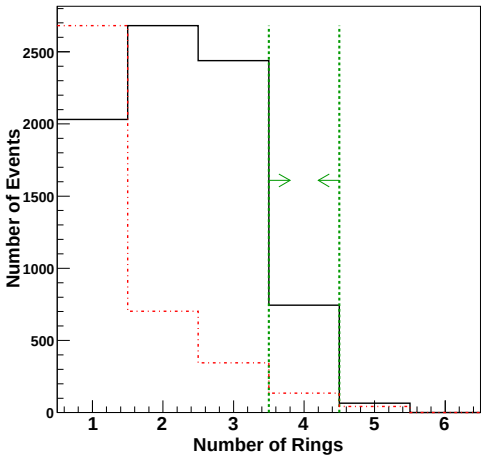

Figure 9.39: The number of ring distributions for the $n \to e^+\rho^-$ MC in SK-I. Dashed lines and arrows indicate the selection criterion. The dashed histogram is the atmospheric neutrino backgrounds.

The invariant mass of the ρ^- meson was reconstructed by two shower type rings and one non-shower type ring and required to be in between 600 to 900 MeV/c^2 as shown in Figure 9.40. In addition to the ρ meson mass, the π^0 invariant mass was also required. This additional cut reduced the atmospheric neutrino background by a factor of 2, while the loss of the detection efficiencies are about 10%.

The tighter total momentum cut of $P_{\rm tot} < 150$ MeV/c was applied to reduce the background for the $n \to \mu^+\rho^-$ mode because the proton invariant mass cannot be reconstructed for the

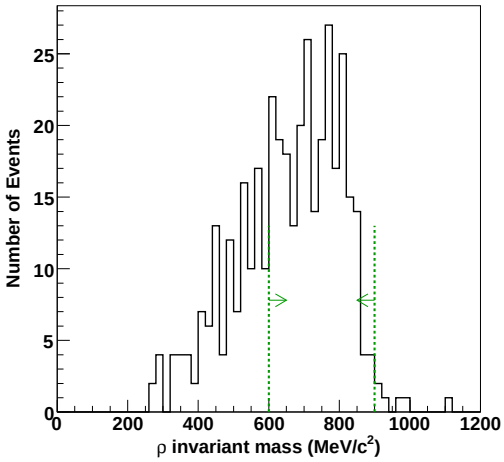

Figure 9.40: ρ^- invariant mass distributions of the $n \to e^+\rho^-$ MC in SK-I. Dashed lines and arrows indicate the selection criterion.

mode due to the invisible muon.

The Search Results The detection efficiencies for the proton decay MC and the number of events for the normalized atmospheric neutrino MC and the observed data at each selection criteria are summarized in Table 9.17. The momentum and the total invariant mass distributions in the final selection criterion are shown in Figure 9.41.

The detection efficiencies for $n \to e^+\rho^-$ and $n \to \mu^+\rho^-$ were estimated to be 1.8% (1.6%) and 1.1% (0.94%) in SK-I (SK-II), respectively. The background events for $n \to e^+\rho^-$ and $n \to \mu^+\rho^-$ were estimated to be 0.38 and 0.29 events in total (SK-I+SK-II), respectively.

Nucleon decay signals were searched in the SK-I and SK-II data. One candidate was found in the SK-I data for $n \to e^+\rho^-$ mode, while the number of expected background event for this mode was 0.38 events. The detail of the candidate is described in Appendix B.5.

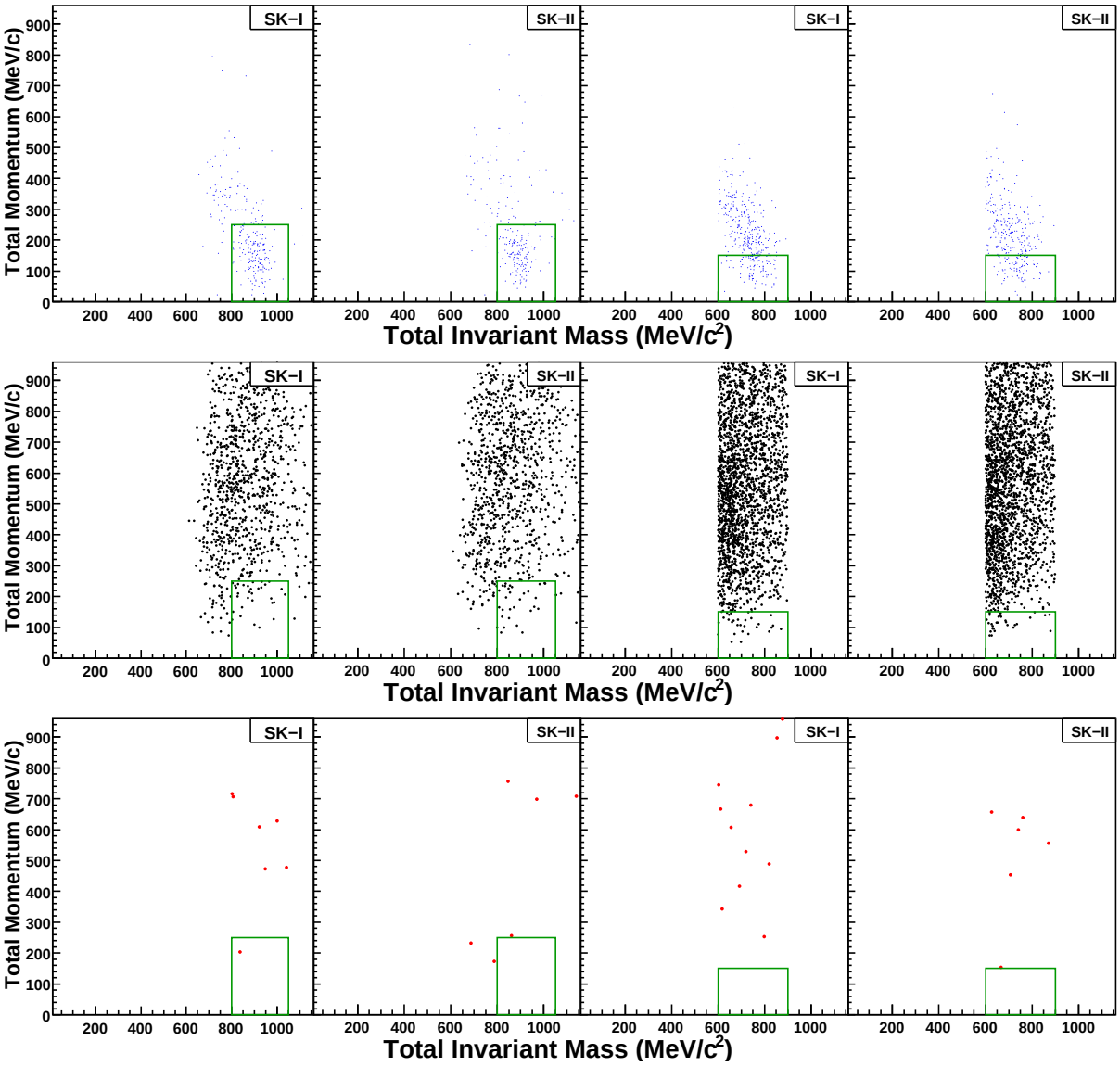

Figure 9.41: Total momentum versus total invariant mass distributions, from left to right: SK-I $n \to e^+\rho^-$; SK-II $n \to e^+\rho^-$; SK-I $n \to \mu^+\rho^-$; and SK-II $n \to \mu^+\rho^-$, from top to bottom: the proton decay MC; the atmospheric neutrino MC; and the observed data. These events satisfy the event selection criteria for $n \to e^+\rho^-$ or $n \to \mu^+\rho^-$ except for the selection by the total momentum and total mass. The boxes in figures indicate the criteria. One candidate was observed in the SK-I data for $n \to e^+\rho^-$ mode.

	$n \to e^+\rho^-$						$n \to \mu^+\rho^-$					
	eff.(%)		atm. ν MC		FC Data		eff.(%)		atm. ν MC		FC Data	
	SK-I	SK-II	SK-I	SK-II	SK-I	SK-II	SK-I	SK-II	SK-I	SK-II	SK-I	SK-II
F.V.	95.2	96.5	12586	6684	12232	6584	75.9	79.1	12586	6684	12232	6584
A	8.9	9.0	432	248	406	236	17.1	16.8	1109	597	1023	572
B	4.6	4.5	139	86	117	77	10.9	10.2	417	232	370	208
C(M_ρ)	3.1	2.7	44	28	51	25	5.7	5.1	96	56	82	44
C(M_π)	2.9	2.5	28	15	36	14	5.3	4.5	49	24	36	14
D	2.9	2.5	13	8	14	7	4.3	3.6	23	11	18	12
E	1.8	1.6	0.25	0.13	1	0	1.1	0.94	0.19	0.10	0	0

Table 9.17: The detection efficiencies for the proton decay MC and the number of surviving event in the atmospheric neutrino MC and in the observed data at each event selection criterion for $n \to e^+\rho^-$ and $n \to \mu^+\rho^-$. The atmospheric neutrino MC is normalized with the observed data using single-ring e-like events. The criteria (A$\sim$E) are described in Section 9.1.1 and Table 9.16.

9.1.8 Summary of the Search Results

The result of the nucleon decay searches are summarized in Table 9.18. The detection efficiencies, the expected backgrounds and the number of candidates are shown in the table.

The detection efficiencies of SK-II are certainly inferior to that of SK-I. However, the difference was a only few% for the modes with high detection efficiencies ($p \to e^+\pi^0$, $p \to e^+\eta$, etc.) and less than about 17% even for the modes with low efficiencies. Therefore, the nucleon decay search using the SK-II data is as valuable as SK-I. The estimated background rates of SK-I and SK-II are also comparable with each other.

The details of the background are described especially for the $p \to e^+\pi^0$ and $p \to \mu^+\pi^0$ modes in Section 9.1.2. The charged current pion production was the dominant background source for most of the studied nucleon decay modes as well as $p \to e^+\pi^0$ and $p \to \mu^+\pi^0$. Pions produced by neutrino interactions and/or hadronic interactions in nuclei and/or in water can mimic the event signatures of nucleon decay signals with a charged lepton. Thus, these pion production processes are important for the background estimation, and their systematical uncertainties are discussed in Section 9.2.1. Especially for the neutrino interactions and the nuclear effects, their consistency were checked by comparing background estimations between our MC and NUANCE [121]. NUANCE has different models of neutrino interactions and nuclear effects. The atmospheric neutrino MC by NUANCE used the same atmospheric neutrino flux of 100 year equivalent and the same detector simulation. The results of these two estimations are shown in Table 9.19. Consistent results with our estimations were obtained with the NUANCE MC.

In total, six candidates were found in the SK-I and SK-II data. The candidates were found in the five largest background modes. Probabilities to observe these candidates from the backgrounds were calculated using the estimations in SK-I+II by Poisson statistics without systematic errors.

- $p \to \mu^+\eta$ ($3\pi^0$): $P(\geq 2\text{events}) = 7.5\%$

	Eff.(×Br.)(%)		BG events		Candidates	
	SK-I	SK-II	SK-I	SK-II	SK-I	SK-II
$p \to e^+\pi^0$	44.6	43.5	0.20	0.11	0	0
$p \to \mu^+\pi^0$	35.5	34.7	0.23	0.11	0	0
$p \to e^+\eta$						
$(\eta \to 2\gamma)$	18.8	18.2	0.19	0.09	0	0
$(\eta \to 3\pi^0)$	8.1	7.6	0.08	0.08	0	0
$p \to \mu^+\eta$						
$(\eta \to 2\gamma)$	12.4	11.7	0.03	0.01	0	0
$(\eta \to 3\pi^0)$	6.1	5.4	0.30	0.15	0	2
$p \to e^+\rho^0$	4.9	4.2	0.23	0.12	0	0
$p \to \mu^+\rho^0$	1.8	1.5	0.30	0.12	1	0
$p \to e^+\omega$						
$(\omega \to \pi^0\gamma)$	2.4	2.2	0.10	0.04	0	0
$(\omega \to \pi^+\pi^-\pi^0)$	2.5	2.3	0.26	0.13	1	0
$p \to \mu^+\omega$						
$(\omega \to \pi^0\gamma)$	2.8	2.8	0.24	0.07	0	0
$(\omega \to \pi^+\pi^-\pi^0)$	2.7	2.4	0.10	0.07	0	0
$n \to e^+\pi^-$	19.4	19.3	0.16	0.11	0	0
$n \to \mu^+\pi^-$	16.7	15.6	0.30	0.13	1	0
$n \to e^+\rho^-$	1.8	1.6	0.25	0.13	1	0
$n \to \mu^+\rho^-$	1.1	0.94	0.19	0.10	0	0

Table 9.18: Summary of the nucleon decay searches in this thesis.

Mode	Our MC	NUANCE	Mode	Our MC	NUANCE
$p \to e^+\pi^0$	0.31 ± 0.04	0.27 ± 0.10	$p \to e^+\omega$		
$p \to \mu^+\pi^0$	0.34 ± 0.05	0.27 ± 0.09	$(\omega \to \pi^0\gamma)$	0.14 ± 0.03	0.29 ± 0.10
$p \to e^+\eta$			$(\omega \to \pi^+\pi^-\pi^0)$	0.39 ± 0.05	0.30 ± 0.11
$(\eta \to 2\gamma)$	0.28 ± 0.05	0.29 ± 0.10	$p \to \mu^+\omega$		
$(\eta \to 3\pi^0)$	0.16 ± 0.03	0.32 ± 0.11	$(\omega \to \pi^0\gamma)$	0.31 ± 0.05	0.37 ± 0.11
$p \to \mu^+\eta$			$(\omega \to \pi^+\pi^-\pi^0)$	0.16 ± 0.03	0.05 ± 0.04
$(\eta \to 2\gamma)$	0.04 ± 0.02	0.04 ± 0.04	$n \to e^+\pi^-$	0.27 ± 0.04	0.37 ± 0.12
$(\eta \to 3\pi^0)$	0.45 ± 0.06	0.44 ± 0.13	$n \to \mu^+\pi^-$	0.43 ± 0.05	0.44 ± 0.12
$p \to e^+\rho^0$	0.35 ± 0.05	0.34 ± 0.11	$n \to e^+\rho^-$	0.38 ± 0.05	0.44 ± 0.12
$p \to \mu^+\rho^0$	0.42 ± 0.05	0.46 ± 0.12	$n \to \mu^+\rho^-$	0.29 ± 0.04	0.69 ± 0.14

Table 9.19: The number of estimated background events in SK-I+II with our MC and NUANCE [121] MC. Only statistical errors are shown. The statistics of our MC and NUANCE MC were 500 and 100 year observation equivalent, respectively.

- $p \to \mu^+\rho^0$: $P(\geq 1\text{event}) = 34.9\%$
- $p \to e^+\omega$ $(\pi^+\pi^-\pi^0)$: $P(\geq 1\text{event}) = 32.3\%$
- $n \to \mu^+\pi^-$: $P(\geq 1\text{event}) = 34.3\%$
- $n \to e^+\rho^-$: $P(\geq 1\text{event}) = 31.6\%$

As listed above, those probabilities are not so small for 16 decay modes that we cannot take the candidates as serious evidences for a nucleon decay. Moreover, the number of background events in total was 4.7 events. Consequently, the number of candidates is consistent with the estimation by the atmospheric neutrino MC. Therefore, nucleon partial lifetime limits were calculated in Section 9.3.

9.2 Systematic Errors

Systematic errors for detection efficiencies and background estimations are described in this section. Systematic errors on detection efficiencies or common systematic errors are first explained. Then, systematic errors only on backgrounds are explained later in the next section. As for the exposure, the systematic error on it is negligible, $< 1\%$.

9.2.1 Systematic Errors for Detection Efficiencies

Nuclear Effect

In most of the modes, meson (π, η, ω) nuclear effects (meson-nucleon interactions in a nucleus) have large effects on detection efficiencies and can be a dominant error source.

π nuclear effect The systematic uncertainties of π nuclear effect was estimated by comparing the nuclear effect simulation with another simulation result based on the model used by the IMB experiment [104] because there are no suitable experimental data which can be used for the systematic error estimation with enough precision at the moment. The comparison of the fraction of the final states for the proton decay of $p \to e^+\pi^0$ in ^{16}O nuclei is shown in Table 9.20. The detection efficiency directly depends on the π^0 escape probability without any scattering. There is a 10% difference for that probability between the two models. This difference corresponds to a 15% difference in the total detection efficiencies of $p \to e^+\pi^0$ and $p \to \mu^+\pi^0$.

nuclear effect in ^{16}O	Our MC	IMB
no interaction	44%	54%
absorption	22%	22%
charge exchange	15%	10%
scattered	19%	14%

Table 9.20: Fraction of the final states of π^0 from the proton decay of $p \to e^+\pi^0$ in ^{16}O compared with the simulation used in the IMB experiment.

The escape probability difference described above for the $p \to e^+\pi^0$ mode is equivalent to $\sim 40\%$ difference in the total cross section of the π nuclear effect. Thus, this difference in the total cross section was used for the systematic error estimations from π nuclear effect for the other nucleon decay modes, since detailed results of the IMB simulation were not available for those modes. As for the $n \to e^+\pi^-$ mode, the effect on the π^- escape probability from 40% uncertainty of the π nuclear effect was estimated by the nucleon decay simulation. This effect corresponds to a 20% difference in the total detection efficiency for $n \to e^+\pi^-$. It is greater than that for $p \to e^+\pi^0$ because there are no free (unbounded) nucleon decay events for $n \to e^+\pi^-$.

η nuclear effect The systematic uncertainty of the η nuclear effect was estimated in Section 4.1.2 by comparing the experimental η photoproduction cross section with the simulated

cross section. The estimated error for the η-nucleon cross section in ^{16}O nuclei was a factor of 2.

η nuclear effect in ^{16}O	default	$\sigma \times \frac{1}{2}$	$\sigma \times 2$
no interaction	56%	73%	43%
scattered	6%	4%	5%
no η survived	38%	23%	53%

Table 9.21: Fraction of the final states of η meson from the proton decay of $p \to l^+\eta$ in ^{16}O.

Table 9.21 shows the effects of the systematic uncertainties of the cross section on the fraction of η meson final states from a proton decay in ^{16}O. The events in which no η meson escapes from a nucleus hardly passed the selection criteria. The efficiency for the events in which the η meson were scattered in a nucleus was less than $\sim 1/4$ of the efficiency for the events without any interactions in a nucleus. Therefore, effects on the detection efficiency could be estimated almost by the change of the escape probability with no interaction in a nucleus. The estimated errors corresponded to a $\sim 20\%$ error in total detection efficiencies for $p \to e^+\eta$ and $p \to \mu^+\eta$.

ω nuclear effect The systematic uncertainty of ω nuclear effect was a factor of 3, which was estimated by the comparison of ω-nucleon cross section between the theoretical calculation and the extracted data from the ω photoproduction experiment as described in Section 4.1.3.

ω nuclear effect in ^{16}O	$p \to e^+\omega$	$\sigma \times 3$	$p \to \mu^+\omega$	$\sigma \times 3$
no interaction	19%	11%	17%	10%
scattered	2%	2%	1%	1%
decay in a nucleus	53%	35%	56%	37%
$\omega N \to N + meson(\neq \omega)$	26%	52%	25%	51%

Table 9.22: Fraction of the final states of the ω meson from the proton decay of $p \to e^+\omega$ or $p \to \mu^+\omega$ in ^{16}O.

The effect of the factor of 3 uncertainty of the cross section had a large effect on the fraction of the ω meson final state from $p \to e^+\omega$ and $p \to \mu^+\omega$ in a ^{16}O nucleus, as shown in Table 9.22. However, these effects corresponded to only a $\sim 20\%$ error on the total detection efficiency, since the fraction of free proton decay events, which do not suffer from the nuclear effect, in the total surviving events was $40 \sim 60$ % for the $p \to e^+\omega$ and $p \to \mu^+\omega$ search.

Hadron Propagation in Water

In some of the nucleon decay mode searches, Cherenkov rings from charged pions were required to be found. Charged pions strongly interact with nucleons in water. Thus, whether charged pion rings can be observed or not depends on the hadronic interaction in water.

The uncertainty of the charged pion cross section in water was considered to be 10% by comparing the detector simulation with the experimental data [51, 122].

Only for the systematic errors on the background, the uncertainty of pion production probability by high momentum ($> \sim$1 GeV/c) hadrons was also considered. This error was conservatively set to 100%.

Fraction of N-N Correlated Decay

As described in Section 4.1, 10% of nucleons in a ^{16}O nucleus are assumed to correlate with another nucleon. Such a decay is calculated as a three body decay. The detection efficiency for this decay can be very low. The uncertainty for this fraction was conservatively set to 100%.

Fermi Motion

The total momentum of a bound nucleon decay event corresponds to the Fermi motion of the source nucleon. The systematic error from the uncertainty of the Fermi motion was estimated by comparing the distributions shown in Figure 4.1 with the Fermi gas model or by changing the momentum by $\pm$20%. If the tighter total momentum cut is used, the systematic error from the Fermi motion can be large.

Detector and Event Reconstruction Performances

Fiducial Volume The systematic errors from the fiducial volume were estimated by the difference between the number of events of the reconstructed and true vertices form multi-ring events. The estimated errors were 3% and 2% for SK-I and SK-II, respectively. This error can directly affect the detection efficiencies, but its magnitude is negligible compared with other systematic errors.

Detector Non-uniformity and Energy Scale The non-uniformity of the detector gain was within $\pm$ 0.6% as described in Chapter 7. The non-uniformity cause the momentum imbalance of an event, 1.2% error for the total momentum. Therefore, the systematic errors on detection efficiencies were estimated by changing the total momentum threshold by 1.2%.

The stability of the energy scale is also described in Chapter 7. The systematic errors from the energy scale was estimated by changing the threshold of total momentum and total invariant mass by 1.1% (1.7%) in SK-I (SK-II).

These two errors have negligible effects on the detection efficiencies.

PID, Ring Counting and Cherenkov Opening Angle The systematic error of the particle identification was estimated by comparing the PID likelihood (Fig 9.42) between the observed data and the atmospheric neutrino MC. The systematic errors of the detection efficiencies were estimated by changing the threshold of the PID likelihood for the MC to fit it with the data. The systematic error from the ring counting was also estimated by comparing its likelihood between the observed data and the atmospheric neutrino MC.

Figure 9.42 shows the PID likelihood distributions for multi-ring events in SK-I and SK-II. The ring counting likelihood are shown in Figure 6.5 in Section 6.2. The data and the MC agree well with each other in these distributions. Therefore, systematic errors from the PID and the ring counting were estimated to be negligible.

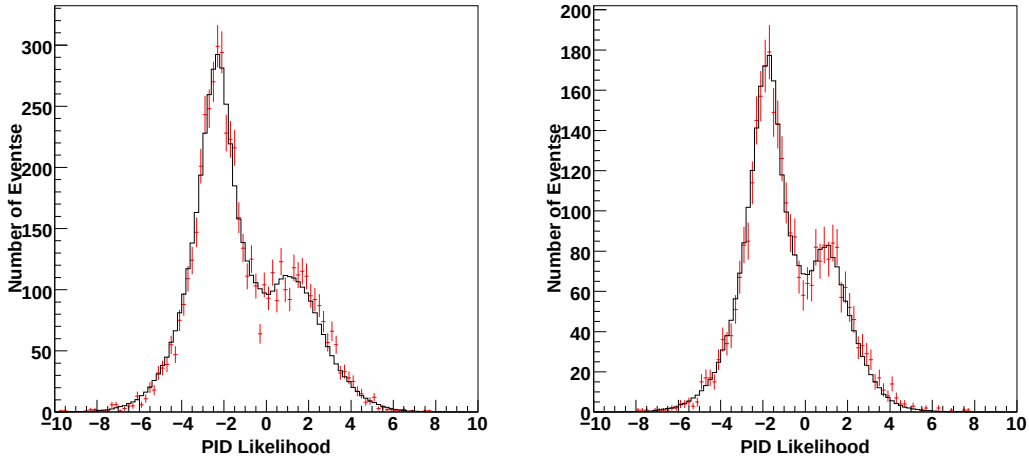

Figure 9.42: The PID likelihood (defined by Equation (6.15)) distributions for SK-I (left) and SK-II (right). The multi ring events of the data (bar) and the atmospheric neutrino MC (histogram) with the visible energy below 1.33 GeV are filled in the figures.

As for the Cherenkov opening angle, the systematical error of the Cherenkov opening angle was estimated to be 0.7 (0.5) degrees in SK-I (SK-II) by comparing the angle distributions between the observed data and the atmospheric neutrino MC. Charged pion momentum reconstruction largely depends on the opening angle. Thus, the systematic errors for the modes which need to reconstruct the charged pion momenta can be relatively large.

Vertex Shift The vertex position was reconstructed at the beginning of the event reconstruction. The reconstructed vertex can affect all of the following reconstruction algorithms like the ring counting, the PID, the momentum determination, etc.

Systematical shift of the reconstructed vertex was estimated to be within about 30 cm by comparing different vertex fitting algorithms and by some measurements. Therefore, the systematic error from the vertex shift was estimated by shifting the reconstructed vertex by 30 cm along with the direction of the most energetic particle.

Summary of the Systematic Errors for Detection Efficiencies

Tables 9.23, 9.24, 9.25 and 9.26 summarize the results of the systematic error estimation for detection efficiencies of all the modes. The systematic errors for detection efficiencies were about $20 \sim 30\%$ except for the much large error of $n \to l^+\rho^-$ mode.

Nuclear effects are the dominant error source for most of the modes. For the $n \to e^+\rho^-$ and $n \to \mu^+\rho^-$ modes, the systematic errors from the pion nuclear effect is very large because both of the two pions from the ρ meson decay were required to escape from a nucleus. Positive and negative errors were individually estimated especially for these two modes. On the other hand, $p \to e^+\rho^0$ and $p \to \mu^+\rho^0$ has a comparably smaller error since most of the surviving events in these modes are free proton decay events. The uncertainty of Fermi motion can be the dominant error source especially in the modes using the tight total momentum cut like $p \to e^+\eta$

($3\pi^0$). Another important error is the reconstruction biases from the Cherenkov opening angle reconstruction and the vertex shift. These biases mostly contributes the errors for the modes which requires charged pion momentum reconstruction.

These dominant errors are mostly common for SK-I and SK-II. Therefore, there are not significant differences between the systematic errors of SK-I and SK-II.

	$p \to e^+\pi^0$		$p \to \mu^+\pi^0$		$n \to e^+\pi^-$		$n \to \mu^+\pi^-$	
	SK-I	SK-II	SK-I	SK-II	SK-I	SK-II	SK-I	SK-II
(Interaction)								
pion nuclear effect	15%		15%		20%		24%	
hadron propagation in water	-		-		9%		6%	
fraction of correlated decay	7%		7%		11%		11%	
Fermi momentum	8%	9%	8%	9%	11%	15%	6%	10%
(Detector Performance)								
fiducial volume	3%	2%	3%	2%	3%	2%	3%	2%
detector non-uniformity	1%	1%	1%	1%	1%	1%	1%	1%
energy scale	<0.5%	1%	1%	1%	2%	1%	1%	<0.5%
PID	2%	1%	1%	<0.5%	4%	2%	4%	3%
ring counting	<0.5%		<0.5%		1%		2%	
opening angle	1%	1%	1%	1%	<0.5%	2%	2%	2%
vertex shift	2%	1%	2%	1%	10%	12%	17%	13%
decay-e detection	-		2%		-		2%	
Total	19%	19%	19%	19%	29%	31%	33%	32%

Table 9.23: Systematic errors for the detection efficiencies of $N \to l^+\pi$ modes.

	$p \to e^+\eta$ ($\eta \to 2\gamma$)		$p \to \mu^+\eta$ ($\eta \to 2\gamma$)		$p \to e^+\eta$ ($\eta \to 3\pi^0$)		$p \to \mu^+\eta$ ($\eta \to 3\pi^0$)	
	SK-I	SK-II	SK-I	SK-II	SK-I	SK-II	SK-I	SK-II
(Interaction)								
η nuclear effect	20%		18%		15%		20%	
fraction of correlated decay	7%		7%		5%		7%	
Fermi momentum	11%	18%	15%	12%	26%	25%	16%	10%
(Detector Performance)								
fiducial volume	3%	2%	3%	2%	3%	2%	3%	2%
detector non-uniformity	1%	1%	1%	1%	1%	2%	1%	1%
energy scale	1%	3%	1%	1%	1%	2%	1%	5%
PID	2%	<0.5%	1%	1%	1%	1%	<0.5%	<0.5%
ring counting	<0.5%		<0.5%		<0.5%		1%	
opening angle	1%	<0.5%	1%	<0.5%	<0.5%	<0.5%	1%	1%
vertex shift	3%	3%	2%	1%	8%	9%	8%	11%
decay-e detection	-		2%		-		2%	
Total	24%	28%	25%	23%	32%	31%	28%	27%

Table 9.24: Systematic errors for the detection efficiencies of $p \to l^+\eta$ modes.

	$p \to e^+\rho^0$		$p \to \mu^+\rho^0$		$n \to e^+\rho^-$		$n \to \mu^+\rho^-$	
	SK-I	SK-II	SK-I	SK-II	SK-I	SK-II	SK-I	SK-II
(Interaction)								
pion nuclear effect	8%		9%		(+51% -23%)		(+51% -25%)	
hadron propagation in water	17%		24%		9%		14%	
fraction of correlated decay	2%		2%		11%		10%	
Fermi momentum	9%	11%	6%	7%	16%	14%	21%	38%
(Detector Performance)								
fiducial volume	3%	2%	3%	2%	3%	2%	3%	2%
detector non-uniformity	1%	1%	1%	1%	2%	1%	4%	3%
energy scale	1%	2%	3%	3%	2%	5%	2%	5%
PID	3%	4%	<0.5%	<0.5%	1%	2%	<0.5%	1%
ring counting	2%		5%		2%		4%	
opening angle	2%	2%	10%	3%	1%	1%	2%	4%
vertex shift	19%	14%	3%	4%	15%	24%	22%	21%
decay-e detection	-		2%		-		2%	
Total	29%	27%	29%	28%	+58% -36%	+60% -39%	+62% -43%	+70% -54%

Table 9.25: Systematic errors for the detection efficiencies of $N \to l^+\rho$ modes.

	$p \to e^+\omega$ ($\omega \to \pi^0\gamma$)		$p \to \mu^+\omega$ ($\omega \to \pi^0\gamma$)		$p \to e^+\omega$ ($\omega \to \pi^+\pi^-\pi^0$)		$p \to \mu^+\omega$ ($\omega \to \pi^+\pi^-\pi^0$)	
	SK-I	SK-II	SK-I	SK-II	SK-I	SK-II	SK-I	SK-II
(Interaction)								
ω nuclear effect	21%		22%		18%		18%	
pion nuclear effect	3%		5%		6%		7%	
hadron propagation in water	-		-		13%		15%	
fraction of correlated decay	5%		6%		5%		5%	
Fermi momentum	24%	23%	11%	17%	8%	19%	2%	3%
(Detector Performance)								
fiducial volume	3%	2%	3%	2%	3%	2%	3%	2%
detector non-uniformity	3%	2%	2%	2%	4%	4%	2%	2%
energy scale	2%	2%	2%	4%	5%	8%	2%	2%
PID	2%	1%	2%	<0.5%	<0.5%	2%	<0.5%	1%
ring counting	<0.5%		<0.5%		<0.5%		1%	
opening angle	2%	<0.5%	1%	1%	7%	3%	4%	<0.5%
vertex shift	9%	5%	4%	7%	20%	14%	14%	15%
decay-e detection	-		2%		-		4%	
Total	34%	32%	27%	30%	33%	35%	29%	30%

Table 9.26: Systematic errors for the detection efficiencies of $p \to l^+\omega$ modes.

9.2.2 Systematic Errors for Background Estimations

For the background estimations from atmospheric neutrinos, the uncertainties of atmospheric neutrino flux and neutrino cross sections should be considered. The systematic uncertainties of the pion nuclear effect, hadron propagation in water and the detector performances were also considered as well as the detection efficiencies.

Even with the large statics of the atmospheric neutrino MC, only a few ten events can survive the nucleon decay event selection criteria. In order to reduce statistical errors for the systematic error estimation of the background, systematic errors were estimated by averaging the estimations of SK-I and SK-II because they were basically common as described in the error estimation for the detection efficiencies. Moreover, for the modes with the same meson decay modes, systematic errors from the uncertainties of pion nuclear effect and hadron interaction in water were estimated by averaging the estimations of different charged lepton modes.

Neutrino Flux and Neutrino Interaction

Almost same systematical uncertainties as the atmospheric neutrino oscillation analysis in the Super-Kamiokande experiment were considered for the errors from the neutrino flux and the neutrino interaction. The details of the source of the uncertainties are given in the other documents [123, 124], and not discussed here.

The following uncertainties listed below were taken into account.

- energy dependent normalization (energy spectrum)
- neutrino flavor ratio
- anti-neutrino/neutrino ratio
- up/down asymmetry
- horizontal/vertical ratio
- K/π production ratio
- neutrino flight length

The systematic errors from the neutrino flux were estimated to be $6 \sim 8\%$, and mostly due to the uncetainty of the energy dependent normalization. These errors are negligible compared with other much larger errors.

As for the uncertainties of the neutrino interaction, the following uncertainties were taken into account.

- M_A (axial vector mass) in quasi-elastic scattering and single-meson production
- quasi-elastic scattering for bound nucleons (total cross section)
- quasi-elastic scattering for bound nucleons ($\bar{\nu}/\nu$)
- quasi-elastic scattering for bound nucleons (flavor ratio)
- single(multi)-meson production (total cross section)

- single(multi)-meson production (model dependence)
- coherent pion production
- NC/CC ratio

The systematic errors from the neutrino interaction were estimated to be 8 ∼16 % in total. These errors are also negligible compared with other errors.

Summary of the Systematic Errors for Backgrounds

The estimated systematic errors for the backgrounds are shown in Tables 9.27, 9.28, 9.29 and 9.30. The detailed values of the estimated systematic errors are shown in Appendix C. The systematic errors for the backgrounds were about 40 ∼ 70%.

One of the dominant errors comes from the uncertainty of pion-nucleon cross section and pion production probability in water. The errors from the detector and event reconstruction performances also have non-negligible contributions. The number of background events is much sensitive to the error of energy and momentum since those events are normally distributed around the threshold of the selection window of momentum and invariant mass. Therefore, the systematic error from the energy scale stability, which was negligible for the detection efficiencies, was estimated to be about 10 ∼ 20%. The systematical shift of the reconstructed vertex can cause the errors of Cherenkov opening angle and opening angles between two particles, which are important for momentum and mass reconstructions. Due to the same reason as the energy scale, the systematic error from the vertex shift was larger than that for the detection efficiency, and estimated to be about 10 ∼ 50%.

	$p \to e^+\pi^0$	$p \to \mu^+\pi^0$	$n \to e^+\pi^-$	$n \to \mu^+\pi^-$
neutrino flux	8%	8%	8%	8%
neutrino cross section	8%	8%	15%	16%
pion nuclear effect	8%		8%	
hadron propagation in water	36%		36%	
detector performance	22%	43%	46%	36%
Total	44%	58%	61%	55%

Table 9.27: Systematic errors for the backgrounds of $N \to l^+\pi$ modes.

	$p \to e^+\eta$ ($\eta \to 2\gamma$)	$p \to \mu^+\eta$ ($\eta \to 2\gamma$)	$p \to e^+\eta$ ($\eta \to 3\pi^0$)	$p \to \mu^+\eta$ ($\eta \to 3\pi^0$)
neutrino flux	8%	8%	8%	8%
neutrino cross section	11%	14%	15%	11%
pion nuclear effect	5%		18%	
hadron propagation in water	36%		67%	
detector performance	26%	28%	13%	20%
Total	47%	49%	76%	73%

Table 9.28: Systematic errors for the backgrounds of $p \to l^+\eta$ modes.

	$p \to e^+\rho^0$	$p \to \mu^+\rho^0$	$n \to e^+\rho^-$	$n \to \mu^+\rho^-$
neutrino flux	6%	8%	8%	6%
neutrino cross section	13%	15%	14%	16%
pion nuclear effect	14%		12%	
hadron propagation in water	33%		18%	
detector performance	33%	23%	54%	27%
Total	51%	46%	60%	39%

Table 9.29: Systematic errors for the backgrounds of $N \to l^+\rho$ modes.

	$p \to e^+\omega$ ($\omega \to \pi^0\gamma$)	$p \to \mu^+\omega$ ($\omega \to \pi^0\gamma$)	$p \to e^+\omega$ ($\omega \to \pi^+\pi^-\pi^0$)	$p \to \mu^+\omega$ ($\omega \to \pi^+\pi^-\pi^0$)
neutrino flux	8%	8%	7%	7%
neutrino cross section	14%	10%	14%	11%
pion nuclear effect	13%		8%	
hadron propagation in water	41%		53%	
detector performance	37%	28%	28%	29%
Total	59%	53%	63%	63%

Table 9.30: Systematic errors for the backgrounds of $p \to l^+\eta$ modes.

9.3 Lifetime Limits

As described in the Section 9.1.8, the observed data in SK-I and SK-II are consistent with the atmospheric neutrino MC. Consequently, the lower limits of the nucleon partial lifetime were calculated.

The partial lifetime limit for each mode is derived from a method [125] based on Bayes' theorem which incorporates systematic errors. The method is first explained in Section 9.3.1. The SK-I and SK-II should be treated as two different experiments. How to combine two different experiments is described in Section 9.3.2.

9.3.1 Lifetime Limit Calculation by Bayes' theorem

Because the nucleon decay search is a counting experiment, the probability to detect n events is given by Poisson statistics as follows.

$$\mathbf{P}(n|\Gamma\lambda\epsilon b) = \frac{e^{-(\Gamma\lambda\epsilon+b)}\,(\Gamma\lambda\epsilon+b)^n}{n!} \tag{9.4}$$

where Γ is the true decay rate, λ is the true exposure, ϵ is the true detection efficiency, b is the true number of background, and $\mathbf{P}(A|B)$ is the conditional probability of A, given that proposition B is true.

Applying Bayes' theorem allows us to write,

$$\mathbf{P}(\Gamma\lambda\epsilon b|n) = \frac{1}{A}\mathbf{P}(n|\Gamma\lambda\epsilon b)\mathbf{P}(\Gamma\lambda\epsilon b) \tag{9.5}$$

where A is the constant to normalize $\mathbf{P}(\Gamma\lambda\epsilon b|n)$. Because the decay rate, the detection efficiency, the exposure and the background are independent, $\mathbf{P}(\Gamma\lambda\epsilon b)$ can be separated into constituents.

$$\mathbf{P}(\Gamma\lambda\epsilon b|n) = \frac{1}{A}\mathbf{P}(n|\Gamma\lambda\epsilon b)\mathbf{P}(\Gamma)\mathbf{P}(\epsilon)\mathbf{P}(\lambda)\mathbf{P}(b) \tag{9.6}$$

The probability density function of Γ can be defined as;

$$\mathbf{P}(\Gamma|n) = \int\int\int \mathbf{P}(\Gamma\epsilon\lambda b|n)d\epsilon d\lambda db. \tag{9.7}$$

Accordingly,

$$\mathbf{P}(\Gamma|n) = \frac{1}{A}\int\int\int \frac{e^{-(\Gamma\lambda\epsilon+b)}\,(\Gamma\lambda\epsilon+b)^n}{n!}\mathbf{P}(\Gamma)\mathbf{P}(\epsilon)\mathbf{P}(\lambda)\mathbf{P}(b)d\epsilon d\lambda db. \tag{9.8}$$

The normalization constant A can be resolved by,

$$A = \int_0^\infty \mathbf{P}(\Gamma|n)d\Gamma. \tag{9.9}$$

$\mathbf{P}(\Gamma)$, $\mathbf{P}(\lambda)$, $\mathbf{P}(\epsilon)$ and $\mathbf{P}(\Gamma)$ are the prior probability distributions, in which systematic uncertainties can be incorporated.

The priors for the exposure, the detection efficiency and the background are assumed to be truncated Gaussian distributions defined as;

$$\mathbf{P}(\lambda) \propto \begin{cases} \exp\left(-\frac{(\lambda-\lambda_0)^2}{2\sigma_\lambda^2}\right) & (\lambda > 0) \\ 0 & (\lambda \leq 0) \end{cases} \tag{9.10}$$

$$\mathbf{P}(\epsilon) \propto \begin{cases} \exp\left(-\frac{(\epsilon-\epsilon_0)^2}{2\sigma_\epsilon^2}\right) & (\epsilon > 0) \\ 0 & (\epsilon \leq 0)\,. \end{cases} \tag{9.11}$$

$$\mathbf{P}(b) \propto \begin{cases} \exp\left(-\frac{(b-b_0)^2}{2\sigma_b^2}\right) & (b > 0) \\ 0 & (b \leq 0)\,. \end{cases} \tag{9.12}$$

where λ_0 (σ_λ), ϵ_0 (σ_ϵ) and b (σ_b) are the estimations (systematic errors) of the detection efficiency, the exposure and the background, respectively.

If the systematic error for the detection efficiency is assumed to be asymmetric, the prior $\mathbf{P}(\epsilon)$ will be an asymmetric Gaussian defined as;

$$\mathbf{P}(\epsilon) \propto \begin{cases} \exp\left(-\frac{(\epsilon-\epsilon_0)^2}{2\sigma_{\epsilon+}^2}\right) & (\epsilon > \epsilon_0) \\ \exp\left(-\frac{(\epsilon-\epsilon_0)^2}{2\sigma_{\epsilon-}^2}\right) & (0 < \epsilon \leq \epsilon_0) \\ 0 & (\epsilon \leq 0) \end{cases} \tag{9.13}$$

where $\sigma_{\epsilon+}$ and $\sigma_{\epsilon-}$ are the positive and negative side of the systematic errors, respectively.

If the number of background events are very small (less than about ~ 10), the statistical error of the background should be taken into account by using the convolution of Gaussian and Poisson distributions as a prior.

$$\mathbf{P}(b) = \int_0^\infty \frac{e^{-b_{\rm MC}}\,(b_{\rm MC})^{n_b}}{n_b!} \exp\left(-\frac{(bC - b_{\rm MC})^2}{2\sigma_b^2}\right) db_{\rm MC} \tag{9.14}$$

where n_b is the number of background events in the 500 year equivalent MC, $b_{\rm MC}$ is the number of true background events in the 500 year MC, and C is the oversampling factor of the MC.

The prior for the decay rate is assumed to be uniform. This is implicitly assumed when calculating limits by simple Poisson statistics without systematic errors.

$$\mathbf{P}(\Gamma) = \begin{cases} 1 & (0 < \Gamma < \Gamma_{\rm cut}) \\ 0 & (\Gamma \leq 0 \text{ or } \Gamma \geq \Gamma_{\rm cut}) \end{cases} \tag{9.15}$$

where $\Gamma_{\rm cut}$ is the upper limit of the decay rate for the calculation of the normalization constant A in order to avoid the divergence. The upper limit Γ is set to be 10^{-31} years^{-1}, which is sufficiently large than the limits by the previous experiments.

By integrating Equation (9.8) using the priors, the confidence level can be calculated as;

$$CL = \int_0^{\Gamma_{\rm limit}} \mathbf{P}(\Gamma|n) d\Gamma. \tag{9.16}$$

Lifetime limits are obtained by;

$$\tau_{\rm limit} = 1/\Gamma_{\rm limit}. \tag{9.17}$$

9.3.2 Combined Limit Calculation

The combined result of SK-I and SK-II is also derived by the method described above. The probability to detect n_1 events in SK-I and n_2 events in SK-II is the product of the two Poisson probabilities.

$$\mathbf{P}(n_1, n_2|\Gamma\lambda_1\epsilon_1 b_1 \lambda_2\epsilon_2 b_2) = \frac{e^{-(\Gamma\lambda_1\epsilon_1+b_1)}\left(\Gamma\lambda_1\epsilon_1 + b_1\right)^{n_1}}{n_1!}\frac{e^{-(\Gamma\lambda_2\epsilon_2+b_2)}\left(\Gamma\lambda_2\epsilon_2 + b_2\right)^{n_2}}{n_2!} \tag{9.18}$$

By applying Bayes' theorem assuming that the decay rate, the exposure, the detection efficiency and the background are independent,

$$\mathbf{P}(\Gamma\lambda_1\epsilon_1 b_1\lambda_2\epsilon_2 b_2|n_1, n_2) = \frac{1}{A}\mathbf{P}(n_1, n_2|\Gamma\lambda_1\epsilon_1 b_1\lambda_2\epsilon_2 b_2)\mathbf{P}(\Gamma)\mathbf{P}(\epsilon_1\epsilon_2)\mathbf{P}(\lambda_1\lambda_2)\mathbf{P}(b_1 b_2). \tag{9.19}$$

Most of the dominant systematic uncertainties like the nuclear effects and hadron propagation in water are common between SK-I and SK-II. Therefore, the systematic errors of SK-I and SK-II are assumed to be fully correlated with each other, which gives conservative lifetime limits for this method. Then, the priors for the exposure, the detection efficiency and the background of SK-I and SK-II are expressed as;

$$\mathbf{P}(\lambda_1\lambda_2) = \mathbf{P}(\delta_\lambda) \propto \exp\left(-\frac{\delta_\lambda^2}{2}\right) \tag{9.20}$$

$$\mathbf{P}(\epsilon_1\epsilon_2) = \mathbf{P}(\delta_\epsilon) \propto \exp\left(-\frac{\delta_\epsilon^2}{2}\right) \tag{9.21}$$

$$\mathbf{P}(b_1 b_2) = \mathbf{P}(\delta_b) \propto \exp\left(-\frac{\delta_b^2}{2}\right) \tag{9.22}$$

where δ_λ, δ_ϵ and δ_b are correlated error factors for SK-I and SK-II. The statistical error term (Equation 9.14) for the background MC is not taken into account because of the large systematic errors. The exposure, the detection efficiency and the background for SK-I and SK-II are calculated as follows.

$$\lambda_i = \lambda_{0i} + \delta_\lambda\sigma_{\lambda i} \quad (i = 1, 2) \tag{9.23}$$

$$\epsilon_i = \epsilon_{0i} + \delta_\epsilon\sigma_{\epsilon i} \quad (i = 1, 2) \tag{9.24}$$

$$b_i = b_{0i} + \delta_b\sigma_{bi} \quad (i = 1, 2) \tag{9.25}$$

where λ_{0i}, ϵ_{0i} and b_{0i} are the estimated exposure, detection efficiency and background for SK-I and SK-II, respectively.

Finally the probability density function can be expressed as;

$$\begin{aligned}\mathbf{P}(\Gamma|n_1, n_2) = \frac{1}{A}\int\int\int &\frac{e^{-(\Gamma\lambda_1\epsilon_1+b_1)}\left(\Gamma\lambda_1\epsilon_1 + b_1\right)^{n_1}}{n_1!}\frac{e^{-(\Gamma\lambda_2\epsilon_2+b_2)}\left(\Gamma\lambda_2\epsilon_2 + b_2\right)^{n_2}}{n_2!} \\ &\times\mathbf{P}(\Gamma)\mathbf{P}(\delta_\epsilon)\mathbf{P}(\delta_\lambda)\mathbf{P}(\delta_b)d\delta_\epsilon d\delta_\lambda d\delta_b.\end{aligned} \tag{9.26}$$

Confidence level is calculated by integrating this probability density function.

For a mode with two different meson decay modes like $\eta \to 2\gamma$ and $\eta \to 3\pi^0$, the efficiencies and the backgrounds were simply added because such different meson decay mode searches are independent. The systematic errors on the detection efficiencies and the backgrounds were also simply added assuming 100% correlation.

9.3.3 The Results

The nucleon partial lifetime limits at 90% confidence level were obtained by the method described in the previous sections. The results are summarized in Table 9.31 with the limits by IMB-3 [5], Kamiokande-I+II [6] and the previous Super-Kamiokande result [38]. They are also shown in Figure 9.43. The obtained results are discussed in the next chapter.

τ/Br (10^{33}yrs)	This Thesis		IMB-3 [5]	Kam-I+II [6]	SK [38]
$p \to e^+\pi^0$	8.2	(9.1)	0.540	0.260	1.6
$p \to \mu^+\pi^0$	6.6	(7.3)	0.473	0.230	
$p \to e^+\eta$	4.2	(5.4)	0.313	0.140	
$p \to \mu^+\eta$	1.3	(1.8)	0.126	0.069	
$p \to e^+\rho^0$	0.71	(0.96)	-	0.075	
$p \to \mu^+\rho^0$	0.16	(0.23)	-	0.110	
$p \to e^+\omega$	0.32	(0.63)	0.107	0.045	
$p \to \mu^+\omega$	0.78	(1.1)	0.117	0.057	
$n \to e^+\pi^-$	2.0	(3.2)	0.158	0.130	
$n \to \mu^+\pi^-$	1.0	(1.7)	0.090	0.10	
$n \to e^+\rho^-$	0.070	(0.18)	0.217	0.058	
$n \to \mu^+\rho^-$	0.036	(0.16)	0.228	0.023	

Table 9.31: Nucleon partial lifetime limits at 90% confidence level. Limits without systematic errors are also shown in parenthesis.

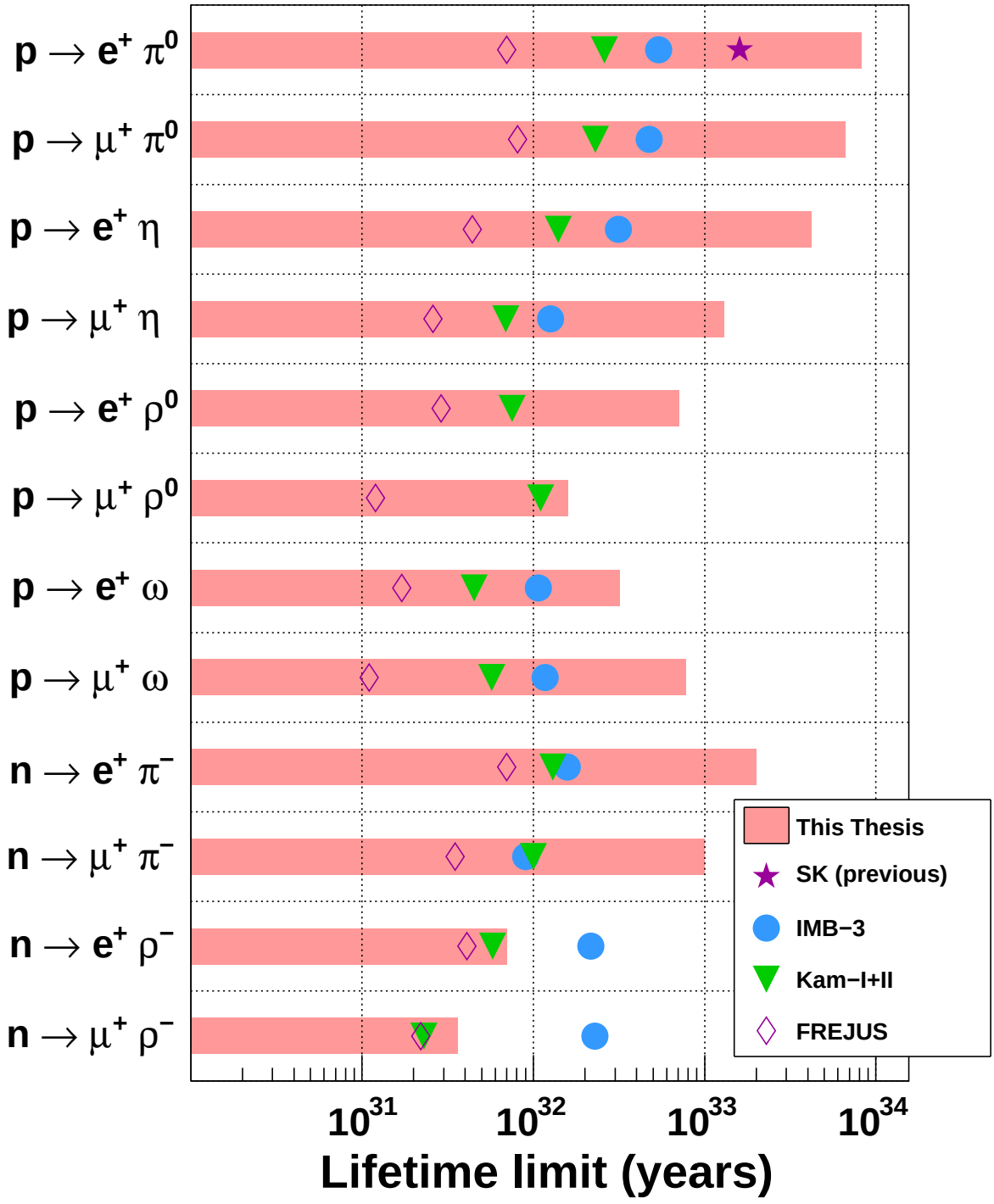

Figure 9.43: Nucleon partial lifetime limits at 90% confidence level.

Chapter 10

Discussions and Conclusions

10.1 Discussion

Comparison with the Theoretical Predictions

Here we compare the experimental nucleon lifetime limit for the $p \to e^+\pi^0$ mode with various theoretical predictions.

The obtained lower limit of proton partial lifetime at 90% confidence level for $p \to e^+\pi^0$ by SK-I and SK-II is

$$\tau/B_{p\to e^+\pi^0} > 8.2 \times 10^{33} \text{ (years)}. \tag{10.1}$$

The theoretical lower limit of proton lifetime by the minimal SUSY SU(5) GUT model is calculated as;

$$\tau/B_{p\to e^+\pi^0} > 4.1 \times 10^{33} \text{ [9]}, \tag{10.2}$$

although the dominant decay mode for this model is $p \to \bar{\nu}K^+$ and strongly constrained by SK [12].

The non-supersymmetric SO(10) GUT which directly breaks to SU(3)×SU(2)×U(1) predicts relatively short proton lifetime and are not consistent with the previous experimental results. On the other hand, the non-supersymmetric SO(10) GUT mediating the SU(4)×SU(2)$_L$×SU(2)$_R$ symmetry predicts the partial lifetime limit as;

$$\tau/B_{p\to e^+\pi^0} \sim 1.44 \times 10^{32.1\pm0.7\pm1.0\pm1.9} \text{ [14]}. \tag{10.3}$$

The sensitivity of the nucleon decay search in this thesis is within the range of the predictions of these models.

In addition, the SUSY SO(10) GUT model predicts the lifetime as;

$$\tau/B_{p\to e^+\pi^0} \sim 10^{35\pm1} \text{ [16]}. \tag{10.4}$$

Another possibility of GUT is the unifications in extra dimensions. One of the 5-D supersymmetric SO(10) GUT modes also predicts the lifetime in the observable range as;

$$\tau/B_{p\to e^+\pi^0} \sim 7 \times 10^{33\pm2} \text{ [17]}. \tag{10.5}$$

These models also predict the possibility of nucleon decays via other charged anti-lepton plus meson modes. This study systematically set their lifetime limits ranging from 3.6×10^{31}

to 8.2×10^{33} years. On the other hand, these models predict the proton partial lifetime to be around $10^{33} \sim 10^{35}$ years. Although we cannot ruled out these models because of their large uncertainties, the experimental results described in this thesis give constraints to these models.

Furthermore, by combining the other mode search results, the lower limit for the proton lifetime which includes all the proton decay branches can be more stringent, though it is strongly depends on the model. If we use the proton decay branching ratio by Machacek [20] as shown in Table 2.2, proton decay detection efficiency is $\sim 15\%$ only by the $p \to e^+\pi^0$ mode. It can be increased by roughly $\sim 30\%$ by combining the other mode searches. In the branching ratio calculation by Donoghue [22], the $p \to e^+\pi^0$ mode is significantly suppressed, and the proton decay detection efficiency only by the $p \to e^+\pi^0$ mode is only $\sim 4\%$. Then, the proton decay efficiency can be increased by a factor of two by using the others. Similarly, the sensitivity for the nucleon lifetime can also be improved by including the neutron decay search results because the neutron lifetime are estimated to be comparable with that of proton in many models.

Comparison with the Other Experiments

Table 10.1 shows the detection efficiencies, background estimations and the number of candidates for the Super-Kamiokande, IMB and KAMIOKANDE experiments. In this study, we decided the selection criteria not to increase sensitivity, but rather to reduce background events to less than 0.5 events. The detection efficiencies in SK-I and SK-II were similar to or lower than those in IMB and KAMIOKANDE. Thus, the nucleon decay searches in this thesis achieved the lower background than the others even with more than one order larger exposure. Especially for the $p \to e^+\pi^0$ mode, the detection efficiency in SK-I and SK-II was similar to the other experiments with the much lower background level.

This is the first systematical search in Super-Kamiokande for nucleon decays mediated by the exchange of the superheavy gauge boson. The systematic errors for the nuclear effect of the η meson and the ω meson were newly evaluated and can be used for other nucleon decay mode searches. Moreover, there are some improvements and updates in the event reconstruction tools for this analysis, especially in the ring separation and the charged pion momentum reconstruction. These can also contribute to the other physics analysis in Super-Kamiokande.

The obtained nucleon partial lifetime limits are longer than the results from the previous experiments except for the $n \to e^+\rho^-$ and $n \to \mu^+\rho^-$ modes. The exposure of IMB-3, KAMIOKANDE-I+II and the previous SK result were 7.6, 3.79 and 25.5 kiloton·year, respectively. The SK-I and SK-II combined data had 18.5, 37.2 and 5.5 times larger exposure than those three results with much better background expectation, respectively. Therefore, the obtained lifetime limits are roughly equivalent to the values obtained by scaling the previous limits by the product of exposure and efficiency. For example, the obtained partial lifetime limit for the $p \to e^+\pi^0$ mode is five times greater than the previous SK limit. However, in some modes, the obtained limit is smaller than the scaled limit from the previous limit. That is mostly because of the differences of the strategy and the treatment of systematic errors. The systematic errors from the uncertainty of the nuclear effects for the $n \to e^+\rho^-$ and $n \to \mu^+\rho^-$ detection are very large because there is no free neutron. In addition to this, only the systematic error of background estimations was taken into account in the lifetime limit calculation in the IMB analysis. If we neglect the systematic error for the detection efficiency, the lifetime limits are almost equivalent to the ratio $((\epsilon \times \lambda)_{\rm SK}/(\epsilon \times \lambda)_{\rm IMB})$ times the limits by IMB, where ϵ and λ are the detection efficiency and the exposure of an experiment.

	SK-I+II				IMB-3				KAM-I+II			
	eff. (%)	BG (/141)	N_c	τ	eff. (%)	BG (/7.6)	N_c	τ	eff. (%)	BG (/3.8)	N_c	τ
$p \to e^+\pi^0$	44.6	0.31	0	8.2	48	0.2	0	0.54	45	<0.04	0	0.26
$p \to \mu^+\pi^0$	35.5	0.34	0	6.6	42	0.6	0	0.47	43	<0.2	0	0.23
$p \to e^+\eta$	26.9	0.44	0	4.2	28	0.2	0	0.31	24	<0.04	0	0.14
$p \to \mu^+\eta$	18.5	0.49	2	1.3	23	2.8	3	0.13	21	<0.08	1	0.07
$p \to e^+\rho^0$	4.9	0.35	0	0.71	-	-	-	-	24	2.7	2	0.08
$p \to \mu^+\rho^0$	1.8	0.42	1	0.16	-	-	-	-	22	1.7	0	0.11
$p \to e^+\omega$	4.9	0.53	1	0.32	21	10.8	7	0.11	11	1.45	2	0.05
$p \to \mu^+\omega$	5.5	0.48	0	0.78	33	12.1	11	0.12	13	1.9	2	0.06
$n \to e^+\pi^-$	19.4	0.27	0	2.0	30	5.0	3	0.16	28	<0.2	0	0.13
$n \to \mu^+\pi^-$	16.7	0.43	1	1.0	14	1.9	1	0.09	23	<0.2	0	0.10
$n \to e^+\rho^-$	1.8	0.38	1	0.07	49	4.8	4	0.22	15	1.9	0	0.06
$n \to e^+\rho^-$	1.1	0.29	0	0.04	36	9.5	3	0.23	6	1.8	1	0.02
Total		4.7	6			47.9	32			11.5	9	

Table 10.1: The comparison of efficiencies, background estimations, candidates and lifetime limits between SK, IMB and KAMIOKANDE. 'BG' is the background estimation for SK, IMB and KAMIOKANDE in 141, 7.6 and 3.79 kiloton·year exposure, respectively. 'N_c' is the number of candidate. 'τ' is the partial lifetime limit in 10^{33} years. The efficiencies for SK and KAMIOKANDE are those in SK-I and KAMIOKANDE-II, respectively.

Future Prospects

The low background observation with the high efficiency were achieved with the Super-Kamiokande detector. Therefore, the sensitivity of the Super-Kamiokande experiment will be improved proportional to the exposure in the future for the modes studied in this thesis. Super-Kamiokande-III was switched to Super-Kamiokande-IV with the newly developed electronics and online systems in September, 2008. The accumulated exposure in the SK-III period was 34 kiloton·year. The lifetime sensitivity for the $p \to e^+\pi^0$ mode including the SK-III data may reach to the order of 10^{34} years. Furthermore, the Super-Kamiokande-IV experiment will continue nucleon decay searches as the largest experiment with the new stable electronics. The more stringent limits or the evidence for nucleon decay signals will be given by the SK-IV experiment in the future.

As for more future prospects, this thesis has some implications to the design of next generation nucleon decay experiments. SK-II has the comparable nucleon decay detection performance even with its half photo coverage of ∼20%. This may imply that the lower PMT density than that of SK-I is acceptable for the next generation experiment. However, this is not obvious for less energetic modes, such as $p \to \bar{\nu}K^+$ and needs to be further studied for those modes. The other implication is for the background rate. If the fiducial volume for the next generation experiment is more than 10 times greater than SK, its background rate from the atmospheric neutrinos will not be negligible any longer. The total momentum cuts for $p \to e^+\pi^0$ are wide enough for the free proton decay events. Thus, one possibility to reduce the background is to use tighter total momentum cut for the $p \to e^+\pi^0$ mode targeting the free proton decay events. The background rate is expected to be reduced by an order of magnitude, while the efficiency is expected to be decreased to about half of the efficiency in this analysis.

10.2 Conclusion

Nucleon decays into a charged anti-lepton (e^+ and μ^+) plus a light meson (π^0, π^-, η, ρ^0, ρ^- and ω) were searched in 91.7 and 49.2 kiloton·year exposures of the SK-I and SK-II data, respectively. The combined 140.9 kiloton·year exposure is six times greater than the previous result for the $p \to e^+\pi^0$ mode [38].

This is the first nucleon decay search results using the SK-II data. Performances for nucleon decay searches were compared between SK-I and SK-II. The observation in the SK-II period had the similar performance to that in the SK-I period even though the photo coverage is half of SK-I.

No evidence for proton decays via the $p \to e^+\pi^0$ mode was found, though this mode has the highest detection efficiency and is the dominant proton decay mode in various GUT models. Six candidate events were found in the SK-I and SK-II data for the five largest background modes. The total expected background from the atmospheric neutrino was 4.7 events. The number and the feature of candidate events are consistent with the background estimation by the atmospheric neutrino MC.

The nucleon partial lifetime limits were calculated based on Bayes' theorem. The lower limit on the partial lifetime of proton via the $p \to e^+\pi^0$ mode was set to be 8.2×10^{33} years at 90% confidence level. This limit is more stringent than the previous results of 1.6×10^{33} years [38] by 25.5 kiloton·year exposure of the SK-I data. The obtained lower partial lifetimes limits via the other modes except for $n \to e^+\rho^-$ and $n \to \mu^+\rho^-$ are also more stringent than the previous

limits by IMB-3 or KAMIOKANDE-I+II. They range from 1.6×10^{32} to 6.6×10^{33} years. The obtained lifetime limits for the $n \to e^+\rho^-$ and $n \to \mu^+\rho^-$ modes are 7.0×10^{31} and 3.6×10^{31} years, respectively. They are less stringent than the IMB-3 result because of the difference of the strategy for the selection criteria determination and the treatment of the systematic errors. This systematical study cannot ruled out the interesting GUT models, such as minimal SUSY SU(5) GUT, SO(10) GUT and so on, but can give constraints on parameters relevant to nucleon decays mediated by a super heavy gauge boson.

Appendix A

Details of the Selection Criteria

A.1 $p \to l^+\eta$ Mode Search

A.1.1 $p \to l^+\eta$ $(\eta \to 2\gamma)$ Mode Search

Event Selection Criteria The selection criteria for the $p \to l^+\eta$ $(\eta \to 2\gamma)$ modes are defined as ;

(A) the number of Cherenkov rings is three,

(B) one of the three rings is a shower (non-shower) type ring for $p \to e^+\eta$ $(p \to \mu^+\eta)$, and the other two rings are shower type rings, (For $p \to \mu^+\eta$, the PID with both a Cherenkov ring pattern and an opening angle is used.)

(C) the invariant mass of η meson is reconstructed in between 480 to 620 MeV/c^2,

(D) the number of Michel electrons is 0 (1) for $p \to e^+\eta$ $(p \to \mu^+\eta)$,

(E) the reconstructed total momentum is less than 250 MeV/c, and the reconstructed total invariant mass is in between 800 to 1050 MeV/c^2.

Figure A.1 shows the number of ring distributions of the proton decay MC. The fraction of 3 rings was 93% for SK-I free proton decay of the $\eta \to 2\gamma$ mode of both $p \to e^+\eta$ and $p \to \mu^+\eta$.

For the $p \to e^+\eta$ mode, the criterion (B) is same as the $p \to e^+\pi^0$ mode. For the $p \to \mu^+\eta$ mode, the momentum of μ^+ is $\sim$ 300 MeV/c. The PID with a Cherenkov ring pattern and an opening angle was used for this mode to improve the PID. The mis-PID probabilities for SK-I free proton decay of the $\eta \to 2\gamma$ mode of $p \to e^+\eta$ $(p \to \mu^+\eta)$ were estimated to be 6.0% (7.9%).

The invariant mass of the η meson was required to be in between 480 to 620 MeV/c^2 (the criterion (C)). The reconstructed η invariant mass distributions of the proton decay MC, the atmospheric neutrino MC and the observed data are shown in Figure A.2. For SK-I free proton decay events of the $\eta \to 2\gamma$ mode of $p \to e^+\eta$ $(p \to \mu^+\eta)$, the mean of the reconstructed η invariant mass distribution was 548 (539) MeV/c^2, and its resolution was 27 (26) MeV/c^2. There is a peak around η meson mass in the atmospheric neutrino MC. This is not due to the η production in the neutrino interaction MC, but due to the invariant mass reconstruction method, in which the best combination for the η mass reconstruction was selected. The same peak is also seen in the data, which is consistent with the atmospheric neutrino MC.

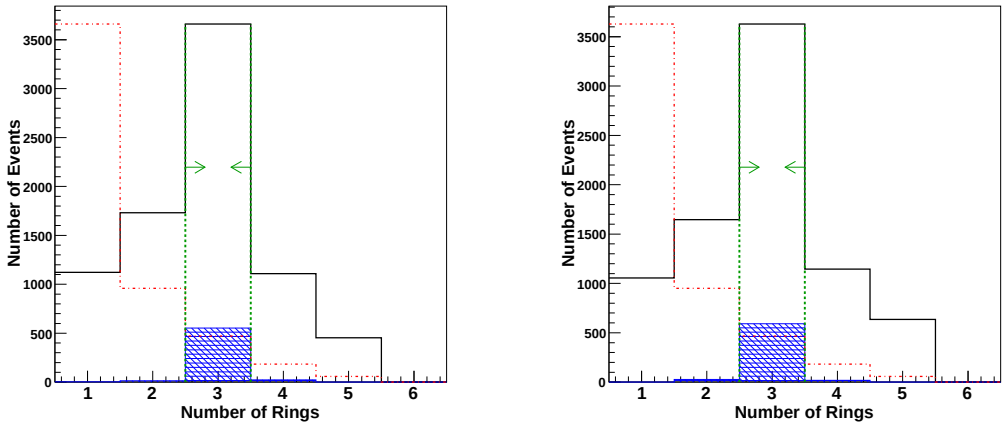

Figure A.1: The number of ring distributions of $p \to e^+\eta$ MC (left) and $p \to \mu^+\eta$ MC (right) in SK-I. Shaded histograms are the distributions of free proton decay events of the $\eta \to 2\gamma$ mode. The distribution of the atmospheric neutrino MC, which is normalized with the proton decay MC using the maximum bin value, is also shown in dashed histograms. Dashed lines and arrows indicate the selection criterion.

Figures A.3 and A.4 show the distributions of the total momentum of the proton decay MC and the total invariant mass of the proton decay MC. The total invariant mass was well reconstructed, and its resolution is comparable to that of $p \to e^+\pi^0$ and $p \to \mu^+\pi^0$. For SK-I free proton decay of the $\eta \to 2\gamma$ mode of $p \to e^+\eta$ ($p \to \mu^+\eta$), the mean of the total invariant mass distribution was 939.4 (923.7) MeV/c^2, and its resolution was 21.8 (24.9) MeV/c^2. The resolution of the total momentum was 25.7 (32.1) MeV/c for $p \to e^+\eta$ ($p \to \mu^+\eta$).

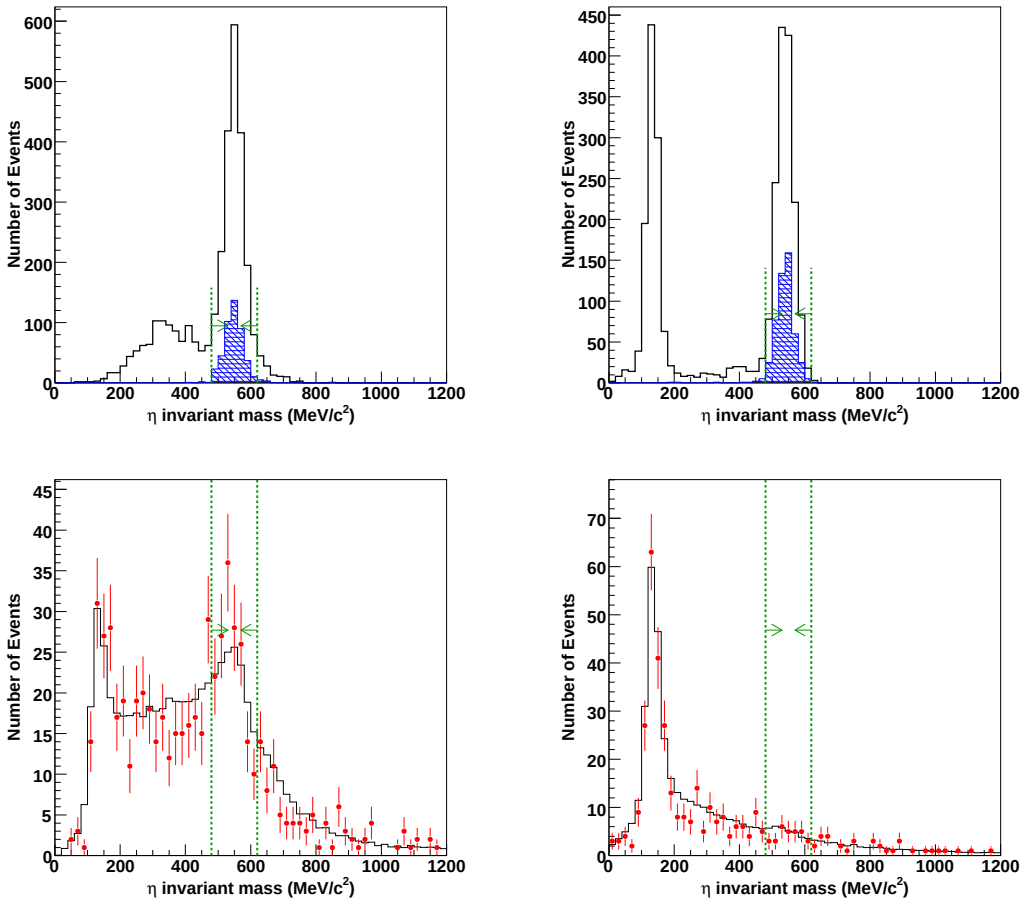

Figure A.2: η invariant mass distributions of $p \to e^+\eta$ MC (left) and $p \to \mu^+\eta$ MC (right) in SK-I. The top two figures are the proton decay MC, and the bottom two figures are the atmospheric neutrino MC (solid lines) and the observed data (points). Shaded histograms in the proton decay MC are the distributions of free proton decay events of the $\eta \to 2\gamma$ mode. Dashed lines and arrows indicate the selection criterion.

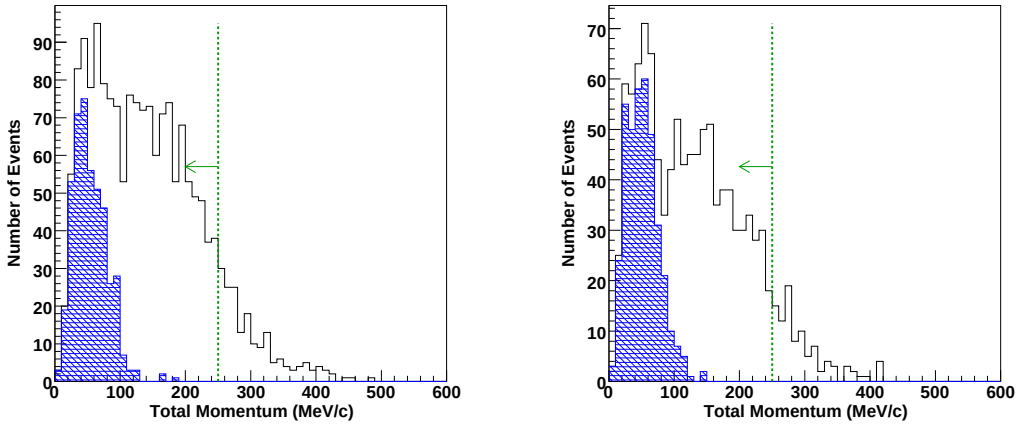

Figure A.3: The total momentum distributions of $p \to e^+\eta$ MC (left) and $p \to \mu^+\eta$ MC (right) in SK-I. Shaded histograms are the distributions of free proton decay events of $\eta \to 2\gamma$ mode. Dashed lines and arrows indicate the selection criterion. Only the events which satisfy the selection criteria (A $\sim$ D) and $800 < M_{\rm tot} < 1050$ MeV/c^2 are plotted.

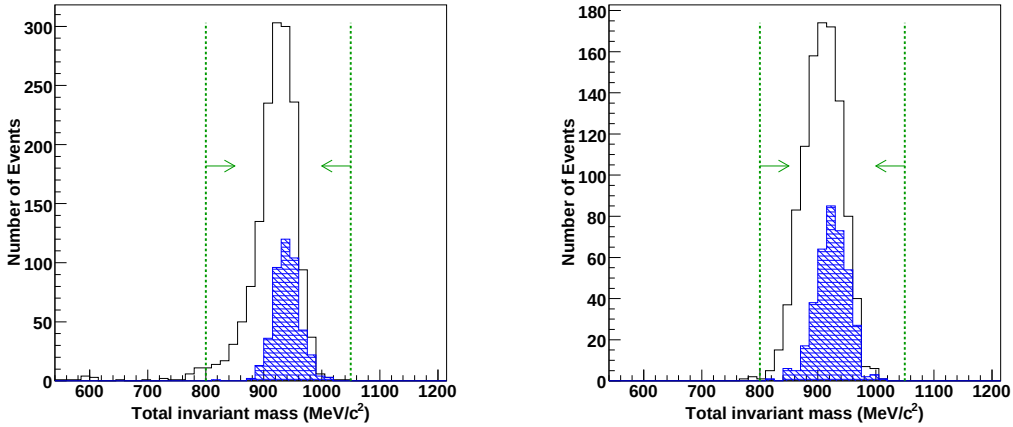

Figure A.4: The total invariant mass distributions of $p \to e^+\eta$ MC (left) and $p \to \mu^+\eta$ MC (right) in SK-I. Shaded histograms are the distributions of free proton decay events of $\eta \to 2\gamma$ mode. Dashed lines and arrows indicate the selection criterion. Only the events which satisfy the selection criteria (A $\sim$ D) and $P_{\rm tot} < 250$ MeV/c are plotted.

A.1.2 $p \to l^+\eta$ ($\eta \to 3\pi^0$) Mode Search

Event Selection Criteria The selection criteria for the $p \to l^+\eta$ ($\eta \to 3\pi^0$) modes are defined as ;

(A) the number of Cherenkov rings is four or five,

(B) one of the rings is a shower (non-shower) type ring for $p \to e^+\eta$ ($p \to \mu^+\eta$), and all the other rings are shower type rings, (For $p \to \mu^+\eta$, the PID with both a Cherenkov ring pattern and an opening angle is used.)

(C) η invariant mass is reconstructed in between 400 to 700 MeV/c^2,

(D) the number of Michel electrons is 0 (1) for $p \to e^+\eta$ ($p \to \mu^+\eta$),

(E) the reconstructed total momentum is less than 150 (250) MeV/c for $p \to e^+\eta$ ($p \to \mu^+\eta$), and the reconstructed total invariant mass is in between 800 to 1050 MeV/c^2.

The ring counting algorithm is only possible to find up to 5 rings. Consequently, the criterion (A) was applied to select events with 4 or 5 rings. The number of ring distributions of the proton decay MC is shown in Figure A.5. The fraction of 4 or 5 rings was 77% (84%) for SK-I free proton decay of the $\eta \to 3\pi^0$ mode of $p \to e^+\eta$ ($p \to \mu^+\eta$).

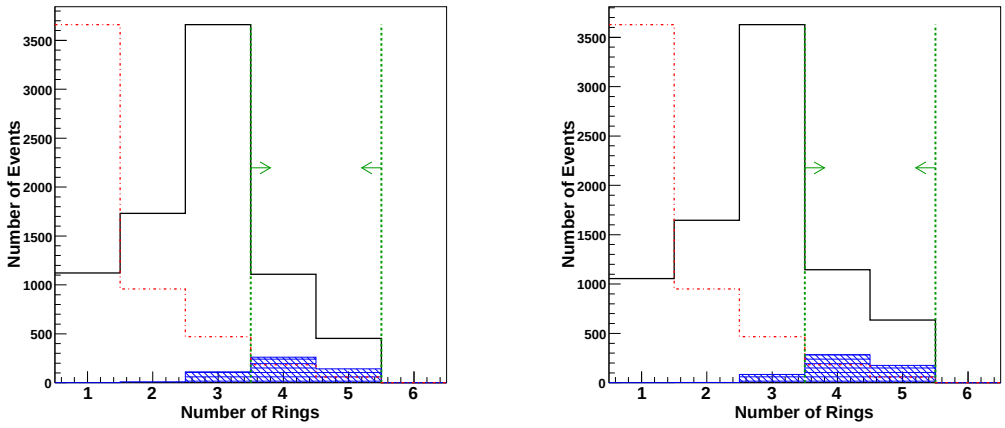

Figure A.5: The number of ring distributions of $p \to e^+\eta$ MC (left) and $p \to \mu^+\eta$ MC (right) in SK-I. Shaded histograms are the distributions of free proton decay events of $\eta \to 3\pi^0$ mode. The distribution of the atmospheric neutrino MC, which is normalized with the proton decay MC using the maximum bin value, is also shown in dashed histograms. Dashed lines and arrows indicate the selection criterion.

In the criterion (B), the PID with a Cherenkov ring pattern and an opening angle was used for for $p \to \mu^+\eta$, which is same as the search via the $\eta \to 2\gamma$ mode.

Therefore, the event selection window of η invariant mass is larger than that in the search via $\eta \to 2\gamma$ mode. The reconstructed η invariant mass distributions of the proton decay MC, the atmospheric neutrino MC and the observed data are shown in Figure A.6. For SK-I free proton

decay events of $\eta \to 3\pi^0$ mode of $p \to e^+\eta$ ($p \to \mu^+\eta$), the mean of the reconstructed η invariant mass distribution was 554 (462) MeV/c^2, and its resolution was 69 (62) MeV/c^2. Because one ring from a charged lepton (e^+) cannot be separately identified from the other shower type rings by the PID for the $p \to e^+\eta$ mode, the best combination which made the reconstructed mass the closest to true η mass was selected. That is why the mean mass for $p \to e^+\eta$ MC is closer to the true η mass than that for $p \to \mu^+\eta$.

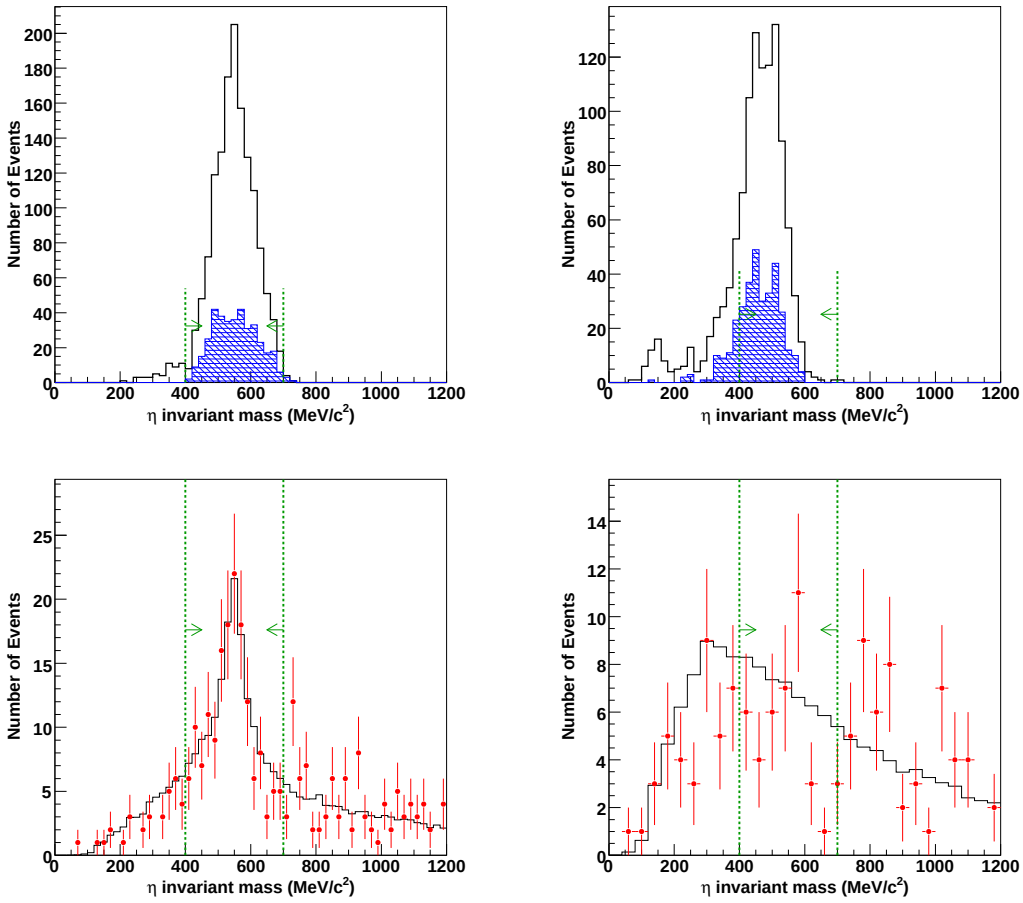

Figure A.6: η invariant mass distributions of $p \to e^+\eta$ MC (left) and $p \to \mu^+\eta$ MC (right) in SK-I. The top two figures are the proton decay MC, and the bottom two figures are the atmospheric neutrino MC and the observed data. Shaded histograms in the proton decay MC are the distributions of free proton decay events of $\eta \to 3\pi^0$ mode. Dashed lines and arrows indicate the selection criterion.

Figure A.7 and A.8 show the distributions of the total momentum of the proton decay MC and the total invariant mass of the proton decay MC. For SK-I free proton decay of the $\eta \to 3\pi^0$ mode of $p \to e^+\eta$ ($p \to \mu^+\eta$) the mean of the total invariant mass distribution was 906.3 (895.0) MeV/c^2, and its resolution was 27.4 (29.9) MeV/c^2. The resolution of the total momentum was 41.9 (88.1) MeV/c for $p \to e^+\eta$ ($p \to \mu^+\eta$). Although the reconstructed invariant mass was systematically lower than the true proton mass, the selection window of the invariant mass is

wide enough to cover the proton decay MC distributions. The number of background rates for $p \to e^+\eta$ was not low enough with the standard event selection criteria of $P_{\rm tot} < 250$ MeV/c. In order to reduce the background, the tighter total momentum cut of $P_{\rm tot} < 150$ MeV/c was applied for the $p \to e^+\eta$ mode.

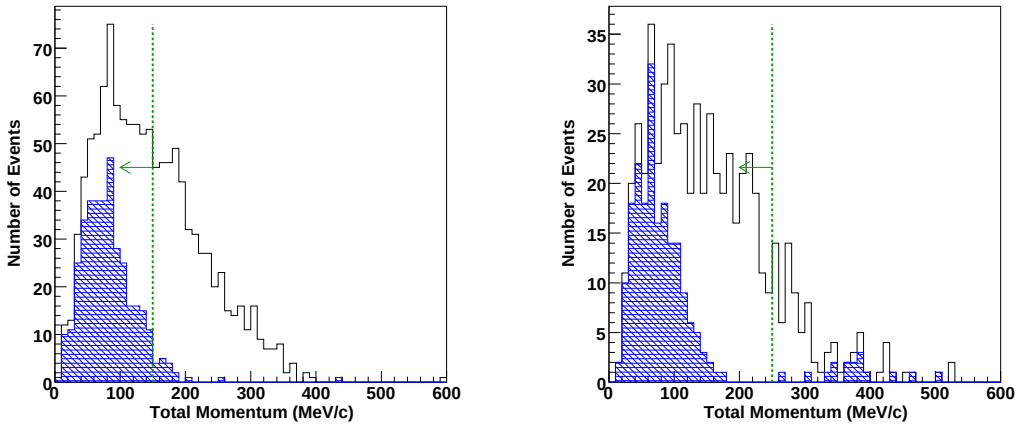

Figure A.7: The total momentum distributions of $p \to e^+\eta$ MC (left) and $p \to \mu^+\eta$ MC (right) in SK-I. Shaded histograms are the distributions of free proton decay events of $\eta \to 3\pi^0$ mode. Dashed lines and arrows indicate the selection criterion. Only the events which satisfy the selection criteria (A $\sim$ D) and $800 < M_{\rm tot} < 1050$ MeV/c^2 are plotted.

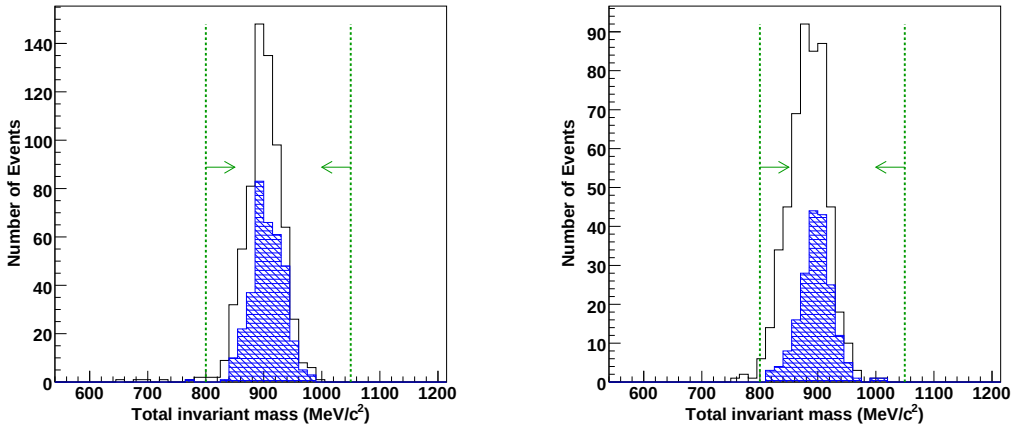

Figure A.8: The total invariant mass distributions of $p \to e^+\eta$ MC (left) and $p \to \mu^+\eta$ MC (right) in SK-I. Shaded histograms are the distributions of free proton decay events of $\eta \to 3\pi^0$ mode. Dashed lines and arrows indicate the selection criterion. Only the events which satisfy the selection criteria (A $\sim$ D) and $P_{\rm tot} < 150$ (250) MeV/c are plotted for $p \to e^+\eta$ ($p \to \mu^+\eta$).

A.2 $p \to l^+\rho^0$ Mode Search

Event Selection Criteria The selection criteria for $p \to l^+\rho^0$ modes are defined as ;

(A) the number of Cherenkov rings is three,

(B) one of the rings is a shower (non-shower) type ring for $p \to e^+\rho^0$ ($p \to \mu^+\rho^0$), and the other two rings are non-shower type rings, (The PID with both a Cherenkov ring pattern and an opening angle is used.)

(C) ρ^0 invariant mass is reconstructed in between 600 to 900 MeV/c^2,

(D) the number of Michel electrons is 0 or 1 (1 or 2) for $p \to e^+\rho^0$ ($p \to \mu^+\rho^0$),

(E) the reconstructed total momentum is less than 150 (250) MeV/c for $p \to e^+\rho^0$ ($p \to \mu^+\rho^0$), and the reconstructed total invariant mass is in between 800 to 1050 MeV/c^2.

The criterion (A) requires to find all the three rings to reconstruct the mass and the momentum of a proton. Figure 9.27 shows the number of ring distributions of the proton decay MC. The fraction of 3 rings was 50% and 27% for the free proton decay of $p \to e^+\rho^0$and $p \to \mu^+\rho^0$, respectively. The lower efficiency for $p \to \mu^+\rho^0$ was due to proton decay events with an invisible muon.

In the criterion (B), the two rings from the two charged pions were required to be identified as non-shower type-rings. The charged pions from the the decay of the ρ meson has a low momentum of about 300 MeV/c. The PID with a Cherenkov ring pattern and an opening angle was used for both $p \to e^+\rho^0$ and $p \to \mu^+\rho^0$.

The invariant mass of ρ meson is reconstructed by two non-shower type rings, and was required to be in between 600 and 900 MeV/c^2 in the criterion (C), as shown in Figure A.9.

For SK-I free proton decay events of $p \to e^+\rho^0$ ($p \to \mu^+\rho^0$), the mean of the reconstructed ρ invariant mass distribution was 730 (664) MeV/c^2, and its resolution was 74 (43) MeV/c^2. For $p \to \mu^+\rho^0$, if the ρ meson mass is greater than about 770 MeV/c^2, the muon momentum will be lower than the Cherenkov threshold. That is why the ρ mass distribution for $p \to \mu^+\rho^0$ had the narrower resolution and the systematically lower compared with $p \to e^+\rho^0$. Due to the same reason, there was a fake peak in the atmospheric neutrino MC, in which ρ meson production by neutrino interaction was not taken into account.

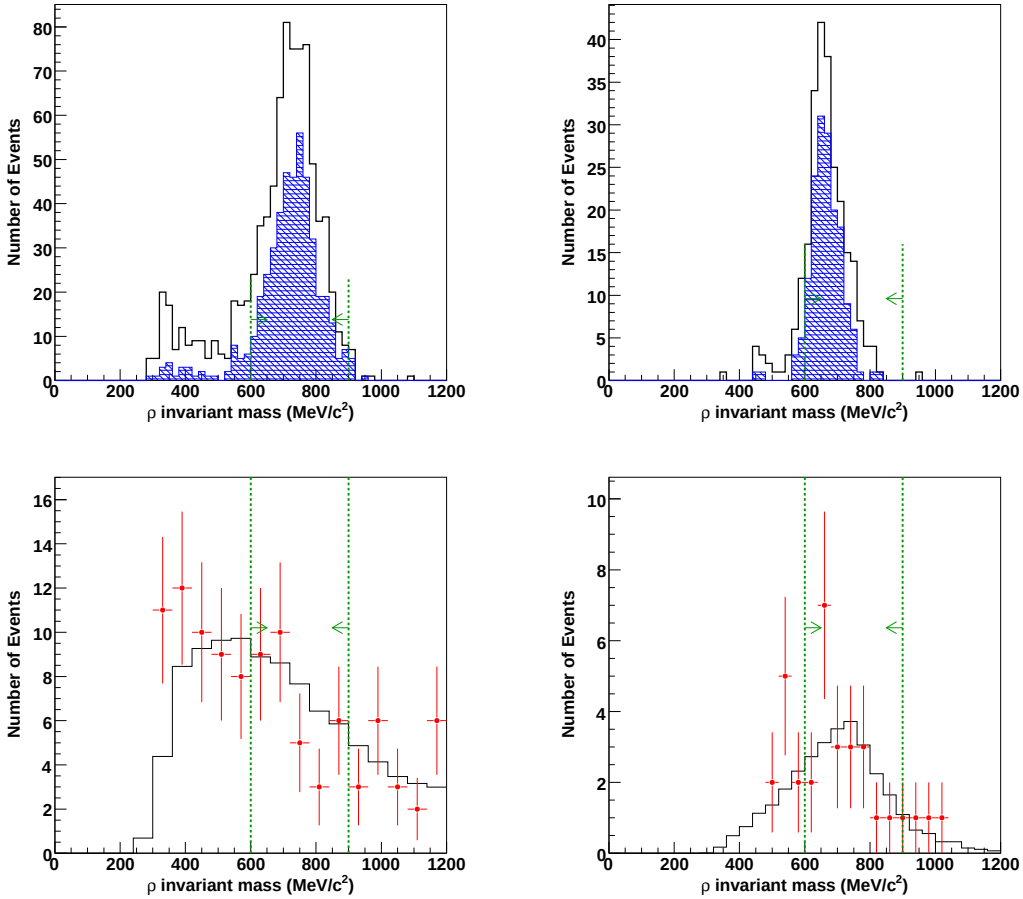

Figure A.9: ρ^0 invariant mass distributions of $p \to e^+\rho^0$ MC (left) and $p \to \mu^+\rho^0$ MC (right) in SK-I. The top two figures are the proton decay MC, and the bottom two figures are the atmospheric neutrino MC (solid lines) and the observed data (points). Shaded histograms are the distributions of free proton decay events. Dashed lines and arrows indicate the selection criterion.

Figures A.10 and A.11 show the distributions of the total momentum of the proton decay MC and the total invariant mass of the proton decay MC. For SK-I free proton decay of $p \to e^+\rho^0$ ($p \to \mu^+\rho^0$), the mean of the total invariant mass distribution was 907.6 (909.1) MeV/c^2, and its resolution was 43.9 (32.0) MeV/c^2. The resolution of the total momentum was 81.9 (96.9) MeV/c for $p \to e^+\rho^0$ ($p \to \mu^+\rho^0$).

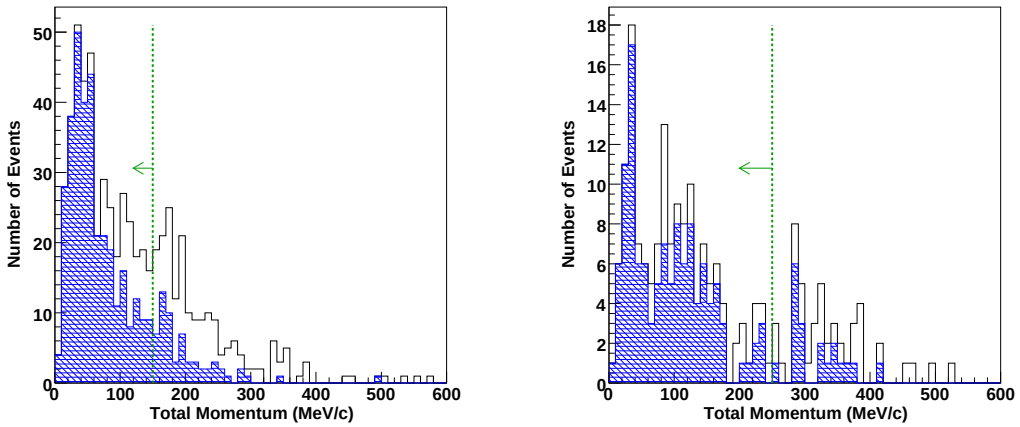

Figure A.10: The total momentum distributions of $p \to e^+\rho^0$ MC (left) and $p \to \mu^+\rho^0$ MC (right) in SK-I. Shaded histograms are the distributions of free proton decay events. Dashed lines and arrows indicate the selection criterion. Only the events which satisfy the selection criteria (A $\sim$ D) and $800 < M_{\rm tot} < 1050$ MeV/c^2 are plotted.

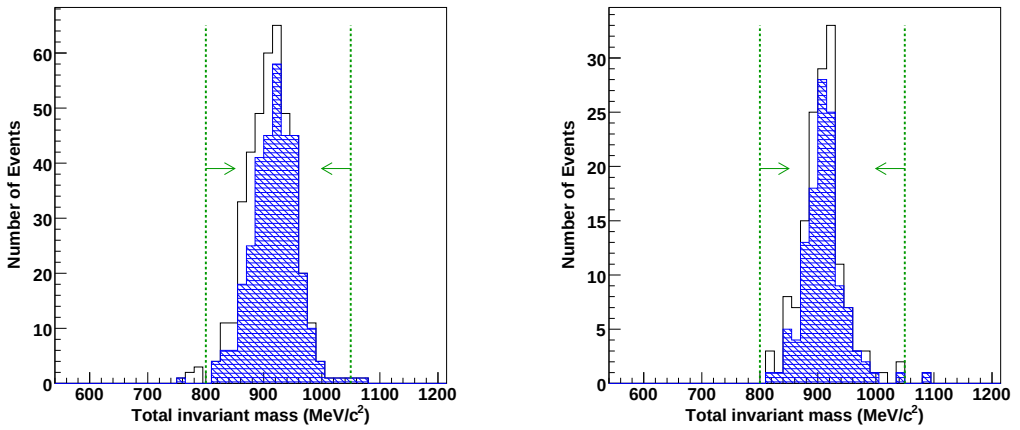

Figure A.11: The total invariant mass distributions of $p \to e^+\rho^0$ MC (left) and $p \to \mu^+\rho^0$ MC (right) in SK-I. Shaded histograms are the distributions of free proton decay events. Dashed lines and arrows indicate the selection criterion. Only the events which satisfy the selection criteria (A $\sim$ D) and $P_{\rm tot} < 150$ (250) MeV/c are plotted for $p \to e^+\rho^0$ ($p \to \mu^+\rho^0$).

A.3 $p \to l^+\omega$ Mode Search

A.3.1 $p \to l^+\omega$ $(\omega \to \pi^0\gamma)$ Mode Search

Event Selection Criteria The selection criteria for the $p \to l^+\omega$ $(\omega \to \pi^0\gamma)$ modes are defined as ;

(A) the number of Cherenkov rings is three or four (two or three) for $p \to e^+\omega$ $(p \to \mu^+\omega)$,

(B) all the rings are shower type rings,

(C) ω invariant mass is reconstructed in between 650 to 900 MeV/c^2,

(D) the number of Michel electrons is 0 (1) for $p \to e^+\omega$ $(p \to \mu^+\omega)$,

(E) the reconstructed total momentum is less than 150 (200) MeV/c for $p \to e^+\omega$ $(p \to \mu^+\omega)$, and the reconstructed total invariant mass is in between 800 to 1050 MeV/c^2 only for $p \to e^+\omega$.

Two or three shower type rings were required from the ω meson decay, and one more shower type ring from e^+ was required only in the case of the $p \to e^+\omega$ mode (the criteria A and B). Figure A.12 shows the the number of ring distributions of the proton decay MC. The fraction of 3-rings or 4-rings (2-rings or 3-rings) was 95% (97%) for SK-I free proton decay of the $\omega \to \pi^0\gamma$ mode for $p \to e^+\omega$ $(p \to \mu^+\omega)$.

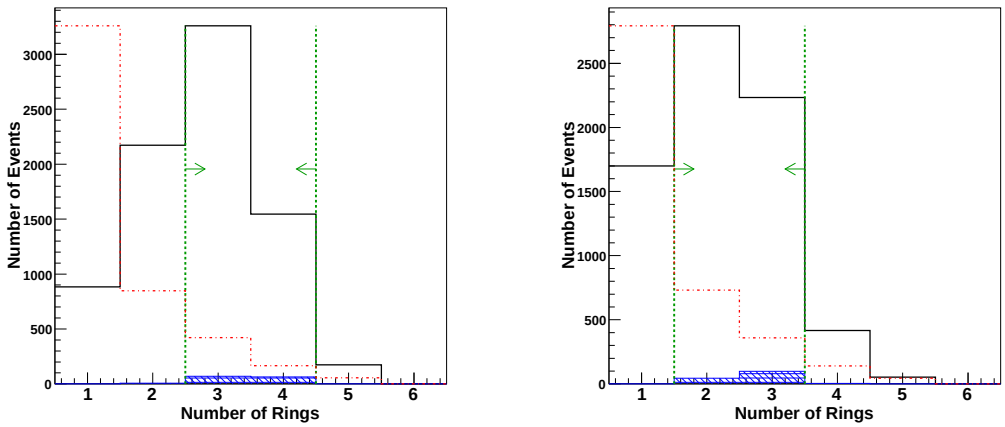

Figure A.12: The number of ring distributions of $p \to e^+\omega$ MC (left) and $p \to \mu^+\omega$ MC (right) in SK-I. Shaded histograms are the distributions of free proton decay events of $\omega \to \pi^0\gamma$ mode. The distribution of the atmospheric neutrino MC, which is normalized with the proton decay MC using the maximum bin value, is also shown in dashed histograms. Dashed lines and arrows indicate the selection criterion.

The ω invariant mass was reconstructed by all the detected rings for the $p \to \mu^+\omega$ mode. For the $p \to e^+\omega$ mode, it was reconstructed by the detected rings except for one ring, which was assumed to be e^+ ring. The reconstructed ω mass was required to be in between 650 to

900 MeV/c^2 (the criterion (C)). Their distributions of the proton decay MC, the atmospheric neutrino MC and the observed data are shown in Figure A.13. The invariant mass was well reconstructed, and the mean of the distribution was 754 (790) MeV/c^2 with the resolution of 36 (31) MeV/c^2. The lower invariant mass peak in the proton decay MC is due to the another ω meson decay mode of $\omega \to \pi^+\pi^-\pi^0$.

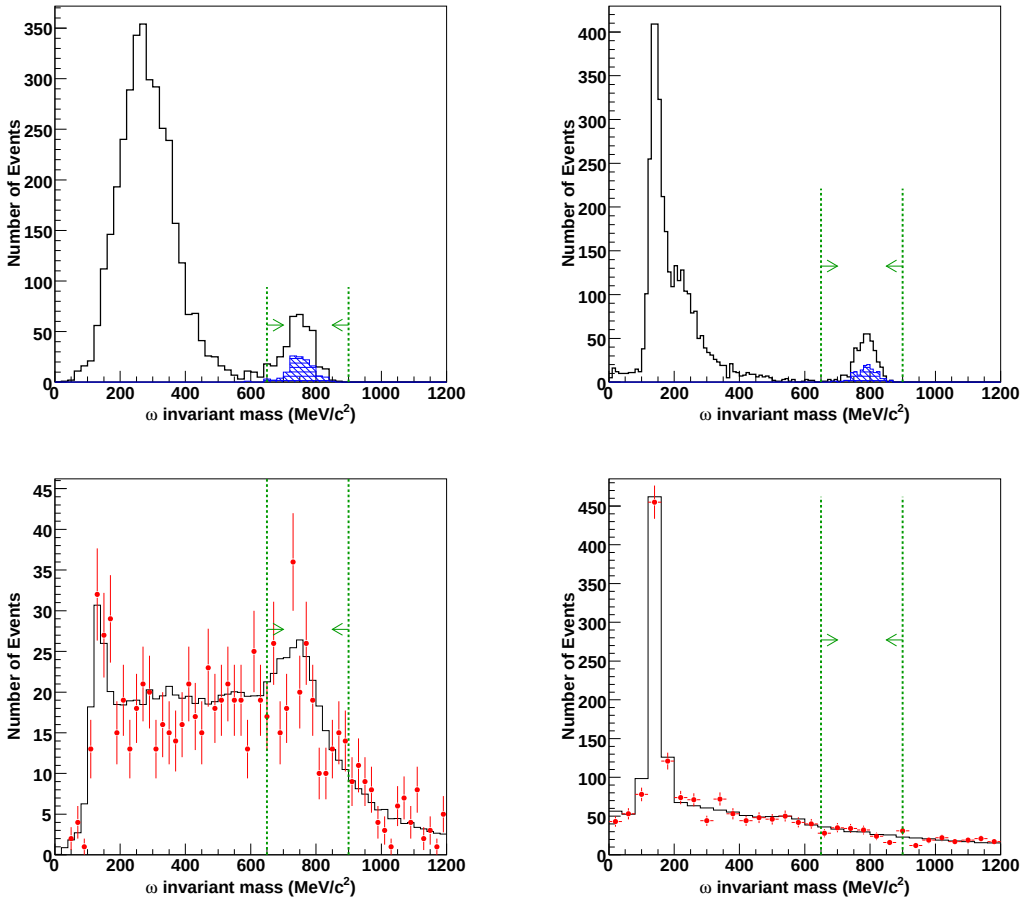

Figure A.13: ω invariant mass distributions of $p \to e^+\omega$ MC (left) and $p \to \mu^+\omega$ MC (right) in SK-I. The top and bottom figures are the proton decay MC and the atmospheric neutrino MC (solid lines) and the observed data (points), respectively. Shaded histograms are the distributions of free proton decay events of $\omega \to \pi^0\gamma$ mode. Dashed lines and arrows indicate the selection criterion.

Figures A.14 and A.15 show the distributions of the total momentum of the proton decay MC and the total invariant mass of the proton decay MC. For $p \to e^+\omega$ mode, the total mass and the total momentum of the source proton can be reconstructed. For SK-I free proton decay of $\omega \to \pi^0\gamma$ mode of $p \to e^+\omega$, the mean of the total invariant mass distribution was 935.3 MeV/c^2, and the resolution was 24.8 MeV/c^2. The resolution of the total momentum was 32 MeV/c for $p \to e^+\omega$. The total momentum threshold of the criterion (E) was determined to keep the background level low enough.

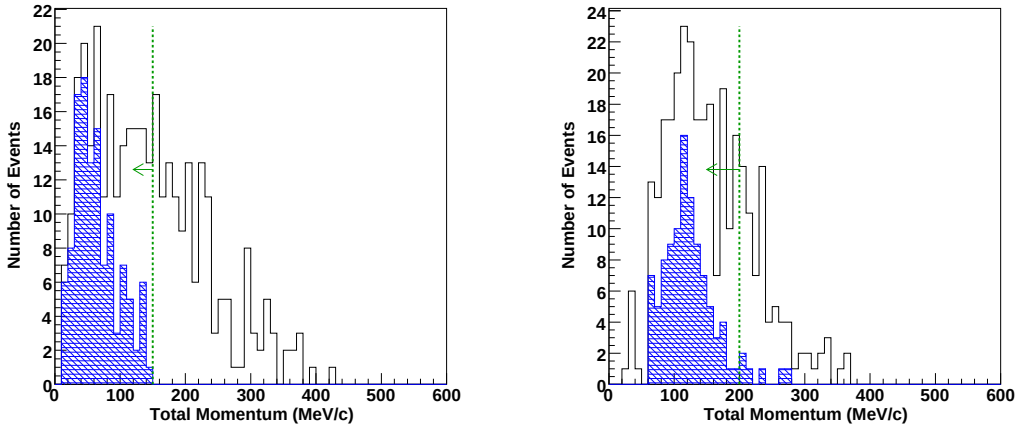

Figure A.14: The total momentum distributions of $p \to e^+\omega$ MC (left) and $p \to \mu^+\omega$ MC (right) in SK-I. Shaded histograms are the distributions of free proton decay events of $\omega \to \pi^0\gamma$ mode. Dashed lines and arrows indicate the selection criterion. Only the events which satisfy the selection criteria (A $\sim$ D) and $800 < M_{\rm tot} < 1050$ MeV/c^2 (only for $p \to e^+\omega$) are plotted.

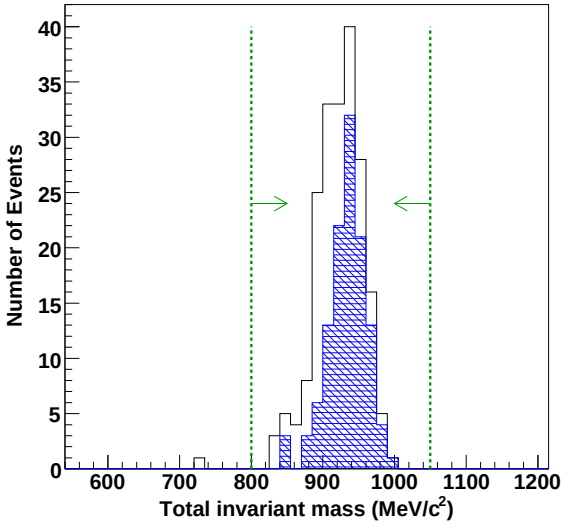

Figure A.15: The total invariant mass distributions of $p \to e^+\omega$ MC in SK-I. Shaded histograms are the distributions of free proton decay events of $\omega \to \pi^0\gamma$ mode. Dashed lines and arrows indicate the selection criterion. Only the events which satisfy the selection criteria (A $\sim$ D) and $P_{\rm tot} < 150$ MeV/c are plotted.

A.3.2 $p \to l^+\omega$ $(\omega \to \pi^+\pi^-\pi^0)$ Mode Search

Event Selection Criteria The selection criteria for $p \to l^+\omega$ $(\omega \to \pi^+\pi^-\pi^0)$ modes are defined as ;

(A) the number of Cherenkov rings is four (three) for $p \to e^+\omega$ $(p \to \mu^+\omega)$,

(B) one of the rings is a non-shower type ring, and all the other rings are shower type rings, (The PID with both a Cherenkov ring pattern and an opening angle is used.)

(C) π^0 invariant mass is reconstructed in between 85 to 185 MeV/c^2,

(D) the number of Michel electrons is 0 or 1 (2) for $p \to e^+\omega$ $(p \to \mu^+\omega)$,

(E) the reconstructed total momentum is less than 200 MeV/c, and the reconstructed total invariant mass is in between 600 to 800 (450 to 700) MeV/c^2,

(F) for only $p \to e^+\omega$, the positron momentum is in between 100 to 200 MeV/c.

In the criterion (A) and (B), only one non-shower type ring from the charged pions, two shower type rings from the neutral pion were required. Additionally, one more shower type ring was also required for the $p \to e^+\omega$ mode. In order to find the low momentum non-shower type ring, the PID with both a Cherenkov ring pattern and an opening angle was used for these modes. The number of ring distributions is shown in Figure A.16. The fraction of 4(3)-rings was 27% (42%) for SK-I free proton decay of the $\omega \to \pi^+\pi^-\pi^0$ mode for $p \to e^+\omega$ $(p \to \mu^+\omega)$.

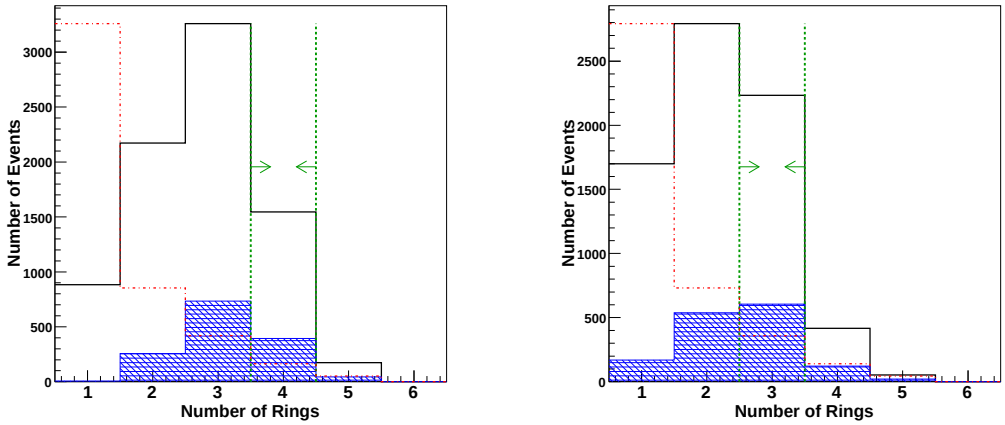

Figure A.16: The number of ring distributions of $p \to e^+\omega$ MC (left) and $p \to \mu^+\omega$ MC (right) in SK-I. Shaded histograms are the distributions of free proton decay events of $\omega \to \pi^+\pi^-\pi^0$ mode. The distribution of the atmospheric neutrino MC, which is normalized with the proton decay MC using the maximum bin value, is also shown in dashed histograms. Dashed lines and arrows indicate the selection criterion.

The π^0 invariant mass instead of the ω meson mass was reconstructed by two of the shower type rings and was required to be in between 85 to 185 MeV/c^2. Figure A.17 shows the π^0 invariant mass distributions of the proton decay MC and the atmospheric neutrino MC.

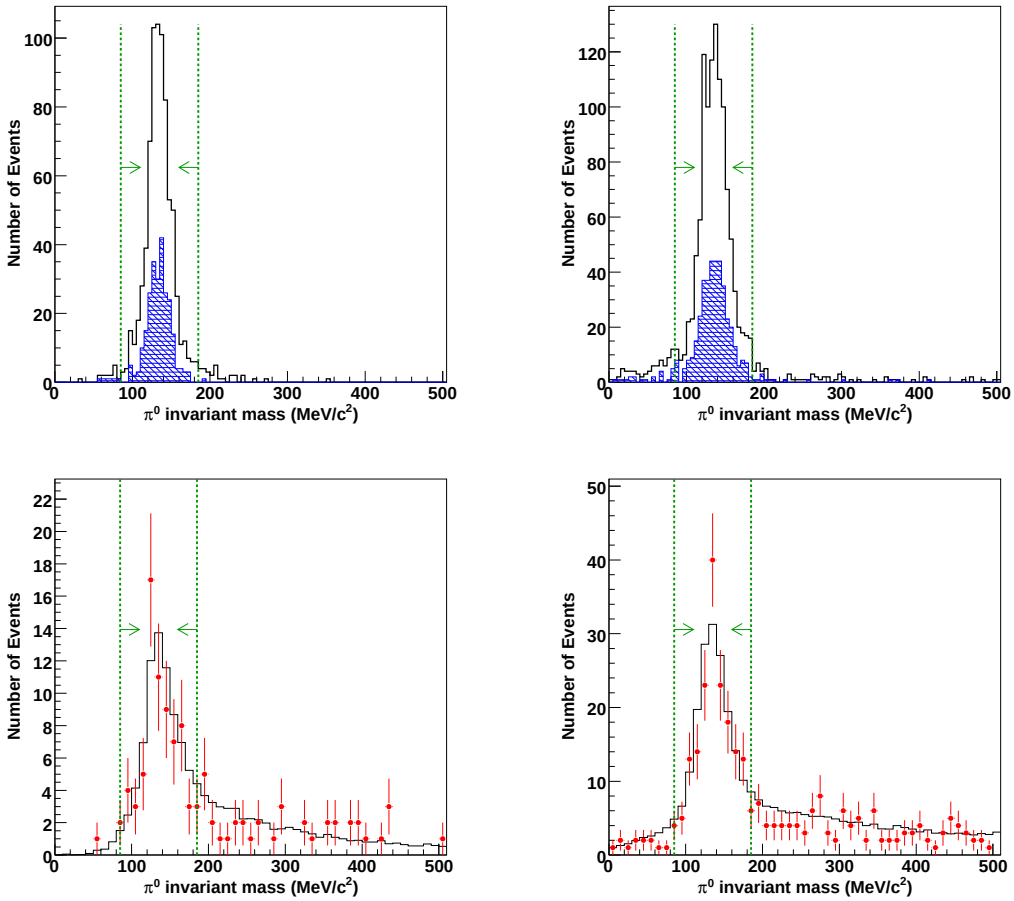

Figure A.17: π^0 invariant mass distributions of the $p \to e^+\omega$ MC (left) and the $p \to \mu^+\omega$ MC (right) in SK-I. The top and bottom figures are the proton decay MC and the atmospheric neutrino MC (solid lines) and the observed data (points), respectively. Shaded histograms are the distributions of free proton decay events of the $\omega \to \pi^+\pi^-\pi^0$ mode. The distribution of the atmospheric neutrino MC, which is normalized with the proton decay MC using the maximum bin value, is also shown in dashed histograms. Dashed lines and arrows indicate the selection criterion.

Figures A.18 and A.19 show the distributions of the total momentum of the proton decay MC and the total invariant mass of the proton decay MC. Since one of the charged pion and the muon was not considered in the total momentum and total invariant mass calculation, the event selection window of the total invariant mass was set to be lower than the normal event selection criteria which corresponds to the source proton mass. The selection windows were determined to reduce the atmospheric neutrino MC though they were not wide enough even for the free proton decay events.

The event selection by the positron momentum was also applied for the $p \to e^+\omega$ mode search. A positron ring was selected as a remaining shower type ring of the combination for π^0 invariant mass reconstruction. Figure 9.35 shows the positron momentum distributions for the proton decay MC, the atmospheric neutrino MC and the observed data. This criteria can reduced the background by a factor of 2, while the detection efficiency was decreased by about 20%.

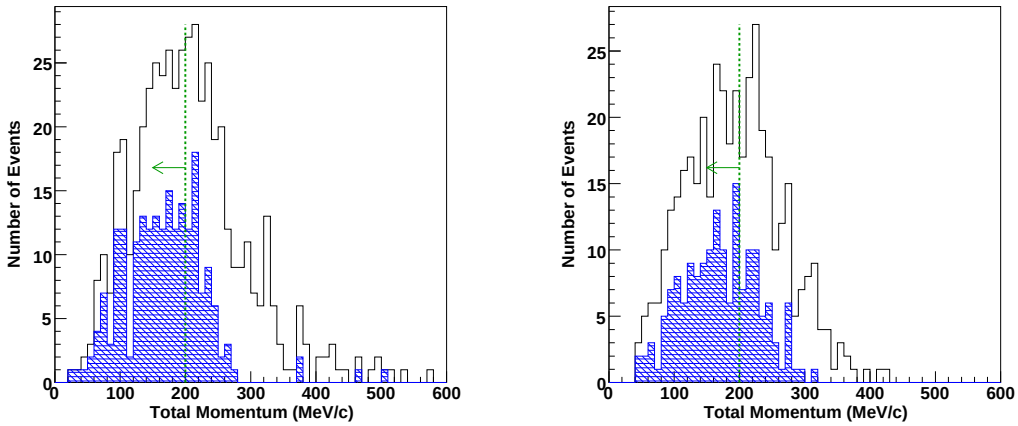

Figure A.18: The total momentum distributions of $p \to e^+\omega$ MC (left) and $p \to \mu^+\omega$ MC (right) in SK-I. Shaded histograms are the distributions of free proton decay events of $\omega \to \pi^+\pi^-\pi^0$ mode. Dashed lines and arrows indicate the selection criterion. Only the events which satisfy the selection criteria (A $\sim$ D) and $600 < M_{\rm tot} < 800$ ($450 < M_{\rm tot} < 700$) MeV/c^2 for $p \to e^+\omega$ ($p \to \mu^+\omega$) are plotted.

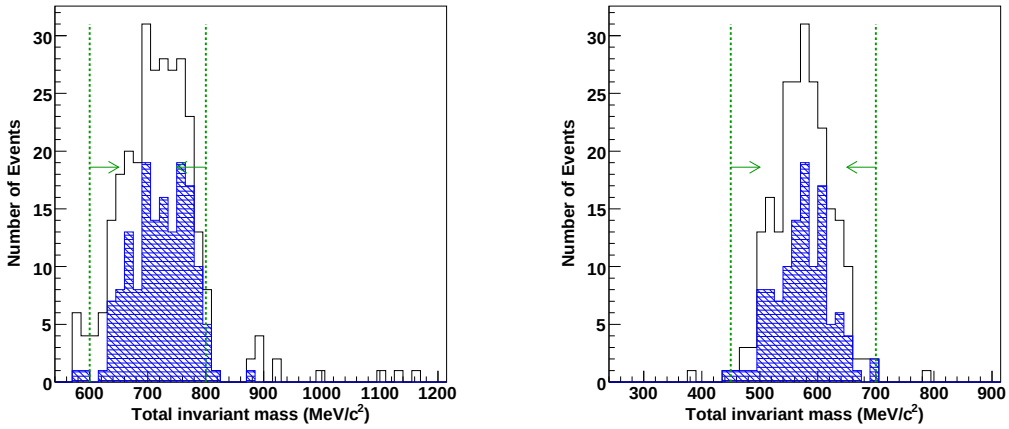

Figure A.19: The total invariant mass distributions of $p \to e^+\omega$ MC (left) and $p \to \mu^+\omega$ (right) in SK-I. Shaded histograms are the distributions of free proton decay events of $\omega \to \pi^+\pi^-\pi^0$ mode. Dashed lines and arrows indicate the selection criterion. Only the events which satisfy the selection criteria (A $\sim$ D) and $P_{\rm tot} < 200$ MeV/c are plotted.

A.4 $n \to l^+\pi^-$ Mode Search

Event Selection Criteria The selection criteria for $p \to l^+\pi^-$ modes are defined as ;

A. the number of Cherenkov rings is two,

B. one of the two rings is a shower (non-shower) type ring for $n \to e^+\pi^-$ ($n \to \mu^+\pi^-$), and the other ring is a non-shower type ring,

D. the number of Michel electrons is 0 (1) for $n \to e^+\pi^-$ ($n \to \mu^+\pi^-$),

E. the reconstructed total momentum is less than 250 MeV/c, and the reconstructed total invariant mass is in between 800 to 1050 MeV/c^2.

One ring from the charged lepton and the other non-shower type ring from the charged pion are required (the criterion (A) and (B)). Figure A.20 shows the number of ring distributions of the neutron decay MC. Approximately 50% of the neutron decay events in SK-I were 2-ring event.

Figures A.21 and A.22 show the distributions of the total momentum of the proton decay MC and the total invariant mass of the proton decay MC, and the same plots for the atmospheric neutrino MC, respectively.

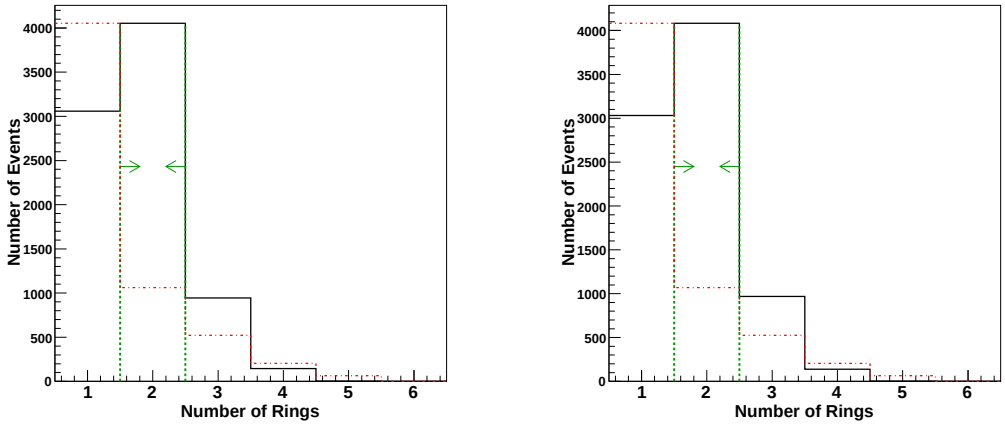

Figure A.20: The number of ring distributions of $n \to e^+\pi^-$ MC (left) and $n \to \mu^+\pi^-$ MC (right) in SK-I. The distribution of the atmospheric neutrino MC, which is normalized with the proton decay MC using the maximum bin value, is also shown in dashed histograms. Dashed lines and arrows indicate the selection criterion.

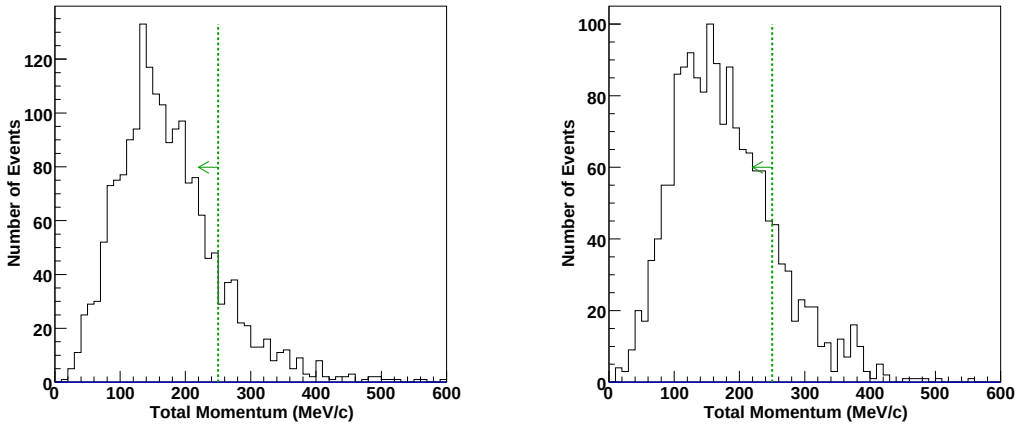

Figure A.21: Total momentum distributions of $n \to e^+\pi^-$ MC (left) and $n \to \mu^+\pi^-$ MC (right) in SK-I. Dashed lines and arrows indicate the selection criterion. Only the events which satisfy the selection criteria (A $\sim$ C) and $800 < M_{\rm tot} < 1050$ MeV/c^2 are plotted.

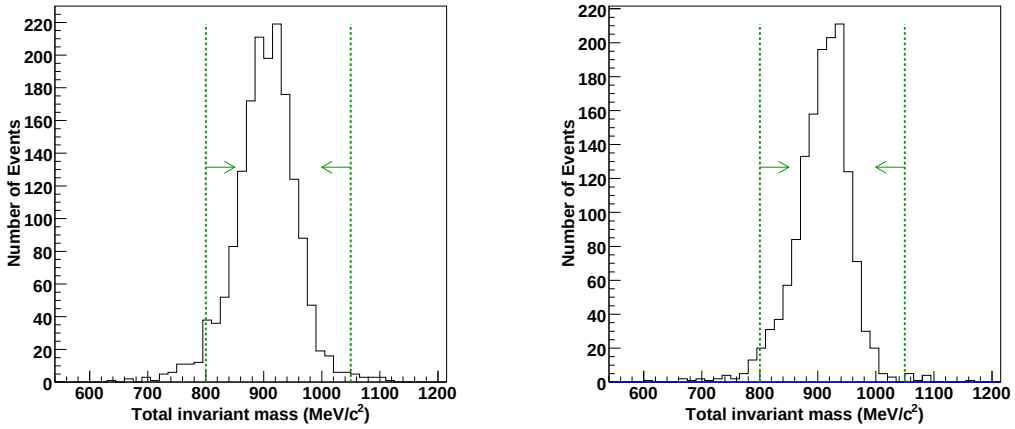

Figure A.22: Total invariant mass distributions of $n \to e^+\pi^-$ MC (left) and $n \to \mu^+\pi^-$ MC (right) in SK-I. Dashed lines and arrows indicate the selection criterion. Only the events which satisfy the selection criteria (A $\sim$ C) and $P_{\rm tot} < 250$ MeV/c are plotted.

A.5 $n \to l^+\rho^-$ Mode Search

Event Selection Criteria The selection criteria for $p \to l^+\rho^-$ modes are defined as ;

A. the number of Cherenkov rings is four (three) for $n \to e^+\rho^-$ ($n \to \mu^+\rho^-$),

B. one of the rings is a non-shower type ring, and all the other ring are shower type rings, (The PID with both a Cherenkov ring pattern and an opening angle is used.)

C.(M_ρ) ρ^- invariant mass is reconstructed in between 600 to 900 MeV/c^2,

C.(M_π) π^0 invariant mass is reconstructed in between 85 to 185 MeV/c^2,

D. the number of Michel electrons is 0 (1) for $n \to e^+\rho^-$ ($n \to \mu^+\rho^-$),

E. the reconstructed total momentum is less than 250 (150) MeV/c for $n \to e^+\rho^-$ ($n \to \mu^+\rho^-$), and the reconstructed total invariant mass is in between 800 to 1050 MeV/c^2 only for $n \to e^+\rho^-$.

Two shower type rings and one non-shower type ring are required from the ρ^- meson decay. One more shower type ring from the positron was required for $n \to e^+\rho^-$ mode search, while one more non-shower type ring from the muon was not required for the $n \to \mu^+\rho^-$ mode search. Figure A.23 shows the number of ring distributions of the neutron decay MC. The fraction of 4(3)-rings was 9% (23%) for $n \to e^+\rho^-$ ($n \to \mu^+\rho^-$).

The invariant mass of the ρ^- meson was reconstructed by two shower type rings and one non-shower type ring and required to be in between 600 to 900 MeV/c^2 (the criterion C(M_ρ)). Figure A.24 shows the ρ^- invariant mass distribution for the neutron decay MC. It was also required that the invariant mass of the these two shower type rings is in between 85 to 185 MeV/c^2 (the criterion C(M_π)).

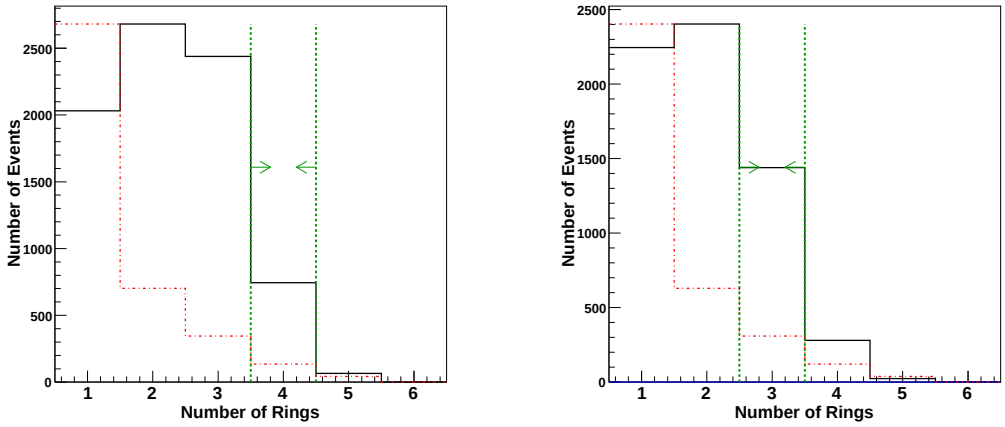

Figure A.23: The number of ring distributions of $n \to e^+\rho^-$ MC (left) and $n \to \mu^+\rho^-$ MC (right) in SK-I. The distribution of the atmospheric neutrino MC, which is normalized with the proton decay MC using the maximum bin value, is also shown in dashed histograms. Dashed lines and arrows indicate the selection criterion.

Figure A.25 shows the distribution of the total momentum of the proton decay MC with the atmospheric neutrino MC. The total invariant of the proton decay MC is shown in Figure A.26. The tighter total momentum cut of $P_{\rm tot} < 150$ MeV/c was applied to reduce the background for $n \to \mu^+\rho^-$ mode because the proton invariant mass cannot be reconstructed for the mode. For $n \to e^+\rho^-$ mode, the total invariant mass was well reconstructed as shown in Figure A.26.

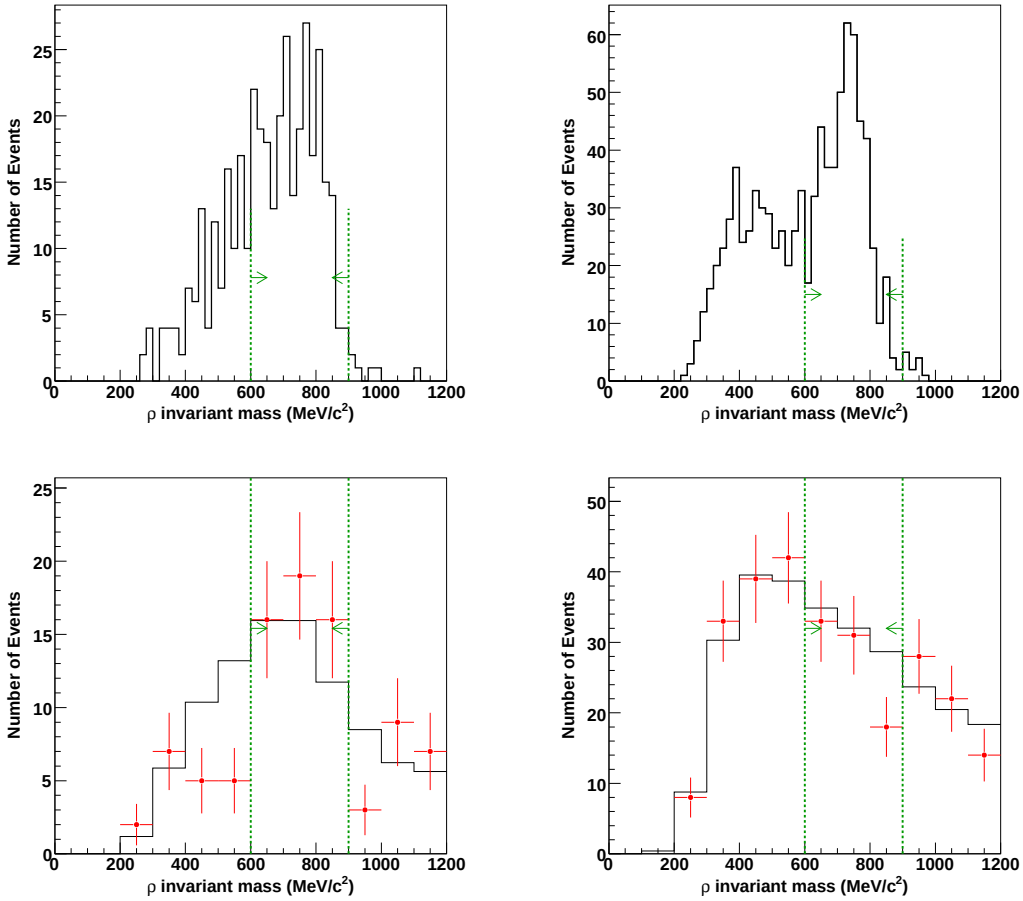

Figure A.24: ρ^- invariant mass distributions of $n \to e^+\rho^-$ MC (left) and $n \to \mu^+\rho^-$ MC (right) in SK-I. Dashed lines and arrows indicate the selection criterion.

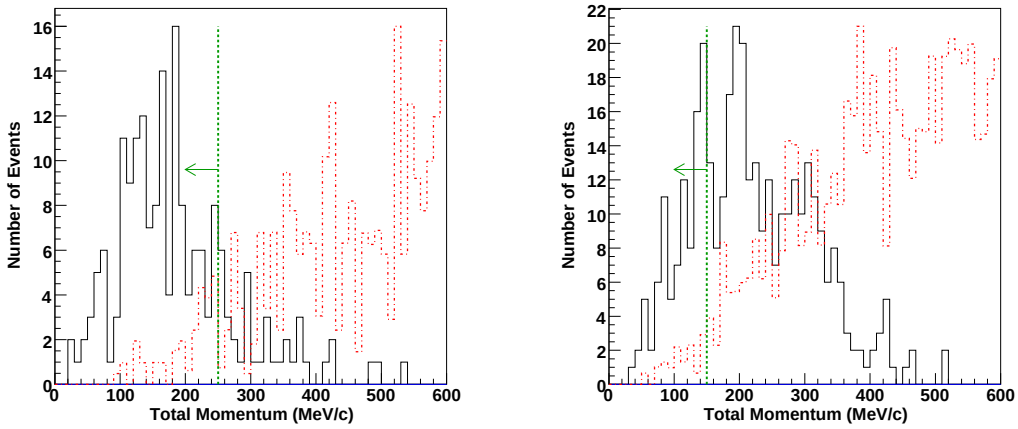

Figure A.25: The total momentum distributions of $n \to e^+\rho^-$ MC (left) and $n \to \mu^+\rho^-$ MC (right) in SK-I. The distribution of the atmospheric neutrino MC, which is normalized with the proton decay MC using the maximum bin value, is also shown in dashed histograms. Dashed lines and arrows indicate the selection criterion. Only the events which satisfy the selection criteria (A $\sim$ E) (and $800 < M_{\rm tot} < 1050$ MeV/c^2 for $n \to e^+\rho^-$) are plotted.

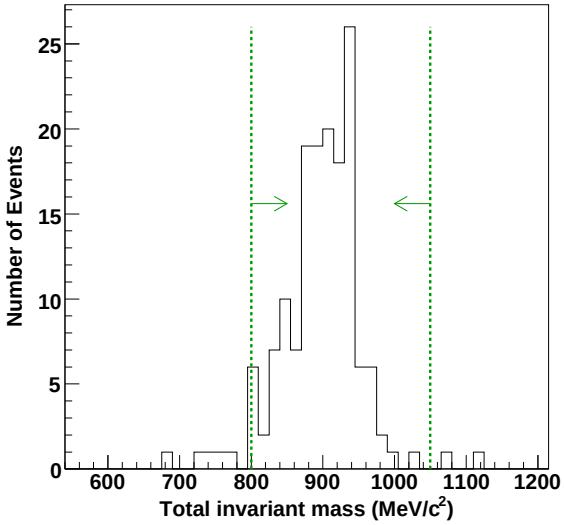

Figure A.26: The total invariant mass distributions of $p \to e^+\rho^0$ MC in SK-I. Dashed lines and arrows indicate the selection criterion. Only the events which satisfy the selection criteria (A $\sim$ E) and $P_{\rm tot} < 250$ MeV/c are plotted.

Appendix B

Candidate Events for Nucleon Decay

B.1 $p \to \mu^+\eta$ ($\eta \to 3\pi^0$) mode

Two candidates were found for the $p \to \mu^+\eta$ ($3\pi^0$) mode. The event displays of the two candidate are shown in Figures B.1 and B.2. Reconstructed basic informations are summarized in Table B.1. The event reconstruction seems to work as expected for these two events. The reconstructed vertices were near the detector wall for both events. The total invariant mass of the first candidate was very close to the proton mass. However, its total momentum was almost on the edge of the selection window. The second candidate had a slightly lower momentum, but its invariant mass was relatively low as the mass of a proton.

candidate for $p \to \mu^+\eta$	1	2
Distance from the wall	209 cm	341 cm
Number of rings	4	4
PID & Momentum	S (γ) 278 MeV/c	S (γ) 300 MeV/c
	S (γ) 244 MeV/c	S (γ) 204 MeV/c
	S (γ) 164 MeV/c	S (γ) 76 MeV/c
	N (μ) 252 MeV/c	N (μ) 252 MeV/c
M_η	564 MeV/c	553 MeV/c
decay-e	1	1
$P_{\rm tot}$	232 MeV/c	189 MeV/c
$M_{\rm tot}$	931 MeV/c^2	832 MeV/c^2

Table B.1: Reconstructed informations of the candidates for $p \to \mu^+\eta$. 'S' and 'N' in the PID mean a shower type ring and a non-shower type ring, respectively.

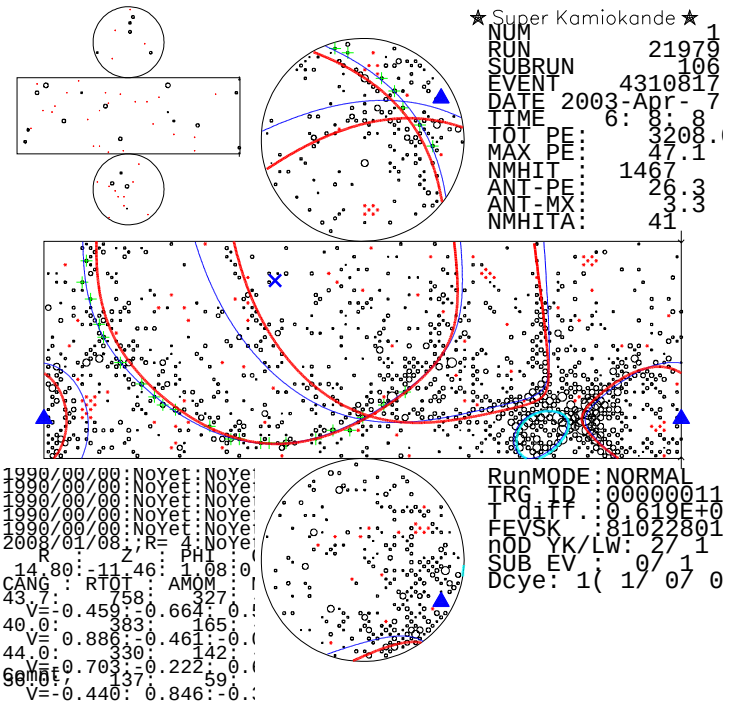

Figure B.1: The first candidate for $p \to \mu^+\eta$ ($3\pi^0$). A blue solid line indicates a reconstructed ring as a non-shower type.

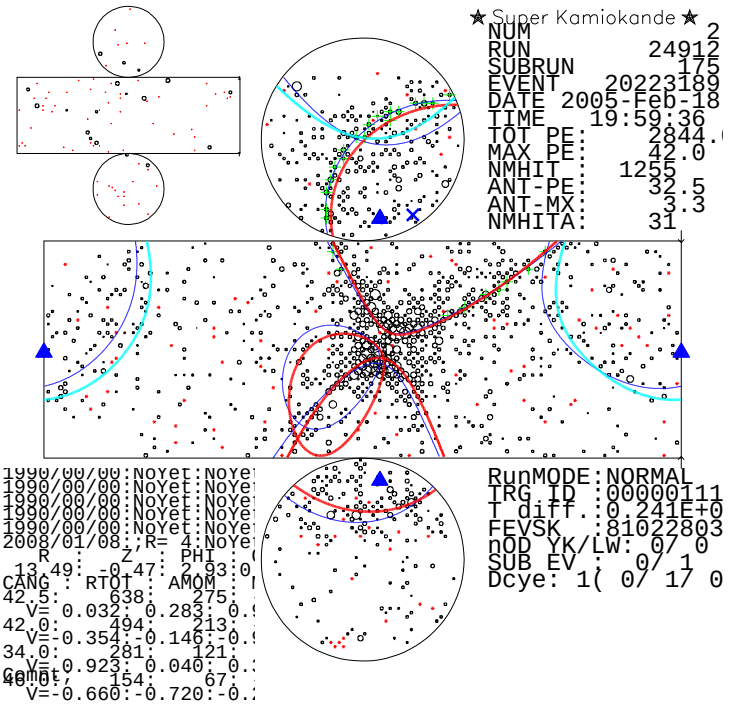

Figure B.2: The second candidate for $p \to \mu^+\eta$. ($3\pi^0$).

B.2 $p \to \mu^+\rho^0$ mode

One candidate was found for the $p \to \mu^+\rho^0$ mode. The event display of the candidate is shown in Figure B.3. Basic informations for the candidate are summarized in Table B.2. The reconstruction seemingly worked well for this event.

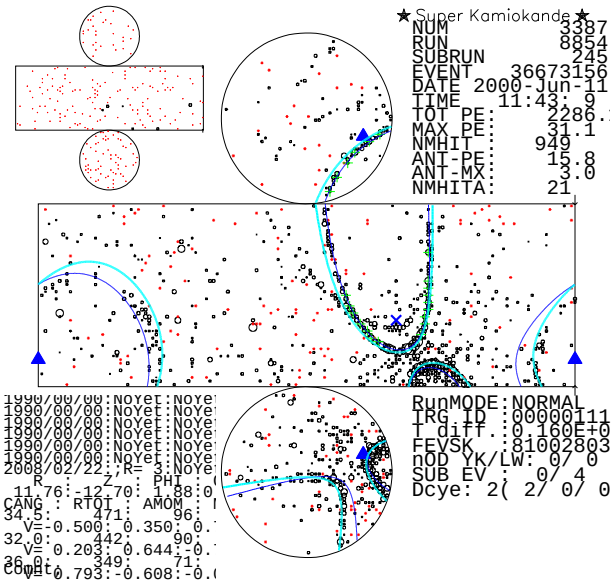

Figure B.3: The candidate for $p \to \mu^+\rho^0$.

candidate for $p \to \mu^+\rho^0$	
Distance from the wall	514 cm
Number of rings	3
PID & Momentum	N (π) 366 MeV/c
	N (π) 302 MeV/c
	N (μ) 284 MeV/c
M_ρ	665 MeV/c
decay-e	2
$P_{\rm tot}$	181 MeV/c
$M_{\rm tot}$	1011 MeV/c^2

Table B.2: Reconstructed informations of the candidates for $p \to \mu^+\rho^0$. In the PID, 'N' means a non-shower type ring, and 'π' and 'μ' are the assumptions for the mass reconstruction.

B.3 $p \to e^+\omega$ $(\omega \to \pi^+\pi^-\pi^0)$ mode

One candidate was found for the $p \to e^+\omega$ $(\omega \to \pi^+\pi^-\pi^0)$ mode. The event display of the candidate is shown in Figure B.4. Basic informations for the candidate are summarized in Table B.3. One of the rings identified as as a shower type ring around the bottom of the event display had a sharp ring edge and seemed a non-shower type ring. This ring may be from a charged pion which was scattered in water and made some multiple rings. Those multiple rings were reconstructed as one ring and may be mis-identified as a shower type ring.

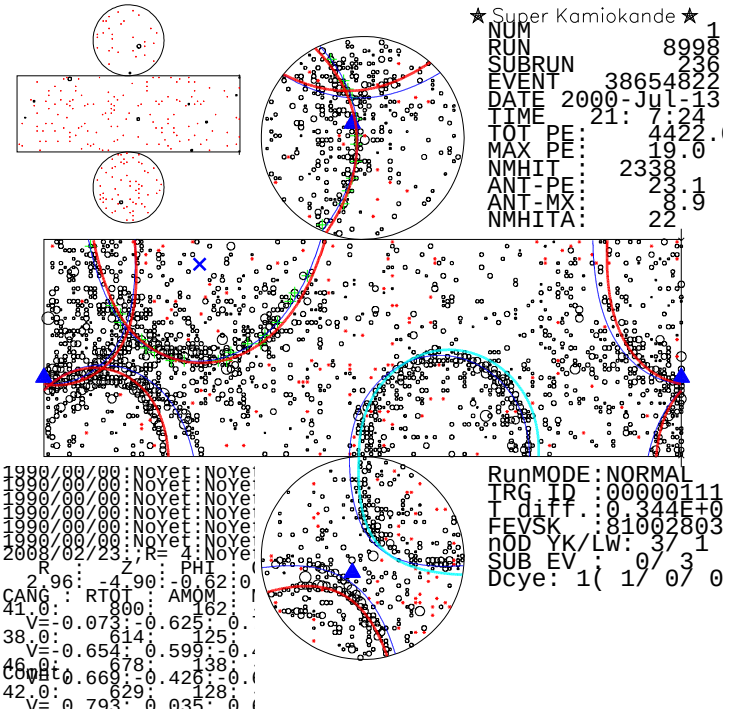

Figure B.4: The candidate for $p \to e^+\omega$. A solid red line indicate a reconstructed ring as a shower type.

candidate for $p \to e^+\omega$	
Distance from the wall	1320 cm
Number of rings	4
PID & Momentum	N (π) 388 MeV/c
	S (e) 148 MeV/c
	S (γ) 127 MeV/c
	S (γ) 119 MeV/c
M_π	147 MeV/c
decay-e	1
$P_{\rm tot}$	137 MeV/c
$M_{\rm tot}$	796 MeV/c^2

Table B.3: Reconstructed informations of the candidates for $p \to e^+\omega$. In the PID, 'S' and 'N' mean a shower-type and a non-shower type ring, respectively, and 'e' and 'γ' are the assumptions for the mass reconstruction.

B.4 $n \to \mu^+\pi^-$ mode

One candidate was observed in the SK-I data for the $n \to \mu^+\pi^-$ mode. The event display of the candidate is shown in Figure B.5. Basic informations are summarized in Table B.4. The reconstructed vertex for this event was very close to the detector wall. Furthermore, the reconstructed total momentum and total invariant mass were one the edge of the signal box of the selection criterion D.

candidate for $n \to \mu^+\pi^-$	
Distance from the wall	209 cm
Number of rings	2
PID & Momentum	N (π) 410 MeV/c
	N (μ) 398 MeV/c
decay-e	1
$P_{\rm tot}$	245 MeV/c
$M_{\rm tot}$	809 MeV/c^2

Table B.4: Reconstructed informations of the candidates for $n \to \mu^+\pi^-$. In the PID, 'S' and 'N' mean a shower-type and a non-shower type ring, respectively, and 'μ' and 'π' are the assumptions for the mass reconstruction.

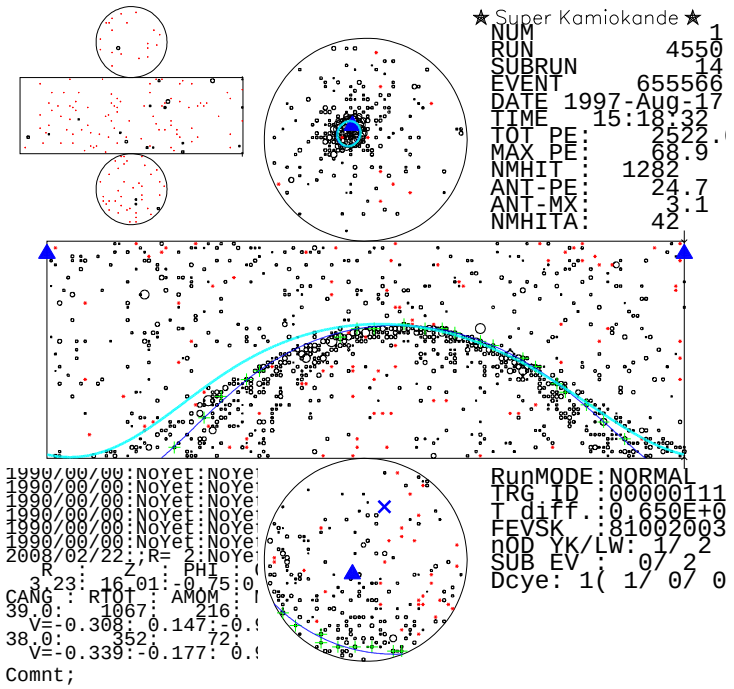

Figure B.5: The candidate for $n \to \mu^+\pi^-$.

B.5 $n \to e^+\rho^-$ mode

One candidate was found for the $n \to e^+\rho^-$ mode. The event display and basic informations of the candidate are shown in Figure B.6 and Table B.5, respectively. The reconstructed vertex for this event was also close to the detector wall. The reconstructed total momentum and total invariant mass were on the edge of the signal box. Furthermore, there may be a mis-reconstruction for this event. The overlapped two rings on the barrel of the detector seem only one ring. It seems that only one charged particle stopped just before the detector wall.

candidate for $n \to e^+\rho^-$	
Distance from the wall	397 cm
Number of rings	4
PID & Momentum	N (π) 271 MeV/c
	S (γ) 190 MeV/c
	S (γ) 186 MeV/c
	S (e) 184 MeV/c
M_ρ	650 MeV/c
M_π	130 MeV/c
decay-e	0
$P_{\rm tot}$	209 MeV/c
$M_{\rm tot}$	839 MeV/c^2

Table B.5: Reconstructed informations of the candidates for $p \to e^+\omega$. In the PID, 'S' and 'N' mean a shower-type and a non-shower type ring, respectively, and 'e' and 'γ' are the assumptions for the mass reconstruction.

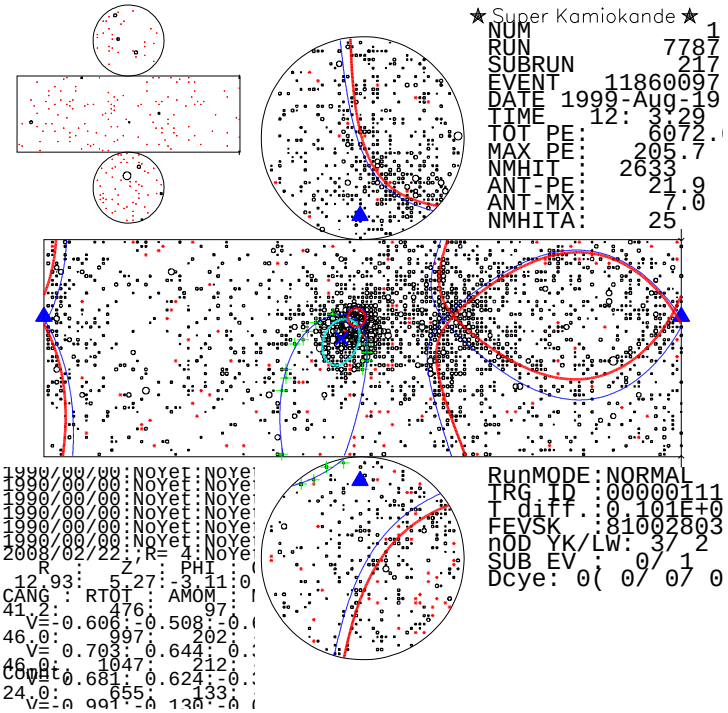

Figure B.6: The candidate for $n \to e^+\rho^-$

Appendix C

Tables of Systematic Errors for Background

The detailed values of the systematic errors are shown in this Appendix. The systematic error estimation method and the source of uncertainties are described in Section 9.2. The details of the neutrino flux and the neutrino interaction are discussed in the other documents [123, 124].

C.1 Systematic Errors from Uncertainties of Neutrino Flux

	$p \to e^+\pi^0$		$p \to \mu^+\pi^0$		$n \to e^+\pi^-$		$n \to \mu^+\pi^-$	
	SK-I	SK-II	SK-I	SK-II	SK-I	SK-II	SK-I	SK-II
energy dependent normalization								
($E_\nu < 1$GeV)	6.8%	6.4%	6.8%	6.7%	6.8%	6.5%	6.6%	6.8%
($E_\nu > 1$GeV)	3.8%	3.4%	3.8%	3.8%	3.9%	3.5%	3.6%	3.8%
ν_μ/ν_e ratio								
($E_\nu < 1$GeV)	0.5%	0.5%	0.5%	0.5%	0.5%	0.5%	0.6%	0.5%
($1< E_\nu < 10$GeV)	0.4%	0.9%	1.3%	1.5%	0.8%	0.1%	1.7%	1.8%
($E_\nu > 10$GeV)	0.0%	0.1%	0.1%	0.1%	0.1%	0.0%	0.1%	0.1%
$\bar{\nu}_e/\nu_e$ ratio								
($E_\nu < 1$GeV)	0.8%	0.6%	0.8%	0.7%	0.8%	0.6%	0.8%	0.8%
($1< E_\nu < 10$GeV)	1.5%	1.7%	0.1%	0.0%	1.5%	0.9%	0.2%	0.3%
($E_\nu > 10$GeV)	0.2%	0.0%	0.0%	0.0%	0.0%	0.0%	0.0%	0.0%
$\bar{\nu}_\mu/\nu_\mu$ ratio								
($E_\nu < 1$GeV)	0.0%	0.0%	0.0%	0.0%	0.0%	0.0%	0.0%	0.0%
($1< E_\nu < 10$GeV)	0.2%	0.1%	2.3%	1.7%	0.1%	0.8%	2.3%	2.8%
($E_\nu > 10$GeV)	0.0%	0.0%	0.0%	0.0%	0.2%	0.1%	0.0%	0.0%
up/down asymmetry	0.1%	0.0%	0.0%	0.0%	0.0%	0.0%	0.0%	0.1%
horizontal/vertical ratio	0.3%	0.5%	0.1%	0.4%	0.5%	0.2%	0.5%	0.4%
K/π production ratio	0.1%	0.0%	0.4%	0.3%	0.1%	0.2%	0.3%	0.3%
neutrino flight length	0.1%	0.0%	0.4%	0.3%	0.1%	0.2%	0.3%	0.3%
Total	8.0%	7.6%	8.3%	8.1%	8.1%	7.5%	8.1%	8.1%

Table C.1: Systematic errors from uncertatinties of neutrino flux for the $N \to l^+\pi$ modes.

	$p \to e^+\eta$ ($\eta \to 2\gamma$)		$p \to \mu^+\eta$ ($\eta \to 2\gamma$)		$p \to e^+\eta$ ($\eta \to 3\pi^0$)		$p \to \mu^+\eta$ ($\eta \to 3\pi^0$)	
	SK-I	SK-II	SK-I	SK-II	SK-I	SK-II	SK-I	SK-II
energy dependent normalization								
($E_\nu < 1$GeV)	6.8%	6.4%	6.8%	6.8%	6.8%	6.8%	6.8%	6.8%
($E_\nu > 1$GeV)	3.8%	3.6%	3.8%	3.8%	3.9%	3.8%	3.9%	3.9%
ν_μ/ν_e ratio								
($E_\nu < 1$GeV)	0.5%	0.5%	0.5%	0.5%	0.5%	0.5%	0.5%	0.5%
($1< E_\nu < 10$GeV)	0.3%	0.7%	0.8%	0.4%	0.4%	0.0%	1.0%	0.7%
($E_\nu > 10$GeV)	0.1%	0.1%	0.1%	0.1%	0.2%	0.1%	0.0%	0.0%
$\bar{\nu}_e/\nu_e$ ratio								
($E_\nu < 1$GeV)	0.8%	0.6%	0.8%	0.8%	0.8%	0.8%	0.8%	0.8%
($1< E_\nu < 10$GeV)	1.0%	0.9%	1.9%	0.9%	0.8%	0.1%	0.4%	0.6%
($E_\nu > 10$GeV)	0.0%	0.0%	0.0%	0.0%	0.4%	0.0%	0.0%	0.0%
$\bar{\nu}_\mu/\nu_\mu$ ratio								
($E_\nu < 1$GeV)	0.0%	0.0%	0.0%	0.0%	0.0%	0.0%	0.0%	0.0%
($1< E_\nu < 10$GeV)	0.3%	0.1%	0.2%	1.4%	1.2%	1.0%	1.7%	0.8%
($E_\nu > 10$GeV)	0.0%	0.1%	0.0%	0.0%	0.0%	0.0%	0.1%	0.1%
up/down asymmetry	0.1%	0.1%	0.0%	0.0%	0.2%	0.1%	0.0%	0.1%
horizontal/vertical ratio	0.5%	1.0%	1.9%	0.5%	0.1%	0.3%	0.2%	0.1%
K/π production ratio	0.2%	0.1%	0.0%	0.1%	0.3%	0.3%	0.4%	0.0%
neutrino flight length	0.0%	0.0%	0.0%	0.0%	0.1%	0.0%	0.0%	0.2%
Total	7.9%	7.5%	8.3%	8.0%	8.1%	7.9%	8.2%	8.0%

Table C.2: Systematic errors from uncertatinties of neutrino flux for the $N \to l^+\eta$ modes.

	$p \to e^+\rho^0$		$p \to \mu^+\rho^0$		$n \to e^+\rho^-$		$n \to \mu^+\rho^-$	
	SK-I	SK-II	SK-I	SK-II	SK-I	SK-II	SK-I	SK-II
energy dependent normalization								
($E_\nu < 1$GeV)	5.9%	4.9%	6.5%	5.9%	6.8%	6.5%	5.5%	3.9%
($E_\nu > 1$GeV)	3.0%	2.2%	3.6%	3.1%	4.1%	3.6%	2.7%	1.4%
ν_μ/ν_e ratio								
($E_\nu < 1$GeV)	0.7%	0.7%	0.6%	0.6%	0.5%	0.5%	0.7%	0.9%
($1< E_\nu < 10$GeV)	1.2%	1.1%	1.9%	1.8%	0.6%	0.9%	1.0%	1.3%
($E_\nu > 10$GeV)	0.1%	0.1%	0.1%	0.1%	0.3%	0.1%	0.0%	0.1%
$\bar{\nu}_e/\nu_e$ ratio								
($E_\nu < 1$GeV)	0.8%	0.7%	0.8%	0.8%	0.8%	0.7%	0.8%	0.8%
($1< E_\nu < 10$GeV)	0.1%	0.0%	0.4%	0.4%	0.6%	0.4%	0.1%	0.2%
($E_\nu > 10$GeV)	0.0%	0.0%	0.0%	0.0%	0.0%	0.0%	0.0%	0.0%
$\bar{\nu}_\mu/\nu_\mu$ ratio								
($E_\nu < 1$GeV)	0.1%	0.2%	0.0%	0.1%	0.0%	0.0%	0.2%	0.3%
($1< E_\nu < 10$GeV)	1.5%	1.3%	2.4%	2.6%	1.0%	0.9%	0.8%	1.4%
($E_\nu > 10$GeV)	0.0%	0.0%	0.0%	0.0%	0.1%	0.0%	0.1%	0.0%
up/down asymmetry	0.1%	0.0%	0.0%	0.1%	0.0%	0.0%	0.0%	0.1%
horizontal/vertical ratio	0.2%	0.2%	0.1%	0.1%	0.4%	0.8%	0.1%	0.5%
K/π production ratio	0.4%	0.3%	0.3%	0.3%	0.3%	0.3%	0.2%	0.3%
neutrino flight length	0.2%	0.3%	0.1%	0.3%	0.1%	0.1%	0.4%	0.7%
Total	7.0%	5.7%	8.1%	7.5%	8.1%	7.6%	6.4%	4.8%

Table C.3: Systematic errors from uncertatinties of neutrino flux for the $N \to l^+\rho$ modes.

	$p \to e^+\omega$ $(\omega \to \pi^0\gamma)$		$p \to \mu^+\omega$ $(\omega \to \pi^0\gamma)$		$p \to e^+\omega$ $(\omega \to \pi^+\pi^-\pi^0)$		$p \to \mu^+\omega$ $(\omega \to \pi^+\pi^-\pi^0)$	
	SK-I	SK-II	SK-I	SK-II	SK-I	SK-II	SK-I	SK-II
energy dependent normalization								
($E_\nu < 1$GeV)	6.8%	6.8%	6.6%	6.8%	6.0%	5.5%	5.9%	6.0%
($E_\nu > 1$GeV)	3.8%	3.8%	3.7%	3.8%	3.2%	2.8%	2.9%	3.1%
ν_μ/ν_e ratio								
($E_\nu < 1$GeV)	0.5%	0.5%	0.6%	0.5%	0.5%	0.6%	0.7%	0.6%
($1< E_\nu < 10$GeV)	0.3%	0.1%	0.1%	0.1%	0.7%	0.9%	1.7%	1.6%
($E_\nu > 10$GeV)	0.1%	0.1%	0.0%	0.1%	0.1%	0.1%	0.1%	0.1%
$\bar{\nu}_e/\nu_e$ ratio								
($E_\nu < 1$GeV)	0.8%	0.8%	0.8%	0.8%	0.6%	0.7%	0.8%	0.8%
($1< E_\nu < 10$GeV)	1.0%	0.7%	1.3%	1.4%	0.6%	0.1%	0.4%	0.2%
($E_\nu > 10$GeV)	0.0%	0.0%	0.0%	0.0%	0.0%	0.0%	0.0%	0.0%
$\bar{\nu}_\mu/\nu_\mu$ ratio								
($E_\nu < 1$GeV)	0.0%	0.2%	0.0%	0.0%	0.0%	0.0%	0.1%	0.1%
($1< E_\nu < 10$GeV)	0.7%	0.9%	0.4%	0.4%	1.3%	0.9%	1.9%	2.2%
($E_\nu > 10$GeV)	0.0%	0.0%	0.1%	0.0%	0.0%	0.0%	0.0%	0.0%
up/down asymmetry	0.0%	0.2%	0.0%	0.2%	0.1%	0.1%	0.1%	0.0%
horizontal/vertical ratio	0.9%	0.2%	0.4%	0.3%	0.2%	0.2%	0.3%	0.1%
K/π production ratio	0.2%	0.4%	0.2%	0.1%	0.3%	0.3%	0.3%	0.3%
neutrino flight length	0.1%	0.0%	0.2%	0.2%	0.1%	0.4%	0.7%	1.0%
Total	8.0%	7.9%	7.8%	8.0%	7.0%	6.4%	7.2%	7.4%

Table C.4: Systematic errors from uncertatinties of neutrino flux for the $N \to l^+\omega$ modes.

C.2 Systematic Errors from Uncertainties of Interactions

	$p \to e^+\pi^0$	$p \to \mu^+\pi^0$	$n \to e^+\pi^-$	$n \to \mu^+\pi^-$
Neutrino Cross Section				
M_A in QE and				
sigle-meson production	6.0%	5.0%	8.8%	9.1%
CCQE total cross section	6.1%	7.3%	6.5%	7.4%
CCQE $\bar{\nu}/\nu$ ratio	1.0%	0.7%	0.9%	0.7%
CCQE μ/e ratio	0.2%	0.5%	0.2%	0.6%
single-meson production				
(total cross section)	4.4%	4.6%	6.6%	9.5%
single-pion production				
($\bar{\nu}/\nu, \pi^{0,+,-}$ ratio)	6.0%	5.0%	6.4%	5.2%
deep inelastic scattering				
(model difference)	0.7%	1.1%	0.5%	0.5%
deep inelastic scattering				
(total cross section)	0.8%	1.3%	0.6%	0.3%
coherent pion production	1.6%	1.6%	1.6%	1.6%
NC/CC ratio	2.0%	1.0%	1.2%	1.4%
pion nuclear effect	7.8%		7.6%	
pion production in water	26.7%		19.5%	
$\pi - N$ **cross section in water**	24.4%		30.0%	
Total	38%	38%	39%	40%

Table C.5: Systematic errors from uncertatinties of interactions for the $N \to l^+\pi$ modes.

	$p \to e^+\eta$ ($\eta \to 2\gamma$)	$p \to \mu^+\eta$ ($\eta \to 2\gamma$)	$p \to e^+\eta$ ($\eta \to 3\pi^0$)	$p \to \mu^+\eta$ ($\eta \to 3\pi^0$)
Neutrino Cross Section				
M_A in QE and				
sigle-meson production	3.7%	4.3%	0.7%	2.0%
CCQE total cross section	7.8%	9.2%	9.2%	8.9%
CCQE $\bar{\nu}/\nu$ ratio	0.7%	0.3%	0.3%	0.4%
CCQE μ/e ratio	0.3%	0.4%	0.4%	0.3%
single-meson production				
(total cross section)	3.5%	7.0%	1.5%	1.7%
single-pion production				
($\bar{\nu}/\nu, \pi^{0,+,-}$ ratio)	4.1%	4.0%	3.3%	1.7%
deep inelastic scattering				
(model difference)	1.2%	0.7%	2.8%	1.9%
deep inelastic scattering				
(total cross section)	1.9%	1.6%	3.1%	2.8%
coherent pion production	1.6%	1.6%	1.6%	1.6%
NC/CC ratio	3.9%	3.0%	10.2%	4.6%
pion nuclear effect	4.7%		17.7%	
pion production in water	22.5%		21.9%	
$\pi - N$ **cross section in water**	28.4%		63.2%	
Total	38%	39%	71%	70%

Table C.6: Systematic errors from uncertatinties of interactions for the $N \to l^+\eta$ modes.

	$p \to e^+\rho^0$	$p \to \mu^+\rho^0$	$n \to e^+\rho^-$	$n \to \mu^+\rho^-$
Neutrino Cross Section				
M_A in QE and				
sigle-meson production	2.6%	9.8%	2.2%	4.9%
CCQE total cross section	8.4%	7.6%	8.8%	8.0%
CCQE $\bar{\nu}/\nu$ ratio	0.5%	0.7%	0.4%	0.6%
CCQE μ/e ratio	0.4%	0.6%	0.3%	0.4%
single-meson production				
(total cross section)	5.9%	8.4%	5.2%	9.0%
single-pion production				
($\bar{\nu}/\nu, \pi^{0,+,-}$ ratio)	4.4%	1.1%	1.4%	8.8%
deep inelastic scattering				
(model difference)	1.5%	0.6%	2.0%	0.5%
deep inelastic scattering				
(total cross section)	1.5%	0.5%	1.9%	0.5%
coherent pion production	1.0%	1.6%	1.6%	1.6%
NC/CC ratio	6.3%	0.9%	8.2%	1.8%
pion nuclear effect	13.9%		12.0%	
pion production in water	15.3%		13.8%	
$\pi - N$ **cross section in water**	29.6%		12.1%	
Total	39%	39%	26%	27%

Table C.7: Systematic errors from uncertatinties of interactions for the $N \to l^+\rho$ modes.

	$p \to e^+\omega$	$p \to \mu^+\omega$	$p \to e^+\omega$	$p \to \mu^+\omega$
	$(\omega \to \pi^0\gamma)$		$(\omega \to \pi^+\pi^-\pi^0)$	
Neutrino Cross Section				
M_A in QE and				
sigle-meson production	2.3%	1.4%	0.9%	1.1%
CCQE total cross section	9.2%	8.0%	8.8%	8.9%
CCQE $\bar{\nu}/\nu$ ratio	0.3%	0.6%	0.4%	0.4%
CCQE μ/e ratio	0.4%	0.4%	0.4%	0.4%
single-meson production				
(total cross section)	5.0%	2.4%	4.2%	1.3%
single-pion production				
($\bar{\nu}/\nu, \pi^{0,+,-}$ ratio)	3.9%	2.8%	5.3%	5.5%
deep inelastic scattering				
(model difference)	0.7%	0.5%	2.1%	1.3%
deep inelastic scattering				
(total cross section)	2.2%	2.5%	2.0%	2.8%
coherent pion production	1.6%	1.6%	1.0%	1.8%
NC/CC ratio	6.7%	2.9%	8.5%	1.2%
pion nuclear effect	13.1%		7.6%	
pion production in water	30.2%		18.9%	
$\pi - N$ **cross section in water**	27.8%		49.9%	
Total	45%	44%	56%	55%

Table C.8: Systematic errors from uncertatinties of interactions for the $N \to l^+\omega$ modes.

C.3 Systematic Errors from Uncertainties of Detector Performances

	$p \to e^+\pi^0$	$p \to \mu^+\pi^0$	$n \to e^+\pi^-$	$n \to \mu^+\pi^-$
detector gain non-uniformity	4.6%	4.5%	7.7%	1.7%
energy scale	13.6%	11.3%	22.6%	14.4%
PID	4.7%	5.3%	7.7%	7.4%
fiducial volume	3%	3%	3%	3%
vertex shift	12.7%	40.5%	37.3%	25.5%
Cherenkov opening angle	9.4%	1.3%	6.5%	18.3%
ring counting	0.4%	(<3%)	5.7%	5.8%
decay-e detection	0.7%	1.3%	1.4%	1.1%
Total	22%	43%	46%	36%

Table C.9: Systematic errors from uncertatinties of detector performances for the $N \to l^+\pi$ modes.

	$p \to e^+\eta$	$p \to \mu^+\eta$	$p \to e^+\eta$	$p \to \mu^+\eta$
	$(\eta \to 2\gamma)$		$(\eta \to 3\pi^0)$	
detector gain non-uniformity	8.2%	(< 14%)	1.9%	3.4%
energy scale	16.4%	11.9%	9.4%	8.4%
PID	5.0%	(< 14%)	(< 4%)	5.0%
fiducial volume	3%	3%	3%	3%
vertex shift	17.4%	3.3%	25.6%	16.1%
Cherenkov opening angle	2.8%	(< 14%)	3.0%	2.7%
ring counting	(< 5%)	(< 25%)	(< 11%)	3.3%
decay-e detection	1.0%	1.8%	1.4%	1.2%
Total	26%	13%	28%	20%

Table C.10: Systematic errors from uncertatinties of detector performances for the $N \to l^+\eta$ modes.

	$p \to e^+\rho^0$	$p \to \mu^+\rho^0$	$n \to e^+\rho^-$	$n \to \mu^+\rho^-$
detector gain non-uniformity	10.5%	4.7%	15.6%	($< 4\%$)
energy scale	5.7%	9.2%	10.5%	10.3%
PID	4.4%	5.8%	12.0%	5.0%
fiducial volume	3%	3%	3%	3%
vertex shift	27.9%	19.3%	47.0%	16.4%
Cherenkov opening angle	9.3%	2.3%	5.4%	18.3%
ring counting	6.0%	($< 2\%$)	11.3%	($< 4\%$)
decay-e detection	0.3%	1.2%	1.1%	1.6%
Total	33%	23%	54%	27%

Table C.11: Systematic errors from uncertatinties of detector performances for the $N \to l^+\rho$ modes.

	$p \to e^+\omega$ ($\omega \to \pi^0\gamma$)	$p \to \mu^+\omega$ ($\omega \to \pi^0\gamma$)	$p \to e^+\omega$ ($\omega \to \pi^+\pi^-\pi^0$)	$p \to \mu^+\omega$ ($\omega \to \pi^+\pi^-\pi^0$)
detector gain non-uniformity	8.9%	2.3%	9.6%	6.5%
energy scale	4.0%	9.6%	15.4%	12.2%
PID	($< 5\%$)	($< 2\%$)	3.9%	5.0%
fiducial volume	3%	3%	3%	3%
vertex shift	35.6%	25.6%	20.1%	18.6%
Cherenkov opening angle	($< 5\%$)	5.2%	3.7%	14.2%
ring counting	($< 9\%$)	($< 4\%$)	1.6%	9.3%
decay-e detection	0.7%	1.3%	0.3%	1.3%
Total	37%	28%	28%	29%

Table C.12: Systematic errors from uncertatinties of detector performances for the $N \to l^+\omega$ modes.

Bibliography

[1] H. Georgi and S.L. Glashow, Phys. Rev. Lett. **32** 438 (1974).

[2] P. Langacker, Phys. Rep. **72** 185 (1981).

[3] P. Langacker (1994), hep-ph/94112471.

[4] P. Nath and P.F. Pérez, Phys. Rep. **441** 191 (2007).

[5] C. McGrew *et al.*, Phys. ReV. D **59**, 052004 (1999).

[6] K.S. Hirata *et al.*, Phys. Lett. B **220**, 308 (1989).

[7] P. Langacker *et al.*, Phys. Rev. D **44**, 817 (1991).

[8] Particle Data Group, Phys. Lett. B **667**, 1 (2008).

[9] J. Hisano *et al.*, Nucl. Phys. B **402**, 46 (1993).

[10] H. Murayama *et al.*, Phys. Rev. D **65**, 055009 (2002).

[11] Y. Hayato *et al.*, Phys. Rev. Lett. **83**, 1529 (1999).

[12] K. Kobayashi *et al.*, Phys. Rev. D **72**, 052007 (2002).

[13] J.C. Pati and A. Salam, Phys. Rev. D **10**, 275 (1974).

[14] D.G. Lee, R.N.Mohapatra, M.K. Parida and M. Rani, Phys. Rev. D **51**, 229 (1995).

[15] N.T. Shaban and W.J. Stirling, Phys. Lett. B **291**, 281 (1992).

[16] J.C. Pati, Int. J. Mod. Phys. A **18**, 4135 (2003).

[17] H.D. Kim and S. Raby, JHEP **0301**, 056 (2003).

[18] W. Buchmuller, L. Covi, D. Emmanuel-Costa and S. Wiesenfeldt, JHEP **0409**, 004 (2004).

[19] J. Ellis, D.V. Nanopoulos and J. Walker, Phys. Lett. B **550**, 99 (2002).

[20] M. Machacek, Nucl. Phys. B **550**, 37 (1979).

[21] M.B. Gavela *et al.*, Phys. Lett. B **98**, 51 (1981).

[22] J.F. Donoghue, Phys. Lett. B **92**, 99 (1980).

[23] F. Buccella *et al.*, Phys. Lett. B **233**, 178 (1989).

[24] J. Ellis, Mary K. Gaillard and D.V. Nanopoulos, Phys. Lett. B **88**, 320 (1979).

[25] M.R. Krishnaswamy *et al.*, Phys. Lett. B **106**, 339 (1981).

[26] M.R. Krishnaswamy *et al.*, Phys. Lett. B **115**, 349 (1982).

[27] J. Bartelt *et al.*, Phys. Rev. Lett. **50**, 651 (1983).

[28] J. Bartelt *et al.*, Phys. Rev. D **36**, 1990 (1987).

[29] G. Battistoni *et al.*, Nucl. Instrum. Meth. A **245** 277 (1986).

[30] G. Battistoni *et al.*, Phys. Lett. B **133** 454 (1984).

[31] Ch. Berger *et al.*, Nucl. Instrum. Meth. A **262** 463 (1987).

[32] Ch. Berger *et al.*, Z. Phys. C **50** 385 (1991).

[33] W.W.M. Allison *et al.*, Nucl. Instrum. Meth. A **376** 36 (1996).

[34] R. Becker-Szendy *et al.*, Nucl. Instrum. Meth. A **324** 363 (1993).

[35] K. Arisaka *et al.*, J. Phys. Soc. Jpn **54** 3213 (1985).

[36] K.S. Hirata *et al.*, Phys. Rev. D **38** 448 (1988).

[37] Y. Fukuda *et al.*, Nucl. Instrum. Meth. A **501** 418 (2003).

[38] M. Shiozawa *et al.*, Phys. Rev. Lett. **81** 3319 (1998).

[39] H. Kume *et al.*, Nucl. Inst. and Meth. A **205**, 443 (1983).

[40] A. Suzuki *et al.*, Nucl. Inst. and Meth. A **329**, 299 (1993).

[41] R. Claus *et al.*, Nucl. Inst. and Meth. A **261**, 540 (1987).

[42] H. Ikeda *et al.*, Nucl. Inst. and Meth. A **320**, 310 (1992).

[43] T. Tanimori *et al.*, IEEE Trans. Nucl. Sci. **NS-36**, 497 (1989).

[44] T. K. Ohsuka *et al.*,*KEK Report* 85-10 (1985)

[45] M. Shiozawa *et al.*, IEEE Nuclear Science Symposium Conference Record, **2**, 632 (1994).

[46] J. George, Ph.D. Thesis, University of Washington (1998).

[47] K. Nakamura *et al.*, Nucl. Phys. **A268** 381 (1976).

[48] T. Yamazaki and Y. Akaishi, Phys.Lett. B **453** 1 (1999)).

[49] L. Salcedo *et al.*, Nucl. Phys. A **484**, 557 (1988).

[50] G. Rowe *et al.*, Phys. Rev. C **18**, 584 (1978).

[51] C. Ingram *et al.*, Phys. Rev. C **27**, 1578 (1983).

[52] M. Röbig-Landau *et al.*, Phys.Lett. B **373** 45 (1996).

[53] R.A. Arndt *et al.*, http://gwdac.phys.gwu.edu.

[54] B. Krusche *et al.*, Phys.Lett. B **358** 40 (1995).

[55] G.I. Lykasov *et al.*, Eur.Phys. J. A **6** 71 (1999).

[56] M. Kotulla, Phys.Rev.Lett. **100** 192302 (2008).

[57] M. Honda *et al.*, Phys.Rev.D. **75** 043006 (2007).

[58] T. Sanuki *et al.*, Astrophys. J. **545** 1135 (2000).

[59] J.Alcarez *et al.*, Phys. Lett. B **490** 27 (2000).

[60] W.R. Webber, R.L. Golden and S.A. Stephens, In *Proceedings of the 20th International Cosmic Ray Conference* (1987).

[61] E.S. Seo *et al.*, Astrophys. J. **378** 763 (1991).

[62] P. Pappini *et al.*, In *Proceedings of the 23rd International Cosmic Ray Conference* (1993).

[63] M. Boezio *et al.*, Astrophys. J. **518** 457 (1999).

[64] W. Menn *et al.*, Astrophys. J. **533** 281 (2000).

[65] M.J. Ryan, J.F. Ormes and V.K. Balasubrahmanyan, Phys. Rev. Lett. **28** 985 (1972).

[66] K. Asakamori *et al.*, Astrophys. J. **502** 985 (1998).

[67] I.P. Ivanenko *et al.*, In *Proceedings of the 23rd International Cosmic Ray Conference* (1993).

[68] Y. Kawamura *et al.*, Phys. Rev. D **40** 729 (1989).

[69] A.V. Apanasenko *et al.*, Astropart. Phys. **16** 13 (2001).

[70] K. Hänssget and J. Ranft, Comput. Phys. **39** 37 (1986).

[71] S. Roesler, R. Engel, and J. Ranft, Phys. Rev. D **57** 2889 (1998).

[72] G. Battistoni *et al.*, Astropart.Phys. **19** 269 (2003) [Erratum-ibid. **19** 291 (2003)]. (http://www.mi.infn.it/~battist/neutrino.html)

[73] G. Barr *et al.*, Phys. Rev. D **70**, 0423006 (2004).

[74] Y. Hayato, Nucl. Phys. Proc. Suppl. **112**, 171 (2002).

[75] G. Mitsuka, AIP Conf. Proc. **967** 208 (2007), AIP Conf. Proc. **981** 262 (2008).

[76] C. H. Llewellyn Smith, Phys. Rep. **3**, 261 (1972).

[77] S. K. Singh and E. Oset, Phys. Rev. C **48**, 1246 (1993).

[78] R. A. Smith and E. J. Moniz, Nucl. Phys. B **43**, 605 (1972). [Erratum-ibid. B **101**, 547 (1975).]

[79] C.H. Albright *et al.*, Phys. Rev. D **14**, 1780 (1976).

[80] K. Abe *et al.*, Phys. Rev. Lett. **56**, 1107 (1986).

[81] S. Barish *et al.*, Phys. Rev. D **16**, 3103 (1977).

[82] S. Bonetti *et al.*, Nouvo Cimento **38**, 260 (1977).

[83] M. Pohl *et al.*, Nuovo Cimento **26**, 332 (1979);
N. Arimenise *et al.*, Nucl. Phys. B **152**, 365 (1979).

[84] A.S. Vovenko *et al.*, Yad. Fiz. **30**, 1014 (1979).

[85] S. Belikov *et al.*, Z. Phys. **320**, 625 (1985).

[86] J. Brunner *et al.*, Z. Phys. C **45**, 551 (1990).

[87] D. Rein and L.M. Sehgal, Ann. of Phys. **133**, 1780 (1981).

[88] R. Feynman *et al.*, Phys. Rev. D **3**, 2706 (1971).

[89] S.K. Singh, M.J. Vicente-Vacas and E.Oset, Phys. Lett. B **416**, 23 (1998).

[90] C.H. Albright and C. Jarlskog, Nucl Phys. B **84**, 467 (1975).

[91] M. Glück, E. Reya and A. Vogt, Eur. Phys. J. C **5**, 461 (1998).

[92] P. Musset and J.P. Vialle, Phys. Rep. C **39**, 1 (1978).

[93] J.E. Kim *et al.*, Rev. Mod. Phys. **53**, 211 (1981).

[94] S.J. Barish *et al.*, Phys. Rev. **D17**, 1 (1978).

[95] S. Barlag *et al.*, Z. Phys. C **11**, 283 (1982).

[96] T. Sjöstrand *et al.*, CERN-TH-7112-93 (1994).

[97] D. Rein and L.M. Sehgal, Nucl. Phys. B **233**, 29 (1983).

[98] M. Hasegawa *et al.*, Phys. Rev. Lett. **95**, 252301 (2005).

[99] A. Kartavtsev, E. A. Paschos, and G. J. Gounaris, Phys. Rev. D **74**, 054007 (2006).

[100] F. Bergsma *et al.*, Phys. Lett. B **157**, 469 (1985).

[101] J. L. Raaf, Ph.D. thesis, University of Cincinnati (2005).

[102] H. Faissner *et al.*, Phys. Lett. B **125**, 230 (1983).

[103] E. Isiksal, D. Rein, and J. G. Morfin, Phys. Rev. Lett. **52**, 1096 (1984).

[104] H.W. Bertini *et al.*, Phys. ReV. C **6**, 631 (1972).

[105] S.J. Lindenbaum *et al.*, Phys. Rev. **105**, 1874 (1957)

[106] GEANT, CERN Program Library Long Writeup W5013 (1994).

[107] T.A. Gabriel *et al.*, IEEE Trans. Nucl. Sci. **36** 14 (1989).

[108] M. Nakahata *et al.*, J. Phys. Soc. Jpn. **55**, 3786 (1986).

[109] E. Bracci *et al.*, CERN/HERA 72-1 (1972).

[110] A.S. Carrol *et al.*, Phys. Rev. C **14**, 635 (1976).

[111] J. Kameda, Ph.D. thesis, University of Tokyo (2002).

[112] Y. Takenaga, Ph.D. thesis, University of Tokyo (2008).

[113] M. Shiozawa Ph.D. thesis, University of Tokyo (1999).

[114] E. R. Davies, *Machine Vision: Theory, Algorithms, Practicalities*, Academic Press, San Diego (1997).

[115] S. Kasuga *et al.*, Phys. Lett. B **374**, 238 (1996).

[116] M. Yamada *et al.*, Phys. Rev. D **44** 617 (1991).

[117] Y. Fukuda *et al.*, Phys. Rev. Lett. **81**, 1562 (1998).

[118] E. Aliu *et al.*Phys. Rev. Lett. **94**, 081802 (2005).

[119] D.G. Michael *et al.*Phys. Rev. Lett. **97**, 191801 (2006).

[120] S. Mine *et al.*, Phys. ReV. D **77**, 032003 (2008).

[121] D. Casper *et al.*, Nucl. Phys. Proc. Suppl. **112**, 161 (2002).

[122] J.P. Albanse *et al.*, Nucl. Phys. A **350**, 301 (1980).

[123] Y. Ashie *et al.*, Phys. ReV. D **71**, 112005 (2005).

[124] G. Mitsuka, Ph.D. thesis, University of Tokyo (2009).

[125] B. Viren, Super-Kamiokande Report No. 98-3,
http://www-sk.icrr.u-tokyo.ac.jp/sk/pub/98-3.pdf .